Aix Marseille Université

NNT : 0000AIXM0000

THÈSE DE DOCTORAT

Soutenue à Aix-Marseille Université
le 19 Décembre 2024 par

Lucas Duvert

Applications laser pour la modélisation du muscle squelettique sain et pathologique

Discipline
Biologie santé

Spécialité
Biotechnologie

École doctorale
ED 62 – Sciences de la vie et de la santé

Laboratoire/Partenaires de recherche
Marseille Medical Genetics (MMG) - U1251
Lasers, Plasmas et Procédés Photoniques (LP3) – UMR7341

Composition du jury

Dr Juan-Marcos Fernández-Pradas Université de Barcelone, Espagne	Rapporteur
Dr Cesare Gargioli Université Rome Tor Vergata, Italie	Rapporteur
Dr Vincent Mouly Centre de Recherche en Myologie	Examinateur
Dr Philippe Delaporte Aix-Marseille Université LP3	Président du jury
Dr Frédérique Magdinier Aix-Marseille Université MMG	Directrice de thèse
Dr Anne-Patricia Alloncle Aix-Marseille Université LP3	Co-directrice de thèse
Dr Didier Hilaire Agence Innovation Défense (AID)	Membre invité

Marseille Medical Genetics

LP3

Affidavit

I, undersigned, Lucas Duvert, hereby declare that the work presented in this manuscript is my own work, carried out under the scientific supervision of Dr Frédérique Magdinier and Dr Anne-Patricia Alloncle, in accordance with the principles of honesty, integrity and responsibility inherent to the research mission. The research work and the writing of this manuscript have been carried out in compliance with both the French national charter for Research Integrity and the Aix-Marseille University charter on the fight against plagiarism.

This work has not been submitted previously either in this country or in another country in the same or in a similar version to any other examination body.

Place Marseille, date 17 octobre 2024



Acknowledgments

Je tiens à exprimer ma profonde gratitude envers ma directrice de thèse, Frédérique Magdinier, pour toute son aide, sa gentillesse et sa bienveillance, surtout pendant la rédaction de ce manuscrit. Merci pour les corrections de dernière minute, à 21 heures le dimanche soir. Merci de m'avoir poussé et soutenu dans tout ce que j'ai entrepris pendant ces trois ans et de continuer à le faire jour après jour.

Merci à Anne-Patricia Alloncle et Adrien Casanova de m'avoir accompagné pendant ces trois années. Merci de m'avoir donné l'opportunité de ce stage de M2 et de cette thèse.

Merci aux rapporteurs et examinateurs d'avoir évalué ce travail.

Merci à l'Agence Innovation et Défense pour son soutien financier et pour avoir soutenu ce projet. Je souhaite également remercier Aix-Marseille Université pour son soutien financier.

Un grand merci à l'Institut MarMaRa pour son soutien à travers les années. Mon accès à cette thèse et la publication de ces travaux de recherche sont en grande partie grâce à vous.

Un immense merci au Pr. Stefano Testa, sans qui la plupart de ces résultats n'auraient pas vu le jour. Merci de m'avoir formé à la biologie cellulaire et merci pour toutes ces idées farfelues qui nous ont fait avancer. Merci d'avoir su trouver la motivation chaque jour, surtout quand je ne l'avais pas.

Merci au Dr Clarissa Murru pour tous ses dramas. Malgré son handicap mental, c'est la princesse qu'elle pense être. Merci de m'avoir accompagné un bout de temps pendant cette thèse. Travailler ensemble a été un plaisir.

Je remercie également le Dr Pol Sopena pour ses précieux conseils, pour m'avoir appris à me servir d'un laser et pour son implication indéfectible dans la vie du labo (et aussi pour ses schémas…).

Un grand merci à Fabrice Dessolis pour son aide et sa patience. Merci de nous avoir guidés dans Marseille (surtout à La Plaine) pendant toutes ces années, c'est toi le Vortex, Fabrice.

Merci à tous les « jeunes » du LP3, Enzo, Romain, Nicolas, merci de m'avoir changé les idées avec des projets annexes. Bonne chance pour vos thèses, vous allez assurer.

Merci à toute l'équipe du LP3 pour son soutien. Ce furent trois belles années en votre compagnie.

Merci à Loeva pour son enthousiasme et sa gentillesse, merci d'avoir jugé (négativement) la stérilité de notre manip. Merci, Solène, de m'avoir embarqué dans des coups fourrés ; les 13 minutes ont été une super expérience, c'est grâce à toi. Merci, plus généralement, à toute l'équipe d'Épigénétique du MMG d'avoir supporté mes présentations sur la physique des lasers – ça ne se reproduira plus, promis.

Merci à tous les stagiaires qui m'ont accompagné et aidé pendant ces trois années. Merci de m'avoir servi de psychologue et d'avoir supporté mon sarcasme permanent.

Merci à Anna d'être arrivée au bon moment. Merci à Sacha d'être aussi nul à Overwatch – un niveau de jeu aussi bas (surtout avec Widow) me redonnera toujours confiance en moi.

Enfin, je remercie mes parents pour leur soutien, même s'ils n'ont probablement toujours pas compris mon métier. Merci à mon frère de m'avoir appris à conduire une pelleteuse et merci à Djack d'avoir été le plus beau chien du monde.

Scientific production

Oral communications

L.Duvert, S. Testa, C. Murru, A. Casanova, F. Magdinier, A. P. Alloncle; Laser processes for skeletal muscle tissue engineering; 3D.Fab Days 2024 9-10 Juillet 2024, Oral, Lyon, France.

L.Duvert, C. Murru, S. Testa, A. Casanova, F. Magdinier, A. P. Alloncle ; Laser bioprinting: a new tool for skeletal muscle tissue engineering; JSFM 2023 15-17 Novembre 2023, Oral, La Baule, France.

L.Duvert, C. Murru, S. Testa, A. Casanova, F. Magdinier, A. P. Alloncle ; Laser-assisted bioprinting and structuring for muscle modeling; 20th IIM Meeting 2023 12-15 Octobre 2023, Oral, Assisi, Italie.

L.Duvert, C. Murru, S. Testa, A. Casanova, F. Magdinier, A. P. Alloncle ; Laser-assisted cell bioprinting and polymer structuring for the creation of bio-models; NanoBio 2023 11-15 Septembre 2023, Oral, Heraklion, Grece.

L.Duvert, C. Murru, S. Testa, A. Casanova, F. Magdinier, A. P. Alloncle; Combination of laser assisted bio-printing and laser structuration for the creation of bio-models; Colloque annuel MARMARA 08-09 Juin 2023, Oral, Marseille, France. (Prix meilleure communication orale)

L.Duvert, A. Casanova, S. Testa, C. Murru, F. Magdinier, A; P. Alloncle; Laser-Induced forward transfer for the creation of relevant bio-models; E-MRS Spring Meeting, symposium L; 29 Mai-2 Juin 2023, Oral, Strasbourg, France.

L. Duvert, A. Casanova, J. D. Robin, F. Magdinier, P. Delaporte, A. P. Alloncle ; Combination of two laser processes for the creation of relevant bio-models for therapeutical applications; Symposium annuel MARMARA 02-03 Juin 2022, Oral, Marseille, France.

Written communications

L.Duvert, A. P. Alloncle, F. Magdinier, S. Testa; A new laser-based subtractive process for creating highly organized *in vitro* human artificial muscles: an interesting tool for FSHD modeling; Myology 2024 22-25 Avril 2024, Poster, Paris, France.

L.Duvert, C. Murru, S. Testa, A. Casanova, F. Magdinier, A. P. Alloncle ; Laser bioprinting for the modelling of FSHD affected skeletal muscle; Myology 2024 22-25 Avril 2024, Poster, Paris, France.

L.Duvert, Adrien Casanova, Jérôme D Robin, Frédérique Magdinier, Anne-Patricia Alloncle; High repetition rate laser-induced printing of biopolymers: time -resolved study of multiple jet dynamics; E-MRS Spring Meeting, symposium Q; 30 Mai-3 Juin 2022; poster; virtual conference.

Publications

High repetition rate laser-induced printing of bioink with picosecond pulse durations: optimization of the printing process

Lucas Duvert, Adrien Casanova, Ahmed Al-Kattan, Stefano Testa, Frédérique Magdinier, Anne-Patricia Alloncle

Published in International journal of Bioprinting (2025) DOI: 10.36922/ijb.778z

Laser-induced Forward Transfer in picosecond regime for cell bioprinting

Lucas Duvert, Clarissa Murru, Ahmed Al-Kattan, Anne-Patricia Alloncle, Frederique Magdinier, Stefano Testa, Adrien Casanova

Published in Advanced Engineering Materials (2025) DOI: 10.1002/adem.202402478

Laser-induced Structuring of Biocompatible Polymers for the Controlled Orientation of Multinucleated Myotubes

Clarissa Murru, **Lucas Duvert,** Adrien Casanova, Ahmed Al-Kattan, Daniel Ferry, Frederique Magdinier, Stefano Testa, Anne-Patricia Alloncle

Under review in Advanced Material Interfaces

Ultrafast infrared laser application for highly organized skeletal muscle tissue modeling: from micrometric laser structuring to LIFT bioprinting

Lucas Duvert, Clarissa Murru, Adrien Casanova, Frederique Magdinier, Anne-Patricia Alloncle, Stefano Testa

In preparation

Assessment of laser-synthesized Si nanoparticle effects on myoblast motility, proliferation, and differentiation: towards potential tissue engineering applications

Clarissa Murru, **Lucas Duvert**, Frederique Magdinier, Adrien Casanova, Anne-Patricia Alloncle, Stefano Testa, Ahmed Al-Kattan

Published in Nanoscale Advances, (2024) DOI: 10.1039/d3na01020a

Résumé

Mon projet de thèse, très interdisciplinaire, est centré sur la combinaison de deux procédés laser : (i) bio-impression assistée par laser et (ii) texturation de surface par laser pour créer des micro-environnements de culture qui favoriseront la différenciation musculaire et permettront de fabriquer des modèles biologiques *in vitro* pertinents pour des études pré-cliniques. L'objectif final est d'optimiser et contrôler la prolifération, la migration, la différenciation, l'organisation et la maturation des cellules musculaires en population de myotubes matures *in vitro*.

La bio-impression assistée par laser consiste en l'utilisation de l'interaction laser-matière pour déposer, point par point, une bio-encre chargée en cellules. Plusieurs méthodes d'impressions existent, mais seule la technique LIFT (Laser-Induced Forward Transfer) permet de combiner une très haute résolution d'impression, la possibilité d'utiliser une large gamme de viscosité de bio-encre et une concentration cellulaire extrêmement importante.

En parallèle de leur application à la bio-impression, les lasers ultra-rapides peuvent aussi être utilisés pour modifier topographiquement la surface de polymères synthétiques et naturels. Ces modifications de surface se font sous la forme de micro-canaux guidant la croissance des progéniteurs musculaires afin d'en contrôler la différenciation et promouvoir la fusion en myotubes. Ce procédé peut alors être naturellement combiné au processus d'impression : des progéniteurs musculaires sont imprimés avec précision le long de repères topographiques induits par laser, ce qui améliore leur organisation tout en montrant un alignement sélectif des myotubes.

Ces modèles constitueront un outil de choix pour des applications diverses en recherche biomédicale. Elles offriront de nouvelles possibilités pour la modélisation de pathologies musculaires y compris en médecine personnalisée et pour le développement de thérapies ciblées.

Mots clés : Fabrication additive par laser, bio-impression, ingénierie tissulaire

Summary

This highly interdisciplinary thesis project focuses on the combination of two laser processes: (i) laser-assisted bioprinting and (ii) laser surface texturing to create culture microenvironments that will promote skeletal muscle differentiation and enable the fabrication of *in vitro* biological models relevant to pre-clinical studies. The ultimate goal is to optimize and control the proliferation, migration, differentiation, organization and maturation of skeletal muscle cells into mature myotube populations *in vitro*.

Laser-assisted bioprinting involves the use of laser-matter interaction to deposit a point-by-point cell-laden bioink. Several printing methods exist, but only the LIFT (Laser-Induced Forward Transfer) technique combines a very high printing resolution, the possibility of using a wide range of bioink viscosities and an extremely high cell concentration. These advantages make LIFT an ideal technique for creating precise 2D and 3D biological structures.

Alongside their application to bioprinting, ultrafast lasers can also be used to topographically modify the surface of natural and synthetic polymers. These surface modifications take the form of microchannels guiding the growth of muscle progenitor cells to control differentiation and promote their fusion into myotubes. This process can then be naturally combined with the printing process: muscle progenitors can be precisely printed along laser-induced topographical cues, enhancing the organization of the tissue while showing a selective and controlled myotube alignment.

Once validated, these models will provide a powerful tool for biomedical research while opening new possibilities for modeling muscle pathologies including for personalized medicine applications.

Keywords: laser additive manufacturing, bioprinting, tissue engineering

Index

Affidavit **2**
Acknowledgments **3**
Scientific production **5**
Oral communications 5
Written communications 5
Publications 6
Résumé **7**
Summary **8**
Index **9**
List of abbreviations **12**
1. Introduction **15**
1.1 Skeletal Muscle 15
1.1.1 Role and organization 15
1.1.2 Biological niche 17
1.1.3 Skeletal muscle cells 18
1.1.4 Muscle damages 21
1.1.4.1 Traumatic injuries 21
1.1.4.1.1 Healing process 21
1.1.4.1.2 Current therapies for VML 24
1.1.4.2 Genetic disorders 25
1.1.4.2.1 Muscle dystrophies 26
1.1.4.2.2 Current therapies 27
1.2 Disease modeling 29
1.2.1 Animal models 29
1.2.2 Cellular models 30
1.2.3 Induced pluripotent stem cells (iPSCs) 31
1.2.3.1 Interest of iPSCs 31
1.2.3.2 Use of iPSCs in cellular therapy 31
1.2.3.3 Improving the relevancy of iPSCs 33
1.3 Tissue engineering 34
1.3.1 *In situ* and *in vivo* strategies for SMTE 36
1.3.1.1 Biomaterials 36
1.3.1.2 Cell-loaded scaffolds 38
1.3.2 *In vitro* strategies for SMTE 40
1.3.2.1 Cell alignment by topography 41
1.3.2.1.1 Principle 41

1.3.2.1.2 Involved mechanisms 42
1.3.2.1.3 Materials and manufacturing 43
1.3.2.1.4 Laser-induced topography 44
1.3.2.2 Mechanical and electrical stimulation 46
1.3.2.3 Bioprinting 48
1.3.2.3.1 Inkjet 49
1.3.2.3.2 Extrusion 50
1.3.2.3.3 Laser-based bioprinting 50
1.4 Laser-induced forward transfer 51
1.4.1 LIFT principle of operation 52
1.4.2 LIFT in solids 54
1.4.3 LIFT in liquids 55
1.4.4 LIFT applied to bioprinting 57
1.4.4.1 Characterization of LIFT bioprinting 58
1.4.4.2 Application to tissue engineering 59
1.4.4.3 Single cell isolation 60
1.4.4.4 Printing of biomolecules 60
2.Objectives 63
3.Results 67
3.1 Article 1: High repetition rate laser-induced printing of bioink with picosecond pulse durations: optimization of the printing process 67
3.2 Article 2: Laser-induced Forward Transfer in picosecond regime for cell bioprinting 83
3.3 Article 3: Laser-induced structuring of biocompatible polymers for the controlled orientation of multi-nucleated myotubes 99
3.4 Article 4: Ultrafast infrared laser application for highly organized skeletal muscle tissue modeling: from micrometric laser structuring to LIFT bioprinting. 118
3.5 Article 5: Assessment of laser-synthesized Si nanoparticle effects on myoblast motility, proliferation, and differentiation: towards potential tissue engineering applications 165
4. Exploratory work 181
4.1 A novel laser-based subtractive process for creating highly organized *in vitro* human artificial muscles: a promising tool for FSHD modeling. 181
4.2 Development of an electrical stimulation system for modeling neuromuscular pathologies 185
5. Discussion 190
5.1 Experimental consideration for LIFT bio-printing 190
5.1.1 Protocols for thin donor layer preparations 190
5.1.2 Optimization for low-viscosity inks 192
5.1.3 Set-up optimization and future improvements 193

5.1.4 Laser choice 195
5.2 Optimization of LIFT for skeletal muscle bioprinting 197
5.2.1 Key parameters for cell survival 197
5.2.2 Receiver coating materials 198
5.2.3 Optimization of the coating layer protocol 199
5.3 Surface structuration 200
5.3.1 Biomaterial choice 200
5.3.2 Surface structuration of biomaterials for myoblast alignment 200
5.3.3 Surface structuration of polymers 202
5.4 Combination of LIFT bioprinting and surface structuration for skeletal muscle modeling 203
5.5 Future prospects 204
6. Conclusion 206
Bibliography 208

List of abbreviations

Numbers

2D = Two dimensions

3D= Three dimensions

A

AAV = Adeno-Associated Viral

ADSC = Adipose Derived Stem Cells

ATP = Adenosine Triphosphate

ATR FTIR = Attenuated total reflection Fourier-transform infrared spectroscopy

AuNP = Gold Nanoparticle

B

BA-LIFT = Blister Assisted Laser Induced Forward Transfer

C

CCD = Charge Coupled Device

cDNA = Complementary DNA

CW = Continuous Wave

CW-LIFT = Continuous Wave Laser Induced Forward Transfer

D

dECM = dECM

DGC = Dystrophin Associated Glycoprotein

DLaTGS = Deuterated lanthanum α-alanine-doped triglycine sulfate

DLS = Dynamic Light Scattering

DM = Differentiation Media

DMD = Duchenne Muscular Dystrophy

DMEM = Dulbecco's Modified Eagle Medium

DNA = Deoxyribonucleic acid

DPBS = Dulbecco's phosphate-buffered saline

DRL = Dynamic Release Layer

DUX4 = Double homeobox4

E

EC = Embryonic Cell

ECM = Extracellular Matrix

EDTA = Ethylenediaminetetraacetic acid

EDX = Energy Dispersive X-Ray

ES = Electric Stimulation

ESC = Embryonic Stem Cell

F

FA = Focal adhesion

FAP = Fibro-adipogenic Progenitor

FBS = Fetal Bovine Serum

FDA = Food and Drug Administration

FFMT = Functional Free Muscle Transfer

FGF = Fibroblast growth factors

FI = Fusion Index

FSHD = FacioScapulo Humeral Dystrophy

FTIR = Fourier-transform infrared spectroscopy

G

GAGs = Glycosaminoglycans

GV = Grey Value

H

hASC = adipose-derived stem cell

hESC = Human Embryonic Stem Cell

hESC-LESC = ESC-derived limbal epithelial stem cells

HGF = Hepatocyte Growth Factor

HLA = Human Leukocyte Antigen

HS = Horse Serum

I

ICP-MS = inductively coupled plasma mass spectrometry

iPSC = Induced Pluripotent Stem Cell

IR = Infrared

K

Klf4 = Kruppel-like factor 4

L

LED = Light Emitting Diode

LIFT = Laser Induced Forward Transfer

LIPSS = Laser-Induced Periodic Surface Structure

LITI = Laser-Induced Thermal Imaging

LMI = Laser Molecular Implantation

LP-LIFT = Long Pulsed Laser Induced Forward Transfer

LS = Laser Structured

M

MAPK = Mitogen-Activated Protein Kinase

MAPLE = Matrix Assisted Pulsed Laser Evaporation

MEA = Multielectrode Array

MGV = Mean Grey Value

MHC = Myosine Heavy Chain

mRNA = messenger ribonucleic acid

MSC = Mesenchymal Stem Cells

MTJ = Myotendinous Junction

MTT = 3-(4,5-dimethylthiazol-2-yl)-2,5-diphenyltetrazolium bromide, colorimetric assay for assessing cell metabolic activity.

N

NIL = Nanoimprint Lithography

NIR = Near Infrared

NMJ = Neuromuscular Junction

NOA = Norland Optical Adhesive

NP = Nanoparticle

O

Oct4 = Octamer-binding transcription factor 4

OoC = Organ-on-Chip

P

PBS = Phosphate-Buffered Saline

PCR = Polymerase Chain Reaction

PEG = Polyethylene Glycol

PEMF = Pulsed Electromagnetic Field Stimulation

PET-G = Polyethylene Terephthalate Glycol

PF = PEG-fibrinogen

PLA = Polylactic Acid

PMMA = Polymethyl Methacrylate

PS = Polystyrene

PUA = Polyurethane Acrylate

Q

qRT-PCR = Quantitative Real Time Polymerase Chain Reaction

R

ROI = Region of Interest

RT = Room Temperature

S

SC = Satellite Cells

SEM = Scanning Electron Microscope

SF = Stress Fibers

SiNp = Silicone Nanoparticle

SLA = Stereolithography

SMCHD1 = Structural maintenance of chromosomes flexible hinge domain containing 1

SMTE = Skeletal Muscle Tissue Engineering

Sox2 = SRY-box transcription factor 2

T

TE = Tissue engineering

TFT = Thin-Film Transistors

TPE-PDT = Two-Photon Excited Photodynamic Therapy

TEM = Transmission Electron Microscopy

U

USC = Urine Derived Stem Cells

UV = Ultraviolet

V

VML = Volumetric Muscle Loss

Introduction

1. Introduction

1.1 Skeletal Muscle

1.1.1 Role and organization

Skeletal muscle is a dynamic and plastic tissue. It corresponds to almost 40% of the human body's weight and 50 to 75% of all body proteins. As the primary component of the musculoskeletal system, skeletal muscles are attached to bones by tendons through the myotendinous junction (MTJ). The majority of muscles are voluntary, meaning they contract in response to a neural stimulus, allowing for conscious control over movement.

The primary functions of skeletal muscle can be categorized into two roles: mechanical and metabolic. Mechanically, skeletal muscle converts chemical energy into mechanical power, facilitating movement and maintaining posture. Metabolically, it acts as a reservoir for nutrients and plays a key role in regulating body temperature.

Skeletal muscle is a highly specialized tissue organized in a complex hierarchical pattern. It comprises several grades of bundled fascicles composed of tightly packed and parallelly aligned muscle fibers, also known as myofibers. These myofibers are further composed of myofibrils (1-2µm in diameter) made of end-to-end joined sarcomeres, the contractile unit of skeletal muscle. Sarcomeres are made by the interspersed arrangement of thin actin myofilaments and thick myosin myofilaments. It is this succession of thin and thick filaments that gives skeletal muscle its striated aspect (**Figure 1**).

Muscle fibers are large, multinucleated cells that range from 10 to 100 µm in diameter and can stretch for several centimeters in length. The nuclei of these fibers, called myonuclei, are located at the periphery of the fibers, beneath the sarcolemma. Importantly, muscle fibers are mitotically inactive and are considered as terminally differentiated, which prevent further mitosis and limits their ability to regenerate (Christopher A. McCuller et al., 2020; Dave et al., 2024).

The sarcolemma is a tubular sheath that surrounds each muscle fiber and functions as the cell membrane, separating the intracellular and extracellular compartments. It also regulates ATP concentrations necessary for muscle contraction. Surrounding the sarcolemma is the endomysium (or basal lamina), a thin layer of innervated connective tissue that contains blood capillaries. Fascicles, in turn, are surrounded by a layer of connective tissue known as the perimysium. The entire muscle is encased in the epimysium, a layer composed of collagen, reticular, and elastic fibers, which houses blood

vessels and nerves. The epimysium extends into the tendon, facilitating the transmission of muscle-generated forces to the bones.

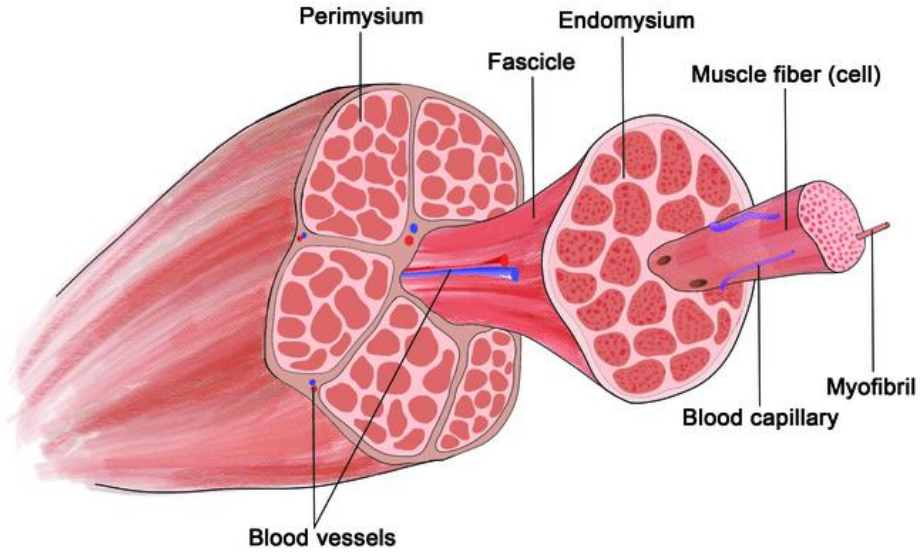

Figure 1 : Structure of skeletal muscle tissue (Fan et al., 2022)

The connective tissues within skeletal muscle, known as the extracellular matrix (ECM), account for 10 to 15% of the muscle volume. These tissues act as the "skeleton" of the muscle by providing structural support to the fibers and as a scaffold to blood vessels and nerves. They also participate heavily in skeletal muscle contraction by relaying the forces generated by the individual fibers and providing them with the necessary nutrients and oxygenation. The ECM composition can be divided into collagenous and non-collagenous glycoproteins, proteoglycans, and glycosaminoglycans (GAGs) (Cretoiu et al., 2018; Mahdy, 2019).

Skeletal muscle's myofibers are directly innerved by motor neurons from the central nervous system. These motor neurons branch throughout the whole muscle, forming connections with the myofiber at specialized sites called neuromuscular junction (NMJ). A single motor neuron can innervate multiple myofibers, collectively forming a motor unit. The size of the motor unit, and the number of fibers innervated depends on the muscle function. It can range from one fiber per axon for fine ocular movement, to several hundred fibers for force and power production (Valentine, 2017). Myofibers innervated by the same axon are typically distributed over a wide area to ensure even distribution of the contractile force (W. Liu & Chakkalakal, 2018, p. 4). The diverse range

of contractile properties and metabolic profiles within skeletal muscle, in combination with adaptive innervation, allows it to meet a broad array of physiological demands, from delicate movements to powerful contractions.

Satellite cells (SCs) are tissue-specific muscle stem cells located at the periphery of the muscle fibers between the sarcolemma and the endomysium. The proportion of SC varies greatly from muscle to muscle, ranging from 2 to 7% of the total muscle nuclei (Yusuf & Brand-Saberi, 2012). When activated by myogenic factors, the satellite cells differentiate into muscle progenitors known as myoblasts. These myoblasts proliferate and differentiate into myocytes, which fuse to form multinucleated myotubes. These myocytes either merge with existing muscle fibers or form new mature myofibers. A fraction of the activated SCs will self-renew to guarantee the sustainability of this process. The pool of SC decreases with age, reducing the capacity of muscle regeneration in aged individuals. Therefore, satellite cells play an essential role in muscle growth and give muscle cells the ability to fully regenerate after damage.

1.1.2 Biological niche

The frequency of satellite cells (SCs) varies significantly depending on muscle location, myofiber type, and developmental stage. SCs have a tendency to be located near blood vessels, making them more abundant in highly vascularized, slow twitch myofibers. A higher density of SCs around NMJs and MTJs suggests the existence of a specific environment ideal for SCs function. This environment, known as the cell "niche", is a complex dynamic network that provides structural support, as well as mechanical and chemical signals, to regulate stem cells activity (**Figure 2**) (Brun et al., 2017). The importance of this niche becomes especially clear during muscle regeneration, where the actions of SCs alone are not sufficient for adequate muscle repair. Indeed, multiple cell populations actively support and regulate SC activity throughout the regeneration process. These populations include immune cells, myogenic and non-myogenic progenitors, endothelial cells, and fibroblasts, creating a complex interaction network within the SC niche (Forcina et al., 2019).

At the core of this niche is the myofibril itself, which regulate the quiescence of SC in resting muscle. The basal lamina provides protection, transmits mechanical forces and encompasses capillaries and peripheral nerve cells. The myofiber expression of a protein called dystrophin associated glycoprotein (DGC), assures the interactions between the

basal lamina and the sarcolemma to stabilize the SC niche. The ECM also plays a key role in muscle regeneration by influencing the retention and activity of inflammatory response mediators. These mediators are partly produced by fibro-adipogenic progenitor (FAPs), a non-myogenic, multipotent cell population within the SC niche. FAPs have been shown to support and promote the proliferation of SCs through the secretion of pro-myogenic mediators. They also influence the *in vivo* commitment of myoblasts to terminal differentiation but can also be co-cultured *in vitro* with myogenic progenitors to downregulate quiescent markers and enhance the expression of myogenic markers such as MyoD and Myogenin (Joe et al., 2010). Endothelial cells (ECs) of blood vessels are also involved in muscle regeneration. Studies show that ECs promote muscle progenitor migration, proliferation, and terminal differentiation, further contributing to the regenerative network.

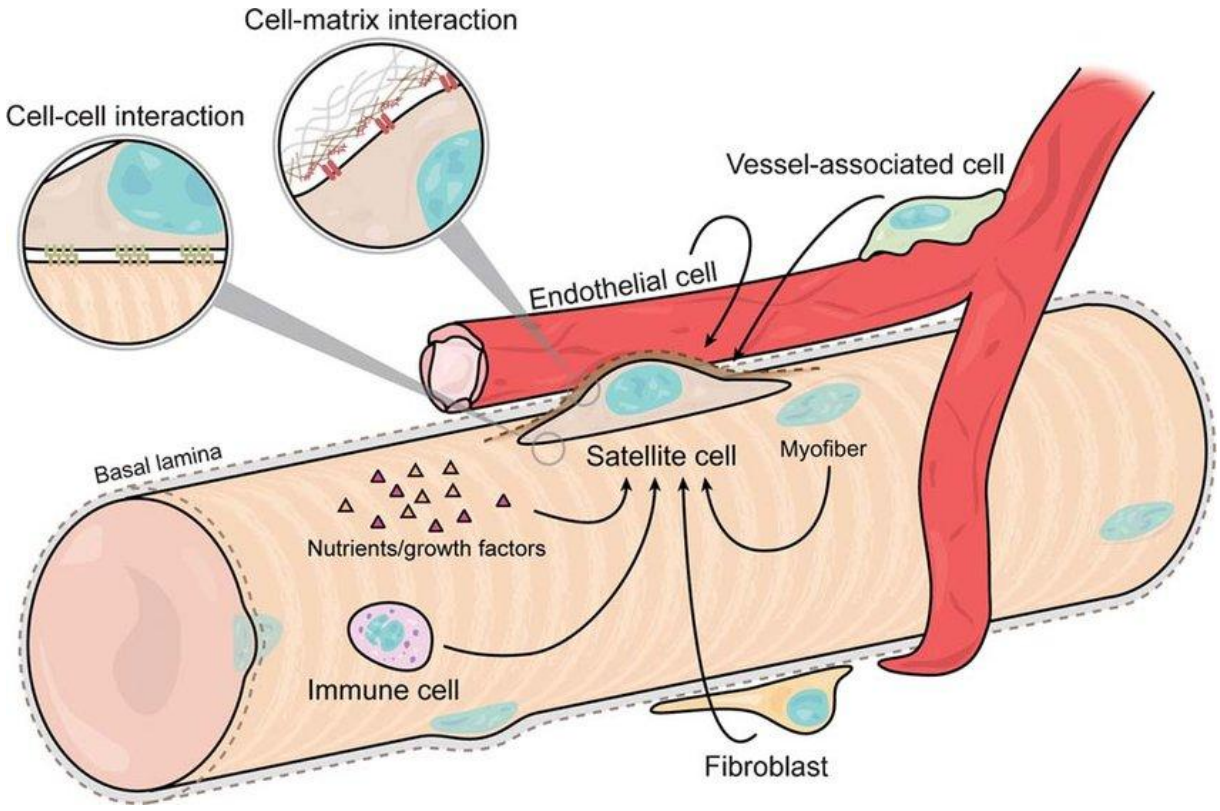

Figure 2: Representation of the satellite cell niche (Bentzinger et al., 2013)

1.1.3 Skeletal muscle cells

Myoblast cultures are typically obtained by isolating muscle stem cells from human or animal biopsies. This is typically achieved through enzymatic digestion of the muscle

tissue to extract quiescent satellite cells (K. H. Kim et al., 2020). Certain protocols allow for the recovery of intact myofibers with its associated SC, which subsequently proliferate and differentiate on the surface of the fiber. Under appropriate culture conditions and adequate surface coating, other isolation techniques can induce the migration of SCs from their original fiber to the culture dish, leading to extensive proliferation and differentiation (Shefer & Yablonka-Reuveni, 2005). However, the recovery method presents limitations, including a low number of extracted cells from a single biopsy batch, which makes it incompatible with robust high-throughput drug screening (Zschüntzsch et al., 2022). This issue is further exacerbated by inherent variation in myogenic potential, fusion capacity and proliferation abilities of the extracted SCs depending on the isolation method and the source donor. Additionally, prolonged *in vitro* culture and repeated passages has been shown to negatively affect the cellular phenotype and biological functions, leading to early senescence of the cultured cells (Machida et al., 2004). While these cells remain the most mature and physiologically relevant option, their use in applications such as drug screening, disease modeling or tissue engineering is severely limited by early degeneration and high variability.

To address the limitations of primary cells, myoblasts have been successfully immortalized, providing a more convenient and expendable source of relatively pure cells. The most commonly used immortalized murine myoblast lines are C212, isolated in 1977 (Yaffe & Saxel, 1977), and L6, isolated in 1968 (Yaffe, 1968). These lines both allow for rapid cell expansion and differentiation into multi-nucleated, contracting myotubes, making them ideal for a variety of studies, including investigations of culture conditions (Jang et al., 2022), myotube fusion (Thakur et al., 2020) and the development of innovative tissue engineering methods (Murru et al., 2024; Obed et al., 2022; Okano et al., 1997). Primary human myoblasts have also been immortalized through the forced expression of a telomerase subunit and cyclin-dependent kinase 4, allowing them to overcome cellular senescence (Mamchaoui et al., 2011; Santoso & McCain, 2020). Despite induced perturbations of the cell cycle, these immortalized human cells retain their myogenic potential both *in vivo* and *in vitro*, differentiating into multi-nucleated myotubes with mature sarcomeres. As a promising cell source, they offer reproducible and well characterized human muscle models (Nagashima et al., 2020) which will greatly contribute to fundamental and therapeutic studies (Shiomi et al., 2011).

Embryonic stem cells (ESCs) are extracted from the inner cell mass during the blastocyst stage of embryonic development. Under suitable conditions, these cells can be

cultured to proliferate indefinitely *in vitro*, while retaining their fundamental ability to differentiate into all three embryonic tissue layers: ectoderm, mesoderm and endoderm (National Research Council, 2002). Since their first successful culture in 1998 (Thomson et al., 1998), human ESCs have been recognized for their potential in clinical therapies, regenerative medicine and tissue engineering (Khademhosseini et al., 2020).

However, due to their origin, the use of hESCs raises significant ethical concerns. The number of mature cells obtained from ESCs differentiation remain too low for large-scale clinical applications and tissue engineering purposes. Additionally, the prospects of utilizing hESCs in clinical settings to restore damaged tissues are hindered by the risk of immune rejection following transplantation, along with the potential presence of genetical instabilities, further raising concerns about their safety (Sun et al., 2014).

Induced pluripotent stem cells (iPSC) are derived somatic cells that have been reprogrammed into embryonic-like pluripotent cells. iPSCs possess ES-like characteristics, including pluripotency, self-renewal capacity, and the ability to differentiate into various cell types found in the body. In this context, iPSCs offer a compelling solution to the allogenic rejection discussed with ESCs, as they can be derived from a patient's own somatic cells (Takahashi et al., 2007). While the true extent of iPSCs' pluripotency, compared to ESCs, remains a key area of investigation, iPSCs have emerged as a significant breakthrough in regenerative and personalized medicine. Since their first description in the mouse in 2006 (Takahashi & Yamanaka, 2006), iPSCs have provided an attractive alternative to ESCs and show prospects in various therapeutic contexts, offering promising potential for clinical applications, particularly in cell-based therapies and *in vitro* disease modeling and drug screening.

The initial reversion for the creation of iPSCs is done by transferring four transcription factors, among which the most used ones are Oct4, Sox2, Klf4, and c-Myc. The expression of these transcription factors initiates the reprogramming process by transitioning somatic cells from a differentiated state to a pluripotent state. Several methods have been used to deliver these factors, including retroviral, lentiviral, and non-viral methods. Non-integrative methods are now preferred to limit genetic variability induced by insertion of the reprogramming vectors.

The final efficiency and quality of iPSC generation are influenced by several factors, such as the nature of the cell source, the age of the donor, culture conditions or number of cell passages (Zhao et al., 2023). The ability of iPSCs to differentiate into specific cell types has generated substantial enthusiasm for their application in regenerative

medicine. Numerous studies have demonstrated the successful generation of various cell types from iPSCs, including cardiovascular (Lyra-Leite et al., 2022), hematopoietic (Demirci et al., 2020), muscle (Delourme et al., 2020), neurons (Autar et al., 2021), retinal, and islet β cells. Additionally, iPSC-derived cells have shown effectiveness in cell therapy for genetic diseases, further underscoring their therapeutic potential (George Kolios et al., 2013; F. Zeng & Zhou, 2011).

1.1.4 Muscle damages

1.1.4.1 Traumatic injuries

1.1.4.1.1 Healing process

Given its predominance in the body and its essential functional role, skeletal muscle is particularly susceptible to injury, lesions, and stress with mechanical trauma being the most common cause. Muscle injuries are typically categorized into three types based on the extent of damage to the basal lamina and myofibers:

- Segmental necrosis

The multinucleated structure of myofibers often results in localized segmental *in situ* necrosis, where only a portion of the myofiber undergoes cell death. The length of the affected segment can vary significantly, thus affecting the chances of a successful regeneration. While segmental necrosis can occur in response to muscle disorders, more extensive necrosis generally follows traumatic events or extreme stress. Damage to the sarcolemma leads to excessive calcium release into the myofiber's intracellular fluid. This calcium accumulation is a common trigger of cell necrosis and leads to the mineralization of the fiber (Valentine, 2017). The cell's death is rapidly followed by a gradual dissolution of the contractile material. Six to eight hours later, macrophages and leukocytes are recruited to clear the necrotic area of cytoplasmic debris (Karpati & Molnar, 2008). Where the entire myofiber section is removed, the basal lamina and the satellite cells adjacent to the necrotic segment are crucially left intact. The basal lamina is able to forms a scaffold to guide the proliferation of newly activated myoblasts, which will, in turn, fuse into myotubes that will mature into new myofiber over a few days, restoring muscle structure and function.

- Muscle strains

Muscle strains mostly arise from undirect trauma when the muscle fiber cannot cope with the mechanical overload placed on them, leading to their tearing. They are characterized by damages to the basal lamina, and surrounding connective tissue, endangering the overall myofiber (**Fig 3.A-E**). The healing process in strains can be divided into three phases: destruction, repair, and remodeling.

As in segmental necrosis, the destruction of the sarcolemma entails the myofiber's necrosis at the injured site. To prevent further necrosis, a contraction band isolates the unaffected sarcomere from the damaged zone, reforming a new sarcolemma (Järvinen et al., 2008).

The initial inflammatory response begins with the arrival of neutrophils, which appear within hours of injury. These cells will be able to phagocyte the damaged cells and release chemoattractant cytokines, further attracting monocytes and M1 macrophages (Mahdy, 2019; Mann et al., 2011). Pro-inflammatory M1 macrophages, known to stimulate satellite cell proliferation, later differentiate into anti-inflammatory M2 macrophages, which promote satellite cell differentiation into myoblasts. The rupture of the basal lamina also releases hepatocyte growth factor (HGF) and fibroblast growth factors (FGF), which further activate and promote the proliferation and migration of SCs, initiating the repair phase.

SCs are guided by the adjacent basal membrane surrounding the necrotic area in the direction of the wound. They differentiate and fuse to form multinucleated myotubes (Carnes & Pins, 2020; Kiran et al., 2021) that will, in 5 to 6 days, bridge gaps in the basal lamina (2 to 4mm wide) and replace the necrotized myofiber (Valentine, 2017). During this process, a hematoma fills the injured myofiber undergoing necrosis, where blood-derived fibrin and fibronectin cross-link to form a temporary ECM. This initial matrix acts as a scaffold for the fibroblasts that will, in turn, synthesize proteins and proteoglycans to restore the lost connective tissue. The scar tissue will then condense into a small connective tissue mass composed mainly of type I collagen (Järvinen et al., 2005). This process occurs in parallel with the regeneration of the myofibers.

The remodeling phase begins 2 to 6 weeks after the injury. This phase concludes the maturing of the myofibers and is accompanied by the repair and replacement of the damaged ECM and the remodeling of the previously formed scar tissue. Newly formed myofibers on each side of the injury adhere to the scar tissue that separates them, thus creating temporary MTJ. The connective tissue's size will diminish with time, bringing the new myofibers together to form a complete and continuous muscle. As previously

discussed, muscle regeneration and tissue maturation are highly dependent on the revascularization and reinnervation of the recently formed myofibers. New capillaries will develop from the remaining blood vessels near the injured area to ensure an adequate oxygen supply. An absence of innervation during the regeneration phase will not prevent the formation of new myotubes but will lead to atrophy if this absence persists (Slater & Schiaffino, 2008; Turner & Badylak, 2012). In normal conditions, these new muscle fibers are morphologically and functionally identical to undamaged muscle tissue (Mahdy, 2019).

- Volumetric muscle loss (VLM)

VLM refers to the traumatic or surgical loss of significant skeletal muscle mass, resulting in chronic functional deficits and cosmetic deformities (Grogan et al., 2011). If more than 20% of the muscle is affected, the injury is beyond the previously described natural regenerative process of skeletal muscle (Greising et al., 2019). In these cases, muscle repair is limited, and the injury results in excessive scar tissue formation, denervation, and permanent loss of muscle function (Corona et al., 2016; Turner & Badylak, 2012).

In these types of injuries, the destruction of the basal lamina in VML interrupts the normal regeneration pathways by removing essential biophysical and biochemical cues required for SCs activation (**Fig 3.F-J**) (Carnes & Pins, 2020). Growth factors in the basal lamina are no longer present, and the absence of mechanical guidance leads to the lateral migration of SCs; the destroyed basal lamina cannot act as a scaffold for myoblast alignment. As a result, fibrosis becomes the predominant response, and scar tissue from the natural inflammatory response now forms faster than new myofibers. This scar tissue prevents the newly formed myotubes from reconnecting the extremities of the injured area. Hence, permanent MTJs form between the remaining myofibers and the scar tissue, resulting in a reduced range of motion and torque production. In addition to excessive fibrotic tissue, the loss of peripheral and intramuscular nerves as well as NMJ and motoneurons-muscle fiber signaling, further impairs muscle function and restricts regeneration. Without adequate innervation, new muscle fibers cannot maintain normal function resulting is increased muscle atrophy and weakening of the overall muscle performance (Ahuja et al., 2021).

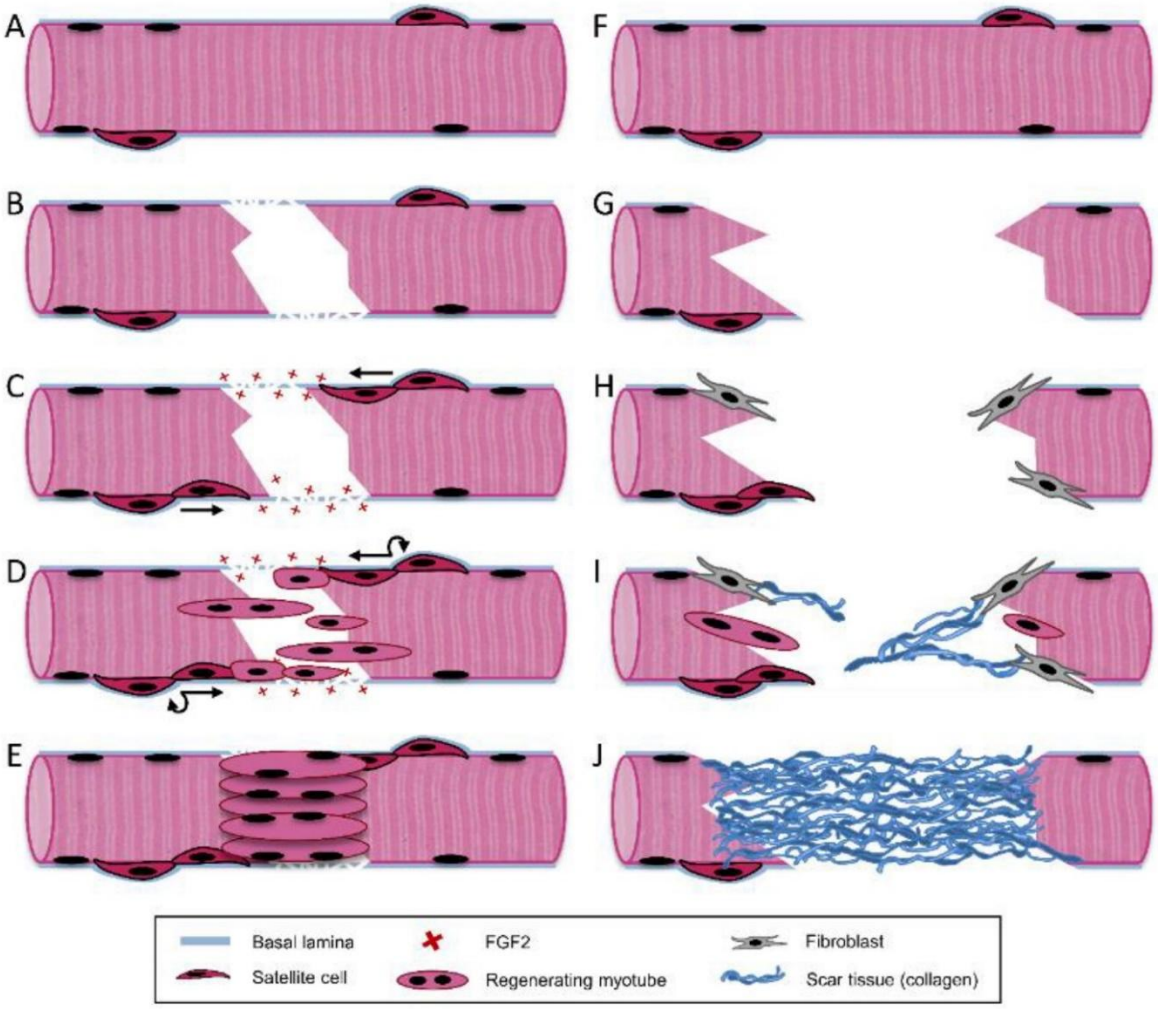

Figure 3: Skeletal muscle regeneration for small scale injuries (**A-E**) and volumetric muscle loss (VML) (**F-J**) Healthy muscle tissue (**A**) experiences a minor injury that damages the myofiber and the surrounding basal lamina (**B**). The damaged basal lamina releases growth factors activating satellite cells, which multiply and move to the injury site along the basal lamina (**C**). These satellite cells then fuse to form myotubes and simultaneously renew themselves (**D**). The muscle tissue fully regenerates, with the myotubes properly aligned (**E**). In the case of a large-scale VML injury (**F**), most of the basal lamina and satellite cells are destroyed (**G**). Without these signals, satellite cell-driven regeneration weakens, and fibroblasts start entering the wound (**H**). This leads to disorganized myoblast infiltration and collagen build-up (**I**), causing scar tissue formation and reduced muscle function (**J**). (Carnes & Pins, 2020).

1.1.4.1.2 Current therapies for VML

VML injuries typically occur as a result of high-energy civilian trauma or combat-related extremity wounds. These injuries often involve open fractures accompanied by significant soft tissue loss. VML is particularly prevalent in battlefield injuries, with studies showing that 54% of soldiers wounded in combat experience musculoskeletal damage, and of those, 53% suffer soft tissue injuries. Among military personnel discharged due to muscle-related conditions, over 90% have sustained injuries resulting in VML (Kozan et al., 2023). Depending on the severity of the injury, the affected limb may

be either saved or amputated. In cases where the limb is salvaged, functional recovery is not guaranteed, and chronic impairment is a frequent outcome (Testa et al., 2021). Post-surgical treatments for VML are largely focused on rehabilitative and physical therapies aimed at adapting the remaining skeletal muscle tissue rather than fully restoring the injured area. Physical exercise helps to alleviate passive muscle stiffness caused by extensive fibrosis. This method involves the release of growth factors, modulation of the immune response, promotion of vascularization, and reduction of scar formation. In addition to these benefits, physical therapy also entails nerve regeneration and improve muscle fiber reinnervation, enhancing overall functionality (Ahuja et al., 2021). The remaining tissues surrounding the injured area also exhibits improved muscle strength and reduced stiffness (Greising et al., 2019). These benefits remain hard to quantify due to the lack of a standardized evaluation methodology and clinical reports.

For more severe cases of VML, the positive effects of therapy are often more limited, but even in these cases, small improvements can have a meaningful impact on the patient's quality of life (Greising et al., 2018).

The preferred treatment for VML is functional free muscle transfer (FFMT), an autologous tissue transfer involving the transplantation of innervated and vascularized skeletal muscle tissue to non-functional areas (S. Das et al., 2020). Donor muscle units are selected based on their strength and the absence of substantial morbidity or functional deficits at the donor site after harvest (Fischer et al., 2013) . This method is commonly used to restore motor function and joint mobility for patients presenting severe functional impairment (Grogan et al., 2011).

However, FFMT's has several limitations, including the scarcity of available donor tissue, donor site morbidity, risks of infection or necrosis of the graft, and the need for multiple surgeries. The success of the surgery can also vary greatly depending on the extent and location of the treated injury. Anyhow, after FFMT surgery, physical therapy once again helps to regain muscle function, increase strength, and improve range of motion up to 2 years postoperatively (Chi et al., 2023).

1.1.4.2 Genetic disorders

Significant muscle loss and atrophy can also result from various physiological factors, including poor lifestyle choices, prolonged inactivity, aging, or genetic conditions like muscular dystrophies and myopathies.

1.1.4.2.1 Muscle dystrophies

Muscular dystrophies are a group of primary muscle disorders, typically characterized by progressive muscle weakness and wasting, along with histological features such as uneven fiber diameter, fibrosis and the presence of central nuclei. This group includes congenital diseases with very early onset, and pathologies with later onset, such as limb-girdle dystrophies (Bushby et al., 2007). The underlying cause of muscular dystrophy lies in the mutation of genes responsible for muscle structure and function, leading to the gradual degeneration and loss of muscle fibers (LaPelusa et al., 2024). To date, over forty genes have been identified as responsible for these diseases, most of which code for proteins associated with ECM, sarcolemma, or sarcomere.

To validate the tools and approaches that were developed during this PhD research project, our experimental approaches were tested in cells from patients affected with muscle dystrophies, and more particularly, Duchenne Muscular Dystrophy (DMD) and FacioScapuloHumeral Dystrophy (FSHD).

Duchenne muscular dystrophy (DMD) is the most common muscular dystrophy, with an incidence of 1:3500 male births. The disease is caused by mutations in the *DMD* gene located on the X chromosome that encodes Dystrophin. DMD is characterized by the progressive wasting of skeletal muscle with symptoms generally appearing in the first years of life. A delay in the acquisition of walking is followed by first limb-girdle muscles weakness by the age of 5 years, the inability to walk by the age of 8 to 12 years followed by respiratory failure and cardiomyopathy. Additionally, the disease is also often associated with delayed speech acquisition, as well as intellectual disability, autism spectrum disorder or attention deficit disorder (Ricotti et al., 2016). The life expectancy of DMD patients ranges between 20 and 45 years.

At the cellular level, pathological changes include the absence of Dystrophin at the membrane of the muscle fibers, increased adipose and connective tissue between muscle fibers, increased variability in muscle fiber size, infiltration of inflammatory cells, and centrally located nuclei, which are indicative of degenerating and regenerating muscle fibers (Lovering et al., 2005).

Facioscapulohumeral muscular dystrophy (FSHD) is the third most common form of muscular dystrophy, after DMD and myotonic dystrophy. Its prevalence is now estimated between 1:8,000 and 1:12,000 (Deenen et al., 2014). FSHD is inherited as an autosomal dominant trait, with about 30% of cases arising *de novo*, often due to somatic mosaicism in the parents (van der Maarel & Frants, 2005). FSHD causes progressive, asymmetrical muscle weakness, initially affecting the face, shoulders, and upper arms muscles. The average onset is in the second decade of life, though a more severe infantile form occurs in 4–21% of cases (Of et al., 1994). Early symptoms include facial weakness, difficulty raising the arms, and scapular winging. The disease may eventually affect trunk and lower limb muscles, making movement difficult (Lim et al., 2020). Symptom severity varies, with some patients remaining asymptomatic and others requiring a wheelchair. Some may develop hearing loss or vision issues due to retinal involvement (Of et al., 1991).

There are two types of FSHD: FSHD1 (95% of cases) is caused by contraction of D4Z4 repeats on chromosome 4q35, while the vast majority of FSHD2 patients (5%) carry a variant in the *SMCHD1* gene. Both types result in epigenetic alterations leading to abnormal expression of the *DUX4* gene, driving disease progression. Clinically, FSHD1 and FSHD2 are very similar, though FSHD2 tends to have a later onset. Diagnosis relies on clinical examination, family history, and genetic testing for D4Z4 repeat contraction (FSHD1) or *SMCHD1* mutations (FSHD2). Muscle biopsies may show signs of inflammation and degeneration (Wang & Tawil, 2016). However, the histological phenotype is not specific to the disease but more representative of a dystrophic phenotype.

1.1.4.2.2 Current therapies

Despite several strategies aimed at delaying the progression of muscle dystrophies, no definitive solutions have been found to stop the diseases entirely, and numerous investigations are pushing in this direction. Gene therapy exploits the ability of viruses to deposit their genome into a variety of cells to replace the defective genomic material of the dystrophic cells. This strategy is not dependent on specific mutations in the patient gene, emphasizing the simplicity of the approach and versatility across various conditions. The main challenge, however, lies in identifying a safe and efficient method

for delivering the corrected genetic material while ensuring long-term expression in muscles throughout the body (Goyenvalle et al., 2011).

Three types of viral vector can be used for this purpose: adenoviral, adeno-associated viral (AAV) and lentiviral vectors. Lentiviral vectors have been proven successful in integrating transgenes into the genome of quiescent and active cells. They offer low inherent immunogenicity and a relatively large carrying capacity, but they have not been shown to achieve widespread tissue transduction *in vivo*, resulting in too low efficiency for therapeutic applications.

Adenoviral viral vectors only exist as non-integrated episomes following infection. Despite presenting large carrying capacity and having been proven effective for gene transfer in immature and regenerating muscle, the use of immunosuppression is required for long-term transduction. Additionally, acute cytotoxic T cell response, toxicity in non-human primate and the reported death of a patient following adenoviral gene therapy are all major safety concerns.

AAV consists of a protein shell surrounding and protecting a single-stranded DNA, they belong to the parvoviruses family which require a helper virus for replication and assembly (Naso et al., 2017). AAV is currently the only vector used in clinical trials. Its recombinant form has demonstrated stable gene expression following intramuscular injection for up to 7 years in dogs. AAV's low immunogenicity and ability to efficiently pass from capillaries to transduce surrounding tissues make it particularly valuable for treating muscular dystrophies. Furthermore, the absence of viral gene and the ability to encapsulate DNA sequences of interest make AAV one of the safest strategies for gene therapy. In the case of DMD, due to the large size of the dystrophin gene, the elaboration of effective vectors has been complimented with methods to truncate the gene of interest into a smaller "micro-dystrophin", able to be transfected through AAV strategies with minimal functional impact. However, AAV vectors are extremely expensive to manufacture, making large-scale treatments currently unfeasible (Collins et al., 2023).

In cases of advanced muscle wasting, the expression of dystrophin in the surviving fibers alone insufficient to restore muscle function (Cordova et al., 2018). Stimulating higher levels of muscle regeneration can have a positive impact on dystrophic muscles. This can be done achieved through the co-expression of factors such as insulin-like growth factor-1 (Philippou & Barton, 2014) or follistatin (Rodino-Klapac et al., 2013) alongside micro-dystrophin. Studies in mice have shown that this approach leads to

increased muscle mass, improved muscle architecture and increased force. Similar results can also be achieved by regulating and controlling fibrosis and inflammation, both of which hindering the effectiveness of gene therapy on dystrophic muscle. Downregulating fibrosis pathways to decrease the expression of ECM proteins, coupled with micro-dystrophin treatment has indeed successfully showed completely restored muscle strength (Heller et al., 2017).

Similarly to VML, supportive therapy and preventive treatment, including physiotherapy, pain management, and, in the case of FSHD, scapular fixation surgery, can all improve the patient's quality of life (Aguirre et al., 2023).

1.2 Disease modeling

1.2.1 Animal models

Disease modeling plays a key role in understanding the molecular and biochemical structure of skeletal muscle myopathies and developing effective treatments. Animal models of diseases are particularly relevant for therapeutic development since they retain the complexity of the native human muscle. However, modeling and recapitulating myopathies such as FSHD, which arises from the rearrangement of a complex genomic region, absent in the animal, is particularly challenging. While orthologous genes can be used in the animal model, the relevance to FSHD remains uncertain, as the underlying pathophysiology described in mouse models often differs when referring to patients.

An alternative approach that has been developed to model the disease, is the direct induction of *DUX4*, in animal muscle tissue. Several models have been developed using this strategy, including mRNA injections into zebrafish or xenopus embryos, generation of transgenic mice and Drosophila, and AAV vector-based infection in mice (DeSimone et al., 2020). While each model offers distinct advantages, none fully encompasses the complete physiological and pathological features of FSHD.

In DMD and other inherited myopathies, the multiplicity of genetic mutations and the associated disease expression also complicate the use of animal models. The diversity of genotypes and phenotypes makes it impractical to create models that fully represent the spectrum of inherited human myopathies (Ariyasinghe et al., 2021). The inadequacy of animal models with drug development and clinical applications is particularly

highlighted in the field of cancer research, where the success rate of translating findings from animal models to clinical trials is less than 8% (Mak et al., 2014). This low success rate is further exacerbated by the fact that animal testing is both relatively low throughput and extremely costly, especially when considering drug development time (Van Norman, 2019).

1.2.2 Cellular models

In contrast to animal modeling, *in vitro* testing based on human tissues is significantly faster, less expensive, and yields more relevant results along with a more straightforward approach. The genetic variability of skeletal muscle dystrophies is addressed by creating large cell banks from affected patients. Primary myogenic cell lines are first isolated from patient biopsies, the associated pathological symptoms are documented, and the cell lines are made available to researchers through various repositories (DeSimone et al., 2020). To counter the senescence of primary cells and avoid the need for additional biopsies, the immortalization of diseased-affected cell lines has been widely used with success (Arandel et al., 2017). While the procedure has expanded the availability and usefulness of the cell lines, immortalized myoblasts are prone to the expression of carcinogenic gene and the acquisition of mutations during prolonged subculturing. These issues can potentially alter the cellular phenotypes and subsequently compromise the physiopathological accuracy of the targeted disease model. Additionally, the *in vitro* environment is often oversimplified, typically relying on a single-cell type cultured in a monolayer. As a result, data from these cultures may fail to encompass the complex cellular interactions of the skeletal muscle niche and the important role of the ECM that are occur *in vivo* (Segeritz & Vallier, 2017, p. 9).

In this context, iPSCs have emerged as a valuable alternative as they address many of the limitations of primary cell lines while maintaining similar gene expression and functional characteristics (Leslie Caron et al., 2016). Importantly, iPSCs offer the ability to generate any affected cell type from a patient, significantly broadening the scope of disease studies.

1.2.3 Induced pluripotent stem cells (iPSCs)

1.2.3.1 Interest of iPSCs

Understanding the mechanisms underlying human pathologies is critical for developing effective therapeutic treatments. Traditional rodent models, while useful, often fail to accurately mirror or fully recapitulate human clinical pathophysiology, presenting significant challenges in disease modeling and drug discovery. iPSCs have emerged as a highly promising platform to address these limitations,

iPSCs can be directly generated from a patient's somatic cells, such as skin fibroblasts or blood cells, offering an unlimited supply of disease-relevant cells that are personalized to the individual. This technology allows for the generation of disease-specific iPSCs, which can be used in established directed differentiation protocols. By doing so, iPSCs help circumvent many of the limitations seen with ESCs, such as the reliance on gene editing to model specific diseases and inevitable ethical issues. Models built with iPSC derivatives also demonstrate functional and phenotypic traits comparable to their human *in vivo* parallel (Nicholson et al., 2022). The development of iPSC reprogramming technology has thus significantly enhanced the potential of *in vitro* disease modeling and drug discovery by providing more biologically relevant, patient-specific cell models (C. Liu et al., 2018; Rowe & Daley, 2019).

However, the reprogramming processes involved in iPSC generation are characterized by epigenetic remodeling and alterations in chromatin structure. These changes can influence the phenotype of iPSCs, and in some cases, the residual epigenetic memory from the somatic donor cells may limit pluripotency, resulting in a biased differentiation potential. Addressing these epigenetic challenges is crucial for ensuring the full therapeutic potential of iPSCs in disease modeling and clinical applications (Iberite et al., 2022).

1.2.3.2 Use of iPSCs in cellular therapy

Recent advancements in gene editing and delivery technologies have made it possible to correct or introduce mutations without the need for viral vectors or non-human genomes (C. Kim, 2014). Combined with iPSC development, the scope of personalized medicine has expanded significantly.

(iPSC)-based cellular therapies can be categorized into two main approaches: autologous and allogeneic cell transplantation (**Fig 4**).

- **Autologous** transplantation involves generating iPSCs from a patient's own cells and differentiating them into the desired cell types for treatment. This method minimizes the risk of immune rejection since the cells originate from the patient. However, autologous transplantation is a lengthy and expensive process, which makes it less adapted for treating acute or rapidly progressing disorders.
- On the other hand, **allogeneic** transplantation uses iPSCs derived from donors with matched human leukocyte antigen (HLA) profiles, similar to organ transplants. While this approach is faster and more clinically scalable, it carries an inherently higher risk of immune rejection due to the nature of the process. Indeed, despite their typically low HLA expression, iPSC derivatives can still trigger an immune response from the recipient. For allogeneic cell therapies to be effective, it is thus essential to achieve a certain level of HLA compatibility between the iPSC donor and the recipient. iPSCs reprogrammed from donors with similar homozygous HLA haplotypes hold great promises in this regard, but finding suitable matches is time-consuming, challenging, and costly (Madrid et al., 2024; Nicholson et al., 2022).

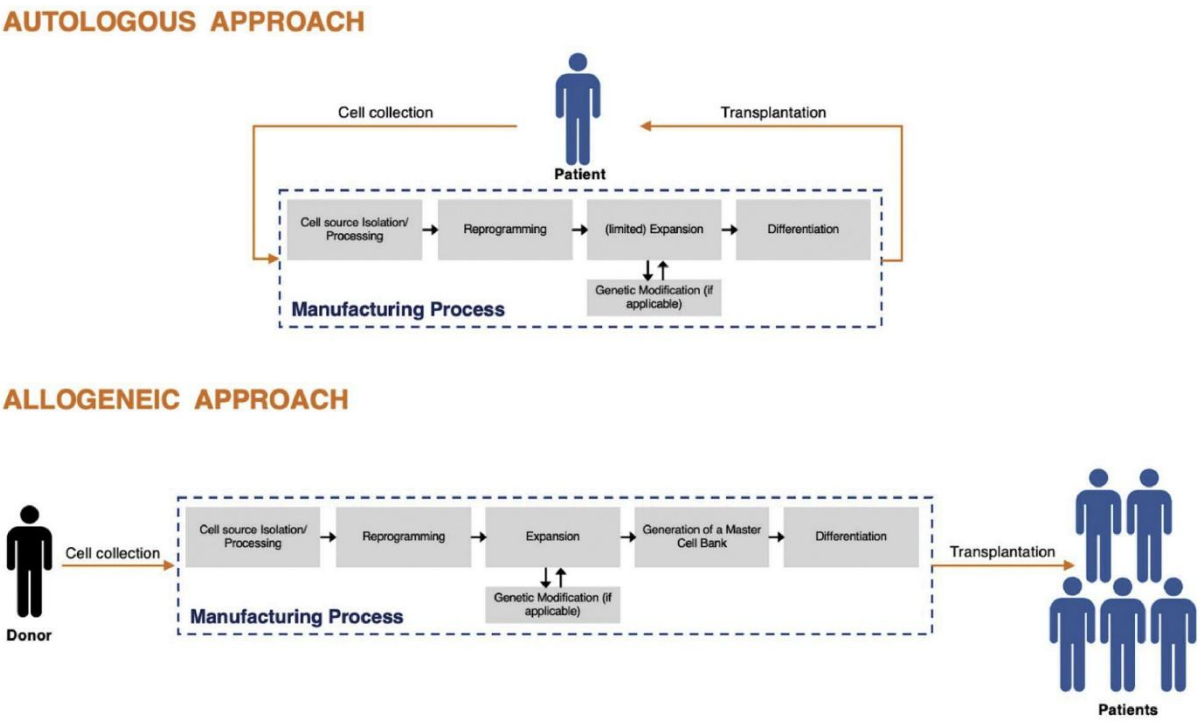

Figure 4: Autologous and allogenic approach for iPSC-based cell therapy (Madrid et al., 2024)

1.2.3.3 Improving the relevancy of iPSCs

The ability of iPSCs to differentiate into any cell type makes them perfectly adapted for generating tissue-engineered skeletal muscle. Their applications range from transplantation to disease modeling and drug screening while offering a valuable alternative to animal models. They allow for more accurate recapitulation of human muscle physiology, providing a robust tool to assess drug effectiveness and investigate rare diseases and patient-specific genetic variations.

The differentiation of iPSCs into myogenic progenitors can be done through the introduction or the modification of key genes such as Pax-7, responsible for satellite cell specification and function, or Pax-3, which plays a role in the myogenic fate during embryogenesis. However, the addition of external genes, along with the potential associated mutations, has to be carefully considered. Another approach to activate the myogenic program lies in the exposure of iPSCs to specific molecules such as CHIR99021 and LDN193189. These molecules have the capacity to influence precise pathways to initiate a myogenic signaling cascade and induce iPSCs differentiation into myogenic progenitors. While effective, this method requires precise protocols and meticulous execution to ensure reliable differentiation.

For skeletal muscle tissue engineering purposes, once the myogenic path has been induced, it remains essential to ensure the formation of mature myofibers. For this purpose, differentiation protocols based on starvation methods through the use of horse serum are commonly used for their simplicity and proven efficiency. However, studies have shown that differentiation can be improved through different 2D tissue engineering strategies such as specially patterned culture surfaces for cell alignment and tunable rigidity and elasticity of the culture substrate.

Despite improvement in myogenic maturation, 2D cultures cannot fully replicate the biological niche characteristic of skeletal muscle. For this reason, three-dimensional (3D) cultures that mimic the extracellular environment are increasingly used to improve the maturation and maintenance of skeletal muscle tissue. The iPSCs-derived muscle tissue can also be used to successfully model various muscle-related diseases. By differentiating affected human muscle progenitors in hydrogels under tension, Maffioletti et al. (2018), achieved aligned myofibers and successfully recapitulated key pathological features of the modeled diseases. In 2013, Tchao and colleagues compared muscle-derived stem cells and hiPSC-derived cardiac cells within a collagen-based scaffold. This 3D model revealed similarities in muscle and cardiac progenitor development, offering a

hybrid system for cardiovascular disease research (Tchao et al., 2013). In 2018, Rao et al. developed a 3D model of hiPSC-derived skeletal muscle in a fibrin-based matrix, which responded to electrical and acetylcholine stimulation, indicating successful differentiation (Rao et al., 2018).

The use of iPSCs greatly expands the possibilities for personalized medicine and disease modeling. However, their application must be supported by advanced *in vitro* tissue engineering techniques to achieve sufficient myofiber maturation for effective use in research and therapy (Caron et al., 2023; Zhao et al., 2023).

1.3 Tissue engineering

Tissue engineering (TE) is described by Robert Langer, one of the founding scientists of the field, as "an interdisciplinary field that applies the principles of engineering and life sciences toward the development of biological substitutes that restore, maintain, or improve tissue function or a whole organ" (Uquillas et al., 2023). This approach encompasses the transplantation of material and highly ordered cell structures, commonly referred to as tissues or organs, to replace damaged biological material and/or promote endogenous regeneration. The organized structure of these engineered tissues contributes to a functionalization that would be unattainable using traditional cell biology (**Fig 5**). The scope of TE applications can be extended to incorporate physiological features, mimicking the architecture found *in vivo*, to improve the relevance of *in vitro* cellular models for disease modeling and drug screening.

In this context, TE aims to generate a completely biomimetic tissue substitute enabled to structurally and functionally integrates with an host tissue (Rangarajan et al., 2014). To this end, the engineered tissue must primarily consider the intended function it aims to replace or mimic, and be specifically designed and functionally characterized as such (Furth & Atala, 2014, p. 6; Olson et al., 2011). With this in mind, skeletal muscle tissue engineering (SMTE) not only offers a promising alternative to the current surgical treatment of VML (Volpi et al., 2022) but also a way to enhance *in vitro* muscle tissue maturation and complexity, to improve the relevance of skeletal muscle myopathy models.

SMTE can be divided into three categories:

- ***In situ* approaches** aim to implant an acellular tissue-engineered scaffold to mimic the native muscle microenvironment. These scaffolds act as templates, promoting host cell activation, proliferation, and differentiation through biophysical and biochemical cues (Motohashi et al., 2019).
- ***In vivo* SMTE** involves combining the previously described scaffolds with the addition of living cells and biological factors. After transplantation, the now enriched ECM directly participates in the regeneration process of the skeletal muscle (Kiran et al., 2021).
- ***In vitro* tissue engineering** focuses on producing *in vitro* skeletal muscle tissues capable of supporting, repairing, or replacing normal function in damaged or completely lost muscles. It involves the use of biomaterial substrate, appropriate cells, growth factors, and scaffolds designed to mimic the host's tissue ECM. The appropriate combination of these elements helps to prevent scar tissue formation while enhancing myoblast survival, migration rate and overall myogenic regeneration. *In vitro* SMTE is an appealing alternative to FFMT for achieving fully functional tissue regeneration after traumatic VML. However, combining all the described parameters remains a field that needs to be explored, and numerous challenges must be accounted for. Indeed, the size of *in vitro* cultured tissue is often limited due to the need of efficient vascularization, and the replacement construct typically produces lower contractile force than the muscle it is supposed to replace (Carnes & Pins, 2020). In contrast, *in vitro* SMTE has extensive applications in pre-clinical drug screening and the study of tissue physiology and pathology. The goal here is to provide favorable culture environments, mimicking the one found *in vivo*, to improve survival, growth, differentiation, alignment, and functional maturation of engineered striated muscles. Finally, more advanced applications can be found in the form of hybrid mechanical actuators and engineered meat as potential alternative food sources (Ostrovidov et al., 2014).

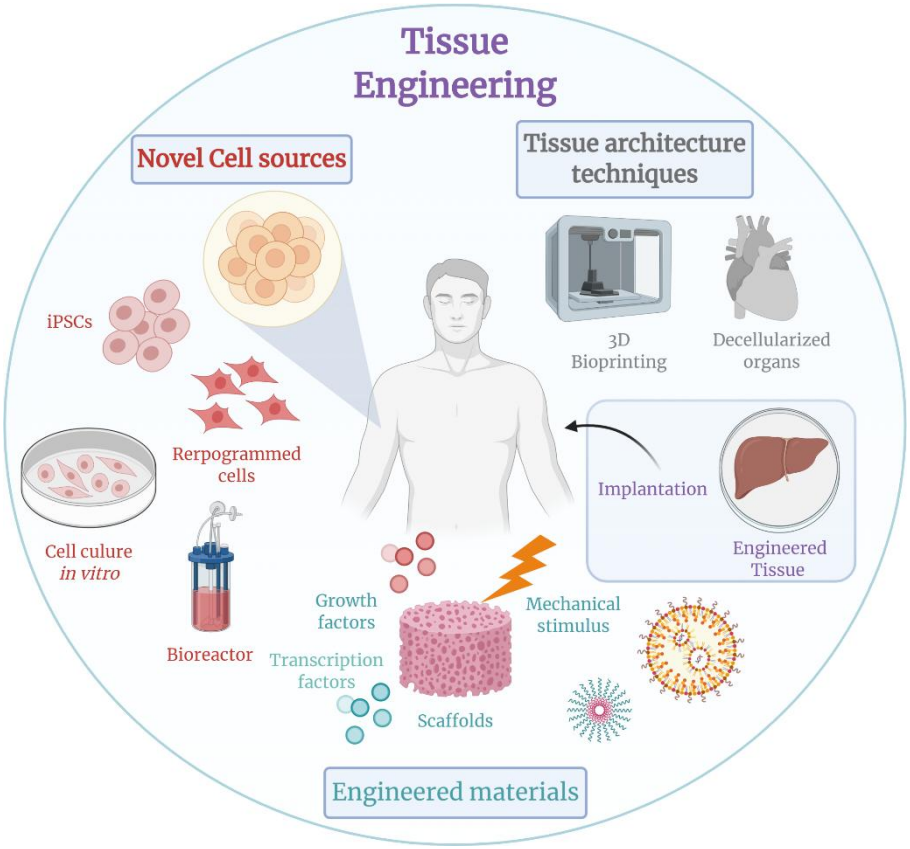

Figure 5: Tissue engineering strategies (faCellitate)

1.3.1 *In situ* and *in vivo* strategies for SMTE

1.3.1.1 Biomaterials

Tissue engineering strategies using rationally designed biomaterials offer promising alternatives to previously described traditional VLM therapies. These biomaterials can provide chemical and physical cues to the host's muscle cells to enhance their survival, promote functional maturation, protect them from foreign body responses, and recruit host vasculature and nerves into the defect site (Kwee & Mooney, 2017). The implanted scaffold should mimic the skeletal muscle characteristic alignment to facilitate the growth of muscle fibers. It must also allow for cell infiltration and nutrient transfer while being mechanically stable to maintain its integrity within a contracting tissue (Kozan et al., 2023).

Among these biomaterials, hydrogels stand out as a class of polymeric materials characterized by their hydrophilic structure, which allows the storage of a large amount of water within a three-dimensional network. Hydrogels possess unique biomimetic properties, including high permeability, biocompatibility, and tunable mechanical

properties. Moreover, they can be easily functionalized to recapitulate the intrinsic features of a specific biological tissue, making them the preferential choice for SMTE and scaffold engineering (Volpi et al., 2022). Hydrogels can be classified into two categories: synthetic and natural. Synthetic scaffolds are easy to fabricate with precise and detailed geometries, they are consistent, and cost-effective. However, they present low cell attachment, limited biocompatibility, and entail pro-inflammatory immune response upon implantation.

Natural polymers, on the other hand, are highly biocompatible, exhibit low inflammatory response, and contain native signaling cues that promote cellular attachment, proliferation, and differentiation. While natural scaffolds' porosity, topography, and mechanical properties can be tuned, they suffer from inherent biological variability affecting the precision and accuracy of the construct (Eugenis et al., 2021).

ECM-derived hydrogels are a subcategory of naturally sourced hydrogels. They are inherently enriched with various bioactive motifs, promoting cell adhesion and growth, enabling the recreation of a cell-supportive physiological-like microenvironment suitable for SMTE. In this context, collagen, the main component of the ECM, and gelatin in its denatured form have been widely used in SMTE.

Collagen type I is a fibrous protein comprising 25 to 35% of the ECM. It can be extracted from various tissues using enzymatic and acid/base processes. Collagen has low antigenicity, high mechanical strength, good biodegradability, and biocompatibility. It also promotes cell growth due to several cell-binding motifs throughout its triple helical structure. It can be used in crude form or processed into porous sponges, gels, or sheets making it versatile for tissue engineering purposes (Jin et al., 2023).

Gelatin, derived from collagen through hydrolysis, retains collagen's cell-binding properties and allows for enhanced cell adhesion and proliferation with reduced immunogenicity. Both collagen and gelatin can be covalently cross-linked for improved mechanical stability using agents such as transglutaminase or genipin. However, collagen type I and its derivatives are directly associated with fibrosis, during which collagen levels are elevated. Consequently, collagen 1 is not easily remodeled, does not stimulate endogenous ECM secretion, and may not provide the optimal stiffness for muscle differentiation (Khodabukus et al., 2018).

Fibrin, another natural scaffold, is the main structural component of blood clots, forming an insoluble matrix following tissue injury. It serves as a scaffold for tissue repair and provides important cues for directing cell phenotype during the inflammatory

response (Brown & Barker, 2014). Fibrin properties include controllable and non-toxic degradation, excellent biocompatibility, and minimal inflammation, as it can be obtained from the patient's own blood (Sanz-Horta et al., 2023). Unlike collagen, fibrin is a preferred matrix for tissue engineering of skeletal muscle due to its ability to be extensively remodeled, degraded, and replaced by endogenously derived ECM. Additionally, its fibrils have a stiffness comparable to that of native muscle and several orders of magnitude lower than the ones of collagen. Fibrin also promotes angiogenesis and neurite extension, which is critical for the formation of a fully functional engineered muscle for *in vivo* applications. The main challenges with fibrin are variability between batches and an inconsistent degradation rate, which can be addressed by lots testing and control of fibrinolysis using cross-linkers or antifibrinolytic compounds such as aminocaproic acid and aprotinin (Khodabukus et al., 2018).

To further increase the biomimetic potential, hydrogels can also be obtained by decellularizing skeletal muscle ECM. Decellularized ECM (dECM) retains the alignment, structure, and geometry of the original tissue, preserving the native microenvironment and providing excellent myogenic cues for muscle regeneration.

Naturally derived polysaccharide hydrogels are also frequently used in SMTE. **Alginate**, obtained from various species of brown seaweeds, is biocompatible, has low toxicity, and has been shown to restrain the maturation of dendritic cells, which can diminish the inflammatory immune response to the material (Ahmad Raus et al., 2021; Farshidfar et al., 2023). However, unmodified alginate is non-degradable and can cause a foreign body response. It also lacks cell binding motifs, which can potentially limit its biocompatibility and ability to direct cell functions.

Other naturally derived materials commonly used in SMTE include agarose, chitosan, hyaluronic acid, and silk (Boso et al., 2020; Chandra & Lee, 2015).

1.3.1.2 Cell-loaded scaffolds

The implantation of acellular scaffolds into injured sites has been shown to enhance endogenous skeletal muscle regeneration by recruiting host cell populations. However, the use of this approach for large scale injuries raises significant concerns, as limited SC infiltration restricts the regeneration potential at the defect site. To address this, cell-loaded scaffolds have been extensively explored as a treatment for large-scale VML injuries. This strategy is based on the use of the previously mentioned biomaterials

as vectors to deliver carefully selected cells with the scaffold matrix improving cell retention, survival and reducing immune response.

Hydrogels are the most commonly used scaffolds for such procedure due to their ease of use and ability to be polymerized after injection at the injured site. Numerous studies have demonstrated the efficacy of this method, reporting on reduced fibrosis, improved muscle function and strength, and increased vascularization of the defect area. However, the poor mechanical properties of hydrogels and their lack of aligned topographical cues have hindered effective functional muscle regeneration.

dECM provides a promising alternative to the limitations of hydrogels. Studies report that the combination of dECM matrices with myoblasts leads to significant angiogenesis, compared to acellular scaffolds that tend to result in fibrosis. dECM efficiently merge appropriate mechanical strength and improved cell retention after implantation. However, the success of this approach is highly dependent on the source of the ECM, the decellularization protocol used, and the site of implantation.

Unlike the previously described methods, microfiber-based matrices provide additional topographical cues to promote the preferential alignment of myoblasts. The organization provided by these scaffolds mimics the anisotropic architecture of the muscle fibers to promote functional skeletal muscle regeneration. For instance, aligned fibrin microthread scaffolds seeded with muscle-derived precursor cells have been shown to reduce fibrosis and improve muscle force generation, making them a promising option for treating VML.

Using genetically modified myoblasts that upregulated myogenic or angiogenic gene expression is an effective way to further enhance the capacity of cell-loaded scaffolds. As previously discussed, the delivery of transfected cells is particularly challenging and often affect their efficiency. Integration of these genetically modified cells directly into the scaffolding helps overcome this issue, leading to significantly improved angiogenesis and muscle density compared to non-genetically modified cells. Although transfection efficiency and gene expression are still under investigation, optimizing biomaterials could enhance these outcomes. Additionally, using iPSCs as a cell source offers a potential solution to the immunogenicity issues associated with genetically modified cells as well as enabling personalized VLM treatment.

1.3.2 *In vitro* strategies for SMTE

While *in vivo* SMTE shows promising results for functional regeneration of skeletal muscle defects, it still faces challenges such as low viability, poor retention, and immune rejection. In contrast, *in vitro* SMTE focuses on growing and differentiating cells into myotubes before implantation, using a combination of scaffolds, biological factors, and cells. These systems often include a coculture of cell types or multipotent cells to promote blood vessel and NMJ formation, which are crucial for proper maturation of the model. Engineered muscle graft are typically conditioned in bioreactors, enhancing their functionality prior to implantation; an advantage over *in situ* and *in vivo* tissue strategies (Ostrovidov et al., 2014) . As a result, *in vitro*-engineered skeletal muscle constructs are expected to integrate into the host defect site more efficiently and promote faster muscle healing and improved contractile function compared to previously described approaches (Smoak & Mikos, 2020).

In addition to regenerative medicine, these 3D constructs are highly suitable for drug screening and disease modeling. Indeed, skeletal muscle biology studies using human subjects raise issues of tissue availability and ethical considerations, while animal models and conventional 2D cultures, though widely used, have significant limitations. Traditional 2D cultures often result in immature myotubes with limited physiological relevance, largely due to the nature of the culture substrate. In this context, *in vitro* STME offers a biomimetic 3D muscle environment supports the formation of more mature myotubes, enables longer culture times, increases protein content, and improves maturation of myosin heavy chain (MHC). Additionally, measuring contractile forces in 3D models is far more reflective of *in vivo* muscle physiology and pathology than in 2D cultures (Khodabukus et al., 2018).

For its application in VML, it is essential to note that the contractile forces generated *in vitro* are still significantly lower than those observed in native muscle tissue. Moreover, these constructs face challenges such as limited oxygen and nutrient diffusion within the bulk of the model. The prolonged *in vitro* culture times necessary for producing functional muscle tissue also makes clinical scalability, cost-effectiveness, off-the-shelf availability, and regulatory approval more difficult to achieve compared to *in situ* or *in vivo* approaches.

To develop highly functional, contractile muscle tissue *in vitro*, it is essential to replicate the structure of skeletal muscle. Generating aligned muscle fibers requires culturing myoblasts in a way that promotes alignment, which subsequently leads to the

formation of aligned myotubes. Various *in vitro* culture techniques in 2D and 3D have been well-characterized to achieve this organization, improve the differentiation of myoblasts and promote myogenic maturation .

1.3.2.1 Cell alignment by topography

1.3.2.1.1 Principle

Cell orientation and locomotion are directed by the geometric features and topographical cues of the underlying substrate, a phenomenon known as contact guidance. In tissue engineering, replicating native tissue accurately in terms of chemical, physical, and biological properties is essential for preventing immunological rejection and restoring tissue function. Numerous studies have demonstrated that the ECM contains a variety of micro- and nanoscale topographies that regulate cell behaviors, underscoring the importance of contact guidance in tissue development and repair. While some of these topographic features are randomly oriented and constitute isotropic cellular cues, others consist of aligned and anisotropic architectures formed by highly organized extracellular matrix components that serve as directional guides for cells.

Topographical cues at the micro- and nanoscale on in-vitro culture substrates are particularly effective for mimicking the *in vivo* cellular environment, directing cell behavior, and ultimately forming tissues that are structurally and functionally analogous to their native counterparts. Some of these topographies, notably grooves and aligned fibers, aim specifically to reproduce anisotropic and aligned environments. In SMTE aligning myoblasts to simulate the native muscle fiber structure is critical for achieving the necessary physical function of regenerated muscle tissue. Micro- and nanotopographical features of scaffolds, such as nanofibers and microgrooves, can guide the orientation of skeletal muscle cells and facilitate the formation of myotubes, aiding in tissue repair (Gao et al., 2021).

Topography also plays a key role in regulating cell function across various tissue types. Cells cultured on topographically patterned substrates exhibit altered morphologies, alignments, and behaviors in response to micro- and nanoscale features. For example, osteoblasts on rough surfaces demonstrate higher bone marker production compared to those on smooth substrates (Refaaq et al., 2020; Rougerie et al., 2021). ECM-generated topographical cues significantly impact cellular behaviors such as adhesion,

proliferation, alignment, migration, and differentiation, as well as cytoskeletal organization and function (Charest et al., 2007).

In the stem cell niche, the surrounding ECM imposes constraints on cell shape, influencing cellular signaling and fate determination. Induced physical cues can thus also be exploited to direct stem cell differentiation into specific lineages by modifying the cell shape, adhesive area, and aspect ratio. Such alterations affect cytoskeletal tension, which regulates gene and protein expression (Chandra & Lee, 2015). This underscores the significance of physical control of cell shape as a potent regulator of stem cell behavior and tissue development.

1.3.2.1.2 Involved mechanisms

The mechanisms involved in this topographical cell alignment are numerous and still under discussion. The focal adhesion (FA)-based model (Ohara & Buck, 1979; Ray et al., 2017) has gained widespread acceptance as a key explanation for cell elongation and alignment in response to anisotropic topographies. According to this model, topographical cues, such as parallel ridges or aligned fibers, direct cellular protrusions and FA elongation along the axis of the topography, while restricting their growth in the orthogonal direction. This lateral constraint of FAs leads to the alignment of actin stress fibers (SFs) and the generation of anisotropic intracellular stresses, causing the cell to become oriented and elongated along the topographical direction. Numerous experimental studies support this model, underlining the central role of FAs in cell alignment on anisotropic surfaces. On the other hand, the fact that certain cell types, such as amoeboid and neuronal cells, exhibit contact guidance without strong FA-based interactions suggests that alternative or complementary mechanisms centered on integrin-based adhesion may also drive cell responses to topography. In this regard, nanoscale patterning (1–100 nm) can influence these cell-substrate interactions by regulating the substrate integrin binding sites.

Another alternative mechanism is membrane deformation, which is particularly relevant for high aspect ratio topographies like nanopillars or deep grooves. Here, the cell membrane engulfs vertical nanostructures, triggering a response by recruiting curvature-sensitive proteins and activating signaling pathways. This membrane deformation mechanism highlights topography-induced curvature as a potential complementary pathway to FA-based guidance (Dipalo et al., 2018).

Once again, in larger-scale topographies, the FA-based model alone does not fully explain cell alignment and elongation. In the case of highly spaced grooves (around 160μm), the observed cell alignment is thought to be driven by entropic factors and spatial constraints imposed on cell morphology at the edges of the stripes. This "mesoscale" guidance is further supported by observations that when cells are exposed to topographical cues of varying scales, their response is determined by the integration of these cues, even when some of the cues are not directly involved in FA confinement (Buskermolen et al., 2019; Leclech & Barakat, 2021).

1.3.2.1.3 Materials and manufacturing

Designing substrates with defined topographies is crucial for creating microenvironments that mimic the native ECM. Similarity in physical, chemical, and biological properties is essential for optimizing cell behavior and tissue formation. Among these properties, the rigidity and elasticity of the substrate and topographical features play a key role in the mechanotransduction of cell response. In this regard, natural polymers, such as polyacrylamide and gelatin gels, have been investigated for their highly tunable biochemical and mechanical properties added to superior biocompatibility. However, their mechanical properties remain too soft to accurately replicate micro- or nanoscale structures. Similarly, collagen, gelatin, alginate, and agarose offer high biocompatibility and elastic moduli comparable to soft tissues, yet they also lack the stiffness required to maintain high-fidelity topographies. This highlights the need to balance material biocompatibility with structuring capability when designing biomaterials for scaffold production.

To address these limitations, a range of synthetic polymers and advanced patterning techniques have been developed. UV-curable synthetic polymers like polyurethane acrylate (PUA), polyethylene glycol (PEG) acrylate, and Norland Optical Adhesive (NOA) are commonly used in soft lithography, while thermoplastic polymers like polymethyl methacrylate (PMMA) and polystyrene (PS) are utilized in methods ranging from electrospinning to nanoimprint lithography (NIL). Each material offers distinct advantages and limitations depending on the desired patterning technique, physiological relevance, and material properties.

Patterning methods for constructing micro- and nanostructures in synthetic polymers can be broadly classified into template-free (bottom-up) methods, such as

electrospinning (Ferraris et al., 2020) and self-assembly (Cox et al., 1999), and template-assisted (top-down) methods, including photolithography, electrochemical deposition, soft lithography, and NIL.

Photolithography is the most widespread technique involving the use of patterned light to create three-dimensional surface structures in a polymer film. In this process, light is transmitted through a photomask, selectively exposing certain regions of a polymer coating. The exposed regions either dissolve or remain intact based on the polymer chemistry, allowing for precise transfer of the topographical pattern onto the underlying substrate. One of the primary advantages of lithographic techniques is their ability to generate arbitrary shapes with well-controlled processes. Once the master mold is created, the pattern can be reproduced efficiently and economically.

In contrast to traditional lithographic methods, which require multiple steps and specialized masks, femtosecond laser ablation offers a more direct and simplified approach to pattern fabrication. This technique can generate diverse patterns on various materials with high precision and reproducibility (Fadeeva et al., 2014; Park et al., 2019). Numerous studies using this method on bio and synthetic polymers report enhanced differentiation and alignment of cultured cells (Babaliari et al., 2018; Buchberger et al., 2023; Dinca et al., 2016; Eaton et al., 2012).

1.3.2.1.4 Laser-induced topography

Laser ablation is a precise top-down material removal process that uses a high-energy laser beam to vaporize or melt a targeted substrate. This process is widely used in industries such as metal, ceramic, and polymer fabrication due to its high precision and non-contact nature (Ravi-Kumar et al., 2019). At its core, laser ablation relies on the interaction between the laser photons and the electrons in the substrate. When the laser excites the electrons, energy is transferred, resulting in localized heating. Once the material's temperature reaches its vaporization or melting point, a portion of it is removed from the surface. The material's phase change (from solid to gas) results in the formation of a plasma plume, which is a mixture of vaporized material and ionized gases (Bulgakova & Bulgakov, 2001; von der Linde & Sokolowski-Tinten, 2000).

Laser ablation for precision applications requires materials that can be processed with minimal impact. While theoretically all materials can be ablated by a laser, they differ in terms of the minimum fluence (energy density) required for material removal—known

as the ablation threshold. Materials with low ablation thresholds are preferred for "gentle" processing, as less energy is transferred to the system, reducing thermal and irradiation effects.

The ablation process begins with the absorption of photons, leading to the formation of a melt pool at the laser interaction zone. The prolonged arrival of laser pulses leads to a temperature increase until the melt pool begins to vaporize. At this stage, the molten material is subjected to high pressure, which pushes it out of the melt pool, often resulting in the redeposition of some material near the interaction zone. In cases where the pulse duration is longer, the material can experience an explosive liquid-vapor transition, potentially resulting in geometric changes in the ablated feature.

Depending on parameters such as laser fluence, reflectivity of the targeted material, wavelength and pulse duration, different mechanisms can intervene in the material ablation process. In photochemical ablation models, UV photons directly break covalent bonds in the polymer. This volumetric approach assumes that ablation occurs after full absorption of the laser pulse, though ablation typically starts as soon as laser-matter interaction begins. Photomechanical models account for the mechanical stresses caused by the formation of small species in the material and the passage of acoustic waves. They are particularly relevant for short pulses (picoseconds or less). Finally, photothermal ablation involves the electronic excitation of the targeted material by the laser pulses, leading to the breaking of bonds. Pulsed lasers are typically preferred for these applications over continuous beams, as excess energy in continuous beams that fails to reach the ablation threshold tends to create a larger heat-affected zone, subsequently causing unwanted material degradation.

Where longer pulses result in linear absorption following Beer Lambert's law, with the use of ultrashort pulses (in the picosecond to femtosecond range) the absorption becomes nonlinear and intensity dependent. The bound electrons of the material can be directly ionized by large absorption coefficient and due to high intensities. The behavior of the laser pulses also varies with their duration. While longer pulses lead to linear absorption following Beer-Lambert's law, ultrashort pulses (in the picosecond or femtosecond range) induce nonlinear, intensity-dependent absorption. These ultrashort pulses are especially effective for high-precision and high-throughput material removal (Žemaitis et al., 2020) because the electrons in the material can be directly ionized by the high-intensity laser, but the heat generated doesn't have enough time to transfer to the surrounding lattice. This limits thermal damage, as the timescale

for electron cooling and energy transfer to the lattice is approximately 1 picosecond (Chichkov et al., 1996). However, extremely high laser intensities can still produce plasma plumes that heat the surrounding material.

The efficiency of laser ablation is highly dependent on the properties of the targeted material, particularly its absorption coefficient, which varies with the wavelength of the laser. Polymers, for example, are highly sensitive to ultraviolet wavelengths and exhibit increased absorption. The molecular weight of the material also plays a role, as illustrated by polymers with higher molecular weights that tend to have higher ablation thresholds, resulting in lower ablation rates (Nayak et al., 2008). Nevertheless, the low thermal conductivity of polymers, which greatly limits heat transfer to surrounding areas makes them an ideal substrate for precise laser machining and structuring of various complex design.

1.3.2.2 Mechanical and electrical stimulation

Mechanical and electrical stimulation have been shown to significantly influence the structure and function of skeletal muscle cells both *in vivo* and *in vitro*. Mechanical stimulation of cultured skeletal muscle cells can induce changes that mirror those observed in mechanically loaded muscle *in vivo*. These changes occur through mechanotransduction pathways, which can improve tissue maturation. This effect is particularly evident with physical exercise, which enhances the volume, mass, and force-generating capacity of *in vivo* skeletal muscle (Y. Zhang & Habibovic, 2022). Mechanical forces are essential for muscle growth, differentiation, and function, making controlled mechanical stimulation a strong addition for successful and enhanced *in vitro* myogenesis.

When applied to skeletal muscle monolayer, mechanical stimulation has been shown to influence various cellular processes, including gene regulation, protein expression, accumulation, localization (Banks et al., 2015; Cè et al., 2008; Grossi et al., 2007; Rangarajan et al., 2014), and metabolic activity (Powell et al., 2002). It also impacts cellular proliferation, myofiber organization, and extracellular matrix (ECM) composition. Furthermore, mechanical stimulation can induce a switch between muscle fiber phenotypes from anaerobic (type II), used for short, high-intensity physical demands, toward slow oxidative (type I) fibers. This ability could help to more closely match the native muscle phenotype of the targeted injury sites, improving the potential for functional tissue regeneration.

Several mechanical stimulation protocols can be used to this aim, including static stretch (a single stretch applied at the beginning of culture), ramp stretch (incremental increases in stretch amplitude), and cyclic stretch (a periodic sequence of stretch pulses with defined parameters). Uniaxial stimulation, the simplest and most widely used technique, is particularly effective in replicating the anisotropic striated muscle tissue architecture (Rangarajan et al., 2014).

On the other hand, electrical stimulation (ES), which aims to mimic the action of motoneurons, triggers the cells to deliver signals through intrinsic pathways, directly enhancing muscle cell survival, proliferation, and hypertrophy.
ES can be classified into three main types: direct coupling, capacitive coupling, and inductive coupling, each offering different methods for delivering stimulation to cells in culture.

- The most commonly used method is **direct coupling** (**Fig 6.A**), where electrodes are inserted directly into the culture medium and attached to the scaffold. This approach is widely favored for its simplicity and ease of operation, allowing efficient delivery of ES to the cells.

- In contrast, **capacitive coupling** (**Fig 6.B**) provides a more biologically safe alternative to direct coupling. In this method, two electrodes are placed at opposite ends of the culture setup, creating a uniform electric field across the scaffold, where the cells are seeded. This non-invasive technique does not require the scaffold to be conductive, making it safer and more effective for delivering uniform ES to the cells without direct contact.

- The third method, **inductive coupling** (**Fig 6.C**), utilizes a controllable electromagnetic field generated by a conductive coil placed around the cell culture system. This technique, also known as pulsed electromagnetic field stimulation (PEMF), transmits the stimulus through electromagnetic pulses, mimicking the natural potential transfer that occurs within the human body. This non-invasive approach offers another alternative for delivering ES in a way that resembles physiological electrical signaling.

Each method provides unique advantages and applications depending on the desired outcomes for cell culture and tissue engineering. The benefits brought by these

external stimulations are particularly valuable for long-term cell viability and *in vitro* differentiation while preparing engineered muscle tissues for functional integration after implantation (C. Chen et al., 2019).

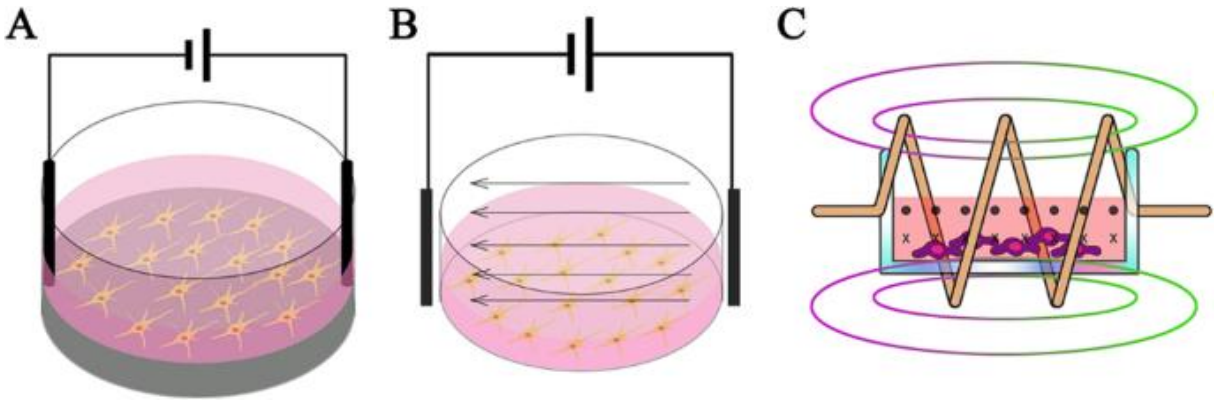

Figure 6: Methods for electrical stimulation of cells: (A) direct coupling, (B) capacitive coupling, (C) inductive coupling (C. Chen et al., 2019).

1.3.2.3 Bioprinting

Where engineered 2D culture offered improved cell behavior compared to traditional methods, the future of cell biology seems to lean toward 3D scaffolds and 3D cell models, proposing even more complex models of cellular organization. As a matter of fact, culturing cells in 3D environments offers a more physiologically relevant setting to guide cell behaviors and enhance their functions. These approaches were recently revolutionized by the advent of 3D bio-fabrication, which allows for the generation of complex, functional 3D architectures that can replicate native microenvironments (Cao et al., 2021; Kačarević et al., 2018).

In this context, bio-printing encompasses a wide range of printing methods that utilize viable cells, biomaterials, and biological molecules to create defined structures. It eliminates the issues of cell homogeneity associated with post-fabrication cell seeding by including cell arrangement during the fabrication of the scaffold. This technology is particularly valuable for developing alternatives to autologous and allogeneic tissue implants and for replacing animal testing in disease research and treatment development. Traditional methods for fabricating 3D scaffolds, such as photomask-guided polymerization of photosensitive biomaterials, are both costly and time-consuming. In contrast, 3D printing is based on the direct assembly of bio-polymers and requires no physical molds or masks. This approach enables the creation of intricate 3D structures at

micro- and nanoscale levels with greater flexibility, efficiency, and reduced cost. Various bioprinting techniques, including inkjet bioprinting, extrusion bioprinting, and light-assisted bioprinting, offer various advantages for tissue engineering (Aljohani et al., 2018; Guillotin & Guillemot, 2011).

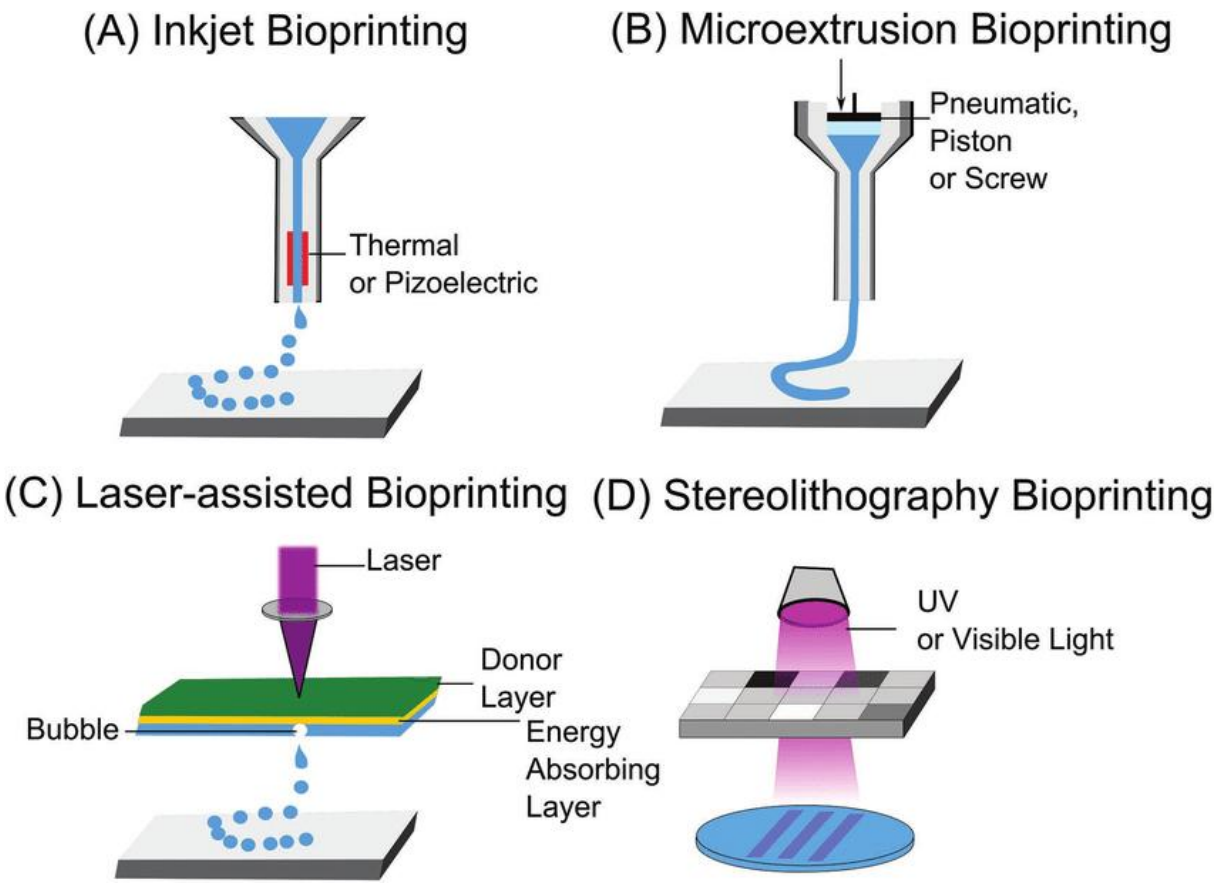

Figure 7: Common bioprinting methods (A) Inkjet bioprinting, (B Micro extrusion bioprinting, (C) Laser-assisted bioprinting (D) Stereolithography bioprinting (Foyt et al., 2018)

1.3.2.3.1 Inkjet

Inkjet bioprinting (**Figure 7.A**) builds on conventional 2D inkjet printing technology but is adapted to dispense biological material such as protein or cell solutions instead of traditional ink. By using thermal or acoustic methods, inkjet printers control the volume and placement of bioinks. Thermal methods generate heat at the print head, forcing bioink out through pressure pulses, while acoustic techniques use piezoelectric crystals to create pressure for droplet deposition. Inkjet printing offers fast, inexpensive, and high-resolution bioprinting with control over droplet size and cell density, enabling the creation of tissue gradients. However, challenges include low droplet directionality, nozzle clogging, and potential thermal or mechanical stress on cells due to the ejection

method. While most studies indicate that these risks are minimal, the fact remains that only low-viscosity liquids and low cell density can be printed to prevent clogging and reduce shear stress (Tao Xu et al., 2005; Thomas Boland et al., 2006).

1.3.2.3.2 Extrusion

Extrusion bioprinting (**Fig 7.B**) involves extruding bioink through a microextrusion head, which moves along the x, y, and z axes to create 3D structures. This technique can handle materials with a wide range of viscosities by using mechanical or pneumatic extrusion methods. Its main advantage is the ability to print bioinks with high cell density, although the use of force during extrusion can reduce cell viability to as low as 40% due to shear stress and small nozzle diameters. The resolution of this printing method is also limited by nozzle size, typically over 50 to 100 µm.

Extrusion-based bioprinting has been used to create complex tissue structures, including liver (Ali et al., 2024), cartilage (Flégeau et al., 2022), and neural tissue constructs (Yao et al., 2022). We can also note its application in complex tissue modeling, such as in bionic ear models that use cell-seeded hydrogels with conductive polymers (Y. Chen et al., 2020; Fornetti et al., 2023; Gillispie et al., 2020; Malekpour & Chen, 2022).

1.3.2.3.3 Laser-based bioprinting

Laser-based bioprinting, especially stereolithography (SLA) (**Fig 7.D**), provides alternatives to nozzle-based methods by using light to cure photosensitive polymers in a layer-by-layer process. This method of operation eliminates the negative effects of shear stress and high pressure inflicted on cells while allowing the printing of highly resolute constructs (Grigoryan et al., 2021; Kumar & Kim, 2020). In SLA, a photosensitive biomaterial is exposed to ultraviolet (UV) or visible light, polymerizing it layer by layer as the platform lowers to allow subsequent layers to form. The polymerization is initiated by photoinitiators: chemical molecules that, when exposed to UV or visible light, create a reagent that interacts with monomers to form polymer chains. The mechanical properties of the final structure, such as stiffness, depend on the concentration of the photoinitiator, although high concentrations may exhibit cytotoxic effects and constitute one of the limitations of this method (Li et al., 2023). Beam shaping of UV laser with the creation of Bessel beams has shown potential in resolute SLA printing. Studies show the fabrication

of tubular constructs and porous scaffolds in shorter fabrication times thanks to the optical work, though they remain limited in structural complexity (Liew & Zhang, 2018).

1.4 Laser-induced forward transfer

The Laser-Induced Forward Transfer (LIFT) is a versatile, non-contact, direct-write technique that enables the precise deposition of small material volumes into high-resolution patterns without requiring vacuum set-ups, masks, or molds (**Fig 7.C**). Unlike traditional nozzle-based techniques like inkjet printing, LIFT circumvents issues such as nozzle clogging and material compatibility, making it suitable for a broader range of materials, including solids, liquids, pastes, and complex fluid mixtures with varying viscosities (Morales et al., 2018).

The principles behind LIFT were first described in a 1968 patent, but it was only twenty years later, in 1986, that the term "laser-induced forward transfer" was coined when the technique was introduced for maskless metal deposition in a vacuum (Bohandy et al., 1986). The latter was rapidly discarded, and LIFT was used for the deposition under atmospheric pressure of metals, oxides, and high-temperature superconductors, with solid donor materials being partially evaporated or melted during the transfer process (Bohandy et al., 1988; Serra & Piqué, 2019). The phase change induced during the printing considerably limited the range of transferable material and its application. For this reason, the application of LIFT was extended to liquids, where the targeted material is suspended in a solution to allow its transfer (Piqué et al., 1999). This solution is deposited as a droplet, and the solvent is evaporated or removed post-printing, leaving only the desired material on the substrate. From this point, the range of materials transferable by LIFT was greatly extended.

LIFT's versatility now allows for the transfer of a broad spectrum of materials, including DNA, polymers, metals, graphene, carbon nanotubes, inks, and biomaterials, including living cells (Delaporte & Alloncle, 2016). It is a single-step process that enables localized deposition and surface micropatterning of nearly any material, all without the need for vacuum or cleanroom environments, further enhancing its simplicity and applicability across numerous fields.

1.4.1 LIFT principle of operation

The LIFT process consists of focusing a pulsed laser on a donor that contains the material of interest. The donor is made of a transparent substrate, typically glass, which serves as the carrier for near-infrared and visible lasers. In contrast, ultraviolet lasers require more specialized materials like quartz or fused silica (Fernández-Pradas et al., 2017). Flexible organic substrates can also be used in certain applications. On this transparent substrate, a thin film of the material to be transferred is applied using methods such as blade coating, spin coating, or, for specific fluids, by simply relying on surface tension. The film's thickness, ranging from 0.1 to 100 µm, and its homogeneity are crucial for a successful transfer. As the laser beam passes through the transparent carrier, the photons are absorbed by the back surface of the donor film. When the laser energy exceeds a certain threshold, a fraction of the material is vaporized, inducing a high-pressure vapor bubble that propels the material toward a receiving substrate (Florian & Serra, 2023). The latter can be positioned in close proximity or in contact with the donor film. The distance between the free surface of the donor film and the acceptor surface is referred to as the gap. It is also a key parameter of the LIFT process and can vary from a few dozen micrometers to a few millimeters. In the case of an ink transparent to the laser wavelength, non-linear absorption with femtosecond pulses can be used, or a thin absorbing layer can be placed between the substrate and the film. This intermediate sacrificial layer called the dynamic release layer (DRL), allows for laser energy absorption and facilitates the transfer. The DRL layer is usually made of a thin metallic film (50 - 100 nm) of titanium, gold, or platinum and is chosen appropriately to limit the contamination of the targeted material. The blister-actuated LIFT (BA-LIFT) method is a specific approach where a polymer or polyimide DRL is used. The laser irradiation induces a gas bubble at the interface between the DRL and the substrate, which deforms the DRL and induces fluid motion and jet formation. In this case, the DRL remains intact during the process, eliminating debris from ablation and reducing contamination of the printed droplets (Kattamis et al., 2007; Turkoz et al., 2018). LIFT is primarily designed for pulsed laser systems, typically in the nanosecond range, although ultrafast lasers with picosecond or femtosecond pulses have also been proven effective. Shorter pulses are generally favored for sensible materials as they reduce thermal effects and enable finer resolution. Nevertheless, some studies also employ longer pulses, from microseconds to continuous wave (CW) (C.-F. Huang et al., 2019). While the laser wavelength is less critical to the quality of the transfer, it must remain compatible with the transparency of the

donor substrate and the absorption characteristics of the donor layer. Among the key parameters for LIFT, laser fluence, which is the energy per unit area of the beam spot, defines the quality and the nature of the transfer.

The size, shape, and amount of transferred material depend on the donor material's properties (e.g., thickness, viscosity, optical characteristics), the receptor substrate's properties (e.g., wetting behavior, temperature), and the laser parameters (e.g., fluence, pulse duration, wavelength). Patterns are created by scanning the laser beam or moving the donor and receiving substrates, allowing precise deposition of material at desired locations. The translation of the substrates or modulation of the laser beam enables the formation of complex patterns, with the speed typically governed by the laser repetition rate. High-resolution patterns can be achieved using commercially available computer-controlled translation stages or galvanometric scanning mirrors, which move the laser beam across the donor layer (Piqué, 2014).

Numerous LIFT variants, such as BA-LIFT, have been developed over the years to overcome the limitations of the original process developed by Bohandy (Bohandy et al., 1986) and enhance its capabilities. These include Long Pulsed LIFT (LP-LIFT), Continuous Wave LIFT (CW-LIFT), Laser-Induced Thermal Imaging (LITI), Laser Molecular Implantation (LMI), and many others. Each approach seeks to improve spatial resolution or facilitate the transfer of delicate materials without damaging them, thus preserving their functionality (A. Das et al., 2024; Morales et al., 2018).

By carefully controlling the laser energy, forward propulsion is generated within the irradiated volume of the donor layer. The absorbed photons cause partial ablation of the film, leading to rapid volume expansion and a pressure jump that catapults the material forward. In the case of liquid films, this action creates a liquid jet that forms a printed pixel, often in the shape of a hemispherical droplet (**Figure 8**).

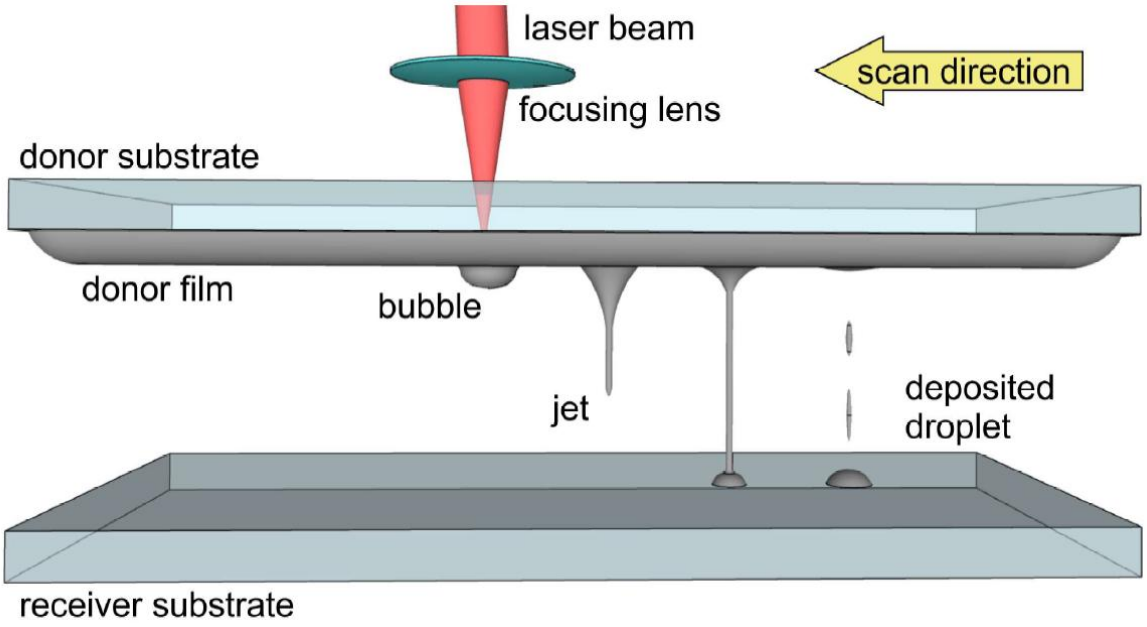

Figure 8: Schematic of a LIFT setup (Sopeña i Martínez, 2020)

1.4.2 LIFT in solids

The first area of application for LIFT was the transfer of solid conductive material applied to electronics. In this case, and as described earlier, the donor film typically consists of a solid layer that absorbs the incoming laser radiation to propel the material. The behavior of the targeted material during transfer depends on its interaction with the laser pulse. In most cases, the deposition of energy will locally melt the solid material, propelling its liquid phase forward. After its deposition it then solidifies on the receptor substrate in the form of droplets. For highly sensitive materials that cannot undergo phase changes or are vulnerable to thermal effects, the addition of a DRL is favored. Besides allowing the transfer of transparent materials, the DRL reduces the risk of photothermal and photochemical damage to sensitive substances (Florian & Serra, 2023).

In this way, the material can also be transferred in the form of a solid pixel that preserves the crystalline structure by preventing phase transitions. This transfer is induced by the mechanical forces generated by laser energy absorption at the interface between the donor substrate and thin film. The rapid increase in temperature and pressure in the confined volume breaks the film around the irradiated area, propelling the solid pixel toward the receiver substrate. Laser energy is partly absorbed to heat the film, while the remaining energy fractures and propels the material. Femtosecond lasers optimize this energy distribution, minimizing heat-affected zones and reducing thermal

degradation risks, making it especially useful for sensitive materials. Additionally, the use of precise beam-shaping that concentrates the energy on the edges of the pixel to print can enable the printing of thicker materials with good resolution (Delaporte & Alloncle, 2016; Papazoglou & Zergioti, 2017).

One drawback of solid-phase LIFT is the generation of shock waves, which can disrupt the material transfer by reflecting off the receiver substrate and interfering with the pixel, potentially destroying it (Fardel et al., 2010).

LIFT's ability to transfer micron-sized metal patterns has made it a valuable tool for electronics, enabling the direct writing of conductive paths for electronic circuits. These circuits can serve as metal cathodes or anodes and are integral to on-chip devices, where LIFT facilitates the simultaneous transfer of semiconductor components, resistors, capacitors, and thin-film transistors (TFTs), along with metal inks for electrical contacts. This versatility makes LIFT a powerful technique in the fabrication of microdevices (Nagel & Lippert, 2012).

1.4.3 LIFT in liquids

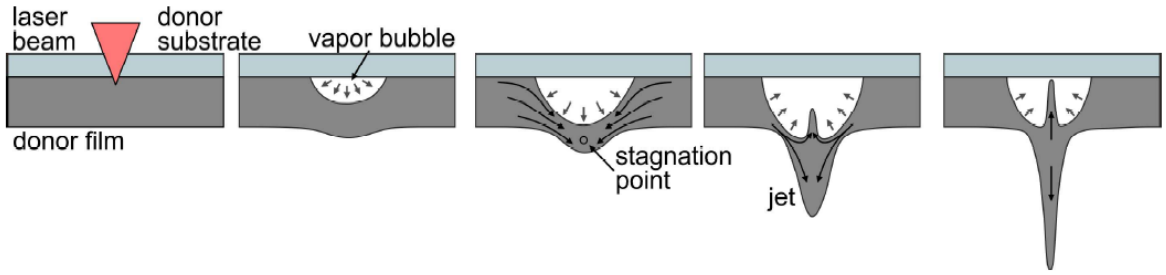

Figure 9: Cavitation bubble formation and evolution of the jet during LIFT printing (Sopeña i Martínez, 2020)

The ejection of material from the donor layer in LIFT is initiated by the absorption of laser radiation at the interface between the donor substrate and the ink layer. This absorption causes a rapid rise in temperature, leading to the formation of a tiny, high-pressure vapor bubble. Due to the presence of the rigid donor substrate, the bubble's expansion is not uniform; instead, the liquid is pushed laterally and toward the free surface of the ink layer. This creates a pressure gradient within the ink, with pressure increasing from the sides of the bubble toward the pole facing the ink's free surface. As the liquid flows toward the pole, pressure builds up at this point. Eventually, the high

pressure is released, generating two jets of material. One jet moves forward, away from the donor layer, leading to ink deposition on the receiving substrate, while the second jet moves backward toward the donor substrate through the collapsing bubble. As the external pressure surpasses the internal pressure, the bubble begins to collapse, but the forward-moving jet continues its trajectory toward the receiving substrate, completing the material transfer (**Fig 9**) (Colina et al., 2006; Fernández-Pradas & Serra, 2020; Patrascioiu et al., 2014).

Several distinct jetting regimes can be observed depending on the laser pulse energy and fluence (**Fig 10**) (Z. Zhang et al., 2015). When the fluence is too low, insufficient pressure is generated around the bubble to initiate jet formation. At fluence levels just below the transfer threshold, jets may still form, but they lack the necessary momentum to reach the receiving substrate, often recoiling as the bubble collapses without transferring any material. Fluence values slightly above the transfer threshold result in an optimal jet with ideal speed, producing a small, precise voxel. As the fluence continues to increase, turbulent and high-speed jets emerge, causing the deposition of droplets accompanied by satellites, which compromise the accuracy of the process. At excessively high fluence, the rapid bubble expansion breaks the film, ejecting material in a burst or plume. This "explosion" of the bio-ink leads to the formation of numerous micro- and nano-droplets, which scatter over the receiving substrate, further reducing precision.

The final deposited droplet is influenced by inertial forces, surface tension, wettability, and viscosity. At low impact velocities, the droplet spreads across the solid surface, while at higher velocities, splashing occurs, resulting in the formation of satellite droplets. The gap distance between the donor and receiving substrates is also crucial in the transfer process.

To achieve smooth, high-resolution deposition, the process parameters must be carefully controlled and optimized. Stable jets, which are critical for high-quality deposition, can be achieved by adjusting laser parameters based on the rheological properties and thickness of the donor layer. These jets travel at high speeds, often reaching hundreds of meters per second, with ink viscosity playing a key role in their stability. Higher viscosity broadens the range of fluences where stable jets can form. Depending on the properties of the film, the liquid jet remains stable over distances of up to one or two millimeters without significantly altering the characteristics of the deposited droplets (Dinca et al., 2012).

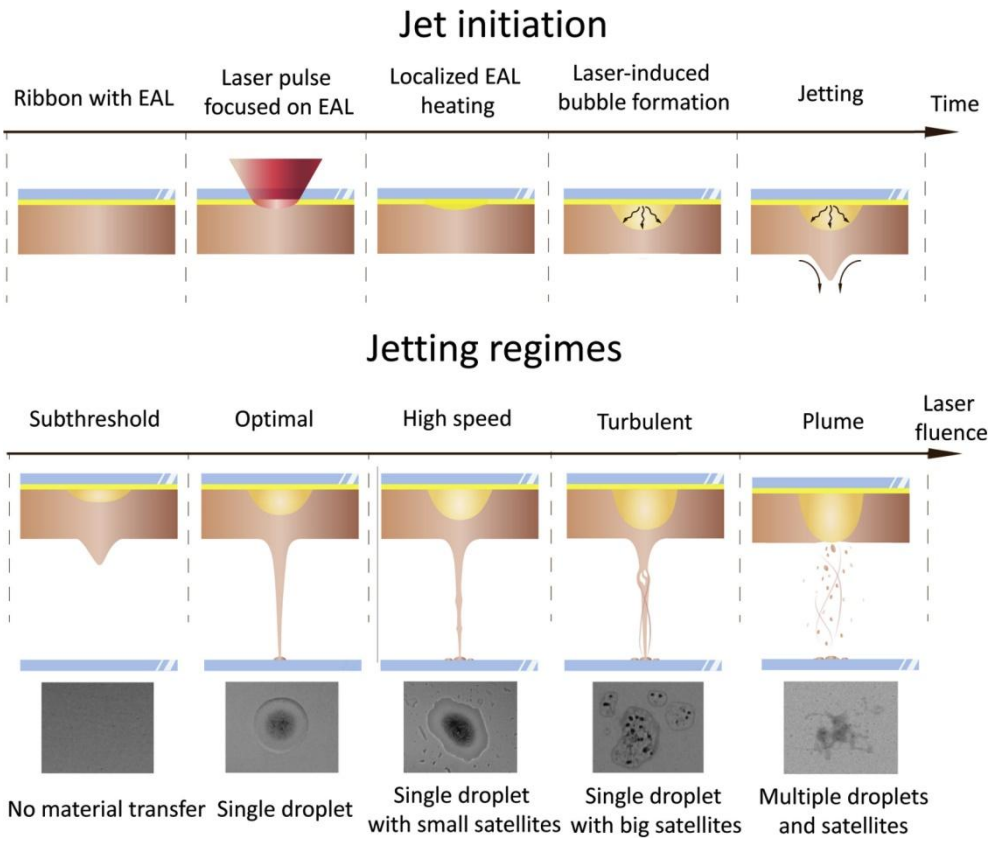

Figure 10: Jetting dynamic depending on time and different observed jetting regimes depending on laser fluence (Antoshin et al., 2019)

1.4.4 LIFT applied to bioprinting

The application of LIFT to biomedical fields is relatively recent but rapidly expanding due to its unique properties and abilities. Unlike other bioprinting methods, LIFT distinguishes itself by the absence of nozzle, eliminating the risk of clogging, and offering both high spatial resolution and remarkable versatility. This flexibility allows LIFT to print virtually any material, which has been demonstrated by successfully transferring biomaterials, including proteins, DNA, and living cells. In addition to providing exceptional spatial resolution, LIFT enables higher survival rates compared to other bioprinting methods and the unique ability to transfer and deposit single cells. Despite its advantages, LIFT is still in its early stages, and its implementation remains challenging due to the lack of commercially available systems, with most studies and applications relying, for now, on custom laboratory setups. Furthermore, applying LIFT to bioprinting requires an interdisciplinary expertise to fully understand the complexity

and implications of transferring living matter, as the primary challenge lies in adapting the bio-ink to the used specific cell types and experimental setup being used.

1.4.4.1 Characterization of LIFT bioprinting

Bio-inks for LIFT bioprinting are typically formulated from standard TE biomaterials and hydrogels. Common materials include cell culture media, gelatin, collagen, alginate, fibrinogen, and more complex solutions like Matrigel, Geltrex, or hyaluronic acid. The desired cells are resuspended at a concentration specific to the application in these biomaterials to create the bio-ink, which will then be printed as previously described. However, the presence of cells slightly alters the viscosity of the source biomaterial, and potential cell aggregates can disrupt the jet formation during printing.

LIFT has successful printed a variety of cell types, including primary cells, immortalized cell lines, ESC, and iPSCs, with excellent survival rates (Bourget et al., 2016; Koch et al., 2018; Pirlo et al., 2012). The impact of laser irradiation on the DNA of printed cells has been evaluated through single-cell-gel electrophoresis (comet assay method), TUNEL assay, and immunostaining, all confirming the absence of damage following the printing process (Koch et al., 2010; Pagès et al., 2015; Xiong et al., 2017). The use of pulsed lasers with nanosecond-range pulse duration, combined with an effective DRL and sufficient bio-ink layer thickness, has demonstrated the absence of thermal transfer from the laser pulse to the bulk of the bio-ink (Mézel et al., 2010). This was further confirmed by Gruene and colleague, who found no increase in heat shock protein expression in printed cells (Gruene, Deiwick, et al., 2011). Although the initiation of apoptosis is still debated, with conflicting studies, no significant changes in cell proliferation rates have been observed when compared to non-printed cells. Additionally, the differentiation potential of printed stem cells was not affected by the process, with successful differentiation into osteogenic, adipogenic, and chondrogenic lineages. iPSCs were also successfully transferred by Koch and colleagues, who demonstrated the maintenance of pluripotency characteristics given an appropriate bio-ink composed of hyaluronic acid (Koch et al., 2018).

1.4.4.2 Application to tissue engineering

LIFT bioprinting shows significant potential in tissue engineering, particularly for the development of autologous skin grafts for patients with extensive skin damage. Traditional skin grafts face challenges, such as insufficient donor sites and immune rejection of allogeneic and xenogeneic grafts. In this context, LIFT bioprinting offers a viable alternative by custom-manufacturing skin substitutes (Chang & Sun, 2023). Studies by Koch et al., (2012) and Michael et al., (2013) demonstrated the feasibility of the idea by creating layered culture of fibroblasts and keratinocytes, which were successfully implanted in mice and showed adhesion to the wound and promotion of angiogenesis within a few days. Guillemot et al., in 2010, also demonstrated their ability to precisely print endothelial cell lines in an alginate bio-ink using a compact laser-based workstation equipped with a galvanometric scanner and allowing for the positioning of five different donor substrate for fast processing and layering of cells. This led to the founding of Poietis in 2014, a company focused on commercializing LIFT bioprinting mainly for skin graft production.

LIFT's precision and spatial resolution have also been applied to create tailored complex vascular substitutes as an alternative to traditional cardiovascular transplants. While some promising results have been reported by Koch et al. in 2021 for the creation of tubular structures of few tens of micrometers, the fabricated vasculature lacked the ranging size gradient of its physiological counterpart and the printed cells rapidly dissolved.

LIFT has been further used to fabricate corneal tissue equivalents (Antoshin et al., 2019). Sorkio et al., (2018) from the group of Koch, printed constructs using ESC-derived limbal epithelial stem cells (hESC-LESCs) and adipose-derived stem cells (hASCs) combined with human laminin and human sourced collagen type 1 as bioink. The tissue was created through the stratifying of the different cell types with the corneal epithelium created from hESC-LESCs and the corneal stroma from hASCs and acellular layers. The resulting tissue exhibited corneal progenitor markers, hASCs mimicked the horizontal layer of the native tissue and synthesized collagen type 1. The resulting tissue resembled native corneal structure and exhibited moderate transparency. When transplanted into a porcine corneal organ culture model, the construct showed cellular migration and

integration into the host tissue, demonstrating the potential for functional corneal replacement.

Additionally, LIFT has been applied for the creation of bone, neural structures and cardiac tissues. Successful examples include the printing of human bone marrow stromal cells (Catros, Fricain, et al., 2011), dorsal root ganglion neurons (Jl et al., 2016), and mesenchymal stem cells for cardiac patches that improved regeneration, angiogenesis and function of a infarcted heart (Gaebel et al., 2011).

1.4.4.3 Single cell isolation

A promising application of LIFT lies in its integration with organ on-chip-technology (OoC). While OoC provides a dynamic and complex *in vitro* platform, the ability to deposit single cells with high precision and selectivity would enable the study of organs and tissues at the cellular level. This approach allows researchers to directly observe how a single transferred cell interacts with a complex tissue environment. Additionally, the deposition of cell types at different stages of differentiation provides greater control over the morphogenesis of intricate structures like organoids (Bosmans et al., 2024). This strategy has already shown promise, as demonstrated by the printing of microarrays of rat pancreatic acinar and ductal cell lines. These cells assembled into spheroids that closely mimicked the structure of pancreatic cancer (Hakobyan et al., 2020). In this context, the combination of precise spatial positioning by LIFT with the use of patient-derived cells offers the potential to replicate the *in vivo* architecture, thus enabling the modeling of complex, personalized biological processes for both therapeutic and disease research purposes.

1.4.4.4 Printing of biomolecules

LIFT's precision and resolution offer an alternative to conventional methods for creating biomolecule arrays for gene expression analysis, genotyping, proteome-wide molecular interactions, and disease diagnostics. LIFT was successfully utilized for the creation of nucleic acid microarrays by depositing cDNA droplets onto substrates coated with L-polylysine. These microarrays were functional, with no reported DNA damage (Colina et al., 2005; Serra et al., 2004). The same approach has been also demonstrated its

efficiency for creating protein microarrays, including peptides, antigens, and enzymes, further highlighting LIFT's versatility in bioprinting.

Objectives

2.Objectives

My thesis project aimed at combining laser-based tissue engineering strategies and human cells to recreate 2D/3D microenvironments that more realistically reflect *in vivo* muscle tissue's complexity and architecture. In particular, we set up and optimized a combination of laser processes to improve the proliferation, migration, orientation, and differentiation of human myoblasts into myotubes while improving maturation of muscle fibers to achieve highly organized muscle models *in vitro*.

The project is articulated around two main axes. The first objective is to utilize the Laser-Induced Forward Transfer (LIFT) process to successfully print living cells on a substrate. In this regard, optimizing the printing set-up and studying post-printing cell survival allowed us to confirm the potentiality of the LIFT process for tissue engineering. The second part aimed to establish direct laser-writing strategies in order to create structures and special topography that could influence cell behavior and improve their organization and maturation. Finally, we sought to efficiently combine these two processes in one unique laser-based platform able to create complex *in vitro* models.

- Laser-Induced Forward Transfer

This thesis started with the setting up and the optimization of the LIFT printing process. We first aimed to evaluate different hydrogels and their associated jetting dynamics regarding the bio-ink compositions and rheological characteristics. The objective was to determine laser parameters and suitable bio-ink capable of producing highly controlled jetting dynamics that would reduce the potential mechanical impact on the cells. The printing process's ability to deposit large numbers of droplets with high spatial resolution in a very short time was then evaluated. I finally studied the ability to control the number of cells per droplet, adding to the versatility of the printing process (**Article 1**, Duvert, Casanova *et al*.).

Once the LIFT experimental protocol was set up and we had a general idea of the critical parameters involved in the bio-printing process, we turned our attention to the survival of the cells. For that, we considered the printing by analyzing separately two distinct key steps: the ejection and the deposition. The ejection accounts for the laser-matter interaction on the donor substrate and the acceleration of the bio-ink. The deposition accounts solely for the arrival of the bio-ink jet onto the receiver substrate.

Both phenomena must be precisely studied to determine their respective impact on cell survival and to achieve excellent post-printing survival rates (**Article 2**, Duvert, Murru, *et al*.).

- Topographical guidance

In parallel with the printing process, various strategies were implemented to guide and control the development of myoblasts. We first explored the possibility of creating topography, especially channels, on bio-polymer surfaces. This choice was motivated by the bio-compatibility and excellent cell interaction associated with these materials. To this aim, I developed and implemented laser-structuration protocols on polymer coatings to create topographies that could impact cell development and maturation (**Article 3**, Murru, Duvert *et al*., under review).

- Combination of laser processes

Once both processes were tested, confirmed, and optimized, we combined them to create *in vitro* muscle models. The main objective here was to print cells by LIFT directly onto structures that we previously designed and created by laser. To do that, we set aside bio-polymer coatings and opted for the direct structuration of polystyrene cell culture coverslips. The structuring of this polymer was extensively studied and evaluated before being combined with LIFT printing (**Article 4**, Duvert, Murru *et al*., in preparation). We assessed the overall process capability for modeling muscle diseases by printing human immortalized myoblasts derived from patients affected with either FacioScapuloHumeral Dystrophy (FSHD) or Duchene Muscular Dystrohy (DMD).

- Exploration of other laser-based tissue engineering approaches

We further investigated the potential of our laser set-up by focusing, on the one hand, on the generation of laser-ablated silicon nanoparticles to improve the quality of skeletal muscle models (**Article 5**, Murru, Duvert et al.). These nanoparticles were morphologically characterized and their application as an abiotic factor to enhance myoblast proliferation, motility and differentiation was assessed.

On the other hand, we explored the possibility of creating three-dimensional cell-laden scaffolds for modeling human skeletal muscle through a two-step process: first, acellularized hydrogels were 3D laser-structured to produce aligned hollow channel patterns; second, the channels were filled with a solution of muscle cells resuspended in

the biomaterial to induce preferential cell alignment in a fiber-like manner, mimicking the architecture of skeletal muscle tissue.

Lastly, we developed an electrical stimulation system to enhance the maturation of muscle cells cultured on the laser-structured polymer described in **Article 4.** We demonstrated its ability to improve the quality of myotubes, obtaining functional muscle models that can be used in disease modeling applications.

Results

3.Results

3.1 Article 1: High repetition rate laser-induced printing of bioink with picosecond pulse durations: optimization of the printing process

Lucas Duvert[a,b*], Adrien Casanova[a], Ahmed Al-Kattan[a], Stefano Testa[b],

Frédérique Magdinier[b], Anne-Patricia Alloncle[a] *

a: Aix Marseille University, CNRS, LP3 UMR 7341 , Marseille, France

b: Aix Marseille University, INSERM, Marseille Medical Genetics, Marseille, France

Published Advanced Engineering Materials (2025)

Context

The Laser-Induced Forward Transfer (LIFT) process uses short laser energy pulses to deposit a targeted material on a receiver substrate. This method allows for the printing of a controlled amount of material with a high spatial resolution and reproducibility. LIFT can also be applied to the bio-printing and the precise deposition of living cells. The process nevertheless induces mechanical stress that could impact cell survival and ability to proliferate. For this reason, the choice of the bio-ink and the characterization of the jetting regime is of crucial importance.

This initial preliminary study aimed to determine a set of laser parameters (pulse energy, gap between the donor and the receiver, pulse duration) and a bio-ink formulation suitable for cell printing. The objective was here to determine and optimize conditions in which the mechanical impact of the laser on the cells will be minimized and to have a comprehensive understanding of the jetting dynamic of biopolymer under picosecond regime.

Results

Among other considered polymers, alginate was chosen as a bio-ink basis for its rheological properties and stability. The evolution of viscosity depending on shear stress was evaluated for several solutions supplemented with different concentrations of alginate (**Fig 11.A**). The inks were tested for printability, and several jetting regimes were identified depending on the ink viscosity and the laser pulse energy. With an alginate concentration ranging from 2.5 to 3% (w/w) and appropriate pulse energy, a special jetting regime was deemed ideal for cell printing (**Fig 11.B**). In these conditions, the jets are, on one hand, highly directive with a precise propagation perpendicular to the donor substrate and, on the other hand, present a maximum propagation length before retracting into the donor substrate. This last property suggests a jet of null velocity with which living cells could be deposited while reducing the mechanical stress. With this in mind, we further optimized the reproducibility and maximum jet propagation length depending on the ink viscosity. We finally chose a bio-ink made of 3% alginate supplemented with 10% glycerol to limit evaporation and increase the thin donor layer quality.

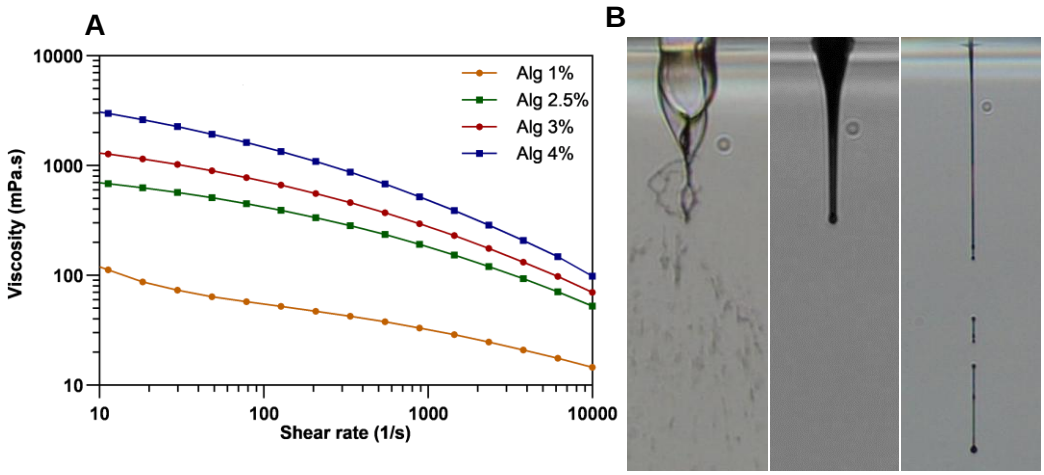

Figure 11 : (**A**) Bio-ink viscosity as a function of alginate concentration (**B**) Jetting pictures taken 40µs after the laser pulse interaction. From left to right: Alginate 4%: no jets / Explosion ; Alginate 3% – 2.5%: Well-defined jets ; Alginate 1%: Jet out of range/fragmenting.

We assessed the bio-ink ability to be printed at high repetition rates and characterized the laser parameters which allowed for the ideal material deposition. Spatial independence of the different jetting coupled with the non-synchronized jet acceleration phases allowed for a succession of directive jets with limited influence on

each other (**Fig 12.A**). These results were applied to cell printing, where we demonstrated the ability of the process to control the quantity of material and, by extension, the number of cells deposited. This cell number could be adjusted through two strategies: increased pulse energy (**Fig 12.B**) or multi-passage printing. The latter presents the advantage of keeping a fixed receiver substrate and preserving the jetting optimization previously described.

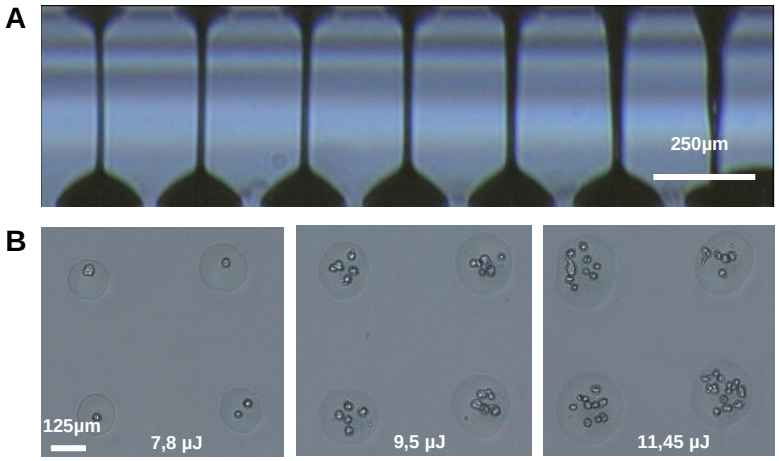

Figure 12 : (**A**) High-speed printing, 13.5µJ Alginate 3%, 30kHz, 32µs between each jet formation. (**B**) Evolution of the printed cells number depending on the laser pulse energy (one path).

Conclusions

This study allowed for the setup of the LIFT experiments and an initial understanding of the laser parameters affecting material transfer. A jetting regime was identified to potentially reduce the mechanical stress on cells. Additionally, we proved our ability to use high scan speeds while printing a controlled number of cells.

Contribution

In this work, I studied the rheology of different biopolymer compositions and concentrations. I also focused my attention on setting up the LIFT experimental process and associated protocol, as well as to study of the chosen polymers' printability regarding cell bio-printing. Finally, I investigated the ability of the process to control the number of cells deposited, thereby validating the capabilities of our experimental setup.

Publication

ADVANCED
ENGINEERING
/MATERIALS
www.aem-journal.com

High Repetition Rate Laser-Induced Printing of Bioink with Picosecond Pulse Durations: Optimization of the Printing Process

Lucas Duvert, Adrien Casanova, Ahmed Al-Kattan, Stefano Testa, Frédérique Magdinier, and Anne-Patricia Alloncle**

It has been more than two decades since laser-induced forward transfer (LIFT) was studied on a laboratory scale for its ability to print biomaterials. Most of the published works in this field are focused on the use of nanosecond lasers. Our final objective is to use the LIFT technique in a picosecond regime to create in vitro biomodels for tissue engineering and regenerative medicine applications. But in a first approach, the work presented here focuses on hydrodynamics and rheological studies for the optimization of the process for bioapplications. In order to precisely control the amount and position of the deposited material, it is necessary to carefully investigate the jetting dynamics as a function of various parameters, including the laser fluence and the rheological properties of the bioink. In this study, time-resolved fast imaging is used to investigate the hydrodynamics of the transfer of successive jets at a high pulse repetition rate. Different conditions have been determined (bioink viscosity, specific jetting dynamic associated with a precise distance for printing, and laser parameters) for precise control of the quantity of ink and number of cells deposited per droplet associated with high accuracy on their location and good reproducibility of the printing process.

1. Introduction

Printing techniques applied to biology have undergone considerable development over the last 20 years.[1–18] A quick search on the web of sciences using the keyword "3D printing" reveals that 75% of the articles published on this topic have been released in the last 5 years. Published works are based on interdisciplinary approaches combining cell biology, chemistry, engineering, and sophisticated protocols to create artificial functional tissues. Two approaches can be distinguished such as the fabrication of scaffolds and their subsequent seeding with cells[19–23] or the direct printing of biological materials such as proteins,[7] DNA,[24] or living cells.[2,3,6,25,26]

The last few years have seen the emergence of an ever-growing market driven by the numerous fields of applications of these technologies. For instance, combining bioprinting and innovative stem cell protocols also aims at developing cost-effective strategies for creating complex and tailored biostructures for personalized medicine applications. These structures have diverse applications in biomedical research, including tissue engineering, disease modeling, drug discovery, and regenerative medicine.[27]

Various bioprinting techniques, such as polymerization-based printing, inkjet, and extrusion, are already widely used in this field. The polymerization-based technique consists of fabricating a scaffold, dot per dot and layer by layer, by inducing polymerization of a material under UV/visible laser radiation. In the case of two-photon polymerization, a femtosecond laser is used to induce non-linear absorption inside a specific material, leading to its polymerization. In the first case, structures down to microscale can be obtained while the second technique allows down to nanoscale resolution.[28] Inkjet-based technology consists of the ejection of droplets through a nozzle under a piezoelectric or thermal effect. This technique allows for the controlled printing of small droplets (50–70 μm), making it well adapted for the fabrication of microscale scaffolds. However, this technique is limited by the bioink viscosity (around 10 mPa s maximum) and high cell density, which can lead to nozzle clogging issues.[29–31] Extrusion-based technology is one of the most widely used 3D printing techniques due to its cost-effectiveness and efficiency. It operates by mechanically ejecting bioinks in a continuous stream from a nozzle through applied pressure

L. Duvert, A. Casanova, A. Al-Kattan, A.-P. Alloncle
Laser Plasma and Photonic Processes
Aix Marseille University, CNRS
LP3 UMR 7341, 13009 Marseille, France
E-mail: lucas.duvert@univ-amu.fr; patricia.alloncle@univ-amu.fr
L. Duvert, S. Testa, F. Magdinier
Marseille Medical Genetics
Aix Marseille University, INSERM, Marseille Medical Genetics
13005 Marseille, France

® The ORCID identification number(s) for the author(s) of this article can be found under https://doi.org/10.1002/adem.202402478.

© 2025 The Author(s). Advanced Engineering Materials published by Wiley-VCH GmbH. This is an open access article under the terms of the Creative Commons Attribution-NonCommercial-NoDerivs License, which permits use and distribution in any medium, provided the original work is properly cited, the use is non-commercial and no modifications or adaptations are made.

DOI: 10.1002/adem.202402478

(e.g., piston-driven), enabling the direct printing of complex structures. This technique can process a large range of materials, both cell laden and acellular, with high viscosities (6-30 x 107 mPa s) while achieving a printing resolution of ^100 pm.[17,32] Every technique has its advantages and limitations, and, depending on the application, optimization is required by controlling various parameters such as ink printability, desired printing resolution, process speed, and reticulation protocols.

For more than two decades, the possibility of using laser techniques to print biomaterials such as biomolecules[33,34] or even living cells[35–37] was demonstrated. The principle of these alternative techniques was to use a laser pulse and the laser–matter interaction to transfer a small volume of material from a support called "donor" to another support called "receiver" placed nearby. The donor is designed in different ways depending on the technique to be used and the type of material to be transferred. In the laser-induced forward transfer (LIFT) process that is used in this work, the laser pulse is usually absorbed by a thin layer of material (called a dynamic release layer (DRL)) deposited between the carrier, transparent to the laser wavelength, and the targeted material to be transferred. Firstly used to create conductive metal lines,[38,39] this technique has been widely studied and used on different types of materials (organic, dielectrics, semiconductors, liquids, solids, powders, etc.) for electronic applications.[40–42] More recently, in the context of biological applications, this printing technique has been adapted and optimized for bioink printing.[43–47] Indeed, laser-assisted printing, particularly laser bioprinting, has shown a massive potential development in modern medical practice and presents several advantages to overcome previously cited limitations. Due to its contactless and nozzle-free characteristics, this technology is perfectly suitable for printing high-viscosity or high-cell-density bioinks.[2,47,48] It offers great promise for the fabrication of complex and organized relevant biomodels for studying diseases or drug discovery.

Indeed, the LIFT process used in this study allows the deposition of a controlled amount of material (a few tens of picoliters) in solid or liquid phases with high resolution. It has already been successfully applied to depositing organic and inorganic compounds, including biomaterials and living cells. We can, for example, mention the printing of a 2D model of human endothelial cells with a high-resolution[49] or the laser-induced printing of a 3D model of multilayer arrangements of fibroblasts and keratinocytes embedded in collagen as a simple model for skin.[50]

The high survival rate of the printed cells is also a key point of this technique. In this regard, the use of ultrashort laser pulses (mainly in the nanosecond regime) avoids temperature issues and ensures a high viability rate.[36,51]

Laser-assisted transfer is a complex process driven by several parameters that play a role in the ejection dynamic and so the printing results such as the thickness of the absorbing layer, the rheological properties of the targeted material and its thickness, and the gap between donor and receiver as well as different laser parameters such as the wavelength, the pulse duration, the spot size, or the laser fluence. When dealing with biological materials, all of these parameters have to be adapted and optimized, and several challenges need to be overcome. The low viscosity of the culture media containing the cells is an excellent example of this need for optimization. It directly impacts the thin film's homogeneity and significantly complicates the printing process, resulting in a loss of control, accuracy, and reproducibility.

We, therefore, present an optimization of the LIFT process to achieve reproducible printing combined with a high spatial resolution of biocompatible polymers.

For that, the formulation of a bioink, accompanied by the study of its viscosity and associated jetting dynamic, is first required. The jet's evolution and speed were thus recorded and measured thanks to a precise visualization to evaluate and minimize the influence of the mentioned mechanical impact on the receiver substrate. In the second phase, the addition of cells to the bioink and possible further optimization will be discussed.

Thanks to this optimization of the LIFT process, we proved our ability to print large, ordered matrices of picoliter droplets. In addition to this precise control, changing the laser pulse energy and using different printing strategies allowed the number of cells in each droplet to be controlled from clusters of cells down to a single-cell level, improving the process versatility. These results open new perspectives for the creation of complex in vitro models with various biomedical applications. The viability of LIFT-printed cells, which is essential for the intended applications, has also been studied and is presented in another document,[52] as it depends on numerous factors beyond jet hydrodynamics.

2. Experimental Section

2.1. Laser-Induced Forward Transfer and Real-Time Visualization Setup

The LIFT technique is a laser printing technique that uses laser pulses to transfer tiny amounts of materials from a donor film to a receptor substrate. The setup consisted of three main parts: 1) a laser source, 2) a donor substrate where the material to transfer is spread as a thin film, and 3) a receiver substrate on which the targeted material will be deposited. Depending on the optical properties of the material to be printed, an absorbing metallic layer (titanium or gold for biocompatibility reasons), also called a DRL, could be deposited on the donor substrate between the transparent substrate and the targeted material in order to absorb the laser energy and promote laser–matter interaction. To initiate the transfer process, the laser beam was focused on the donor, and, depending on the experimental conditions (laser pulse energy, thin film thickness, rheological properties, and gap between donor and receiver), the targeted material was melted and partially vaporized.

This vaporization created a high-pressure and high-temperature vapor bubble. Due to this expansion, the liquid film formed a jet that propagated towards the receiver, leading to the deposition of droplets.

Here, we aimed to print droplets or lines filled with cells with high control of their location and on the printed volume of material with high repeatability and reproducibility. The main influencing parameters to achieve these results were 1) the bioink

© 2025 The Author(s). Advanced Engineering Materials published by Wiley-VCH GmbH

thickness, composition, and physical properties; 2) the laser beam spot size; 3) the energy per laser pulse; and 4) the gap distance between the donor and receiver. All these variables were closely linked and influenced each other. Therefore, the presented study would focus on the composition of the bioink and the laser pulse energy, both of which affected the propagation distance and, consequently, the printing gap. The printing optimization was first performed with an ink without cells.

For all the following work, a laser Carbide CB1-05 (Light Conversion) emitting at 1030 nm with a repetition rate from a single shot to 1 MHz and a pulse duration of 10ps was used. The laser's average power was 5 W, and its maximum energy per pulse was close to 85 μJat60KHz.

The choice of wavelength was motivated by its suitability to work with biomaterials and living cells. Indeed, to avoid alteration in biological properties due to the potential distortion of DNA by ultraviolet radiation, near-infrared lasers were preferred.[53,54] In addition, the laser pulse needed to be very short (in nano- or picosecond regime) to limit the thermally affected area around the laser/matter interaction and prevent the degradation of the biological material due to an increase in the local temperature.

A combination of mirrors and lenses was added along the optical path to drive the laser beam to the donor substrate and focus it. A polarizer coupled with a half-wave plate positioned in the optical path was used to reduce and tune the energy in a range suitable for bioprinting (a few microjoules).

The laser beam was finally routed onto an optical scan system (SCANLAB intelliSCAN 14). The scanner allowed us to drive the beam on an area of 25 cm^2 to cover the entirety of the donor's surface with desired prepared patterns. The associated software LaserDESK was used to create the printing patterns. The beam was focused on the donor substrate with an F-Theta lens (Linos F-Theta-Ronar lenses with 70 mm of focal distance).

A translational system composed of six motorized microtranslation stages (MFA Newport 25 mm) allowed the translation of the donor substrate in the direction of the incident laser beam (vertical direction z) as well as the translation of both donor and receiver in the other perpendicular directions (x and y). The scanner, coupled with the F-Theta lens, was motorized to adjust its position according to the gap between the donor and the receiver and the lens focal length. All the stages were driven by a six-axis motion controller (Newport Motion Controller XPS)(Figure 1).

A Ximea xiQ USB3.0 camera coupled with a Navitar x12 zoom lens and a nanosecond flash (Nanolite, 12 ns) was selected to visualize and study the ejection dynamics. A beam splitter and a photodiode were added to the beam optical path to detect the laser pulse (in addition to the oscillator pulse train), and a delay generator (Stanford DG645) controlled the flash triggering and the camera shutter regarding the laser pulse arrival. By changing the delay for successive laser pulses, the whole ejection dynamic could be artificially reconstructed from a series of jets and easily visualized (Figure 1).

2.2. Cell Line

Murine myoblasts C2C12 (ATCC) were cultured in T-75 flasks (Sarstedt) at 37 °C and 5% CO2 in Dulbecco's Modified

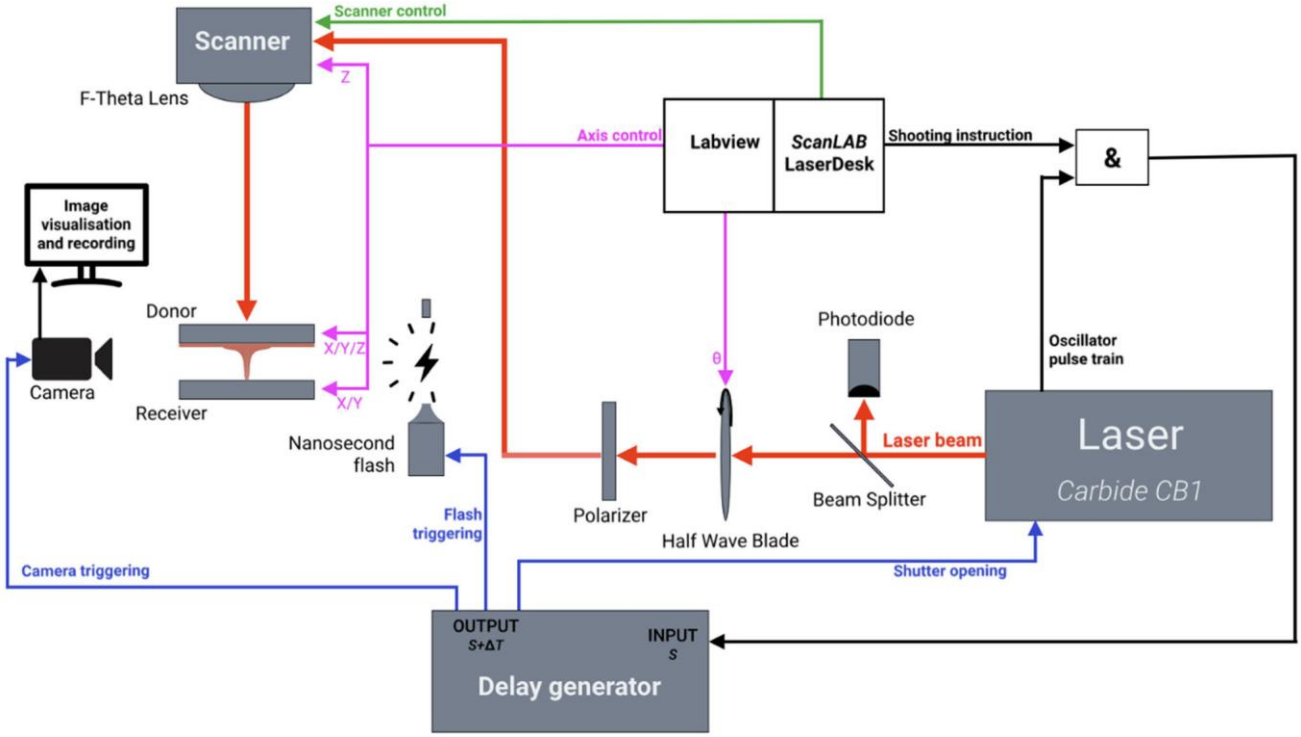

Figure 1. LIFT set up for living cell printing and jetting analysis.

© 2025 The Author(s). Advanced Engineering Materials published by Wiley-VCH GmbH

Eagle Medium (DMEM) GlutaMAX (Gibco) supplemented with 10% heat-inactivated fetal bovine serum (FBS, EuroClone), penicillin (100IUmL"1, Gibco), and streptomycin (100mgmL^{-1}, Gibco). For bioprinting experiments, once 80% of confluence was reached, cells were collected and centrifuged (125 g for 10 min), and the cell pellet was then resuspended in the bioink before spreading it on the donor substrate. A concentration of 50 x 106 cells mL^{-1} was chosen for the bioprinting experiments. The images and counting of the cells were obtained with a reverse microscope (EVOS M5000, Invitrogen, Thermo Fisher, America).

2.3. Donor Substrate Preparation

The donor system consisted of a bioink film (targeted material) spread on a transparent substrate to the laser radiation (500 μm glass slides), previously coated with an absorbing layer. During our experiments, the absorbing layer was a 50 nm layer of titanium deposited with an evaporation technique (LAAS CNRS Renatech). Titanium was chosen due to its biologically inert behavior, capacity to absorb the laser's 1030 nm radiation used in our setup, and good adhesion with glass. This layer (DRL) forced the laser–matter interaction to initiate the ejection process and protected the biological material from damage due to the laser irradiation.

The cells were embedded in a hydrogel suitable for their survival, and its rheological properties were investigated to obtain optimal printing conditions. The thin bioink layer was performed using a micrometer film coater, Elcometer 3580. The Blade Coater, of which the gap has been previously set up, was automatically pushed over the samples at a constant speed. We obtained thin bioink layers of about 100 μm, and the blade wiped out the excess ink to create a uniform surface of the required thickness.

2.4. Image Analysis for Dynamic Study

A homemade MATLAB program was developed to extract the jetting characteristics from the pictures taken by the previously described camera/**fl**ash setup. Pictures were taken over a period of 100 μs after the laser impact with a time spacing of 1 μs. The analysis of the pictures began with the focusing and the centering of the jet (Figure 2A), followed by its isolation to create a binary image (Figure 2B). The boundaries of the jet were determined through a combination of edge-detection functions (Figure 2C). The jet was then isolated from the substrate (Figure 2D). From there, the position of the jet's tip could be easily identified and plotted (Figure 2E). An analysis of each jet was automatically done before compiling the results for plotting (Figure 3B). This process allowed us to quickly process large quantities of images to extract the characteristics of the associated printing parameters. The data were smoothed with a moving average throughout 3 points to eliminate the intrinsic variation of the jetting mechanism.

2.5. Process Optimization and Bioink Preparation for Living Cell Printing

As previously mentioned, the use of biological material, and especially living cells, as part of the LIFT process, presented some challenges that need to be considered. One of the difficulties came from the reproducibility of the thin layer (targeted material) deposited on the donor substrate, of which the thickness will determine the jetting quality and characteristics. In our case, the bioink was mainly composed of cell culture media suitable for the chosen cell line (DMEM) or appropriate buffer (Dulbecco's phosphate-buffered saline solution (DPBS)) supplemented with various weight percentages of biocompatible polymers (alginate, gelatin, or glycerol). Polymers mainly increased the viscosity of the bioink, leading to a better layer thickness homogeneity needed to ensure a more reproducible printing process. Prior to the bioink spreading, donor substrates were treated by plasma torch (AcXys ULS Omega) to increase the surface hydrophilicity and facilitate the uniform spreading of the bioink, once again improving the layer thickness homogeneity. The viscosity of different bioinks was characterized by rheological studies using a rheometer MCR 102 (Anton Paar).

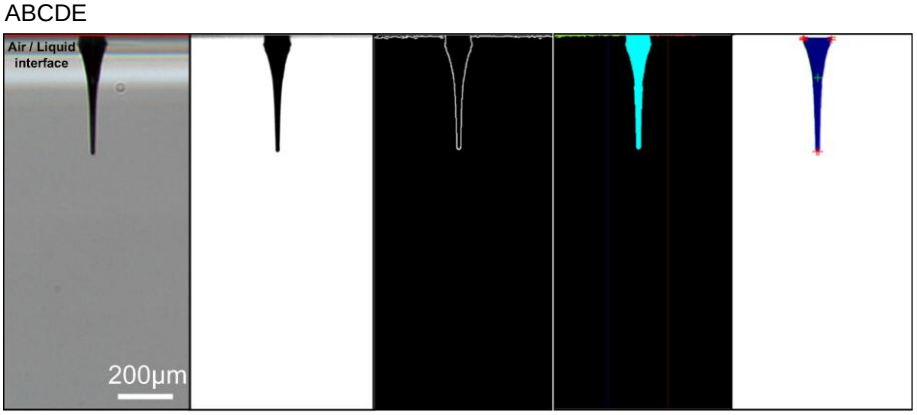

Figure 2. Image analysis by MATLAB for jet detection and following of the dynamic. A) Original shadow image of the jet during the printing process (alginate 2.5%, 18 μs after laser impact, 13.5 μJ). B) Binary image of the previous picture. C) Edge detection of the jet. D) Removal of the substrate and unwanted objects. E) Detection of the extremities of the jets (red cross) and its barycenter (green cross).

© 2025 The Author(s). Advanced Engineering Materials published by Wiley-VCH GmbH

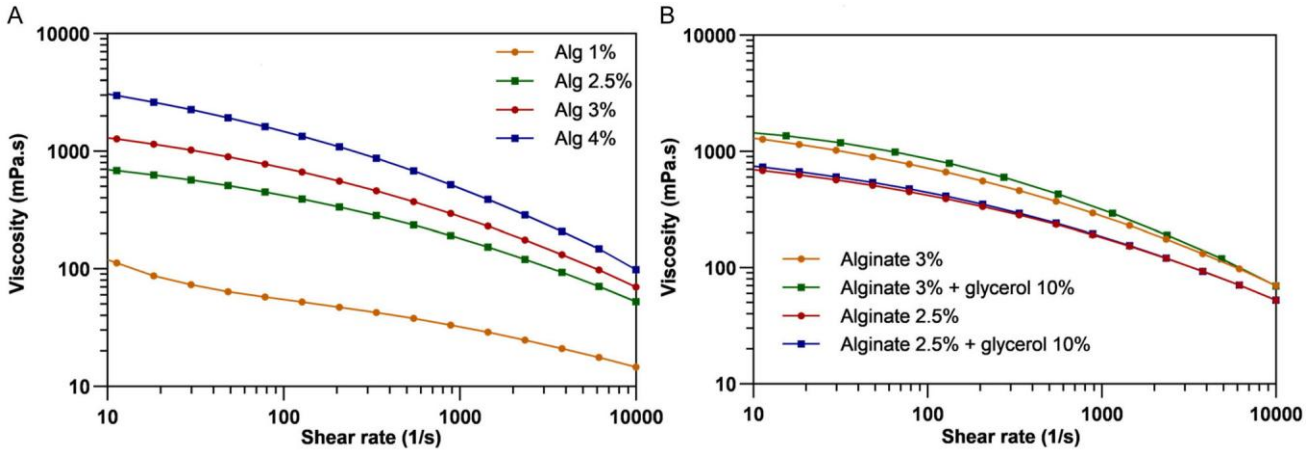

Figure 3. A) Bioink viscosity as a function of alginate concentration. B) Bioink viscosity as a function of glycerol concentration. Alginate 2.5% (red) and 3% (orange) in PBS compared to their counterpart complemented with 10% of glycerol (w/w) (blue curve 2.5%, green 3%).

3. Results and Discussion

The first set of experiments aimed to identify an optimal range of parameters to start the process optimization. Our objective was to determine suitable settings and bioink composition where a jet of defined length can be obtained and easily tuned. This precise control of the jetting dynamics gives us control over the mechanical impact of the transfer. By precisely studying the dynamic and the printing parameters affecting it, this impact can indeed be limited to its maximum extent while allowing for controlled pattern printing with a high resolution.

3.1. Formulation and Study of Printability of a Standard Bioink

The first parameter we investigated was the rheological properties of the bioink. Alginate was chosen as the main component of the bioink for its biocompatibility, stability regarding time and temperature, and the large range of ink viscosities easily obtainable by tuning its concentration. Several experiments have been conducted with various alginate concentrations, and the jetting dynamics have been recorded and compared. Figure 3A shows the viscosity variation of a DPBS solution supplemented with different alginate concentrations as a function of the shear rate. The range of tested formulations was set between 1% and 4% of alginate for practical considerations. Above 4%, the solution becomes too viscous to guarantee a homogeneous cell suspension. Under 1% alginate, the solution is, however, too liquid, leading to inhomogeneous cell distribution on the donor substrate.

The non-Newtonian and rheo-fluidizing behavior of bioinks are highlighted in Figure 3A. A significant difference can indeed be observed in the rheological behavior of the tested bioink formulations at low shear gradients. Respectively, for 1, 2.5, 3, and 4% of alginate at a shear rate of 10 s^{-1}, the viscosity is about 110, 690, 1275, and 3000 mPa s. This difference decreases for high shear gradients.

To further increase the reproducibility of the jetting dynamic and, therefore, of the resulting printing, glycerol was added to the bioink composition. Glycerol limits the thin film evaporation to preserve the rheological properties of the ink during a more extended period.[47] Indeed, once spread on the donor substrate, a bioink without glycerol will show signs of drying about 30 s after its spreading, underlying rheological changes to the entire layer. This drying time is extended to more than 120 s by adding 10% (w/w) of glycerol to the bioink composition. Given the fast-printing times enabled by the galvanometric scanner—only a few seconds for complex patterns—this extended evaporation time is especially crucial for the delicate donor preparation protocol, leading to improved overall reproducibility. As can be seen in Figure 3B, the addition of glycerol to the alginate-based bioink does not significantly modify its viscosity and, consequently, its printing behavior. Studies show that glycerol causes cytotoxic effects at higher concentrations, with 10% being the maximum value safely achievable.[55]

For Newtonian fluids, jet dynamics—including the breakup phase caused by instabilities—have been extensively studied for various viscosities.[56,57] Additionally, most studies in the literature focus on jets formed either by flow through nozzles or by the deformation of a free surface under various mechanisms (shock wave, cavitation bubble).[57,58] In the case of the jet induced by LIFT, the jet forms through the deformation of a thin liquid film's free surface. A detailed study of jet formation from thin liquid films in a process similar to LIFT, known as BA-LIFT, has been reported by Brown et al.[59] In this process, the DRL is composed of a thin layer of solid polymer. The beam energy absorbed by this film forms a gaseous cavity which expands while remaining confined by the polymer. If the energy produced by the blister is high enough, a jet is generated. For non-Newtonian bioinks, such as our alginate-based inks, the dynamics and breakup of the jet are significantly more difficult to model and control.

To study the ink's printability, the receiver substrate was removed to record the formation of the jets and investigate their complete evolution in time. At fixed bioink layer thickness (150 μm), three main jetting behaviors can be distinguished depending on the laser energy deposited and the viscosity of the bioink used (Figure 4). 1) High viscosity (>4% alginate) will

© 2025 The Author(s). Advanced Engineering Materials published by Wiley-VCH GmbH

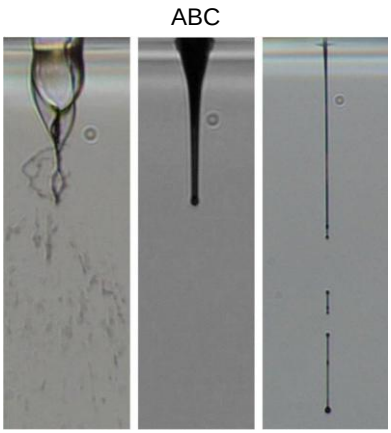

Figure 4. Jetting pictures taken 40 µs after the laser pulse interaction. A) Alginate 4%: no jets/explosion. B) Alginate 3–2.5%: well-defined jets. C) Alginate 1%: jet out of range/fragmenting.

require more energy to reach the jetting threshold. A laser pulse with an energy comprised between 28 and 36 µJ will induce the formation of a short jet with no sign of elongation over time. The length of the jet does not exceed the size of the initially formed bubble. Under 28 µJ, there is not enough energy deposited to induce the jetting, and only a slight deformation of the thin **fi**lm can be noticed. Higher energies (above 36 µJ) will lead to a turbulent/explosive printing (Figure 4A). 2) The viscosity obtained with about 2.5–3% of alginate will induce a well-de**fi**ned perpendicular jet with a de**fi**nite propagation distance (Figure 4B). Once the jet's maximum length is reached, an accumulation of matter can be seen forming at the extremity of the jet. It then withdraws back into the donor substrate without any sign of breakup. We observed this quality of jetting for energies ranging from 6 to 23 µJ. Above 23 µJ, the accumulated matter previously mentioned detaches from the jet, leading to fragmentation. For higher energies, the jetting becomes explosive or turbulent, and the characteristic jet's shrinkage back inside the donor **fi**lm, associated with a maximum propagation length reached, no longer occurs. Below an energy of 6 µJ, there is, again, not enough energy to induce a jet of adequate length for LIFT bioprinting. 3) Finally, a decrease of viscosity (alginate 1%) will lead to thinner, fragmented jets with no reabsorption of the jet back into the donor substrate (Figure 4C). This phenomenon is observed with low energies comprised between 1 and 5 µJ. Once again, outside of this range, the jetting will be compromised. This low range of usable energies reduces the possibility of tuning and adjusting the jet's maximum propagation distance.

In order to effectively transfer matter between the donor and receiver with a 4% alginate bioink, the gap between the two substrates should be set to less than 250 µm. This reduced required gap will increase the substrate's placement constraints, making it unsuitable for LIFT bioprinting.

A bioink composed of 1% alginate in DBPS will induce the formation of jets following the typical behavior already described in the literature,[48,60–62] with long and directive jets followed by their fragmentation. However, considering the non-Newtonian properties of our ink, the jet pinches off later in its propagation, rather than immediately after formation, as previously shown by Turkov et al.[63]

Finally, a range of viscosities obtained with between 2.5% and 3% of alginate will induce a jet that retracts back into the donor substrate under the effect of surface tension. The Weber number is typically used in **fl**uid mechanics to characterize the ratio of inertial forces to surface tension forces in a **fl**ow. The Weber number is de**fi**ned as $W_e = \rho\ v^2\ l/\sigma$ with ρ as the liquid density, v as the tip jet velocity, l as the jet characteristic dimension, and σas the surface tension. A high W_e number indicates that inertial forces prevail, which is true during the initial formation of the jet. However, as the jet tip velocity decreases, the Weber number drops, and surface tension forces begin to dominate, leading to the jet's retractation. Consequently, there is a moment corresponding to the maximum jet's propagation length during which the jet's speed is minimal and becomes null before starting to withdraw. Additionally, by placing a receiver substrate at this precise area, we can suppose that the mechanical impact of the jet onto the receiver is minimal.

Given these observations, a bioink composition of alginate between 2.5% and 3% will be used for further analysis. With this range of viscosities, the donor layer thickness is also more reproducible, guaranteeing a homogeneous distribution of the cells.

3.2. Characterization of the Jetting Dynamics

Once a range of suitable bioink viscosity was determined, the jet's complete dynamic induced by the interaction of the laser with the donor substrate can be studied and broken down into several distinct steps (Figure 5A,B). For a laser pulse energy of 13.5 µJ, we can see the formation of an initial bubble between 0 and 3 µs after the laser pulse. The surface deformation becomes quickly conical as the bubble begins a collapse phase and consequently induces the formation of a liquid jet, quite thick (^30 pm), propagating perpendicular from the donor substrate. The jet's length increases during 15 µs before reaching the maximum propagation distance. It then stabilizes at this maximum length for about 15 µs, during which the accumulation of matter previously described occurs. After this short amount of time, the jet **fi**nally retracts, and the ink re-enters the thin donor **fi**lm. The total duration of the dynamic, from the formation of the initial bubble to the complete withdrawal of the jet inside the donor substrate, is about 80 µs. This duration, as well as the presence of stable and directive jets of determined maximum length, depends largely on the viscosity of the considered bioink and of the laser pulse energy.

To achieve precise and successful cell deposition using LIFT, the receiver substrate should be positioned at a distance corresponding to the jet's maximum length region. This is where the jet's speed is minimal, helping to minimize the mechanical impact. The high ejection speed highlighted in Figure 5C (up to 50 ms^{-1}) underlines the importance of precisely positioning the donor substrate to ensure accurate printing. The maximum jet's length region should be situated around 300–800 µm depending on the viscosity of the bioink and the chosen laser pulse energy: a receiver placed too close to the donor will increase the possibility of contact between the substrate and parasite cell transfer, while a too great distance would reduce the

© 2025 The Author(s). Advanced Engineering Materials published by Wiley-VCH GmbH

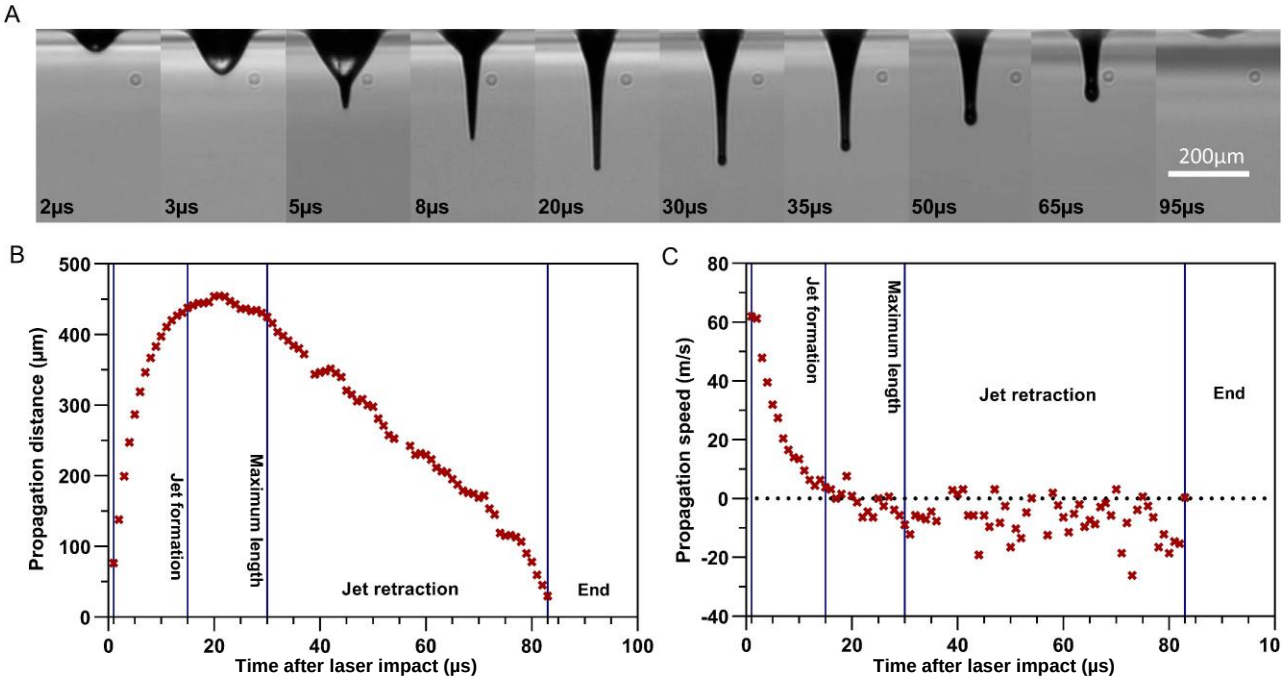

Figure 5. A) Timeline of the jetting mechanism, time after laser impact. B) Propagation distance of the jet depending on time after laser impact. Key moments of the dynamic are highlighted in blue. C) Speed of the jet depending on time after laser impact (positive speeds correspond to the growth of the jet, and a negative sign in front of the speed values corresponds to the decrease of the jet length).

number of jets reaching the receiver. In order to achieve this range of positions with the different bioinks considered, the laser's energy is tuned.

3.3. Influence of Viscosity and Layer Thickness on the Printing Process

The precise influence of the bioink viscosity was investigated to further improve the quality of the jetting dynamic and thus obtain highly reproducible printed patterns. The previously described procedure was conducted for alginate 2.5% and alginate 3%, both supplemented with 10% of glycerol in DPBS. The energy was adjusted for both bioinks to have similar maximum propagation lengths of about 400 µm, adapted to our experimental conditions. The results are recorded and reported in Figure 6A.

For an alginate concentration of 3% at an energy of 13.5 µJ, the maximum length reached is 460 µm with a standard deviation of 24% at this value. For a concentration of 2.5% with 9.5 µJ, this length is 335 µm with a standard deviation of 31%. We can notice that the reproducibility is better for a bioink of higher viscosity due to stable jetting (slower velocity) while lower viscosities are prone to more turbulent jetting behavior. We also suppose that higher viscosities produce more reproducible donor layer preparation leading to more reproducible results. The gap between both substrates will be set at the maximum distance reached by the jet, considering the value of the error, in order to guarantee the transfer of the targeted material with a minimum jet velocity.

The influence of the bioink thickness deposited on the donor substrate was investigated by adjusting the height of the blade-coating device. The height of the blade relative to the donor surface was set at 100, 150, and 200 µm. After deposition of the bioink, here alginate 3% supplemented with 10% of glycerol (w/w), the jetting dynamic was recorded as previously described, and the distance of propagation of the jet was plotted (Figure 6B) with the distance of propagation in the y-axis as a function of time normalized at the maximum length reached by the jet. As expected, the overall dynamic of the resulting jets is modified by the amount of bioink deposited on the donor substrate. The maximum jet's length reached in this experiment is 765, 609, and 264 µm for, respectively, 100, 150, and 200 µm of bioink layer thickness. When a vapor bubble is created on a solid wall surrounded by a liquid by instantaneous energy deposition (short laser pulse), its motion depends, partly, on the depth of the liquid. If the size of the bubble is much smaller than this depth, its motion follows a spherical pattern. The bubble evolves under isotropic conditions, with similar radii parallel and perpendicular to the solid wall. When the liquid thickness is reduced, the conditions are no longer isotropic. The influence of the free-surface boundary condition and a compressible medium of much lower density than the liquid (air) induce a preferred direction of bubble motion, as observed by several authors. In its expansion phase, the bubble's radius perpendicular to the wall becomes much greater than the parallel one.[48,60] The liquid jet forms from the protuberance at the tip of the gas cavity as the bubble begins its collapse phase. The more the bubble develops perpendicularly to the wall, the stronger the associated jet phenomenon is. This apparent reduction of

© 2025 The Author(s). Advanced Engineering Materials published by Wiley-VCH GmbH

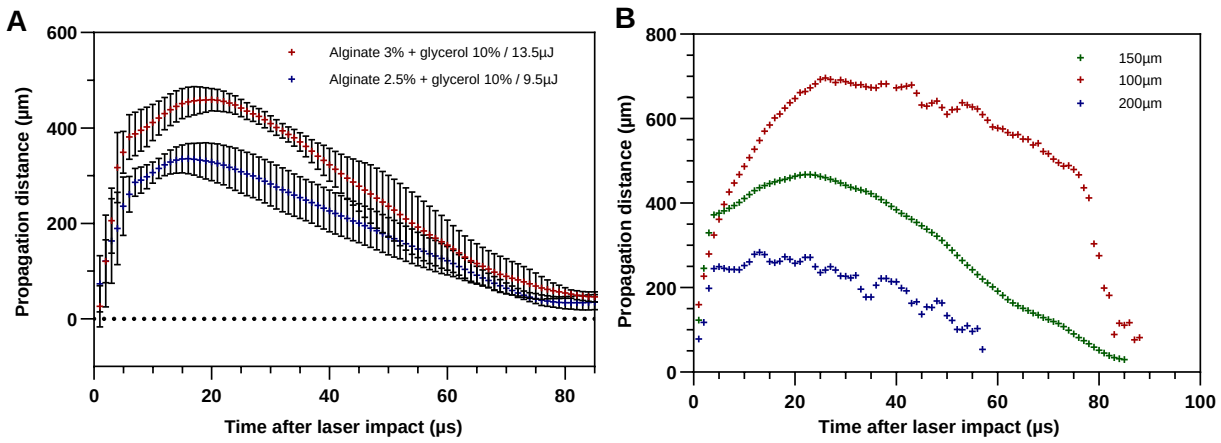

Figure 6. A) Evolution of the jet propagation distance as a function of time after the laser impact at 13.5 pJ. a) Alginate 2.5% + glycerol 10%, measure realized on 6 different samples, mean of standard deviation 61 pm (relative standard deviation 28%). b) Alginate 3% + glycerol 10%, measure realized on 6 different samples, mean of standard deviation 49 µm (relative standard deviation 21%). B) Evolution of the jet propagation distance as a function of time after the laser impact and gel thickness. The gels are made of alginate 3% supplemented with 10% glycerol (w/w) and applied by blade coating at different thicknesses.

the jet's propagation distance for an increasing film thickness is thus directly linked to the increase of donor material. With the maximum layer of 200 µm, the jetting threshold is barely reached, as confirmed by the very short jet detachment, followed directly by its immediate decrease. The reduction of the bioink thickness is logically followed by longer propagation length and stretching of the jetting dynamic. For a layer thickness of 200 µm, the dynamic duration from the bubble's formation to the jet's retraction on the donor substrate lasts around 40 µs. This period is extended to 75 µs for 150 µm and around 95 µs for a layer of 100 µm.

Less material on the donor substrate will offer less resistance to the energy brought by the laser pulse. This way, more ink is propelled with higher inertia, leading to a more extended dynamic. However, a too-thin layer resulting in a higher jet maximum can also lead to more turbulent jets or fragmentation (Figure 4), ultimately resulting in a loss of resolution and reduced accuracy on the receiver substrate. Even though the addition of glycerol to the bioink helps in reducing evaporation, thinner films are also prone to faster drying, causing rheological changes in the ink's properties that modify the jetting behavior while jeopardizing cell survival in the bioink. The intermediate thickness of 150 µm is thus identified as the best option for cell printing.

3.4. Multi-Jet Printing

Another parameter to be considered to control the precise location of the deposit is the time and space between the formation of >two successive jets. The jet is formed following the expansion/collapse of a gas bubble in the liquid film. This jet is highly directive, propagating perpendicularly to the surface of the donor if nothing interferes with the initiation and development of the gas bubble in the liquid film. The presence of cells, impurities, microgas bubbles, and movements of the liquid/air interface can also affect the dynamics of the vapor bubble creation, and the resulting jet propagation is disturbed (tilt, deflection, etc.). For our conditions (donor film thickness of 150 µm, energy per pulse of 13.5 µJ, laser repetition rate of 30 kHz), some real-time visualizations of jets with various initial spacing (from 80 to 250 µm) are shown in Figure 7A. The diameter of the liquid film protrusion due to bubble expansion can reach up to 200 µm for our conditions, and the lifetime of the jet phenomenon is relatively long (several tens of µs).

Consequently, and as it has been observed in the literature,[64] tilts and deviations of the jet dynamics are noted for all the considered spacing until 250 µm. Larger spacing could result in perfectly independent jetting, but it would increase the donor size necessary and complicate the process for close droplet printing.

Therefore, it is necessary to find conditions under which the laser energy is deposited in an undisturbed film or one that has returned to its initial equilibrium conditions. The laser frequency is thus adjusted from 60 to 30 kHz, resulting in a time difference of around 32 µs instead of 16 µs. As previously shown, a jet's life span, from the bubble's creation to its withdrawal into the donor film, does not exceed 100 µs, and the duration of the propagation phase is about 20 µs. By considering a laser frequency of 30 kHz and an ideal spacing of 250 µm between laser shots, we guarantee the spatial and temporal independence of the jets. Indeed, a single laser pulse will induce a jet that will reach the receiver substrate and consequently go through its propagation phase before the next laser pulse and the creation of the next jet. In this way, as shown in Figure 7B, several jets will make prolonged contact with the receiver, the latter promoting the inertia of the dynamic, facilitating the transfer of the targeted material, and, consequently, extending the life span of the jets for far longer periods than the average 80 µs previously determined.

© 2025 The Author(s). Advanced Engineering Materials published by Wiley-VCH GmbH

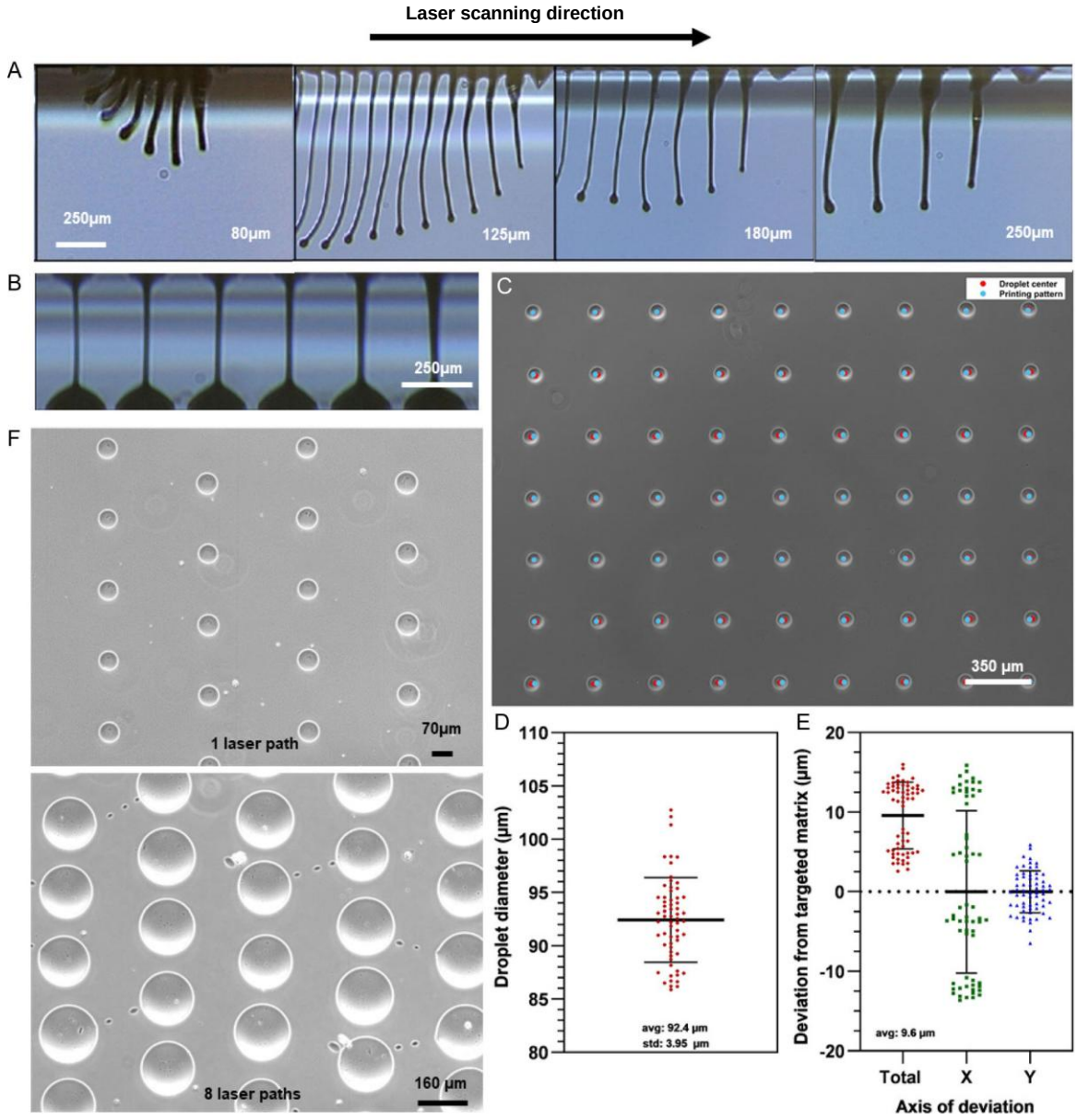

Figure 7. A) High-speed printing with different spatial spacing. 13.5 µJ alginate 3%, 60 kHz, 16 µs between each jet formation. B) 13.5 µJ alginate 3%, 30 kHz, 32 µs between each jet formation. C) Spatial resolution analysis of the printed droplets; the center of the printed droplets is compared to the printing pattern of the galvanometric scanner. The diameter of the droplets is reported in D), and their associated deviation from the original printing pattern along the *x*- and *y*-axis is reported in E). F) Matrices of droplets, 13.5 µJ Alginate 3%, 30 kHz after 1 and 8 consecutive printing; size of the droplets can be adjusted depending on the number of laser paths.

With these printing parameters and the previous bioink optimization, we can print large matrices of hydrogel droplets with high resolution and reproducibility (Figure 7C). The printed alginate droplets are 94 µm wide with a standard deviation of only 3.9 µm (Figure 7D). The average spatial deviation from the original printing pattern programmed in the galvanometric scanner is limited to 9.6 µm, from which most originate from the x-axis where the deviation can reach 15 µm (Figure 7C,E). Due to the larger deviations along the x-axis compared to the y-axis, and the absence of a Gaussian distribution that would suggest randomness, these significant deviations are more likely caused by scanning speed errors (along the a-axis) rather than inaccuracies in the jetting process. The printing process remains highly reproducible in both spatial localization and deposited material.

The size of the deposited droplets can be adjusted through multi-path laser printing, as demonstrated in Figure 7F, by superimposing material on the same location. This first step gives us a solid and essential basis to incorporate the cells into the bioink for bioprinting.

© 2025 The Author(s). Advanced Engineering Materials published by Wiley-VCH GmbH

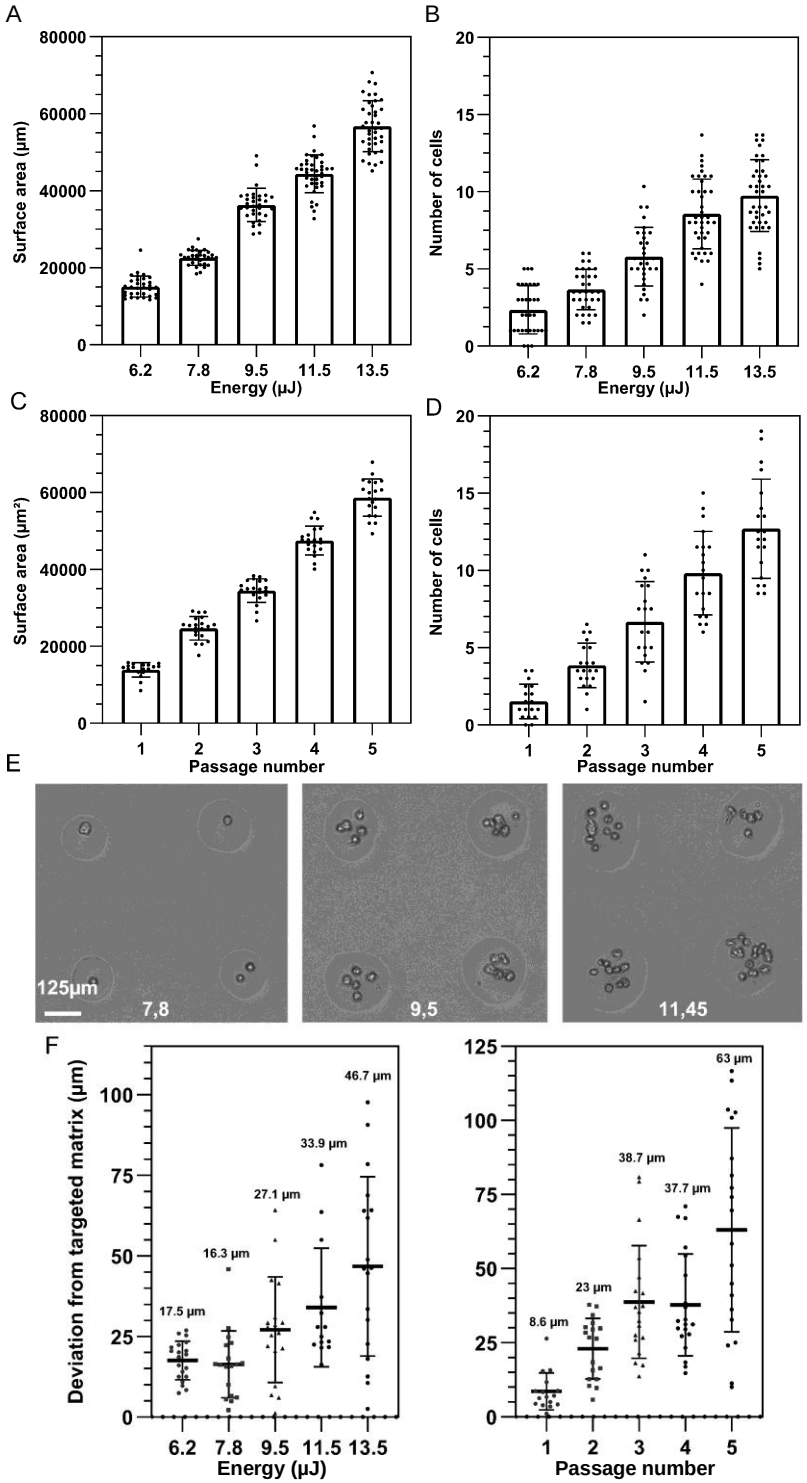

Figure 8. A) Surface area of the printed droplets depending on the energy deposited on the donor substrate. B) Number of cells contained inside the printed droplets depending on the energy deposited on the donor substrate; (A,B) alginate 3%, gap 400 pm, cell concentration 50 x 106 cells mL^{-1}. C) Surface area of the printed droplets depending on the number of consecutive printings. D) Number of cells contained inside the printed droplets depending on the number of consecutive printings. (C,D) alginate 3%, gap 400 pm, 6.2 pJ, cell concentration 50 x 106 cells mL^{-1}. E) Associated pictures of the evolution of the printed cells number depending on the laser pulse energy (one path). F) Spatial resolution analysis of the printed droplets containing the cells; the center of the printed droplets is compared to the printing pattern of the galvanometric scanner. The deviation from the original printing pattern along the *x*- and *y*-axis is reported for both cell printing strategies (increasing energies and consecutive printing). The deviation means are indicated for each condition tested.

© 2025 The Author(s). Advanced Engineering Materials published by Wiley-VCH GmbH

3.5. Optimization of Cell Printing

Adding living cells to the bioink inherently leads to more instability of the jetting dynamic. The presence of micrometric particles and even small aggregates will indeed modify the jetting quality and the maximum length reached by the jet. Nonetheless, the optimization previously described gives us an accurate basis of the receiver's position and printing parameters to effectively transfer the targeted material while avoiding the jet's elongation period, during which the maximum jet's speed is reached and where the cells would have suffered significant mechanical strain.

To demonstrate and characterize the process's ability to modulate the size of the printed droplets, the receiver substrate is placed from the donor substrate. This way, given an ink composed of alginate 3% with a cell concentration of 50 x 106 cells mL^{-1}, energies ranging from 6.2 to 13.5 μm can effectively transfer the targeted material with different spatial resolutions while minimizing mechanical impacts.

An increase in energy leads to a coherent linear increase in the surface area of the printed droplets (Figure 8A). Higher energies induce larger jets with a longer retraction period and, consequently, a longer contact phase with the receiver, thus transferring more bioink to the substrate. The equivalent diameter of the measured areas ranges between 270 μm for 13.5 μJ and 138 μm for the lowest energy considered 6.2 μJ.

Logically, and as can be noticed in Figure 8B, an increase in the amount of transferred matter is accompanied by an increase in the number of cells per droplet. This number varies from an average of 2 cells per droplet for an energy of 6.2 μJ to 10 cells per droplet for 13.5 μJ.

Thus, the number of cells printed can be adjusted according to the amount of energy deposited on the donor substrate.

Another method to adapt the number of cells per droplet is accomplished through multiple laser path printing. Here, we use a single defined energy of 6.2 μJ to print the bioink several times in the exact same location. In this way, as can be seen in Figure 8C, the superimposition of droplets allows the same previously described control of area, with equivalent diameters ranging from 140 μm for one droplet to 280 μm for five consecutive printed droplets. The number of printed cells varies from 1.5 to 12 for 1 and 5 consecutive droplets, respectively (Figure 8D).

Using a variation of energy to adjust the cell number implies a variation of the jet's speed in contact with the receiver substrate. In these conditions, the jet's speed on the receiver is not null. The mechanical impact on the receiver depends on the amount of energy deposited on the donor substrate. On the other hand, multiple laser path printing allows us to control the number of printed cells while positioning the donor substrate ata unique, precisely adjusted position. In this way, the receiver is positioned at the point where the length of the jet is at its maximum, that is, where its speed is close to zero. Hence, this method is preferred to obtain precise control over the number of deposited cells via the LIFT process.

The positioning accuracy of the bioink containing the cells was evaluated in a similar manner as described in Section 3.4 for both cell printing methods. For the two strategies, as shown in Figure 8F, the increased size of the deposited droplet inherently leads to an increase in deviation with a maximum of 46.7 μm for the maximum energy considered and 63 μm in the case of 5 consecutive printings. This difference in mean deviation can be explained by the cumulative error of the successive jet formation, combined with the imperfect expansion of the droplet area due to the presence of the cells in the ink. These results emphasize the inaccuracies in the jetting process caused by the introduction of cells in the bioink.

Increasing the laser pulse energy in order to increase the number of deposited cells induces more variation in the jetting, precisely because of this high number of cells. Nevertheless, in this context, even though the results suggest a superior spatial deviation with a high number of consecutive cell printing, we hypothesize that this deviation can be more easily predicted than the high-energy strategy for highly concentrated cell droplets. In a similar manner, the impact of the addition of cells on the jetting quality can be observed in Figure 8 with the variation of the mean deviation for the printing at 6.2 μJ (Figure 8, left), with a mean of 17.5 μm, and its direct one printing equivalent (Figure 8, right) with a mean of 8.6 μm. Even though the value differs significantly between experiments due to the previously mentioned variation of the bioink, it still allows for accurate and reproducible deposition of the droplets.

4. Conclusion

Here, we have demonstrated the ability of the LIFT printing process to deposit precise amounts of cells with a high spatial resolution and high control of the dimension of the printed bioink droplets. The bioink composition and viscosity have been evaluated for their ability to produce thin films with homogeneous cell repartition and reproducible jetting dynamics. A specific jetting regime was identified where, given a certain bioink viscosity and range of laser pulse energies, the formed jets retract to the donor substrate after reaching a maximum propagation length, implying the existence of a zero-velocity tip jet. This way, we place ourselves in the most favorable condition for cell bioprinting. The determined printing conditions were tested on cell-laden bioinks, which demonstrated high spatial accuracy of the printed droplets while ensuring precise control over the quantity of ink and the number of cells deposited per droplet, with particular attention to the cumulative effect of beam paths on the same location. This study offers a solid practical basis for developing complex in vitro models that could be instrumental in studying diseases or testing therapeutic approaches.

Acknowledgements

The work was funded by the French Defense Innovation Agency (ANR Medilibs and Diagem projects) together with the French Defense Innovation Agency (ANR—DGA/AID—ICELARE Project ID ANR—20—ASTR—0004). The PhD thesis of Lucas Duvert was co-funded by Aix-Marseille University and the French Defense Innovation Agency. This work received support from the French government under the France 2030 investment plan, as part of the Initiative d'Excellence d'Aix-Marseille Université – A*MIDEX "AMX-23-CPJ-05." The project leading to this publication has received funding from the Excellence Initiative of Aix-Marseille University-A*Midex, a French "investissement d'avenir programme" AMX-19-IET-007, through the MarMaRa funding

© 2025 The Author(s). Advanced Engineering Materials published by Wiley-VCH GmbH

scheme. This work was conducted using LaMP facilities at LP3. The authors also express their thanks to “Region SUD.”

Conflict of Interest

The authors declare no conflict of interest.

Author Contributions

Lucas Duvert: data curation (lead); investigation (lead); methodology (equal); writing—original draft (lead); writing—review and editing (equal). Adrien Casanova: conceptualization (equal); data curation (supporting); investigation (equal); methodology (equal); supervision (equal); writing—original draft (supporting); writing—review and editing (equal). Ahmed Al-Kattan: conceptualization (supporting); resources (supporting); supervision (supporting). Stefano Testa: data curation (equal); investigation (supporting); methodology (supporting). Frédérique Magdinier: conceptualization (equal); supervision (equal); writing—review and editing (equal). Anne-Patricia Alloncle: conceptualization (equal); supervision (equal); validation (equal); writing—original draft (supporting); writing—review and editing (equal).

Data Availability Statement

The data that support the findings of this study are available from the corresponding author upon reasonable request.

Keywords

bioinks, biomaterials, laser-induced bioprinting, laser-induced forward transfer

Received: October 24, 2024
Revised: February 24, 2025
Published online:

[1] J. Li, M. Chen, X. Fan, H. Zhou, *J. Transl. Med.* 2016, *14*, 271.
[2] C. Mandrycky, Z. Wang, K. Kim, D.-H. Kim, *Biotechnol. Adv.* 2016, *34*, 422.
[3] N. Mehrban, G. Z. Teoh, M. Birchall, *Int. J. Bioprint.* 2015, *2*,6.
[4] I. Ozbolat, H. Gudapati, *Bioprinting* 2016, *3–4*, 1.
[5] D. J. Ravnic, A. N. Leberfinger, I. T. Ozbolat, *Trends Biotechnol.* 2017, *35*, 1025.
[6] D. Thomas, *Biomaterials* 2016, *1*, 36.
[7] M. K. W+odarczyk-Biegun, A. Del Campo, *Biomaterials* 2017, *134,* 180.
[8] W. Aljohani, M. W. Ullah, X. Zhang, G. Yang, *Int. J. Biol. Macromol.* 2018, *107*, 261.
[9] D. Choudhury, S. Anand, M. W. Naing, *Int. J. Bioprint.* 2018, *4*, 139.
[10] Z. Zhang, B. Wang, D. Hui, J. Qiu, S. Wang, *Composites, Part B* 2017, *123*, 279.
[11] W. Zhu, X. Ma, M. Gou, D. Mei, K. Zhang, S. Chen, *Curr. Opin. Biotechnol.* 2016, *40*, 103.
[12] S. Kumar, R. Malviya, *Appl. Mater. Today* 2024, *39*, 102307.
[13] V. S. Reddy, B. Ramasubramanian, V. M. Telrandhe, S. Ramakrishna, *Curr. Opin. Biomed. Eng.* 2023, *27*, 100461.
[14] S. Zhao, J. Chen, L. Wu, X. Tao, N. Yaqub, J. Chang, *Int. J. Mol. Sci.* 2023, *24*, 11520.
[15] T. Zhao, Y. Liu, Y. Wu, M. Zhao, Y. Zhao, *Biotechnol. Adv.* 2023, *69*, 108242.
[16] Q. Wang, Y. Feng, A. Wang, Y. Hu, Y. Cao, J. Zheng, Y. Le, J. Liu, *iLIVER* 2024, *3*, 100080.
[17] O. B. Omondi, Y. N. Arroyan, B. Onyango, L. Kong, G. Wang, Z. Ye, *Eur. Polym. J.* 2024, *217*, 113210.
[18] N. Bhardwaj, S. K. Yadav, A. Saneja, *Drug Discovery Today* 2024, *29*, 103924.
[19] T. Amna, M. Shamshi Hassan, M.-S. Khil, I. Hwang, *Ceram. Int.* 2014, *40*, 14305.
[20] E. Choi, D. Kim, D. Kang, G. H. Yang, B. Jung, M. Yeo, M.-J. Park, S. An, K. Lee, J. S. Kim, J. C. Kim, W. Jeong, H. H. Yoo, H. Jeon, *Regen. Biomater.* 2021, *8*, rbab001.
[21] J. N. Hanson Shepherd, S. T. Parker, R. F. Shepherd, M. U. Gillette, J. A. Lewis, R. G. Nuzzo, *Adv. Funct. Mater.* 2011, *21*, 47.
[22] A. R. Murphy, A. Laslett, C. M. O'Brien, N. R. Cameron, *Acta Biomater.* 2017, *54*, 1.
[23] A. Ovsianikov, A. Deiwick, S. Van Vlierberghe, M. Pflaum, M. Wilhelmi, P. Dubruel, B. Chichkov, *Materials* 2011, *4*, 288.
[24] M. Colina, P. Serra, J. M. Fernández-Pradas, L. Sevilla, J. L. Morenza, *Biosens. Bioelectron.* 2005, *20*, 1638.
[25] S. Khalil, W. Sun, *J. Biomech. Eng.* 2009, *131*, 111002.
[26] E. Fornetti, F. De Paolis, C. Fuoco, S. Bernardini, S. M. Giannitelli, A. Rainer, D. Seliktar, F. Magdinier, J. Baldi, R. Biagini, S. Cannata, S. Testa, C. Gargioli, *Biofabrication* 2023, *15*, 025009.
[27] L. Caron, S. Testa, F. Magdinier, *J. Neuromuscul. Dis.* 2023, *10*, 761.
[28] V. Harinarayana, Y. C. Shin, *Opt. Laser Technol.* 2021, *142*, 107180.
[29] G. Gillispie, P. Prim, J. Copus, J. Fisher, A. G. Mikos, J. J. Yoo, A. Atala, S. J. Lee, *Biofabrication* 2020, *12*, 022003.
[30] M. H. Shao, B. Cui, T. F. Zheng, C. H. Wang, *J. Phys. Conf. Ser.* 2021, *1798*, 012009.
[31] A. Malekpour, X. Chen, *J. Funct. Biomater.* 2022, *13*, 40.
[32] H.-J. Jeong, H. Nam, J. Jang, S.-J. Lee, *Bioengineering* 2020, *7*, 32.
[33] A. Karaiskou, I. Zergioti, C. Fotakis, M. Kapsetaki, D. Kafetzopoulos, *Appl. Surf. Sci.* 2003, *208–209*, 245.
[34] P. Serra, M. Colina, J. M. Fernández-Pradas, L. Sevilla, J. L. Morenza, *Appl. Phys. Lett.* 2004, *85*, 1639.
[35] J. A. Barron, B. J. Spargo, B. R. Ringeisen, *Appl. Phys. A* 2004, *79*, 1027.
[36] B. Hopp, T. Smausz, N. Kresz, N. Barna, Z. Bor, L. Kolozsvári, D. B. Chrisey, A. Szabó, A. Nógrádi, *Tissue Eng.* 2005, *11*, 1817.
[37] P. K. Wu, B. R. Ringeisen, J. Callahan, M. Brooks, D. M. Bubb, H. D. Wu, A. Piqué, B. Spargo, R. A. McGill, D. B. Chrisey, *Thin Solid Films* 2001, *398–399*, 607.
[38] J. Bohandy, B. F. Kim, F. J. Adrian, *J. Appl. Phys.* 1986, *60*, 1538.
[39] J. Bohandy, B. F. Kim, F. J. Adrian, A. N. Jette, *J. Appl. Phys.* 1988, *63,* 1158.
[40] P. Delaporte, A. Ainsebaa, A.-P. Alloncle, M. Benetti, C. Boutopoulos, D. Cannatà, F. Di Pietrantonio, V. Dinca, M. Dinescu, J. Dutroncy, R. Eason, M. Feinaugle, J.-M. Fernández-Pradas, A. Grisel, K. Kaur, U. Lehmann, T. Lippert, C. Loussert, M. Makrygianni, I. Zergioti, in *SPIE Proceedings*, San Francisco USA 2013, p. 86070Z.
[41] V. Tsouti, C. Boutopoulos, D. Goustouridis, I. Zergioti, P. Normand, D. Tsoukalas, S. Chatzandroulis, *Sens. Actuators, B* 2010, *150*, 148.
[42] E. Breckenfeld, H. Kim, R. C. Y. Auyeung, N. Charipar, P. Serra, A. Piqué, *Appl. Surf. Sci.* 2015, *331*, 254.
[43] C. Unger, M. Gruene, L. Koch, J. Koch, B. N. Chichkov, *Appl. Phys. A* 2011, *103*, 271.
[44] L. Koch, A. Deiwick, B. Chichkov, *Laser Additive Manufacturing*, Elsevier 2017, pp. 421–437.
[45] L. Koch, O. Brandt, A. Deiwick, B. Chichkov, *Int. J. Bioprint.* 2017, *3*, 42.
[46] A. A. Antoshin, S. N. Churbanov, N. V. Minaev, D. Zhang, Y. Zhang, A. I. Shpichka, P. S. Timashev, *Bioprinting* 2019, *15*, e00052.
[47] A. Zennifer, A. Subramanian, S. Sethuraman, *Bioprinting* 2022, *27*, e00205.

© 2025 The Author(s). Advanced Engineering Materials published by Wiley-VCH GmbH

[48] M. Gruene, C. Unger, L. Koch, A. Deiwick, B. Chichkov, *Biomed. Eng. OnLine* 2011, *10*, 19.
[49] F. Guillemot, A. Souquet, S. Catros, B. Guillotin, J. Lopez, M. Faucon, B. Pippenger, R. Bareille, M. Rémy, S. Bellance, P. Chabassier, J. C. Fricain, J. Amédée, *Acta Biomater.* 2010, *6*, 2494.
[50] L. Koch, A. Deiwick, S. Schlie, S. Michael, M. Gruene, V. Coger, D. Zychlinski, A. Schambach, K. Reimers, P. M. Vogt, B. Chichkov, *Biotechnol. Bioeng.* 2012, *109*, 1855.
[51] J. A. Barron, H. D. Young, D. D. Dlott, M. M. Darfler, D. B. Krizman, B. R. Ringeisen, *Proteomics* 2005, *5*, 4138.
[52] L. Duvert, C. Murru, A. Al-Kattan, A.-P. Alloncle, F. Magdinier, S. Testa, A. Casanova, *Int. J. Bioprint.* 2025, 7788.
[53] T. Schwarz, *J. Photochem. Photobiol. B* 1998, *44*, 91.
[54] R. Masuma, S. Kashima, M. Kurasaki, T. Okuno, *J. Photochem. Photobiol. B* 2013, *125*, 202.
[55] Y. Deng, P. Renaud, Z. Guo, Z. Huang, Y. Chen, *J. Biol. Eng.* 2017, *11*, 2.
[56] J. Eggers, E. Villermaux, *Rep. Prog. Phys.* 2008, *71*, 036601.
[57] L. Duchemin, *Phys. Fluids* 2002, *14*, 3000.
[58] J. R. Blake, D. C. Gibson, *Annu. Rev. Fluid Mech.* 1987, *19*, 99.
[59] M. S. Brown, C. F. Brasz, Y. Ventikos, C. B. Arnold, *J. Fluid Mech.* 2012, *709*, 341.
[60] M. Duocastella, J. M. Fernández-Pradas, P. Serra, J. L. Morenza, *Appl. Phys. A* 2008, *93*, 453.
[61] M. S. Brown, N. T. Kattamis, C. B. Arnold, *J. Appl. Phys.* 2010, *107*, 083103.
[62] M. S. Brown, N. T. Kattamis, C. B. Arnold, *Microfluid. Nanofluid.* 2011, *11*, 199.
[63] E. Turkoz, L. Deike, C. B. Arnold, *Appl. Phys. A* 2017, *123*, 652.
[64] E. Biver, L. Rapp, A.-P. Alloncle, P. Serra, P. Delaporte, *Opt. Express*

© 2025 The Author(s). Advanced Engineering Materials published by Wiley-VCH GmbH

3.2 Article 2: Laser-induced Forward Transfer in picosecond regime for cell bioprinting

Lucas Duvert[a,b], Clarissa Murru[a], Anne-Patricia Alloncle[a], Frederique Magdinier[b], Stefano Testa[b]*, Adrien Casanova[a]*

a. Aix-Marseille University, CNRS, LP3 UMR 7341, Campus de Luminy, C13288, Marseille, France.

b. Aix-Marseille University, INSERM, MMG, Marseille Medical Genetics, 13385 Marseille, France.

Published International Journal of Bioprinting (2025)

Context

The printing of cells by LIFT comes with several challenges that must be overcome to guarantee their survival. During the process, the targeted material is ejected from the donor substrate to the receiver through the vaporization of the Dynamic Release Layer (DRL), inducing a high-pressure vapor bubble in the bio-ink. This vapor bubble expands and collapses, creating a jet of targeted material that propagates perpendicularly to the initial surface. This jet is propelled at a high speed, and the ejected bio-ink, containing the cells, is deposited on a receiver substrate in the form of little droplets. From this description, the printing process can be decomposed into two parts: (i) the deposition of the laser pulse energy on the donor substrate and the jet's creation; (ii) the deposit of the jet containing the cells on the receiver substrate. These two events are accompanied by a high thermal and mechanical stress that could potentially compromise cell integrity. For this reason, both phenomena were evaluated separately to assess their significance and respective contribution to cell survival.

This work, designed as the logical continuation of the previous article, provides a deeper understanding of the mechanisms that enable LIFT printing of living cells. The

previous work, which focused on reducing mechanical impact thanks to a precise jetting control, showed poor results during preliminary cell survival testing. For this reason, we investigated here the reasons that could explain this outcome, and we focused on the use of polymer coatings as receiver substrates to reduce the previously mentioned mechanical stress.

Results

We first investigated the influence of the laser pulse deposition on the donor substrate, followed by the vaporization of the DRL and the creation and acceleration of the jetting on cell survival. For this first experiment, we considered two laser pulse duration, 10 ps and 4 ns, and a range of laser pulse energy that allows the creation of a jet. We used a specially designed receiver to negate the mechanical impact of cells landing on a hard surface. This experimentation showed survival rates between 89 and 96% for all tested parameters, proving that the laser interaction and the jetting that propels the cells do not negatively affect their survival (**Fig 13.A**).

Then, different receiver hydrogel coatings were tested for their ability to soften the impact of the cells on the receiver substrate. Using picosecond pulses, cells were printed at different energies on thin layers of different gels. Among the tested gelatin, alginate, and Matrigel, the latter allowed for a maximum cell survival while preserving the spatial resolution of the print thanks to its gelation properties (**Fig 13.B-E**). We also noted that the resulting cell survival could drastically vary depending on the laser pulse energy, which changes the jetting properties and the quantity of material transferred. Cells survived and could proliferate if either a coating of polymer was present to soften the landing of the cells and prevent them from drying or if the jet was large enough for the transferred material to act as its own coating. In the latter case, a significant cell death could be observed.

Finally, three-dimensional LIFT printing can be achieved by depositing droplets of cells directly in the bulk of the Matrigel. Depending on the layer height and stiffness of the Matrigel and/or the laser pulse energy used, the position of the droplets could be adjusted not only on the *x*- and *y*-axis but also along a *z*-axis, in the direction of the incident jet.

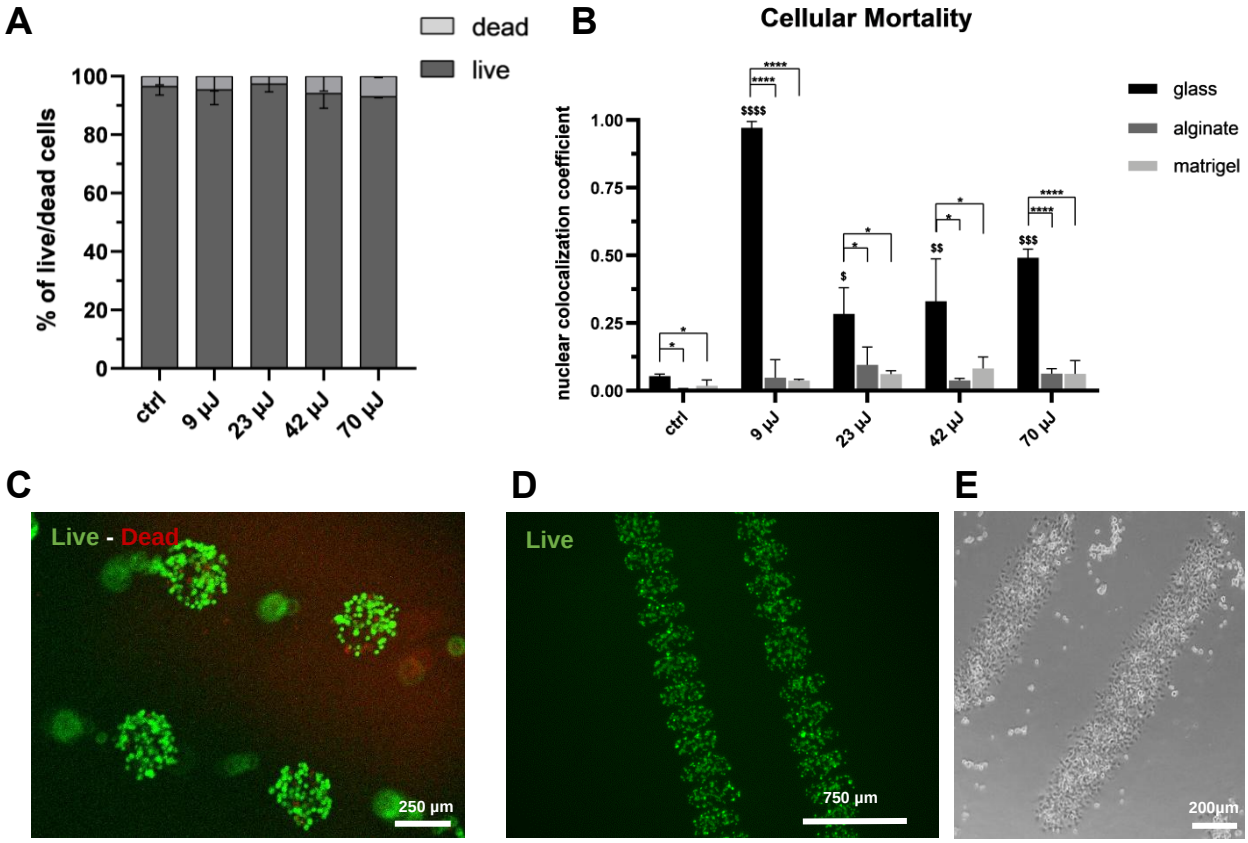

Figure 13: (**A**) Post-printing statistical analysis of cell survival with reduced mechanical impact and picosecond pulse duration. Survival was determined after Trypan Blue staining. The *x*-axis displays the laser pulse energy tested and the *y*-axis, the percentage of viable (dark grey) or dead (light grey) cells. (**B**) Statistical analysis of cell survival after printing on coating layers. Nuclear colocalization coefficient of dead cell nuclei over the total number of cell nuclei for each experimental condition. (**C**) Post printing LIVE (green) -DEAD (red) cell assay on Matrigel coatings showing excellent cell survival in both matrices and lines (**D**) deposition patterns. (**E**) Proliferation of C2C12 cells visible 24h after printing. (p values. $$$$ <0,0001, $ = 0,0238, $$ = 0,0081, $$$ = 0,0003; Ctrl: glass vs alginate. * = 0,0109, glass vs matrigel. * = 0,0368; 8,91 µJ: **** < 0,0001; 22,7 µJ: glass vs alginate. * = 0,0335, glass vs matrigel. * = 0,0167; 42,4 µJ: glass vs alginate. * = 0,0207, glass vs matrigel. * 0,0406; 69,8 µJ: **** < 0,0001)

Conclusions

This study proved that LIFT, specifically our experimental set-up, can ensure an extremely high post-printing cell survival. The deposition of picosecond pulses on the donor substrate and the induced jetting mechanism do not affect the cells. In contrast, mechanical stress during their landing was found to be the main cause of cell mortality. Adding a thin layer of Matrigel on the receiver substrate can nonetheless eliminate this effect. Finally, the ability to print in 3D by LIFT also opens the door for more intricate printing patterns and the creation of complex physiognomic models.

Contribution

In this work, I set up, performed and analyzed the experiments assessing cell survival depending on the receiver coating material.

Publication

ACCSCIENCE PUBLISHING

International Journal of Bioprinting

RESEARCH ARTICLE

Laser-induced forward transfer in picosecond regime for cell bioprinting

Lucas Duvert[1,2], Clarissa Murru[1], Ahmed Al-Kattan[1], Anne-Patricia Alloncle[1], Frederique Magdinier[2], Stefano Testa[2*], and Adrien Casanova[1*]

[1]Laser, Plasmas et Procédés Photoniques (LP3), Aix-Marseille University, Centre National de la Recherche Scientifique (CNRS), Campus de Luminy, Marseille, France

[2]Marseille Medical genetics (MMG), Aix-Marseille University, Institut national de la santé et de la recherche médicale (INSERM), Marseille, France

(This article belongs to the *Special Issue*: *Intelligent 3D Bioprinting Strategies for Future Regenerative Medicine*)

Abstract

Based on interdisciplinary approaches, bioprinting methods aim to create and design highly organized 2D and 3D cultures. In this context, it has been more than a decade since laser-induced forward transfer (LIFT) was studied on a lab scale for its ability to transfer biomaterials, specifically bioink loaded with living cells, onto a substrate. Extreme physical and mechanical phenomena contribute to the jetting dynamic of the targeted bioink, raising a spontaneous biological question: does this process negatively affect the survival rate of transferred cells? This study demonstrates that laser pulse durations in the range of picoseconds to nanoseconds do not directly affect cell viability, indicating that LIFT is a valuable bioprinting method for transferring living cells. Moreover, we highlight the necessity of using hydrogel coatings on the surface of the receiver substrate to guarantee optimal post-printing viability of the cells. We demonstrate that the nature of the hydrogel also contributes to the resolution of the printed pattern. Among the tested materials, Matrigel demonstrated all the qualities required to ensure successful printing and should therefore be considered for future work. Overall, the results show the suitability of our LIFT setup for printing living cells in the picosecond regime with a high survival rate, paving the way for a wide range of biological applications.

Keywords: Cell viability; Laser-assisted bioprinting; LIFT bioprinting; Living cells printing; Regenerative medicine;Skeletal muscle; Tissue engineering

***Corresponding authors:**
Stefano Testa
(stefano.TESTA@univ-amu.fr)
Adrien Casanova
(adrien.casanova@univ-amu.fr)

Citation: Duvert L, Murru C, Al-Kattan A, *et al.* Laser-induced forward transfer in picosecond regime for cell bioprinting. *Int J Bioprint*. doi: 10.36922/ijb.7788

Received: December 17, 2024
1st revised: January 14, 2025
2nd revised: January 23, 2025
Accepted: January 24, 2025
Published Online: January 24, 2025

Copyright: © 2025 Author(s). This is an Open Access article distributed under the terms of the Creative Commons Attribution License, permitting distribution, and reproduction in any medium, provided the original work is properly cited.

Publisher's Note: AccScience Publishing remains neutral with regard to jurisdictional claims in published maps and institutional affiliations.

1. Introduction

Bioprinting techniques began to develop in the 2000s and have since proven to be an ideal tool for tissue engineering,[1–6] representing a novel strategy to create complex biological constructs inspired by organs and tissues. Thanks to a multidisciplinary approach, bioprinting allows the accurate arrangement of cells in space, providing a well-structured 3D environment fundamental for cell survival, organization, and differentiation. Nowadays, 3D bioprinting can be divided into extrusion, inkjet, and laser-based bioprinting. In extrusion-based techniques, the bioink (the mixture of cells and biomaterials[7]) is deposited as a continuous filament by mechanical, pneumatic, or solenoid-based dispensing systems. On the other hand, inkjet systems make use of

thermal, acoustic, or electrical stimulation to deposit small droplets of bioink. The laser-based bioprinting techniques exploit the laser-matter interaction to create organized biological systems.[8] Among them, laser-induced forward transfer (LIFT), a printing technique first developed for electronic purposes,[9–13] was recently applied for transferring biomolecules[14–16] or even living cells.[17–26] This technique uses a short laser pulse to transfer tiny amounts of material from a thin donor film to a receptor substrate. Under appropriate conditions, the laser pulse induces the formation of a highly directive jet that propagates perpendicularly to the donor substrate. The bioink, previously spread as a thin film (a few tens of microns thick) on the donor substrate, is subsequently deposited as droplets onto the collector slide.

The donor substrate is composed of a thin glass slide with the potential addition of a metallic dynamic release layer (DRL), which the laser pulse will vaporize to induce the creation of the jetting.[27–29] The DRL is employed when the ink is susceptible to damage from direct laser interaction, such as bioinks containing living cells or biological material, or when the ink is transparent to the wavelength of the laser; adding a thin metal layer allows controlled deposition of laser energy and promotes laser–matter interaction. The cells in direct proximity to the vapor bubble created by the vaporization of the DRL will be inevitably sacrificed due to the sudden elevation of temperature and immediate mechanical stress.[17,30] Nevertheless, as previously simulated,[31] the use of an ultrashort pulse laser (with a duration of nanoseconds or less) in combination with a DRL makes any further thermal transfer to the bulk of the ink negligible, thus preventing cells from potential thermal damages. Considering these observations and the high-cell concentration within the targeted bioinks, the thermal effect and vaporization of the DRL are not critical parameters influencing post-printing cell survival. In this context, we extended the range of studied laser pulse duration typically found in the literature (nanosecond regime)[32] to investigate the impact on "pre-transfer" cell survival over several orders of magnitude of pulse width, from nanoseconds to picoseconds, using the same optical setup and experimental protocols.

Despite these observations, it is essential to note that pulse duration is not only associated with thermal diffusion properties but also with jet ejection speed and shockwave formation.[33] The creation of the jet induced by the interaction of the short laser pulse with the DRL also causes high mechanical stress on the cells contained in the bioink. The jet acceleration reaches several meters per second in a few microseconds[28,34] after the laser pulse interaction, which can potentially damage cell membranes and reduce the overall cell survival rate. Adding to this initial shear stress, the propagation of the jet and its landing on the receiver substrate further increases the eventual damage to the cells. The necessity of a polymer layer to mitigate the impact on cells remains a topic of debate, with some studies supporting its use,[35–38] while others suggest it may not be required.[2,39] Moreover, the nature and thickness of the receiver coating are also subject to variation and can lead to a wide range of observable cell survival rates.

This work aims to identify the key factors affecting cell survival during LIFT bioprinting. As mentioned before, the printing process can be divided into two distinct steps: ejection of the targeted material from the donor slide and landing of the created jet on the receiver substrate. Both events are accompanied by high mechanical stress that might heavily affect cell survival rates. Most studies in the literature are focused on the first step, investigating the effects of different laser wavelengths (UV or visible),[40] different bioink formulations,[41] and energy levels on the jet formation and propagation, often reporting high cellular viability values.[25]

In this study, we separately evaluated the respective contribution and significance of the ejection and landing processes to define optimized and successful cell transfer. We first studied the impact of picosecond and nanosecond laser pulses at different energy levels on the direct survival of the cells. The landing's mechanical strain was evaluated by studying the effects, benefits, and challenges of adding or omitting a thin protective layer to the receiver substrate. These results are finally used to print living cells with an extremely high survival rate, a high spatial resolution, and good reproducibility.

2. Material and methods

2.1. Cell culture and bioink preparation

Murine myoblasts C2C12 (ATCC, USA) were cultured following previously published protocols[42] in T-75 Flasks (Sarstedt, Germany) at 37 °C with 5% CO_2 in DMEM GlutaMAX (Gibco, USA) supplemented with 10% heat-inactivated fetal bovine serum (FBS, EuroClone, Italy), penicillin (100 IU/mL, Gibco, USA), and streptomycin (100 mg/mL, Gibco, USA).

For bioink formulation, cells were harvested using a trypsin/EDTA 1× solution (Gibco, USA) and centrifuged in phosphate-buffered saline (PBS, Gibco, USA) at 115 × *g* for 10 min. PBS was carefully removed and replaced by an adequate volume of a 2% gelatin (Sigma-Aldrich, Germany) solution in DMEM (final concentration 5×10^7 cells/mL).

2.2. LIFT printing setup

The bioink (5 µL) was spread on a titanium wafer (LAAS France) used as a donor substrate. This titanium layer acted as DRL and was chosen for its biologically inert behavior.[43] Several layers of polyimide tape were applied onto the titanium coating before being laser-cut to create individual wells on the substrate. The well was about 50 mm² for 80 µm of height (Figure 1B). The bioink was spread homogeneously in the confined area to guarantee a uniform layer of 80 µm. This method was inspired by Rapp et al.[13]

A motorized stage (*X*, *Y*, *Z*) controlled by a Newport Motion controller (Newport Corporation, USA) allows the translation of the donor substrate along the vertical direction (*Z*) of the incident laser beam and the perpendicular directions (*X* and *Y*). The receiver substrate is also motorized along the *X* and *Y* axes, allowing precise and independent positioning of the samples. After the deposition of the bioink, the donor substrate is positioned with the ink facing downward (Figure 1A) and secured using a suction system. It is then lowered toward the receiver, with the gap between the two substrates precisely controlled using a camera.

The following two laser sources were used for these experiments: (i) a Light Conversion Carbide CB-1 Yb: KGW laser (Light Conversion, Lithuania) with a fundamental wavelength of 1030 nm (IR), a repetition rate of 60–1000 kHz, and a pulse duration of 10 ps; (ii) a Quantel Brio Nd: YAG laser (Lumibird, France) with a wavelength of 1064 nm (IR), a repetition rate of 20 Hz, and a pulse duration of 4 ns. Both lasers were set up on the same optical path with a removable mirror, allowing the switch between the two sources. A polarizer and a half-wave plate were positioned to reduce and tune the energy of the laser

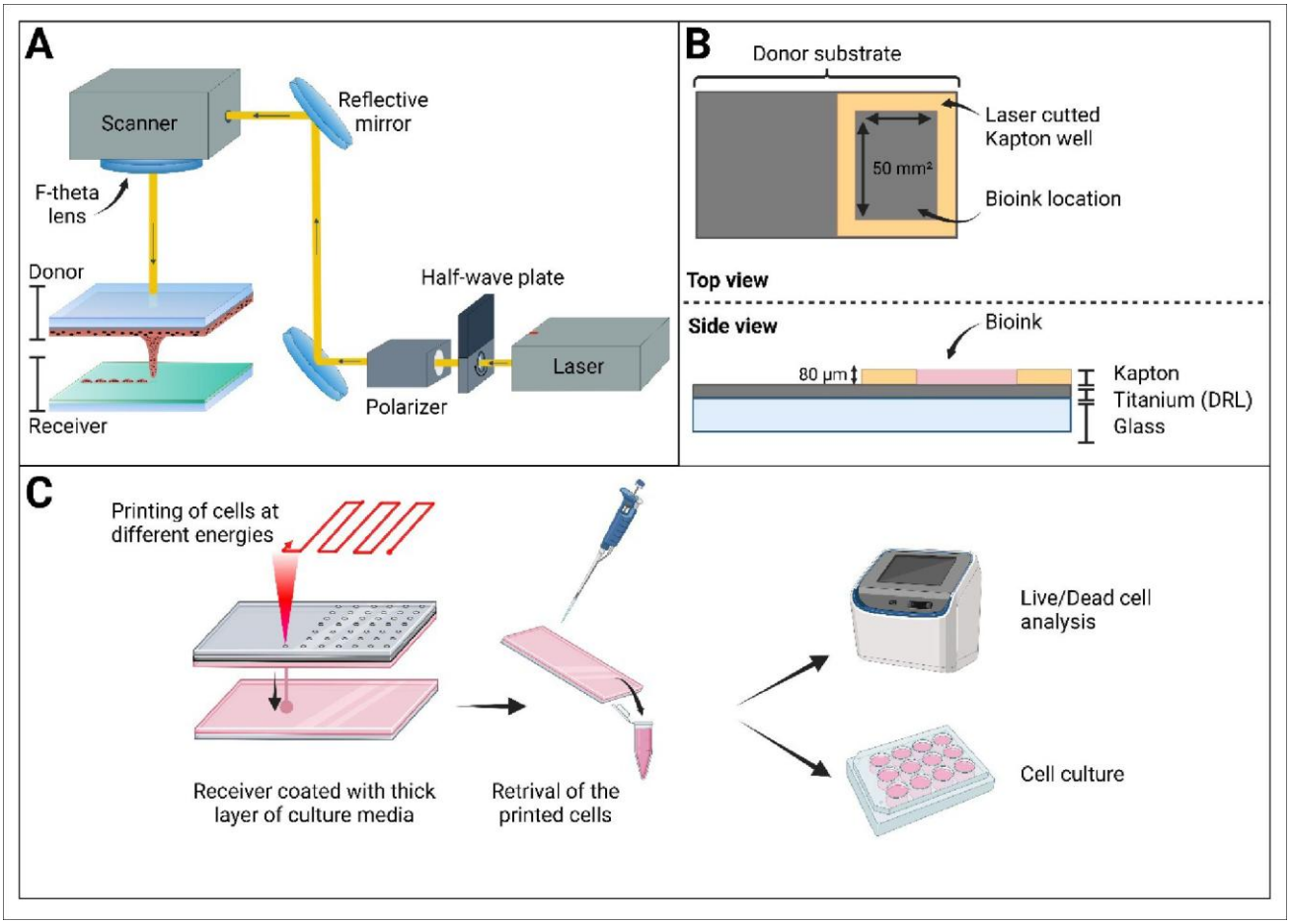

Figure 1. Scheme of the LIFT bioprinting process. (A) LIFT optical setup for cell-printing. (B) Schematic of titanium donor substrate preparation with individual wells. The bioink containing the cells is deposited inside the well, allowing the control of the layer thickness. (C) Experimental protocol for isolating laser-induced damages and evaluating post-transfer cell survival rates. Abbreviations: DRL, dynamic release layer; LIFT, laser-induced forward transfer. Created in BioRender. Magdinier, F. (2025) https://BioRender.com/a90p035

pulses. An optical scan system (intelliSCAN 14, Scanlab, Germany) coupled with a 70 mm f-theta lens allowed us to direct and control the tuned laser beams on an area of 25 cm^2 to scan the entire donor substrate. The scanning system is motorized in the *Z*-axis direction allowing us to account for the donor–receiver gap, while maintaining accurate focus on the donor substrate.

Pulse energies for each laser were calibrated using an energy meter, with four increasing energy values (9–23–42–70 µJ) tested for both laser sources. The spot size and determination of the average fluence per pulse were based on the ablation size of the titanium layer on the donor substrate after the printing. The target surface was illuminated from above (through the glass of the wafer) with a 450-point matrix of single pulses. The large number of points allowed us to transfer enough bioink (and consequently cells) for statistical relevance. The illuminated areas were separated by 0.25 mm, guaranteeing the independence of the jetting mechanism and an intact titanium layer for each shot.

2.3. Cell survival: impact of laser pulses

In order to measure only the specific effect of the laser on cell survival, we used a homemade receiver substrate designed to isolate this factor. This substrate consisted of a 3D-printed well made of polylactic acid (PLA, Bambu Lab, China), with a height of 4 mm, attached to a 0.17-mm-thick glass slide, and filled with DMEM. The gap between the surface of the well and the donor slide was adjusted depending on the experiment, between 0.2 and 2 mm, and monitored through a Charge coupled device (CCD) camera. The important thickness of the culture medium (4 mm) was intended to minimize the mechanical impact with the receiver glass slide during cell deposition, allowing us to isolate and evaluate the sole effect of laser pulses on cell viability. After the transfer, particular attention was given to the presence of cells attached to the glass slide, indicating that the jetting reached the hard surface. In such cases, the gap was adjusted, and the experiment was repeated.

Immediately after printing, the well content (printed cells and medium) was retrieved and stained with 0.5% trypan blue before manual counting to determine cell viability (Figure 1C). Experiments were done in triplicates for each tested energy and both pulse durations (Carbide 10ps and Brio 4ns).

2.4. Cell survival: impact of the landing

A second set of experiments aimed at determining the effects of the jet's landing on cell survival. A glass slide with a gap of 0.5 mm was first used as a receiver, and the same matrix previously described was used as a printing pattern. The same process was repeated with thin layers of Matrigel (Corning, USA) or 1.5% w/w sodium alginate (ThermoFisher Scientific, USA) in PBS as coatings on the receiver substrate before the printing (50 µL for 19 mm diameter glass slide). The gap between the donor and the surface of the coating was maintained at 0.5 mm.

For all conditions, glass slides were placed immediately after printing in a sterile culture dish, and 150 µL of LIVE-DEAD assay (ThermoFisher) supplemented with Hoechst solution (ThermoFisher) was added. This assay allows the simultaneous display of total cells (nuclear blue signal, Hoechst), live cells (green cytoplasmatic signal, calcein-AM), and dead cells (red nuclear signal, iodure BOBO-3). After 30 min of incubation at 37 °C, samples were observed by fluorescence microscopy (Evos M5000, Invitrogen, ThermoFisher, America), followed by culture medium addition and storage of the samples in an incubator for long-term analysis.

2.5. Colocalization analysis

To quantify the effect of the cell impact with the receiver substrate on cell survival, in the presence or absence of a coating layer, live/dead images were analyzed using the Fiji software[44] (https://fiji.sc;10.1038/nmeth.2019), using the "Colocalization Threshold" plugin. The "thresholded Mander's split colocalization coefficients" were considered to quantify the ratio of dead cells (iodure BOBO-3, nuclei of dead cells) to the total cells (Hoechst signal, total nuclei), a coefficient ranging from zero (no colocalization) to one (perfect colocalization). The result can be considered as an index of cell mortality where "one" represents 100% of dead cells and "zero" 100% of live cells.

2.6. Statistical analysis

All experiments were performed in biological triplicates. Data were analyzed using GraphPad Prism 8, and values were expressed as means ± standard error. Statistical significance was tested using a one-way ANOVA test with the appropriate multiple comparison tests. A probability of less than 5% ($p < 0.05$) was considered as statistically significant.

3. Results

3.1. Impact of laser energy on cell survival

To study the effect of the direct laser impact on cell viability, four increasing energy values (9–23–42–70 µJ) were chosen for both tested lasers (with picosecond or nanosecond pulse durations). The energy range was chosen to widely cover usable energy for LIFT bioprinting and for the creation of the jetting mechanism. The experiment was first performed with a 10 ps pulse duration. To guarantee a sufficient number of transferred cells (minimum 1000 cells per replicate) and given the reduced size of the jets at

low energy, the distance between the donor and the top of the receiver well was adjusted to its minimum of 0.2 mm. For this experimental set, trypan blue staining showed 93–95% cell survival for all energy values considered, and no statistically significant differences were found compared to the control (survival rate of 96%) (Figure 2A).

Next, the optical setup was adjusted as previously described to accommodate nanosecond pulses. A longer pulse duration of 4 ns drastically changes the printing mechanism with a wider and more explosive jetting dynamic. For this reason, the gap was adjusted to 2 mm to avoid direct contact between the donor and the receiver as well as avoiding cell redeposition on the donor substrate. The staining showed a cell survival rate of about 90% with statistically significant differences compared to the control (Figure 2A). For this experimental set, we observed a decrease in the cell survival rate that correlates with the increase in laser pulse energy. Even if statistically significant, this impact is limited, with a survival rate of about 89% for the highest energy considered, compared to 96% for the control.

The measurement of the associated fluences (energy per laser spot area) showed that the spatial repartition of the energy on the donor slide further influences cell survival (Figure 2B). The significant reduction in cell viability observed for the energies above 23 µJ, in the case of nanosecond pulses, can be explained by the important increase in laser fluence. At the maximum laser energy considered (70 µJ), the laser fluence is almost three times more important for the nanosecond pulses (Figure 2B). This point corresponds to the lowest observed cell viability of 89%.

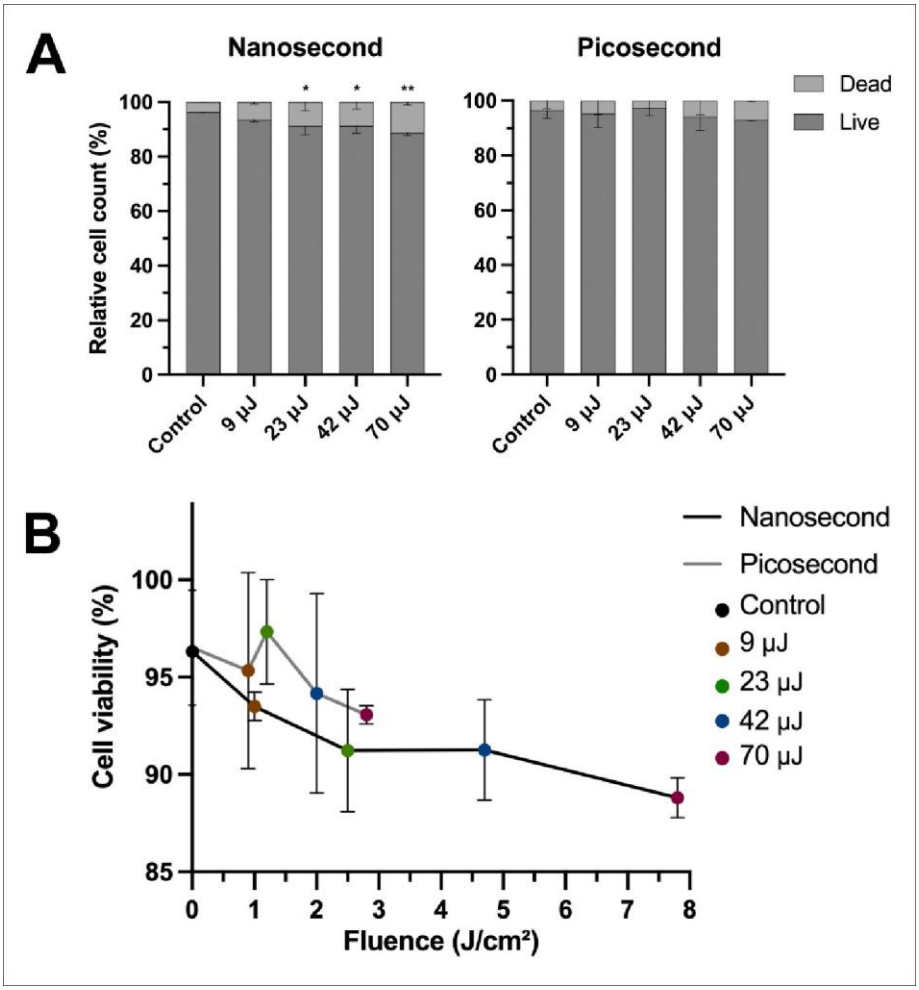

Figure 2. Impact of laser on cell survival. (A) Post-printing statistical analysis of cell survival determined after Trypan Blue staining. For each pulse duration considered, the *X*-axis displays the laser pulse energy tested and the *Y*-axis, the percentage of viable (dark grey) or dead (light grey) cells. **(B)** The previously described cell survival rates (*Y*-axis) are displayed in terms of energy per surface area on the *X*-axis (fluence).

3.2. Impact of the landing on cell survival

Given the previously described results, only the 10 ps pulse duration was chosen for the subsequent experiments, which focused on evaluating the impact of the receiving surface during cell landing on survival (Figure 3). The same range of energies was used. Printing on a dry receiver (glass substrate) showed an extremely poor survival rate (3%) at the lowest energy considered. Nevertheless, the survival rate increased drastically for 23 µJ (around 71%) before decreasing back to 51% for 70 µJ (Figure 3B). Interestingly, the presence of a coating layer on the receiver for both alginate and Matrigel attenuated the negative impact on cell viability with a high rate of cell survival for each energy tested and no statistically significant difference compared to the control (Figure 3B).

For all the conditions tested, the fluorescent markers (Live/Dead and Hoechst) were added directly after printing to prevent drying of the cell suspension that might negatively impact the viability (especially without coating), and the samples were incubated for 30 min. The

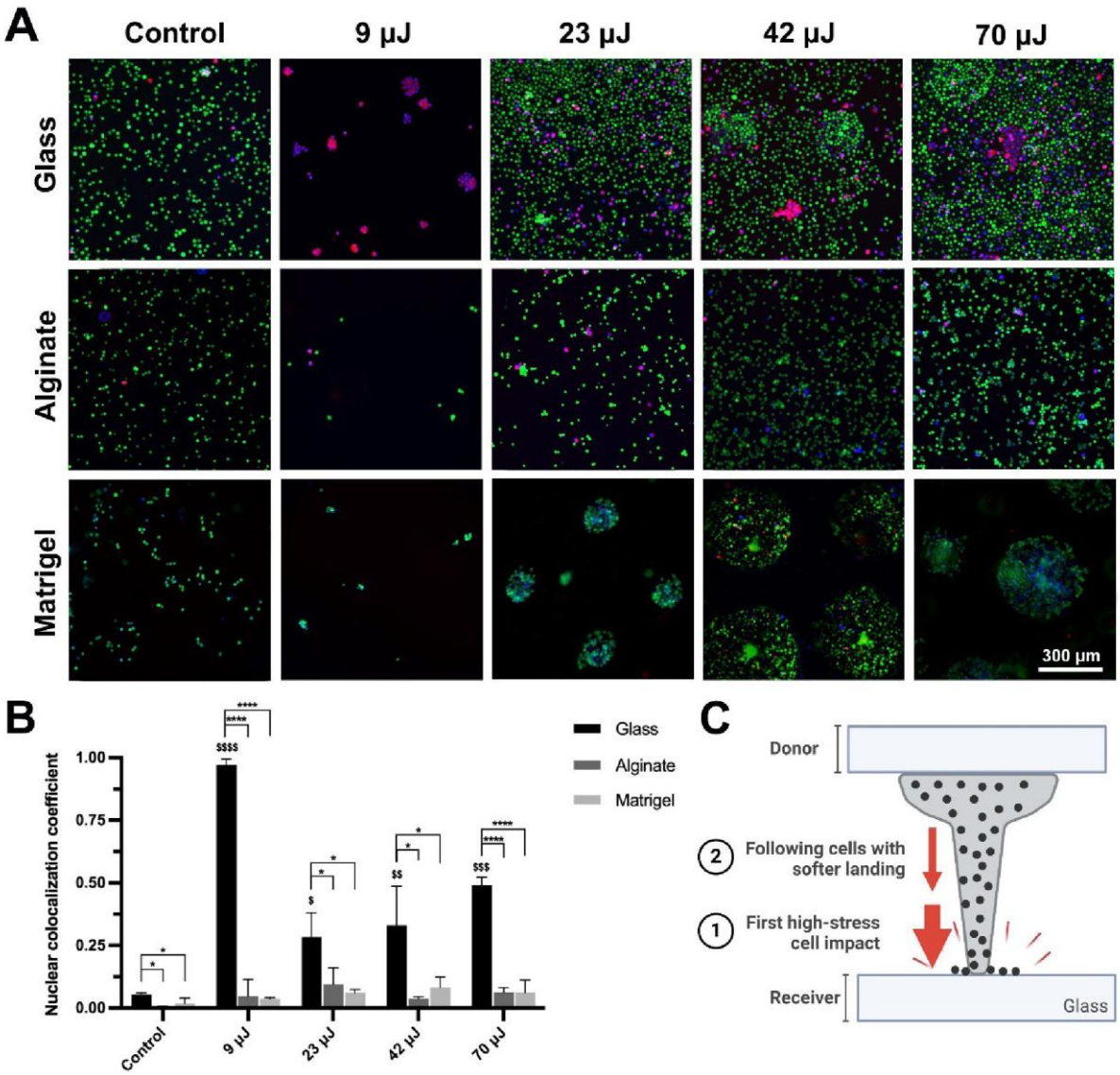

Figure 3. Cell survival in the presence of coating. (A) Representative immunofluorescence images of live/dead cell staining for each experimental condition (live cells in green, dead cells in red, nuclei in blue). **(B)** The graph shows the nuclear colocalization coefficient of dead cell nuclei over the total number of cell nuclei for each experimental condition. Created in BioRender. Magdinier, F. (2025) https://BioRender.com/l57q296. **(C)** Schematic representation of the effect of impact on the receiver surface during cell landing.

immediate addition of a solution (fluorescent markers or culture medium) onto the receiving substrate caused a loss of printing resolution on uncoated or alginate-coated samples (Figure 3A) as the cells did not have sufficient time to adhere to the substrate. Furthermore, alginate is soluble in aqueous solutions, and attempts to add a calcium chloride solution immediately after printing to promote its crosslinking resulted in the formation of a floating hydrogel layer, as it could not adhere to the glass. In this context, Matrigel showed better adhesion to the glass substrate, and its fast gelation preserved the printing resolution even before the adhesion of the cells to the substrate (Figure 3A).

3.3. LIFT bioprinting resolution

Once conditions for optimal cell survival were successfully set up and characterized, picosecond pulses, and a Matrigel-coated receiver (50 µL on a 19-mm-diameter glass slide) were chosen to design the precise deposition of C2C12 cells in matrix (Figure 4A**,** top) and line patterns (Figure 4A**,** bottom). The laser energy used was tuned around the previously determined value of 23 µJ. Indeed, the amount of energy per pulse required for the creation of reproducible and stable jets is extremely sensitive to cell concentration, which modifies the rheological properties of the bioink, as well as to minor variations in the ink composition. To ensure well-defined and highly concentrated cell deposition, empirical testing must be performed beforehand for each experimental session to slightly adjust the energy value. Cell survival just after printing was characterized by Live/Dead cell staining to confirm the safety of this printing system (Figure 4B). Cell adhesion and elongation were noticeable 24 h after printing (Figure 4C).

A thicker layer of Matrigel on the receiver substrates (70 µL for 19-mm-diameter glass slide) directly affected the proliferation of the printed cells. The cells deposited in a matrix pattern showed very different morphological arrangements, with clear signs of adhesion 1 day after printing for some of the matrix spots (Figure 5A**,** left, red circle) and a spheroidal organization for others (Figure 5A**,** left, blue circles). Live/Dead assay showed a very high survival rate for both configurations (adherent and spheroidal spots). Three days after printing, the printed cells that aggregated in spheroids reached the glass surface. Cell elongation was visible at the periphery of some spheroids with varying rates depending on the area considered (Figure 5A**,** right).

Interestingly, we could observe that some spheroids moved and merged due to the remodeling of the surface coating combined with cell migration. On the other hand, cells that reached the glass surface during the transfer

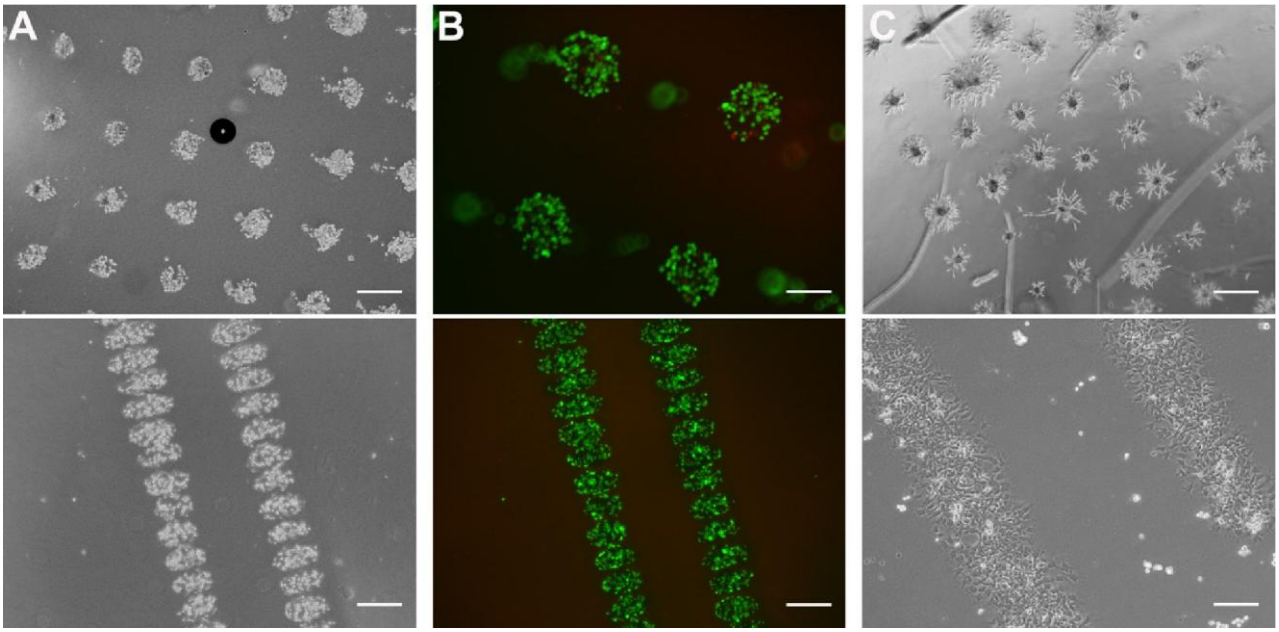

Figure 4. High resolution printing of living cells by LIFT bioprinting. **(A)** C2C12 cells printed by LIFT on a Matrigel coating in matrix patterns (top, scale bar = 200 ^m) and line patterns (bottom, scale bar = 200 ^m). **(B)** Post-printing Live (green)/Dead (red) cell assay showing excellent cell survival in both matrix (top, scale bar = 250 ^m) and line (bottom, scale bar = 200 ^m) deposition patterns. **(C)** C2C12 cells observed 24 h after the printing in matrices (top, scale bar = 200 µm) and lines (bottom, scale bar = 250 µm), showing elongated adherent cells. Abbreviation: LIFT, laser-induced forward transfer.

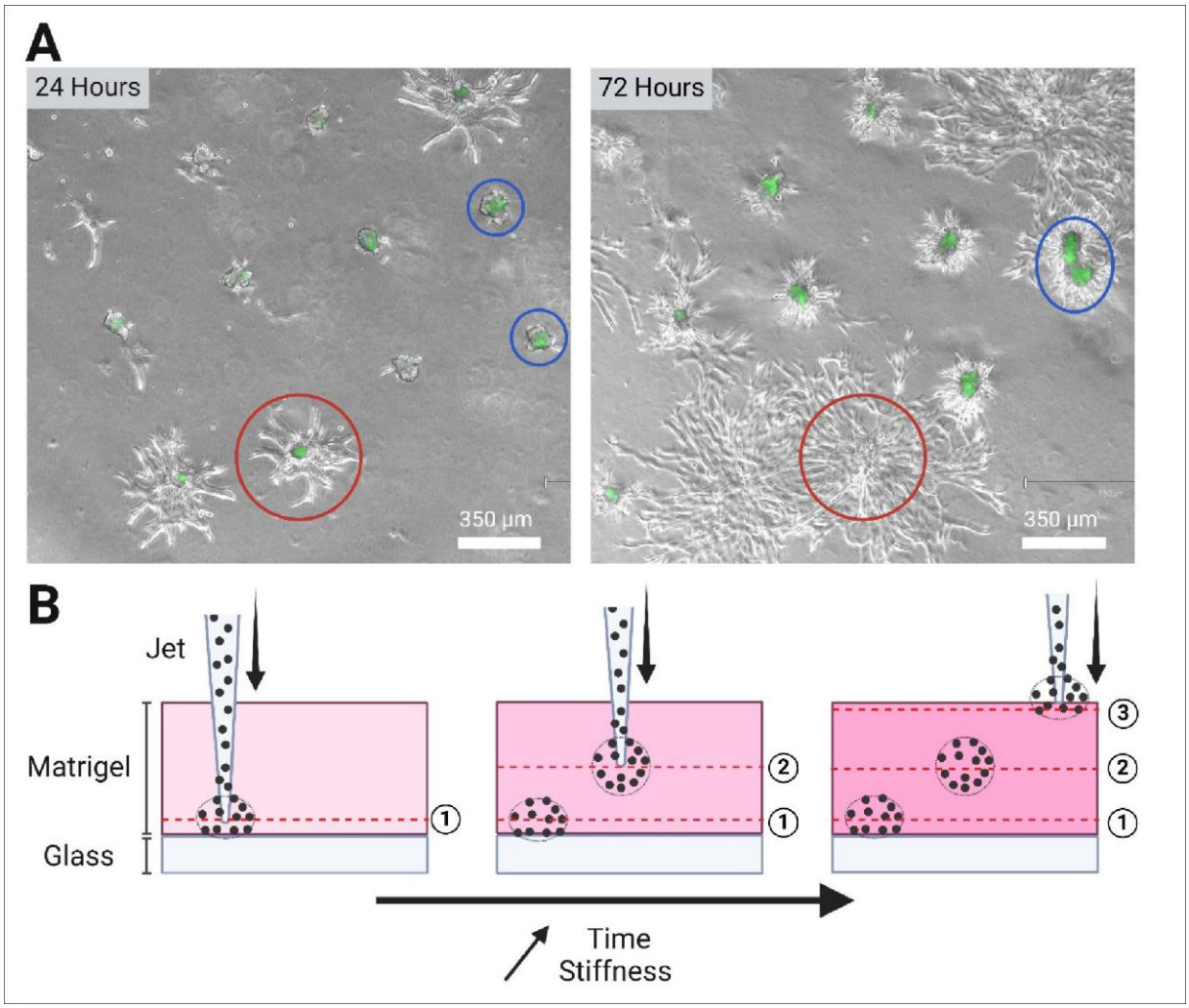

Figure 5. Variability in cell deposition during LIFT bioprinting. **(A)** C2C12 cells deposited by LIFT on Matrigel coatings 24 and 72 h after printing. Cells deposited close to the glass surface, leading to their fast adhesion and expansion, are circled in red. Spheroids and their apparent motility are highlighted in blue circles. Live cells still rounded are stained in green. Created in BioRender. Magdinier, F. (2025) https://BioRender.com/n99y226. **(B)** Schematic representation of cell deposition in three dimensions directly within the bulk of Matrigel by LIFT. The stiffening of Matrigel over time leads to jets depositing cells closer to the surface of the gel. The same effect could be obtained with a stable gel stiffness and a precisely controlled jet length. Abbreviation: LIFT, laser-induced forward transfer.

exhibited cell adhesion and elongation precisely at their printing location (Figure 5A**,** right).

The distribution of the two configurations did not follow any explicit pattern on the receiver substrate, being randomly located on the coating of the receiver surface. We concluded that these differences in cell behavior were thus directly linked to the variability of the jetting mechanism, the local properties of the Matrigel, and its progressive stiffening over time. Longer jets directed the cells to the bottom of the coating layer, allowing them to adhere to the substrate, while shorter jets left the cells suspended in the middle of the Matrigel layer, generating spheroids (Figure 5B). In both cases, the quantity of gel allowed the gentle deposition of cells onto the receiver substrate, ensuring their survival.

4. Discussion

Currently, the majority of studies investigating LIFT suitability for bioprinting living cells focus on the study and characterization of parameters that could affect cell viability during the initial phase of the process,[41,45,46] with fewer studies addressing the implication of the landing phase.[37,47] Based on our results, the latter constitutes a critical parameter that should be taken into account when defining an experimental LIFT bioprinting setup, in order to replicate results published in the field. For this reason,

we decided to study LIFT bioprinting as a whole, focusing on both the ejection and landing phases, to establish experimentally validated procedures that ensure high cell viability.

To deeply investigate the effect of LIFT on living cells, we conducted a systematic study to characterize the specific implication of the two main phenomena occurring during the printing process, the interaction of the laser with living matter (ejection phase) and the subsequent mechanical transfer of cells from a donor to a receiver substrate (landing phase). In this regard, a bioink composed of gelatin was used to facilitate the transfer of cells,[48,49] while guaranteeing good compatibility with muscle cell culture.[50] The mechanical effect of the laser pulse on cells was first evaluated through bioprinting on a liquid container. Using a receiver specially designed to protect cells from potential landing damage, a high survival rate (about 90%) was observed across all tested energy conditions, and both laser pulse durations (10 ps and 4 ns). It is important to highlight that some of the energy values considered in this study are significantly higher than those typically reported in the literature for bioprinting applications,[35,51,52] further emphasizing the safety of the LIFT printing strategy. The only significant decrease in survival rate was noted for the highest energy considered with nanosecond pulses. This decrease can be directly linked to the significant increase in laser fluence associated with nanosecond pulses, combined with the characteristics of the jetting mechanism in the nanoseconds regime.[41]

Vogel et al. investigated the shockwave generation from pulsed lasers focused on water (an infinite medium) for 30 ps and 6 ns pulse durations.[33] Beyond a certain threshold, medium breakdown occurs, causing the laser pulse energy to be deposited in the medium, which creates a gas bubble (plasma) initially at high pressure and temperature, accompanied by a shockwave. This process can be compared to the mechanisms induced during the LIFT process. Vogel et al. demonstrated that, for equivalent laser pulse energy, longer pulse durations yielded significantly higher shockwave amplitude, higher initial bubble pressure, faster initial bubble wall velocities, and greater associated mechanical energy generation. This higher mechanical energy generation in the nanosecond regime is consistent with the lower cell survival rate observed in our study for energies higher than 23 µJ. Guven similar energy per pulse, nanosecond transfer is thus significantly more violent than its picosecond counterpart. Under those conditions, the mechanical impact of the cells on the liquid interface must be considered. The acceleration of the cells in the jet induced by the expansion of the vapor bubble is also a potential cause of cell death. Therefore, the impact of the cells on the liquid receiver, along with the high ejection speed and associated shear stress, could explain the higher cell death rate observed.

Secondly, the landing of the cells on the receiver substrates was studied and evaluated, with and without a coating layer. The unusual survival trend observed when printing directly on glass could be explained by the explosive nature of the jetting dynamic at high energies. As mentioned in this work, higher pulse energy leads to a wider and more explosive jetting regime; more material is thus transferred from the donor to the receiver substrate in a more extended period. Similarly, to the cells printed at low energy, the first cells to land on the glass substrate will perish due to the mechanical impact. This early deposition of soft matter, however, creates a layer on the receiver that serves as a coating for the remaining cells contained in the jet (Figure 3C). Based on these observations and in the absence of a coating on the receiver substrate, an optimum energy of 23 µJ can be identified, where the mechanical strain created by the jet impact is balanced by the quantity of material transferred and the number of cells contained in the bioink, leading to a cell survival rate of about 71%. This hypothesis and explanation are in line with observations made in experiments conducted in the presence of a coating layer. Indeed, the presence of a coating applied to the substrate before the printing eliminates the previously mentioned mechanical forces and allows a smooth transfer of the cells onto the receiver substrate for all energy values considered. Therefore, a coating is essential for the printing process, allowing a high post-printing cell survival rate (with viability rates comparable to those of the control when using both alginate and Matrigel coatings, Figure 3B), while also preventing the drying out of the printed cells. The coating also plays a key role in maintaining the resolution of the printed droplets without waiting for them to adhere to the substrate, thus significantly speeding up the printing process and improving the overall versatility of the LIFT process. Once again, given the results presented, a 23 µJ pulse seemed to present the best compromise between the number of cells printed, droplet resolution on Matrigel, and cell survival with a 10 ps pulse.

Finally, the results and observations depicted in Figure 5 suggest the possibility of directly depositing cells in 3D within the bulk of the Matrigel. As shown in Figure 5B, the typical progressive stiffening of the Matrigel at room temperature can give rise to a gradual deposition of cells along the *Z* direction. Extending this concept, by adjusting and maintaining the stiffness of the receiver's polymer layer, controlling the viscosity of the bioink, and fine-tuning the energy deposited on the donor substrate, cells could be precisely deposited not only along the *X* and *Y* axes but also

along the *Z*-axis within the gel layer. This property could enable the creation of organized 3D structures quickly and efficiently within the gel's bulk, potentially replicating tissues and organ architectures through LIFT bioprinting. However, the motility of cells in suspension, as observed in Figure 5A, remains an issue that must be addressed to preserve LIFT's spatial resolution and its ability to deposit cells at precise locations over time.

5. Conclusion

In this study, we demonstrate the conditions under which the LIFT printing process can ensure highly satisfying cell survival rates. The effect of the laser pulse deposition on cell viability was evaluated and we showed that the energy required to induce jetting does not jeopardize cell survival. This conclusion is supported by results across a wide range of laser pulse energies and durations. Mechanical strain and stress are, however, the primary cause of cell death during the bioprinting process. The presence of a coating on the receiver substrate is an ideal solution to achieve high survival rates with LIFT. Ideally, this coating should be carefully chosen to maintain the resolution of the printed droplets. Cross-linkable and polymerizable hydrogels are thus preferred to maximize the potential of this technology.

Nevertheless, we demonstrated that this coating is not necessarily required, and in a worst-case scenario, moderate cell survival (~71%) can be reached with an adapted laser pulse energy and controlled jetting dynamic. These results further emphasize the versatility of the LIFT process and its ability to arrange cells across a wide range of substrates, maintaining a moderate to extremely high survival rate. In this work, both the ejection and the landing phases of the bioink transfer are independently studied, highlighting the key factors affecting cell survival and providing deeper insights into the LIFT of living cells. The data reported in this study are valuable for establishing frameworks and protocols tailored to specific experimental needs, while contributing to the growing knowledge in this emerging field.

Acknowledgments

Not applicable.

Funding

The work was funded by the French National Research Agency (ANR Medilibs and Diagem projects) together with the French Defense Innovation Agency (ANR—DGA/AID—ICELARE Project ID: ANR—20—ASTR—0004). The PhD thesis of Lucas Duvert was co-funded by Aix-Marseille University, the French Defense Innovation Agency and the MarMaRa funding scheme. This work received support from the French government under the France 2030 investment plan, as part of the Initiative d'Excellence d'Aix-Marseille Université – A*MIDEX "AMX-23-CPJ-05". The project leading to this publication has received funding from the Excellence Initiative of Aix-Marseille University-A*Midex, a French "investissement d'avenir programme" AMX-19-IET-007, through the MarMaRa funding scheme. This work was conducted using LaMP facilities at LP3. The authors also acknowledge the "Region SUD" for their financial support.

Conflict of interest

The authors declare that they have no competing interests.

Author contributions

Conceptualization: Anne-Patricia Alloncle, Frederique Magdinier, Adrien Casanova, Stefano Testa

Formal analysis: Lucas Duvert, Stefano Testa

Investigation: Lucas Duvert, Stefano Testa, Adrien Casanova, Anne-Patricia Alloncle

Methodology: Lucas Duvert, Stefano Testa, Ahmed Al-Kattan, Anne-Patricia Alloncle, Frederique Magdinier, Adrien Casanova

Writing – original draft: Lucas Duvert, Stefano Testa

Writing – review & editing: Lucas Duvert, Clarissa Murru, Ahmed Al-Kattan, Anne-Patricia Alloncle, Frederique Magdinier, Stefano Testa, Adrien Casanova

Ethics approval and consent to participate

Not applicable.

Consent for publication

Not applicable.

Availability of data

Data are available from the corresponding author upon reasonable request.

References

1. Tarassoli SP, Jessop ZM, Al-Sabah A, et al. Skin tissue engineering using 3D bioprinting: an evolving research field. *J Plast Reconstr Aesthet Surg*. 2018;71(5):615-623. doi: 10.1016/j.bjps.2017.12.006
2. Guillemot F, Souquet A, Catros S, et al. High-throughput laser printing of cells and biomaterials for tissue engineering. *Acta Biomater*. 2010;6(7):2494-2500. doi: 10.1016/j.actbio.2009.09.029
3. Zhu W, Ma X, Gou M, Mei D, Zhang K, Chen S. 3D printing of functional biomaterials for tissue engineering. *Curr Opin Biotechnol*. 2016;40:103-112. doi: 10.1016/j.copbio.2016.03.014

4. Kačarević Ž, Rider P, Alkildani S, et al. An introduction to 3D bioprinting: possibilities, challenges and future aspects. *Materials*. 2018;11(11):2199.
doi: 10.3390/ma11112199

5. Li J, Chen M, Fan X, Zhou H. Recent advances in bioprinting
techniques: approaches, applications and future prospects. *J Transl Med*. 2016;14(1):271.
doi: 10.1186/s12967-016-1028-0

6. Vinson BT, Sklare SC, Chrisey DB. Laser-based cell printing
techniques for additive biomanufacturing. *Curr Opin Biomed Eng*. 2017;2:14-21.
doi: 10.1016/j.cobme.2017.05.005

7. Raees S, Ullah F, Javed F, et al. Classification, processing, and
applications of bioink and 3D bioprinting: a detailed review. *Int J Biol Macromol*. 2023;232:123476.
doi: 10.1016/j.ijbiomac.2023.123476

8. Dey M, Ozbolat IT. 3D bioprinting of cells, tissues and organs. *Sci Rep*. 2020;10(1):14023.
doi: 10.1038/s41598-020-70086-y

9. Bohandy J, Kim BF, Adrian FJ. Metal deposition from a supported metal film using an excimer laser. *J Appl Phys*. 1986;60(4):1538-1539.
doi: 10.1063/1.337287

10. Bohandy J, Kim BF, Adrian FJ, Jette AN. Metal deposition at 532 nm using a laser transfer technique. *J Appl Phys*. 1988;63(4):1158-1162.
doi: 10.1063/1.340023

11. Rapp L, Cibert C, Nénon S, et al. Improvement in semiconductor laser printing using a sacrificial protecting layer for organic thin-film transistors fabrication. *Appl Surf Sci*. 2011;257(12):5245-5249.
doi: 10.1016/j.apsusc.2010.10.147

12. Rapp L, Constantinescu C, Delaporte P, Alloncle AP. Laser-induced forward transfer of polythiophene-based derivatives for fully polymeric thin film transistors. *Org Electron*. 2014;15(8):1868-1875.
doi: 10.1016/j.orgel.2014.04.029

13. Rapp L, Cibert C, Alloncle AP, et al. LIFT of organic materials for application in plastic micro-electronics. In: *3eme Russian-French Laser Physics Worshop for Young Scientist*; 2008. Accessed December 3, 2024.
https://hal.science/hal-00446484

14. Colina M, Serra P, Fernández-Pradas JM, Sevilla L, Morenza
JL. DNA deposition through laser induced forward transfer. *Biosens Bioelectron*. 2005;20(8):1638-1642.
doi: 10.1016/j.bios.2004.08.047

15. Serra P, Colina M, Fernández-Pradas JM, Sevilla L, Morenza JL. Preparation of functional DNA microarrays through laser-induced forward transfer. *Appl Phys Lett*. 2004;85(9):1639-1641.
doi: 10.1063/1.1787614

16. Fernández-Pradas JM, Colina M, Serra P, Domínguez J, Morenza JL. Laser-induced forward transfer of biomolecules. *Thin Solid Films*. 2004;453-454:27-30.
doi: 10.1016/j.tsf.2003.11.154

17. Barron JA, Spargo BJ, Ringeisen BR. Biological laser printing of three dimensional cellular structures. *Appl Phys A*. 2004;79(4-6):1027-1030.
doi: 10.1007/s00339-004-2620-3

18. Ringeisen BR, Kim H, Barron JA, et al. Laser printing of pluripotent embryonal carcinoma cells. *Tissue Eng*. 2004;10(3-4):483-491.
doi: 10.1089/107632704323061843

19. Guillotin B, Guillemot F. Cell patterning technologies for organotypic tissue fabrication. *Trends Biotechnol*. 2011;29(4):183-190.
doi: 10.1016/j.tibtech.2010.12.008

20. Koch L, Deiwick A, Chichkov B. Capillary-like formations of endothelial cells in defined patterns generated by laser bioprinting. *Micromachines (Basel)*. 2021;12(12):1538.
doi: 10.3390/mi12121538

21. Koch L, Deiwick A, Schlie S, et al. Skin tissue generation by
laser cell printing. *Biotechnol Bioeng*. 2012;109(7):1855-1863.
doi: 10.1002/bit.24455

22. Bosmans C, Rodriguez NG, Karperien M, et al. Towards single-cell bioprinting: micropatterning tools for organ-on-chip development. *Trends Biotechnol*. 2024;42(6):739-759.
doi: 10.1016/j.tibtech.2023.11.014

23. Hakobyan D, Médina C, Dusserre N, et al. Laser-assisted 3D
bioprinting of exocrine pancreas spheroid models for cancer initiation study. *Biofabrication*. 2020;12(3):035001.
doi: 10.1088/1758-5090/ab7cb8

24. Sorkio A, Koch L, Koivusalo L, et al. Human stem cell based
corneal tissue mimicking structures using laser-assisted 3D bioprinting and functional bioinks. *Biomaterials*. 2018;171:57-71.
doi: 10.1016/j.biomaterials.2018.04.034

25. Chang J, Sun X. Laser-induced forward transfer based laser bioprinting in biomedical applications. *Front Bioeng Biotechnol*. 2023;11:1255782.
doi: 10.3389/fbioe.2023.1255782

26. Curley JL, Sklare SC, Bowser DA, Saksena J, Moore MJ, Chrisey DB. Isolated node engineering of neuronal systems using laser direct write. *Biofabrication*. 2016;8(1):015013.
doi: 10.1088/1758-5090/8/1/015013

27. Colina M, Duocastella M, Fernández-Pradas JM, Serra P, Morenza JL. Laser-induced forward transfer of liquids: study of the droplet ejection process. *J Appl Phys*. 2006;99(8):084909.
doi: 10.1063/1.2191569

28. Fernández-Pradas JM, Florian C, Caballero-Lucas F, Sopeña
P, Morenza JL, Serra P. Laser-induced forward transfer: propelling liquids with light. *Appl Surf Sci*. 2017;418:559-564.
doi: 10.1016/j.apsusc.2016.10.197

29. Gruene M, Unger C, Koch L, Deiwick A, Chichkov B. Dispensing pico to nanolitre of a natural hydrogel by laser-assisted bioprinting. *BioMed Eng OnLine*. 2011;10(1):19. doi: 10.1186/1475-925X-10-19
30. Barron JA, Krizman DB, Ringeisen BR. Laser printing of single cells: statistical analysis, cell viability, and stress. *Ann Biomed Eng*. 2005;33(2):121-130. doi: 10.1007/s10439-005-8971-x
31. Mézel C, Souquet A, Hallo L, Guillemot F. Bioprinting by laser-induced forward transfer for tissue engineering applications: jet formation modeling. *Biofabrication*. 2010;2(1):014103. doi: 10.1088/1758-5082/2/1/014103
32. Koch L, Brandt O, Deiwick A, Chichkov B. Laser-assisted bioprinting at different wavelengths and pulse durations with a metal dynamic release layer: A parametric study. *Int J Bioprint*. 2017;3(1):001. doi: 10.18063/IJB.2017.01.001
33. Vogel A, Busch S, Parlitz U. Shock wave emission and cavitation bubble generation by picosecond and nanosecond optical breakdown in water. *J Acoust Soc Amer*. 1996;100(1):148-165. doi: 10.1121/1.415878
34. Duocastella M, Fernández-Pradas JM, Morenza JL, Serra P. Time-resolved imaging of the laser forward transfer of liquids. *J Appl Phys*. 2009;106(8):084907. doi: 10.1063/1.3248304
35. Deng Y, Renaud P, Guo Z, Huang Z, Chen Y. Single cell isolation process with laser induced forward transfer. *J Biol Eng*. 2017;11(1):2. doi: 10.1186/s13036-016-0045-0
36. Koch L, Kuhn S, Sorg H, et al. Laser printing of skin cells and human stem cells. *Tissue Eng Part C Methods*. 2010;16(5):847-854. doi: 10.1089/ten.tec.2009.0397
37. Hopp B, Smausz T, Kresz N, et al. Survival and proliferative ability of various living cell types after laser-induced forward transfer. *Tissue Eng*. 2005;11(11-12):1817-1823. doi: 10.1089/ten.2005.11.1817
38. Schiele NR, Chrisey DB, Corr DT. Gelatin-based laser direct-write technique for the precise spatial patterning of cells. *Tissue Eng Part C Methods*. 2011;17(3):289-298. doi: 10.1089/ten.tec.2010.0442
39. Guillotin B, Souquet A, Catros S, et al. Laser assisted bioprinting of engineered tissue with high cell density and microscale organization. *Biomaterials*. 2010;31(28):7250-7256. doi: 10.1016/j.biomaterials.2010.05.055
40. Karakaidos P, Kryou C, Simigdala N, Klinakis A, Zergioti I. Laser bioprinting of cells using UV and visible wavelengths: a comparative DNA damage study. *Bioengineering*. 2022;9(8):378. doi: 10.3390/bioengineering9080378
41. Kryou C, Theodorakos I, Karakaidos P, Klinakis A, Hatziapostolou A, Zergioti I. Parametric study of Jet/Droplet formation process during LIFT printing of living Cell-Laden bioink. *Micromachines*. 2021;12(11):1408. doi: 10.3390/mi12111408
42. Murru C, Duvert L, Magdinier F, et al. Assessment of laser-synthesized Si nanoparticle effects on myoblast motility, proliferation and differentiation: towards potential tissue engineering applications. *Nanoscale Adv*. 2024;6(8):2104-2112. doi: 10.1039/D3NA01020A
43. Hanawa T. Biocompatibility of titanium from the viewpoint of its surface. *Sci Technol Adv Mater*. 2022;23(1):457-472. doi: 10.1080/14686996.2022.2106156
44. Schindelin J, Arganda-Carreras I, Frise E, et al. Fiji: an open-source platform for biological-image analysis. *Nat Methods*. 2012;9(7):676-682. doi: 10.1038/nmeth.2019
45. Zhang Z, Xu C, Xiong R, Chrisey DB, Huang Y. Effects of living cells on the bioink printability during laser printing. *Biomicrofluidics*. 2017;11(3):034120. doi: 10.1063/1.4985652
46. Xiong R, Zhang Z, Chai W, Chrisey DB, Huang Y. Study of gelatin as an effective energy absorbing layer for laser bioprinting. *Biofabrication*. 2017;9(2):024103. doi: 10.1088/1758-5090/aa74f2
47. Catros S, Guillotin B, Bačáková M, Fricain JC, Guillemot F. Effect of laser energy, substrate film thickness and bioink viscosity on viability of endothelial cells printed by laser-assisted bioprinting. *Appl Surf Sci*. 2011;257(12):5142-5147. doi: 10.1016/j.apsusc.2010.11.049
48. Riester D. High speed photography of laser induced forward transfer (LIFT) of single and double-layered transfer layers for single cell transfer. *JLMN*. 2016;11(2):199-203. doi: 10.2961/jlmn.2016.02.0010
49. Antoshin AA, Churbanov SN, Minaev NV, et al. LIFT-bioprinting, is it worth it? *Bioprinting*. 2019;15:e00052. doi: 10.1016/j.bprint.2019.e00052
50. Liu X, Zu E, Chang X, et al. Bi-phasic effect of gelatin in myogenesis and skeletal muscle regeneration. *Dis Model Mech*. 2021;14(12):dmm049290. doi: 10.1242/dmm.049290
51. Minaev NV, Yusupov VI, Zhigarkov VS, et al. Laser Printing of Gel Microdrops with Living Cells and Microorganisms. *KnE Energy*. 2018;3(3):23-31. doi: 10.18502/ken.v3i3.2010
52. Ali M, Pages E, Ducom A, Fontaine A, Guillemot F. Controlling laser-induced jet formation for bioprinting mesenchymal stem cells with high viability and high resolution. *Biofabrication*. 2014;6(4):045001. doi: 10.1088/1758-5082/6/4/045001

3.3 Article 3: Laser-induced Structuring of Biocompatible Polymers for the Controlled Orientation of Multinucleated Myotubes.

Clarissa Murru[a], **Lucas Duvert[a,b]**, , Ahmed Al-Kattan[a], Daniel Ferry[c], Frederique Magdinier[b], Anne-Patricia Alloncle[a], Stefano Testa[b]*, Adrien Casanova[a]*

a. Aix-Marseille University, CNRS, LP3 UMR 7341, Campus de Luminy, C13288, Marseille, France.

b. Aix-Marseille University, INSERM, MMG, Marseille Medical Genetics, 13385 Marseille, France.

c. Centre Interdisciplinaire de Nanoscience de Marseille (CINaM), Aix-Marseille University, Centre National de la Recherche Scientifique (CNRS), Campus de Luminy, Marseille, France

Under Review Advanced Material Interfaces

Context

A key aspect of regenerative medicine is the search to control cell fate by engineering the extracellular matrix (ECM), which provides structural and functional support for cells. Additionally, the ECM's specific geometric organization in tissues like tendons and muscles is crucial for their functions, such as tensile strength and contraction force. Advances in tissue engineering have led to the development of 3D matrices that mimic the natural ECM, supporting cell growth and differentiation to increase the relevance of cultured biological tissues.

Beyond providing mechanical support, the ECM plays a critical role in coordinating cellular processes such as adhesion, proliferation, and differentiation, which are essential for tissue homeostasis and development. The surface properties of the ECM, including topography, can significantly influence these cellular mechanisms. For instance, specific surface patterns can enhance cell adhesion, promote proliferation, and direct the orientation and differentiation of cells.

Topographical techniques like lithography have been developed to create precise patterns on substrates, aiding in the study of how surface structures affect cell behavior. However, lithography remains a complex process with high production costs and limited processable materials. An alternative can be found in laser-induced topography, which allows for the efficient surface structuring of a wide range of materials, especially biopolymers. This method enables a precise control over micro and submicron features, making it ideal for studying the influence of topography on cell alignment, especially in tissues like skeletal muscle, which require highly organized architectures.

In this article, we applied ultrafast laser-induced surface structuring to biopolymers to create channels for human myoblast alignment and fusion into myotubes. The study evaluated the effects of these structured surfaces on muscle cell alignment, demonstrating the potential of this approach in replicating skeletal muscle organization, a key requirement for tissue engineering.

Results

We first investigated the capacity of several biopolymers to withstand the laser structuration process and studied the induced topography. Alginate, gelatin, and collagen Type 1 were selected as substrates for the laser process. Coatings were done on glass slides, and the structuration was achieved using femtosecond pulses and a high-speed scan system. The three tested polymers displayed homogenous channels of reproducible width and depth with the creation of a highly porous surface **(Fig 14.A)**.

While infrared analysis revealed no photochemical modification to the polymers **(Fig 14.B)**, contact angle studies showed a statistically significant increase in hydrophilicity with specific channel spacing values **(Fig 14.C)**. The first *in-situ* testing, with coatings immersed in culture media and seeded with human immortalized myoblasts, revealed, however, the lack of structural integrity of gelatin and alginate coatings. Due to its gelation capacity and ability to retain water, collagen type 1 was therefore selected as the ideal coating material for laser-induced topography. Several spacings between channels were tested to determine their ability to guide cell development **(Fig 14.D-F)**. All the tested parameters, from 35 to 150 µm, showed an efficient alignment of cells confined in the hydrophilic channels, with a maximum coherency for 55 µm channel spacing.

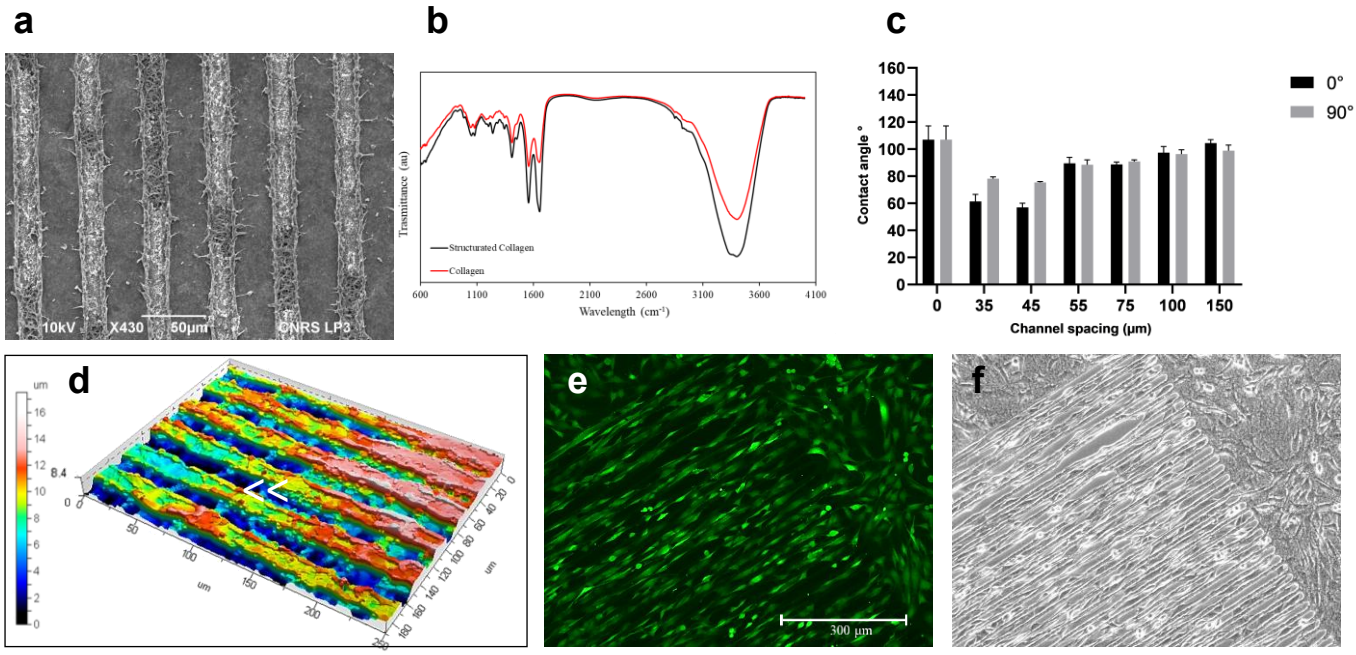

Figure 14: Study of micro-structured collagen surfaces (**a**) SEM images of collagen micropatterned surface. (**b**) Infrared spectra (**c**) Evolution of the contact angle depending on the channel spacing and orientation of the channel regarding to the camera (orange curve 0° angle, blue curve 90° angle) (**d**) Confocal analysis of the surface (**e**) Calcein-AM analysis (**f**) associated brightfield image.

Conclusions

Here, we demonstrated the ability of ultra-fast lasers to create topography on biopolymers that can guide cell development. Collagen Type 1 was chosen as the best substrate for its stability and biocompatibility. Its structuration remains flexible as all tested parameters allowed for controlled cell proliferation. This process, being done in the same laser set-up as the LIFT printing, can thus be coupled to the latter to promote the alignment of the printed cells, thereby favoring their alignment and the subsequent formation of myotubes when grown in the presence of differentiation medium.

Contribution

In this work I optimized and established the coating preparation methodology, performed the laser structuration process to create the topography and performed the image analysis on the processed samples.

Publication

Laser-induced Structuring of Biocompatible Polymers for the Controlled Orientation of Multinucleated Myotubes.

Clarissa Murru*[1], Lucas Duvert*[2,3], Daniel Ferry[4], Ahmed Al-Kattan[2], Frederique Magdinier[3], Anne-Patricia Alloncle[2], Stefano Testa[$3], Adrien Casanova[$2]

*Co-first authors
[$] Co-corresponding authors
Stefano Testa: stefano.testa@univ-amu.fr
Adrien Casanova: adrien.casanova@univ-amu.fr

[1]National Institute of Optics, National Research Council (INO-CNR), Sesto Fiorentino, Italy
[2]Laser, Plasmas et Procédés Photoniques (LP3), Aix-Marseille University, Centre National de la Recherche Scientifique (CNRS), Campus de Luminy, Marseille, France
[3]Marseille Medical genetics (MMG), Aix-Marseille University, Institut national de la santé et de la recherche médicale (INSERM), Marseille, France
[4]Centre Interdisciplinaire de Nanoscience de Marseille (CINaM), Aix-Marseille University, Centre National de la Recherche Scientifique (CNRS), Campus de Luminy, Marseille, France

Keywords: Laser direct writing, biomaterials, surface structuring, muscle tissue engineering, contact guidance

Abstract

Surface topography plays a critical role in regulating cellular behaviour through contact guidance. In this context, micro-nanostructured materials have gained widespread use in biomedicine with applications in biosensing, bioimaging, or tissue engineering. Among the different strategies that can be applied for surface structuration, laser-induced surface patterning offers a precise and versatile alternative to traditional lithographic techniques by enabling the rapid processing and tailored modifications of material properties. Using an ultrafast femtosecond laser, we investigated here the laser structuring of three different biopolymers, sodium alginate, gelatin, and collagen. The resulting surfaces were analysed using confocal and scanning electron microscopy. In parallel, the structural and chemical modifications induced by the laser ablation were thoroughly characterized. The interaction of human myoblasts cultured on these engineered surfaces was evaluated revealing that the laser-induced topographical features had a significant impact on myoblasts alignment. Specifically, optimal channel widths of 20-25 µm and interline spacings ranging from 35 µm to 150 µm promoted efficient cell organization mimicking the native constraint of skeletal muscle tissue. These findings emphasize the potential of laser-patterned polymer surfaces to guide muscle cell orientation and differentiation, providing a promising approach for developing functional surfaces in skeletal muscle tissue engineering.

Table of contents

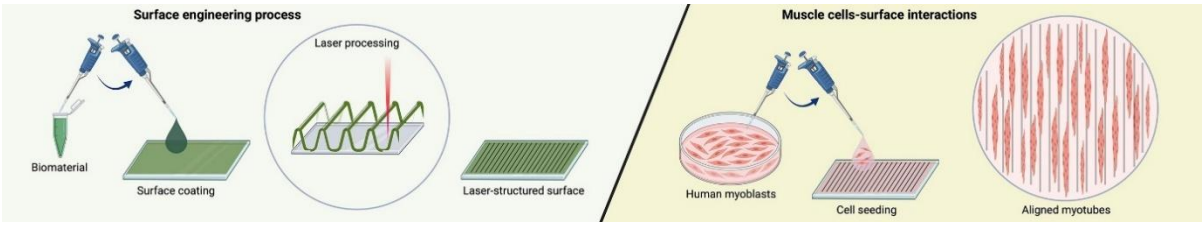

Laser structuring of biocompatible polymers creates precise surface patterns that influence cell organization. By imaging, contact angle measurements, and chemical analysis, this study demonstrates the ability of laser induced micro-structured surfaces to guide muscle cell alignment. These findings support laser patterning of biopolymers as a promising approach for skeletal muscle tissue engineering and biomedical applications.

1- Introduction

In vivo, cell behaviour is influenced among others by the physical properties of the extracellular matrix (ECM) and its associated mechanical cues[1,2]. *In vitro*, cell to surface interactions modulate cell morphology, cytoskeletal organization and gene expression. Cell adhesion plays a critical role in cell survival and fate determination. In recent years, surface properties, including topography, stiffness and chemical composition, have been shown to profoundly affect cellular processes by providing both mechanical and biochemical signals that regulate cell response[5]. Recent developments in materials science and tissue engineering have highlighted the crucial role of surface topography in precisely controlling cellular functions. In particular, structural features, such as surface roughness, geometric patterns and porosity, are recognized by cells via mechanotransduction pathways[6,7]. Multiple studies have demonstrated that micro- and nano-patterned surfaces with specific geometries can significantly affect cell adhesion[8], increase the orientation[9,10] and promote the proliferation [11] and differentiation of several lines of cells [12].

The design of surface patterns can be realized through a range of advanced techniques, each offering unique capabilities for achieving specific structural and functional features[13–18]. For instance, Casanova *et al*. described a self-aligning chemical functionalization method that enables the creation of low-density neuronal networks with precise control over soma positioning and dendritic growth on aligned nanostructures, allowing for accurate monitoring of neuronal activity at the single-cell level[19]. In contrast, lithography-based approaches are more commonly employed to fabricate highly precise and complex three-dimensional structures[20,21]. Despite the high spatial resolution achieved through lithography, its applicability is limited by several factors, including the significant costs associated with the materials required for pattern generation[22], and the complexity of the fabrication process[23] which requires specific environmental conditions (vacuum, clean room)[24]. In this context, laser-induced topography, as a direct writing and digital process, appears as an opportunity to process a wide range of materials in a simple and efficient way. By enabling the design of three-dimensional structures, laser-induced topography overcomes the limitations of complex traditional lithography and avoids the use of cell-interactive chemicals. The use of high repetition rate lasers allows the rapid processing of a large number of samples under standard environmental conditions. The process is also environmentally friendly as it does not require nor produce chemical pollutants [25]. Laser-based approaches for the design of bio-interfaces range from additive approaches (Matrix Assisted Pulsed Evaporation MAPLE or Laser-Induced Forward transfer LIFT) [26,27], laser direct writing (two photons polymerisation

to create 3D scaffolds at a nanoscale [28,29] or LIPSS formation) or laser texturing techniques [30]. These last methods rely on the ability to induce localized deformation or ablation of the targeted substrate in one straightforward step under a laser beam irradiation. Modification of the material can here be induced through photothermal and/or photochemical processes, depending on laser parameters (wavelength and pulse duration) and the composition of the substrate (optical properties).

The use of ultrafast lasers has become increasingly popular in recent years thanks to their unique ability to interact with a wide range of materials [31]. Given the transparency of most bio-polymers in the visible and near-infrared range, femtosecond laser pulses provide the high-intensity energy needed to induce non-linear absorption [32]. This enables precise processing of the material at micro and submicron scales level, on a large range of structures (pillars, ripples, spikes, grooves) providing a unique control over the uniformity and regularity of the structured surfaces and allowing their use in tissue engineering applications[25]. The ability of laser-structured surfaces to influence cell behaviour via topographic guidance has been largely studied [24,33,34]; Dinca *et al*. reported that the precise control of surface topography can regulate the differentiation and proliferation of various mesenchymal stem cell lineages[23]. Similarly, Angelaki *et al*. observed that the same topographical patterns elicit distinct responses for peripheral nervous system cells (murine Schwann (SW10) and Neuro2a (N2a) cells), either facilitating or inhibiting their adhesion[35]. These findings question the potential of laser-structured surfaces for modelling skeletal muscle, a tissue characterized by a highly organized anisotropic architecture consisting of parallel and aligned myofibers arranged in bundles[36]. The unidirectional arrangement of these myofibers is crucial for generating efficient contractile force and ensuring functionality[37]. For these reasons, the alignment of myoblasts, precursor cells that fuse to form multinucleated myotubes, which subsequently develop into myofibers in culture is essential for the proper formation of skeletal muscle tissue *in vitro*.
This work introduces an innovative approach for controlling skeletal muscle cell alignment using ultrafast laser-induced surface structuring of biopolymers. Through precise laser modification, anisotropic topography gradients were created on three widely used biopolymers: (i) alginate, known for its biocompatibility and use in controlled drug delivery and skin repair [38,39]; ii) gelatin, a versatile polypeptide that can easily form hybrid biomaterials due to its functional groups [40–42] and iii) collagen, a fundamental structural protein extensively used in the engineering of nerve, musculoskeletal tissues, and vascular grafts[43–46]. A significant breakthrough is the fabrication of microscale channels (20-25 µm wide) with adjustable interline spacings (ranging from 35 µm to 150 µm), allowing precise tailoring of surface features. This advanced surface structuring approach offers an effective method to influence cellular behaviour, specifically enhancing the organization and alignment of human myoblasts, to mimic the natural skeletal muscle tissue architecture [47]. By combining ultrafast laser technology with biopolymer engineering, this work not only deepens the understanding of cell-material interactions but also offers a scalable and adaptable system for designing biomimetic surfaces. The described process could pave the way for the development of advanced and easily accessible engineered culture surfaces, with applications ranging from skeletal muscle modelling and neuromuscular disease studies to personalized and regenerative medicine.

2- Materials and methods

2.1- Coatings preparation

Sodium alginate (ThermoFisher Scientific) and gelatin powder (Acros Organics) were suspended in deionized water at a concentration of 3% w/v, and the dissolution process of the polymers was optimized by stirring the mixtures for 2 hours at 60 °C. A volume of 400 µL was finally cast onto a round glass coverslip with a diameter of 17 mm with a graduated pipette. For the sodium alginate coating, the coverslips were dipped in a 0.5 M $CaCl_2$ solution (ionic cross-linking agent) to promote its reticulation: several tests were carried out by soaking the sodium alginate coatings in $CaCl_2$ for different durations, and the time of 1 minute was chosen for subsequent experiments. Gelatin coatings were left to dry at room temperature overnight. The collagen mixture was prepared as follows: 715 µL of a 0.3 mg/mL solution of collagen was mixed with 85 µL of 10x PBS and 184 µL of cell culture medium (DMEM). Finally, 16 µL of a NaOH solution 1M was added to promote the gelation of the polymer and reach the final volume of 1 mL. The manipulation of the mixture was carried out while keeping all reagents on ice in order to avoid premature gelling of the collagen. 400 µL were cast onto round glass coverslips to obtain the coatings that spontaneously reticulated after 15 minutes.

2.2. Experimental set-up for the micro-structuration of polymer samples

A 60 kHz femtosecond laser (Carbide CB-01 Light Conversion) emitting at a fundamental wavelength of 1030 nm with an average pulse duration of 213 fs and a maximum power output of 5W was used to create the micro-structuration. To achieve high processing speed, a galvanometric scanning system (ScanLab intelliSCAN14) coupled with a 70 mm focus length F-Theta lens (Linos F-Theta-Ronar lenses) was used (**Figure 1**).The beam waist, determined by the Liu's regression technique [48], is calculated to be 2wo = 36 µm. The average fluence values will be calculated using this value. Biopolymer surfaces were ablated at a fluence of 0.8J/cm² and at a scan speed of 320mm/s, corresponding to a pulse overlap of 80%.
With these parameters, the typical channel width ranged from 20 to 25 µm, depending on the processed material. This value is strongly influenced by the beam quality, size, and wavelength. To maximize process speed and efficiency - particularly given the density of topographic features - we used a high-speed galvanometric scanner. Higher processing resolution could be achieved with specialized magnification optics, though at the expense of speed and overall efficiency. The round glass coverslips coated with the different biopolymers were laser-structured to produce micropatterned surfaces (area of 227 mm²) consisting of arrays of lines with a spacing ranging from 35 to 150 µm. Then, the micro-structured substrates were washed three times in a 70% ethanol solution and rinsed with sterile PBS to ensure sterility for subsequent cell culture experiments.

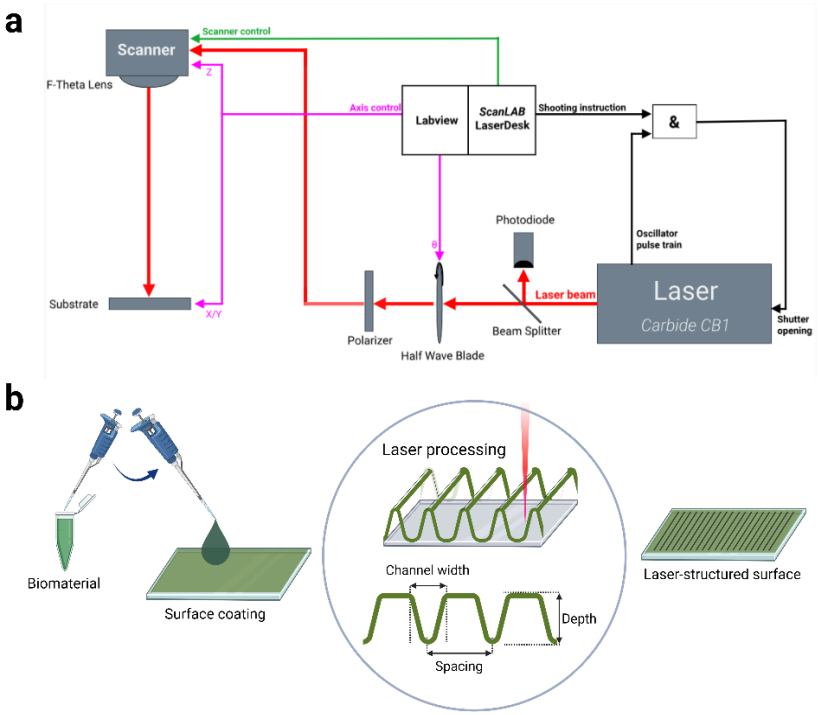

Figure.1 Experimental laser set-up for the micro-structuration of polymer samples (a). Preparation protocol of the samples (b).

The patterns created on the surface of the coatings were observed in detail using SEM (JEOL JSM-6390, Tokyo, Japan) and characterized with a confocal microscope (LEICA DCM3D, Nanterre, France).

2.3. Infrared analysis

The surface chemistry and thermal behaviour of the structured samples were recorded in Attenuated Total Reflectance (ATR, germanium crystal) mode using a Bruker VERTEX70 mid-IR Fourier Transform spectrometer equipped with a temperature-stabilized DLaTGS detector (Deuterated lanthanum α-alanine-doped triglycine sulphate). All spectra were accumulated on the surface of the different areas in a spectral range of 650–4000 cm^{-1} by recording 200 scans at a resolution of 4 cm^{-1}.

2.4 Contact angle analysis

Wettability modifications of the laser-structured surface were characterized by studying contact angles. Five µL of distilled water was deposited on the created topography and photographed through a camera (DAHUA) equipped with a 10X zoom lens (Computar). The droplets are illuminated by a white light (Wild Heerbrugg). The angle formed between the surface and the tangent to the droplet surface along their line of contact is calculated using the Contact Angles plugin for FIJI software [49]. The obtained value is used as an index of hydrophobicity: values ranging from 0° to 90° indicate a hydrophilic surface, while values comprised between 90° and 180° a hydrophobic one.

2.5 Cell cultures

Human immortalized myoblasts were cultured according to a previously published protocol [47] on 10 cm culture dishes (Falcon) at 37°C with 5% CO_2 in Basal Medium (BM) composed of 4:1 volumes parts of Dulbecco's modified Eagle medium (DMEM, Gibco) and 1 volume of Medium 199 (Gibco), supplemented with 15% foetal bovine serum (Euroclone); 0.02 M HEPES buffer (Invitrogen); 1.4 mg/L vitamin B12 (Sigma); 0.03 mg/L ZnSO4 (Fisher Scientific), 0.055 mg/L dexamethasone (Sigma), 2.5 µg/L hepatocyte growth factor (Chemicon International) and 10 µg/L basic fibroblast growth factor (BioPioneer). Once 90% confluency was reached, cells were transferred to Differentiation Media (DM) composed of BM supplemented with 2% Horse Serum (Gibco) to induce final differentiation. For biological experiments, cells were seeded on top of the different micro-patterned coated supports at a concentration of 5 x 10^4 cells per support and grown depending on experimental needs: 3 days of incubation for myoblast-surface interaction experiments and 7 days (3 days in culture medium and 4 days in differentiation medium) for myotubes orientation experiments.
To clearly visualize the cells and to monitor their interactions with the surfaces, samples were incubated with calcein-AM live staining solution (Thermofisher) for 30 min at 37 °C.
Imaging analyses were performed with a reverse microscope (EVOS M5000, Invitrogen, ThermoFisher) and a reverse fluorescence microscope (Axio Observer Z1/7, Zeiss).

2.6 Cell fixation and Immunofluorescence analysis

The samples were fixed in paraformaldehyde (4%, for 15 min at 4 °C), washed in PBS, and stored at 4°C. Immunofluorescence was performed as previously described [50]. Briefly, cells were permeabilized in a solution of Triton X-100 (Sigma) 0.3% in PBS for 1 h at room temperature (RT) and blocked with a blocking solution consisting of 10% natural goat serum (Thermo Fisher Scientific), 1% glycine (Thermo fisher Scientific), and 0.1% Triton X- 100 in PBS for 1 h at RT. Subsequently, the cells were incubated with rabbit polyclonal anti-Desmin (Abcam) primary antibody, diluted 1:100 in blocking solution for 2 h at RT, and then rinsed with a washing solution consisting of 1% bovine serum albumin (BSA, Sigma) and 0.2% Triton X-100 in PBS. After washing, the cells were incubated with Alexa Fluor 488-conjugated goat anti-rabbit IgG secondary antibody (H + L; Thermo Fisher Scientific, diluted 1:400) for 1 h. Finally, the nuclei were counterstained with 300 nM DAPI (Thermo Fisher Scientific) in PBS for 10 min.

2.7 Image analysis

Once myoblasts were differentiated into myotubes expressing Desmin, their organization was studied using the *OrientationJ* plugin [51] of the Fiji software [52]. In particular, the pictures (832 x 832 mm^2) were converted into highly contrasted 8-bit images and processed using *the OrientationJ distribution* tool to obtain a weighted histogram of muscle elements orientations; the "weight" of this distribution is represented by the coherency value, a value ranging between 0 (no orientation) and 1 (perfect orientation) calculated using *OrientationJ dominant direction* tool [53].

2.8 Statistical analysis

All experiments were performed in biological triplicates. Data were analyzed using GraphPad Prism 8, and values were expressed as means ± standard error. Statistical significance was

tested using one-way ANOVA with the appropriate multiple comparison tests. A probability of less than 5% ($P < 0.05$) was considered as statistically significant.

3- Result and discussion

3.1 Morphological Characterization

The aligned patterning obtained on the surface of the polymers was characterized by electron microscopy (SEM). The 50 µm spaced channels showed a homogeneous and compact structure, with a width of 20 µm for sodium alginate (**Figure 2.a**) and 25 µm for gelatin and collagen (**Figure 2.b,c**) coatings. These dimensions were selected according to the myoblast cells that feature an observed mean dimension of 20 µm[54]. For the different biomaterials, a difference in the morphology and the porosity of the channel surface was observed (**Figure 2.d-f**).

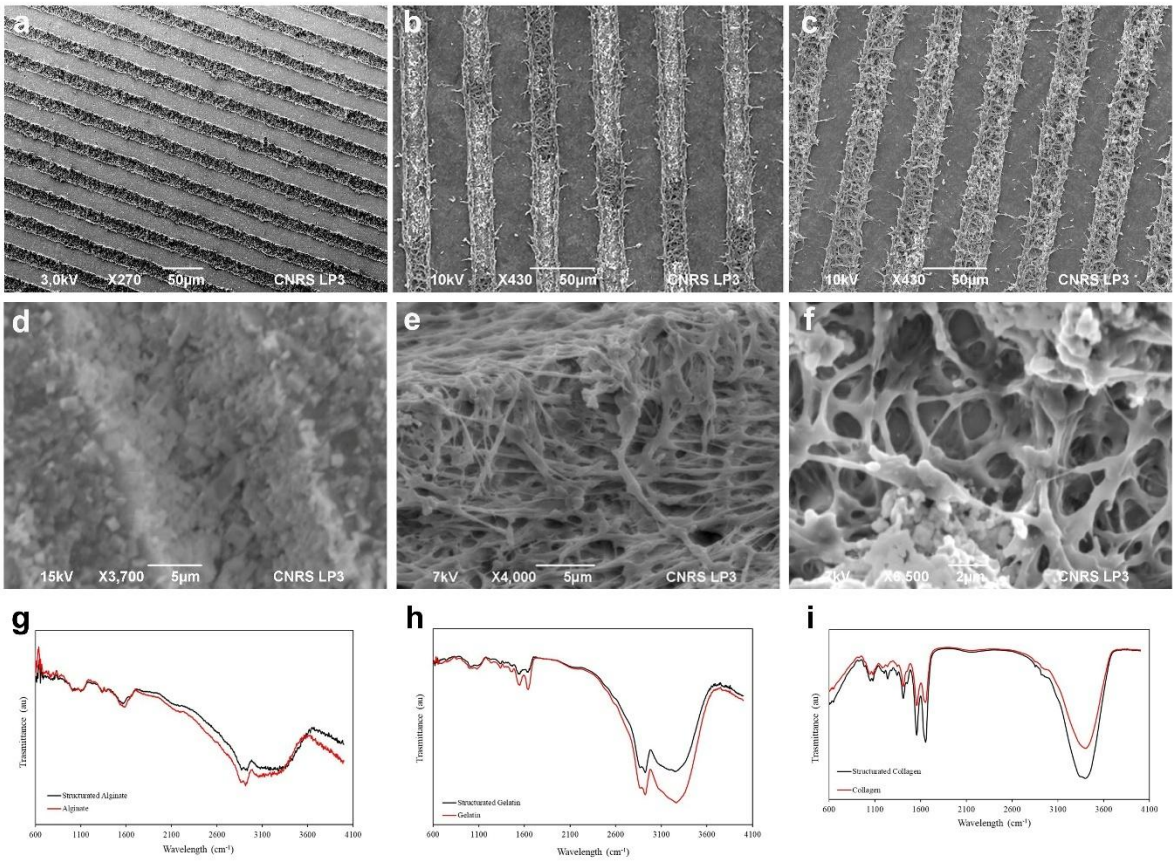

Figure.2 Morphological and chemical characterizations of the structured surfaces; SEM images of micropatterned surfaces of sodium alginate (a,d), gelatin (b,e), and collagen (c,f)**.** Infrared spectra for the fine layers of sodium alginate (g), gelatin (h), and collagen (i). The samples were studied both in their structured and in their initial form.

3.2 Characterization of Functional Groups

In a second step, the functional groups were studied both in laser-treated and untreated samples through Fourier-transform infrared spectroscopy (FT-IR). Sodium alginate spectra showed stretching vibrations of Oxygen–Hydrogen (O-H) bonds in the range of 3000–3600 cm^{-1} while stretching vibrations of aliphatic Carbon–Hydrogen (C-H) were observed at 2900–

2800 cm^{-1} (**Figure 2.g-i**). The increase in the peak intensity at 1635 cm^{-1} corresponds to the symmetrical stretching of COO-while the peaks observed at 1580 cm^{-1}, 1416 cm^{-1}, and 1340 cm^{-1} are attributed to the asymmetrical stretching of the COO- group. Peaks at 1110 cm^{-1} and 1034 cm^{-1} are associated with the stretching of the C-O group. In the case of gelatin, both spectra showed similar patterns, and four regions were observed: 3600-2300 cm-1(Amide A), 1656-1644 cm^{-1} (Amide I), 1560-1335 cm^{-1} (Amide II) and 1240-670 cm^{-1} (Amide III). Collagen absorption bands can be distinguished in the amide I at 1657 cm^{-1} resulting from the stretching vibration of the peptide carbonyl group C=O, amide II at 1560 cm^{-1} that corresponds to a combination of the N–H in-plane bend, and the C–H stretch and a set of three weaker bands that represent amide III vibration modes centred at 1245 cm^{-1} belonging to a combination of the C–N stretch and the N–H in-plane bend. Moreover, the absorption registered between 1360 cm^{-1} and 1560 cm^{-1} belongs to the symmetric vibrations of CH_2 and CH_3, while the peaks identified around 1100 cm^{-1} correspond to the asymmetric C-O and C-O-C stretching vibration. The similarity of the spectra obtained from structured or unstructured samples demonstrates that, at the chosen irradiation conditions, the laser treatment did not cause the appearance of new functional groups that might be potentially toxic for cell survival or growth.

3.3 Study of coating suitability for cell culture

Once morphologically and chemically characterized, we studied the behaviour of the micro-structured supports in a typical cell culture environment. The supports were placed in a 12-well plate, then 2 ml of culture medium containing $5x10^4$ cells were added in each well and incubated for 24 hours at 37 °C. In these conditions, sodium alginate detached from the glass surface while the structuring process cut the coating layer, resulting in loss of structural integrity (**Figure 3.a**). On the other hand, the gelatin dissolved rapidly in water (less than 1 hour) (**Figure 3.b**) while the collagen surface (**Figure 3.c**) was able to maintain its morphology and adhesion throughout the experiment and therefore proved to be the only stable and suitable coating for a long-term study with muscle cells. For this reason, only the collagen-coated supports were used for the following experiments.
Collagen coatings were characterized after laser structuring through confocal (**Figure 3.d**) and SEM (**Figure 3.e**) analysis, which revealed reproducible channels of about 12 to 14 µm depth and 25 µm width (**Figure 3.d,e**). Finally, we prepared half-structured coatings in order to study the long-term cell interaction with collagen-coated surfaces and emphasize the effect of the laser induced topography on cell organization. In this regard, channel spacing was adjusted to 35 µm to maximise the processed area. Interestingly, after 3-day of culture, human immortalized myoblasts displayed signs of organization in the laser structured compartment (**Figure 3.f**) with a preferential alignment in the direction of the channels.

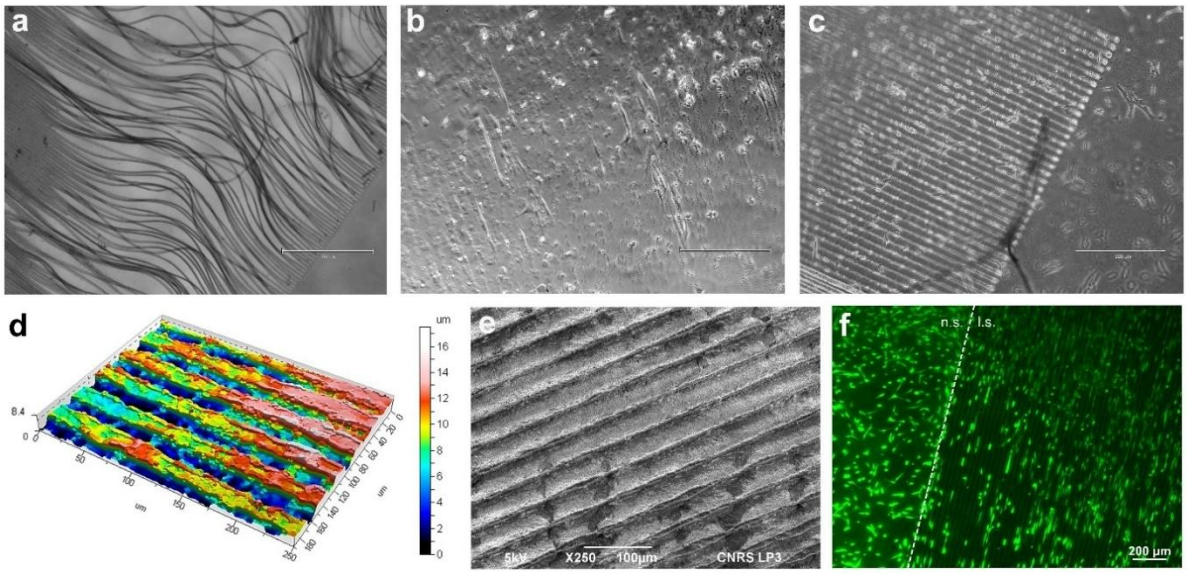

Figure.3 Top: coatings response to the cell culture environment. Inverted microscope images of laser-assisted structuring of sodium alginate (a), gelatin (b), and collagen (c) coatings after hydration. **Bottom: collagen coating analysis.** Confocal analysis of the laser-structured collagen-coated surfaces (d) and related SEM picture (e). Human immortalized myoblasts (stained for calcein-AM, green) orientation on non-structured and laser-structured collagen-coated surface. The dotted line indicates the boundary between the non-structured and laser-structured areas.

3.4 Analysis of myoblast orientation on laser micro-patterned surfaces

Myoblast differentiation is an ordered multistep process guided by the stepwise activation of myogenic factors that lead to the fusion of myoblasts into multinucleated myotubes. Eventually, myotubes will give rise to the diverse muscle fibre types to build the complex skeletal muscle architecture essential to carry out its most important functions, such as body movement, postural behaviour, and breathing [55]. The orientation of muscle fibres *in vivo* is an automatic process driven by the interaction of muscle cells with a well-organized environment and the exposure to mechanical forces. *In vitro*, cells must be guided in adhesion and growth to replicate, once differentiated, the typical organization of human skeletal muscle tissue with parallel aligned muscle fibres [56]. The aim of this study was to promote the orientation of the human myoblasts through an anisotropic surface obtained with the assistance of the laser. To better understand and characterize the previous observations on cell alignment, human immortalized myoblasts were seeded on collagen micro-patterned substrates with different laser-ablated channel spacing (control without structuring, 35, 45, 55, 75, 100, and 150 µm) and cultured for 7 days to allow for myotubes formation.
Myotubes organization was analysed and we observed an excellent rate of orientation for all the spacing tested (**Figure 4.a-f**), as indicated by the presence of a single peak in the graph displaying the distribution of cells in space (**Figure 4.h**). In contrast, myotubes grown on the unstructured control substrates spread randomly without a prevalent orientation (**Figure 4.g**), as shown by the black line in the orientation graph (**Figure 4.h**). For spacing ranging from 35 to 55 µm we observed a myotube density similar to that of structured channels, with cells grown both within and between channels (**Fig 4.a-c**). As the spacing increased to 75, 100 and 150 µm, the reduction in structured channels density led to a decreased number of myotubes (**Figure 4.d-f**). This observation could be due to the increased area between channels, resulting in reduced geometric constraints on cultured myoblasts. However, even at these higher

spacing, sufficient topographical cues are still present to induce preferential orientation (**Figure 4.h**).

Interestingly, a comparison of the myoblast immunostaining pictures with their brightfield counterparts (**Figure 4.a-g, left half**) reveals that at a spacing of 150 µm, the cells do not align with the laser-ablated channel (**Figure, 4.f**), despite exhibiting a single orientation peak comparable to the other spacing values (**Figure 4.h**). We concluded that the surface topography at 150 µm can still facilitate the myotubes alignment due to contact geometry, an aspect that should be further investigated by expanding the tested values.

Finally, as shown by the coherency analysis, all tested spacing values were significantly higher than the control, with a maximum of 55 µm (**Figure 4.i**). However, the differences between the individual spacing values were not significant, confirming the effectiveness of the ultrafast laser-induced surface structuring process in creating micro-patterned collagen-coated surfaces capable of guiding muscle cells organization.

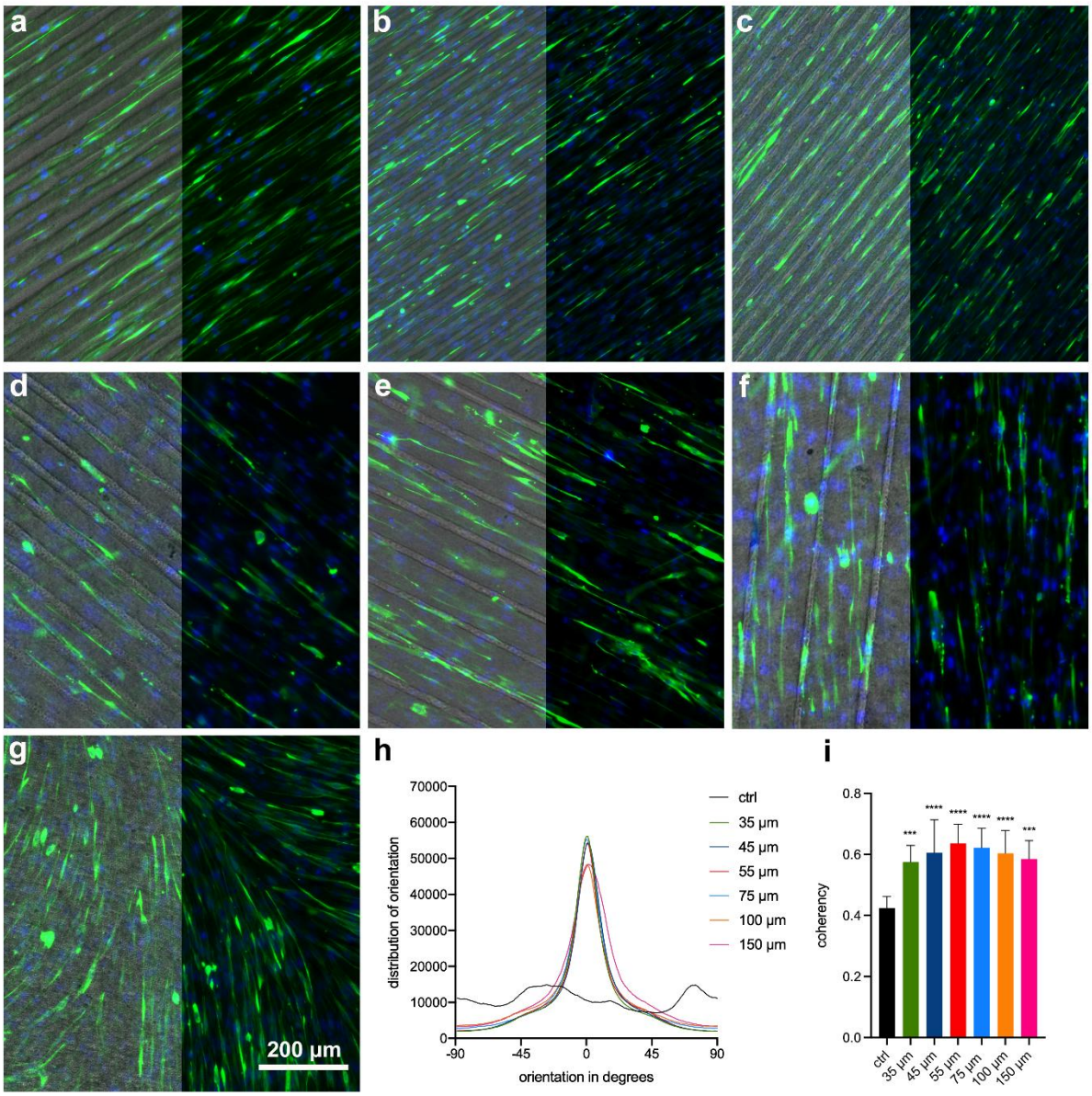

Figure.4 Alignment analysis. Immunofluorescence analysis of human myotubes positive for Desmin (green), juxtaposed with relative brightfield image (left half), grown on collagen coated laser-structured supports with different spacing values: 35µm (a), 45µm (b), 55µm (c), 75µm (d), 100µm (e),

150 µm (f) and non-structured control (g). Nuclei are counterstained with Dapi (blue); graph of the distribution of orientation for all the experimental conditions (h) and the relative coherency values (i). *P values*: p=0,001 (35 µm), p<0,0001 (45, 55, 75, 100 µm), p=0004 (150 µm).

3.5 Contact angle study on collagen layers

To better understand the mechanisms behind cell orientation, the hydrophilicity of the processed collagen surfaces was analysed through water contact angles (**Figure 5.a**). The previously studied spacing values that resulted in controlled cell organization (35, 45, 55, 75, 100 µm) were chosen to assess the influence of the topography on the surface hydrophilicity. Two measurements were taken, parallel and perpendicular to the channels. Interestingly, for smaller spacings (35 µm and 45 µm), the orientation clearly affects the contact angle, with values significantly higher when measurement was done in a perpendicular orientation relative to the channels. Moreover, at these spacing we found a drastic decrease in the measured contact angles compared to the control, with a minimum reached for 45 µm spacing (**Figure 5.b**). The difference between the structured samples and the control decreased while remaining significant for larger spacings, with values around 90° and no differences between orientations (**Figure 5.b**).

Studies have demonstrated that the hierarchical structure and porosity in collagen scaffolds enhance the availability of hydroxyl, carboxyl, and amine groups on the scaffold surface. This occurs because porosity and microtopography increase the surface area where these functional groups can interact with the environment, making them more accessible for cellular attachment and biochemical interactions [57]. In this work, we observed that the increase in surface area due to laser-induced topography and associated porosity (**Figure 2.c,f**) leads to an increased in the amount of exposed polar groups, promoting hydrophilicity (**Figure 5.b**), providing preferential conditions for muscle cells differentiation (**Figure 3.f**). This effect undergoes a natural decay with increased spacing due to a lesser percentage of processed surfaces, ultimately leading to the loss of cell organization (**Figure 4.f**).

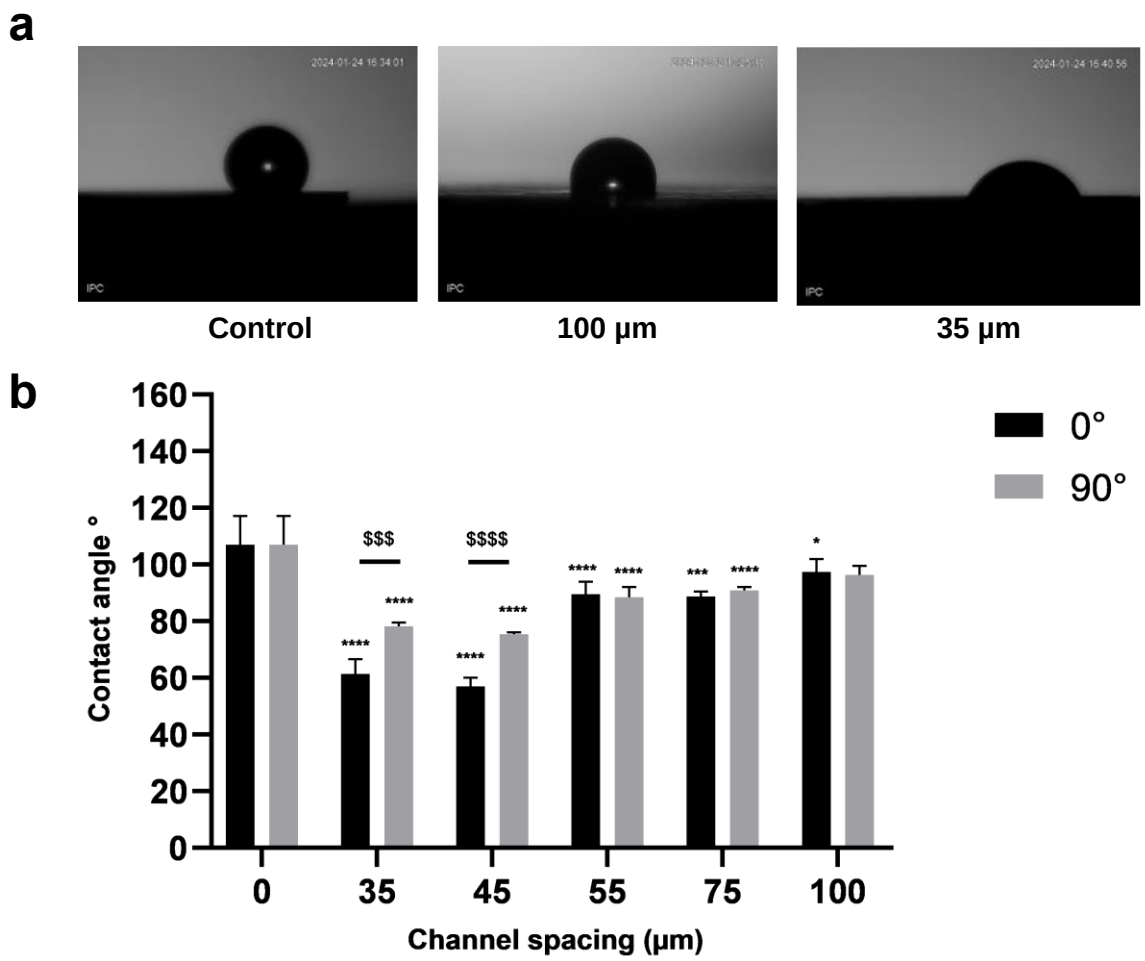

Figure.5 Contact angle measurement on structured collagen surfaces at different spacing values (a). Evolution of the contact angle depending on the channel spacing and orientation of the channel, parallel (0°) or perpendicular (90°) to the recording direction (b). (* compared to control 0°) (p values: **** p < 0,0001, *** p = 0,0003, * p = 0,0477, $$$$ p < 0,0001, $$$ p < 0,0002)

Conclusions

We report here the application of an ultra-fast laser system to structure the surface of biopolymers. The aim was to develop cell culture supports capable of driving cell growth, orientation and differentiation in a well-defined and pre-designed structured support.
Different biocompatible biopolymers, such as sodium alginate, gelatin, and collagen, were tested. However, despite the good physico-chemical stability of all three biopolymers during the laser-structuring phase, only the collagen coating proved able to tolerate the biological conditions, being the only one to show stable adhesion to the glass support and excellent resistance to a prolonged exposure in the aqueous environment of cell culture conditions.
For this reason, the collagen-coated supports were used to create micro-patterned surfaces thanks to the ultra-fast laser-ablation technique. Anisotropic topographies composed of parallel lines at different spacing (from 35 to 150 µm) were tested for their ability to promote human myoblasts organization. The pattern was specially designed to replicate the skeletal muscle tissue architecture composed of parallel, aligned and elongated elements corresponding to the muscle fibres. Interestingly, the laser-structured surfaces were able to

promote myoblasts organization via contact guidance and to foster their differentiation into highly aligned myotubes. This organization is correlated with the increased hydrophilicity of the substrates following the structuring process for spacing ranging from 35 to 100 µm, as demonstrated by contact angle measurements. Above 100 µm, the density of channels on the collagen surface becomes insufficient to achieve a proper control of cell culture conditions.
In conclusion, the reported micro-patterned supports are based on an ultra-fast laser processing of regularly used bio-compatible polymers. They integrate seamlessly into the cell culture workflow without additional steps or chemical consideration. Their potentiality was here demonstrated with the alignment of skeletal muscle cells, but their use can easily be extended to other cell types to mimic tissue-specific organisation, by varying the spacing and the pattern geometry. The processed surfaces also proved their ability in creating well-defined and pre-designed cell cultures that can be effectively utilized for skeletal muscle modelling or for the organization of more complex models such as neuromuscular and myotendinous junctions. Finally, the possibility to obtain well aligned cell culture allows for precise morphological studies with the discrimination of single independent myotubes. This level of detailed analysis would not be possible with traditional cell culture surface where myotubes are randomly oriented (**Figure 4.g**). Given their versatility and ease of integration laser micro-patterned supports represent a powerful tool for tissue engineering and biomedical applications.

Conflicts of interest

The authors declare that they have no competing interests.

Acknowledgments

The work was funded by the French National Research Agency (ANR Medilibs and Diagem projects) together with the French Defense Innovation Agency (ANR—DGA/AID—ICELARE Project ID ANR—20—ASTR—0004). The PhD thesis of Lucas Duvert was co-funded by Aix-Marseille university, the French Defense Innovation Agency and the MarMaRa funding scheme. This work received support from the French government under the France 2030 investment plan, as part of the Initiative d'Excellence d'Aix-Marseille Université – A*MIDEX "AMX-23-CPJ-05". The project leading to this publication has received funding from the Excellence Initiative of Aix-Marseille University-A*Midex, a French "investissement d'avenir programme" AMX-19-IET-007, through the MarMaRa funding scheme. This work was conducted using LaMP facilities at LP3. The authors also acknowledge the "Region SUD" for their financial support.

Bibliography

[1] S. Testa, M. Costantini, E. Fornetti, S. Bernardini, M. Trombetta, D. Seliktar, S. Cannata, A. Rainer, C. Gargioli, *Journal of Cellular and Molecular Medicine* **2017**, *21*, 2711.

[2] H. Kim, M.-C. Kim, H. H. Asada, *Sci Rep* **2019**, *9*, 2732.

[3] J. Na, C. Tai, Z. Wang, Z. Yang, X. Chen, J. Zhang, L. Zheng, Y. Fan, *Biomaterials* **2025**, *312*, 122715.

[4] L. Rijns, M. G. T. A. Rutten, A. F. Vrehen, A. A. Aldana, M. B. Baker, P. Y. W. Dankers, *Nanoscale* **2024**, DOI 10.1039/D4NR02088J.

[5] J. R. Libby, H. Royce, S. R. Walker, L. Li, *Biomaterials and Biosystems* **2024**, *15*, 100097.

[6] L. Papadimitriou, A. Karagiannaki, E. Stratakis, A. Ranella, *Mechanobiology in Medicine* **2024**, *2*, 100039.

[7] F. Martino, A. R. Perestrelo, V. Vinarský, S. Pagliari, G. Forte, *Front. Physiol.* **2018**, *9*, DOI 10.3389/fphys.2018.00824.

[8] C. Y. Guo, R. Mo, H. Kim, *Journal of Oral Biology and Craniofacial Research* **2024**, *14*, 471.

[9] M. Cong, X. Wu, L. Zhu, G. Gu, F. Ding, G. Li, H. Shi, *Regenerative Biomaterials* **2024**, *11*, rbae005.

[10] A. Lecomte, A. Casanova, M.-C. Blatché, J. Gonzalès, A. Ajagli, L. Mazenq, D. Gonzalez-Dunia, G. Larrieu, **2024**.

[11] V. Errico, G. Arrabito, E. Fornetti, C. Fuoco, S. Testa, G. Saggio, S. Rufini, S. Cannata, A. Desideri, C. Falconi, C. Gargioli, *ACS Appl. Mater. Interfaces* **2018**, *10*, 14097.

[12] G. H. Yang, J. Lee, G. Kim, *Biofabrication* **2019**, *11*, 025005.

[13] Y. Nishimura, K. Yano, M. Itoh, M. Ito, in *Flat Panel Display Manufacturing*, John Wiley & Sons, Ltd, **2018**, pp. 287–310.

[14] J. L. Charest, A. J. García, W. P. King, *Biomaterials* **2007**, *28*, 2202.

[15] N. Kaga, R. Horiuchi, A. Yokoyama, T. Akasaka, Y. Yoshida, *e-J. Surf. Sci. Nanotech.* **2017**, *15*, 1.

[16] M. Patel, S. Ahn, W.-G. Koh, *Journal of Industrial and Engineering Chemistry* **2022**, *114*, 19.

[17] T. Limongi, L. Brigo, L. Tirinato, F. Pagliari, A. Gandin, P. Contessotto, A. Giugni, G. Brusatin, *Biomed. Mater.* **2021**, *16*, 035013.

[18] H. Sariogullari, A. Z. Aroguz, Z. Adiguzel, *Mol Biotechnol* **2023**, *65*, 786.

[19] A. Casanova, M.-C. Blatche, C. A. Ferre, H. Martin, D. Gonzalez-Dunia, L. Nicu, G. Larrieu, *Langmuir* **2018**, *34*, 6612.

[20] D. Qin, Y. Xia, G. M. Whitesides, *Nat Protoc* **2010**, *5*, 491.

[21] Y. Xia, G. M. Whitesides, *Angewandte Chemie International Edition* **1998**, *37*, 550.

[22] X. Liu, A. Zanut, M. Sladkova-Faure, L. Xie, M. Weck, X. Zheng, E. Riedo, G. M. de Peppo, *Advanced Functional Materials* **2021**, *31*, 2008662.

[23] S. Fruncillo, X. Su, H. Liu, L. S. Wong, *ACS Sens.* **2021**, *6*, 2002.

[24] A. Riveiro, A. L. B. Maçon, J. del Val, R. Comesaña, J. Pou, *Front. Phys.* **2018**, *6*, DOI 10.3389/fphy.2018.00016.

[25] E. Stratakis, A. Ranella, M. Farsari, C. Fotakis, *Progress in Quantum Electronics* **2009**, *33*, 127.

[26] A. A. Antoshin, S. N. Churbanov, N. V. Minaev, D. Zhang, Y. Zhang, A. I. Shpichka, P. S. Timashev, *Bioprinting* **2019**, *15*, e00052.

[27] J. Chang, X. Sun, *Front Bioeng Biotechnol* **2023**, *11*, 1255782.

[28] M. Malinauskas, M. Farsari, A. Piskarskas, S. Juodkazis, *Physics Reports* **2013**, *533*, 1.

[29] V. Harinarayana, Y. C. Shin, *Optics & Laser Technology* **2021**, *142*, 107180.

[30] V. Dinca, L. E. Sima, L. Rusen, A. Bonciu, T. Lippert, M. Dinescu, M. Farsari, in *Recent Advances in Biopolymers* (Ed.: F. K. Parveen), InTech, **2016**.

[31] E. Rebollar, J. Mildner, N. Götte, D. Otto, C. Sarpe, J. Köhler, M. Wollenhaupt, T. Baumert, M. Castillejo, *Applied Surface Science* **2014**, *302*, 231.

[32] Z. K. Wang, H. Y. Zheng, C. P. Lim, Y. C. Lam, *Applied Physics Letters* **2009**, *95*, 111110.

[33] P. Shukla, D. G. Waugh, J. Lawrence, R. Vilar, in *Laser Surface Modification of Biomaterials*, Elsevier, **2016**, pp. 281–299.

[34] B. Neuenschwander, B. Jaeggi, M. Schmid, G. Hennig, *Physics Procedia* **2014**, *56*, 1047.

[35] D. Angelaki, P. Kavatzikidou, C. Fotakis, E. Stratakis, A. Ranella, *Materials Science and Engineering: C* **2020**, *115*, 111144.

[36] N. Pien, H. Krzyslak, S. Shastry Kallaje, J. Van Meerssche, D. Mantovani, C. De Schauwer, P. Dubruel, S. Van Vlierberghe, C. P. Pennisi, *Applied Materials Today* **2023**, *31*, 101737.

[37] R. Hashiguchi, H. Ichikawa, M. Kumeta, D. Koyama, *Sci Rep* **2024**, *14*, 25737.

[38] R. Ahmad Raus, W. M. F. Wan Nawawi, R. R. Nasaruddin, *Asian Journal of Pharmaceutical Sciences* **2021**, *16*, 280.

[39] N. Farshidfar, S. Iravani, R. S. Varma, *Marine Drugs* **2023**, *21*, 189.

[40] Y. He, C. Wang, C. Wang, Y. Xiao, W. Lin, *Polymers* **2021**, *13*, 2299.

[41] Y. Piao, H. You, T. Xu, H.-P. Bei, I. Z. Piwko, Y. Y. Kwan, X. Zhao, *Engineered Regeneration* **2021**, *2*, 47.

[42] S. Sethi, Medha, B. S. Kaith, *Reactive and Functional Polymers* **2022**, *179*, 105362.

[43] W. Peng, D. Li, K. Dai, Y. Wang, P. Song, H. Li, P. Tang, Z. Zhang, Z. Li, Y. Zhou, C. Zhou, *International Journal of Biological Macromolecules* **2022**, *208*, 400.

[44] T. A. T. Araujo, M. C. Almeida, I. Avanzi, J. Parisi, A. F. Simon Sales, Y. Na, A. Renno, *J Biomater Appl* **2021**, *36*, 95.

[45] F. Wehrhan, E. Nkenke, I. Melnychenko, K. Amann, K. A. Schlegel, C. Goerlach, W.-H. Zimmermann, S. Schultze-Mosgau, *Dermatologic Surgery* **2010**, *36*, 919.

[46] N. Ray, T. van Noorden, F. a. Radu, W. Friess, P. Knabner, *ZAMM - Journal of Applied Mathematics and Mechanics / Zeitschrift für Angewandte Mathematik und Mechanik* **2013**, *93*, 811.

[47] J. D. Robin, W. E. Wright, Y. Zou, S. C. Cossette, M. W. Lawlor, E. Gussoni, *J Vis Exp* **2015**, 52307.

[48] J. M. Liu, *Opt. Lett.* **1982**, *7*, 196.

[49] M. Brugnara, *ImageJ. nih* **2006**.

[50] C. Murru, L. Duvert, F. Magdinier, A. Casanova, A.-P. Alloncle, S. Testa, A. Al-Kattan, *Nanoscale Adv.* **2024**, *6*, 2104.

[51] Z. Püspöki, M. Storath, D. Sage, M. Unser, in *Focus on Bio-Image Informatics* (Eds.: W. H. De Vos, S. Munck, J.-P. Timmermans), Springer International Publishing, Cham, **2016**, pp. 69–93.

[52] J. Schindelin, I. Arganda-Carreras, E. Frise, V. Kaynig, M. Longair, T. Pietzsch, S. Preibisch, C. Rueden, S. Saalfeld, B. Schmid, J.-Y. Tinevez, D. J. White, V. Hartenstein, K. Eliceiri, P. Tomancak, A. Cardona, *Nat Methods* **2012**, *9*, 676.

[53] M. Costantini, S. Testa, P. Mozetic, A. Barbetta, C. Fuoco, E. Fornetti, F. Tamiro, S. Bernardini, J. Jaroszewicz, W. Święszkowski, M. Trombetta, L. Castagnoli, D. Seliktar, P. Garstecki, G. Cesareni, S. Cannata, A. Rainer, C. Gargioli, *Biomaterials* **2017**, *131*, 98.

[54] L. Terrie, M. Burattini, S. Van Vlierberghe, L. Fassina, L. Thorrez, *Front Bioeng Biotechnol* **2022**, *10*, 892287.

[55] D. Cretoiu, L. Pavelescu, F. Duica, M. Radu, N. Suciu, S. M. Cretoiu, *Adv Exp Med Biol* **2018**, *1088*, 23.

[56] F. Yusuf, B. Brand-Saberi, *Histochem Cell Biol* **2012**, *138*, 187.

[57] M. Moncayo-Donoso, G. A. Rico-Llanos, D. A. Garzón-Alvarado, J. Becerra, R. Visser, M. R. Fontanilla, *Polymers* **2021**, *13*, 3187.

3.4 Article 4: Ultrafast infrared laser application for highly organized skeletal muscle tissue modeling: from micrometric laser structuring to LIFT bioprinting.

Lucas Duvert[a,b], Clarissa Murru[a], Adrien Casanova[a], Frederique Magdinier[b], Anne-Patricia Alloncle[a], Stefano Testa[b].

a. Aix-Marseille University, CNRS, LP3 UMR 7341, Campus de Luminy, C13288, Marseille, France.

b. Aix-Marseille University, INSERM, MMG, Marseille Medical Genetics, 13385 Marseille, France.

In preparation

Context

Our last study demonstrated the efficiency of laser-induced topography in guiding cell differentiation on bio-polymers. Nevertheless, limitations to this process are still to be considered. Producing thin collagen layers reproducibly, efficiently, and cost-effectively is an engineering challenge by itself. For this reason, the application of this approach to traditional cell culture and large-scale analysis is, for now, held back by these technical considerations despite promising biological results.

To counteract this technical issue, we propose here another strategy for effective *in vitro* tissue and organ reproduction, with a particular emphasis on skeletal muscle cell alignment to create organized muscle fibers. We set aside biopolymers to explore the option of femtosecond laser processing of polystyrene (PS), a common cell culture surface. Our goal was to create structured surfaces able to promote the alignment and organization of muscle cells, ultimately developing a highly organized 2D skeletal muscle cells model. The laser structuring process presented some caveats, such as enhanced autofluorescence of PS-structured surfaces. We tackled this problem by exploiting photobleaching effects and the use of appropriate analysis tools and reagents for cell imaging. The fast, single-step, and chemical-free method we propose is a practical and efficient alternative to traditional complex manufacturing methods for producing

topographical cues on cell culture surfaces. After setting up the experimental conditions using different cells lines from healthy donors, we then applied this process to cells from patients affected with muscular dystrophies, specifically Duchenne muscular dystrophy (DMD) and facioscapulohumeral dystrophy (FSHD). DMD is an X-linked disease that causes muscle wasting and is linked to mutations in the Dystrophin gene. FSHD is an autosomal dominant disease that affects specific muscles and involves the misexpression of the DUX4 protein, leading to muscle degradation.

In parallel, we took advantage of our expertise in LIFT and previous results to further increase the versatility of the process by combining laser-assisted bio-printing and laser-induced topography in a single set-up. The objective is here to palliate the inability of LIFT to provide intrinsic scaffolding during the printing process that could guide cell development. Here, we propose to deposit cells in predefined patterns to exploit LIFT resolution while enhancing surface-guided cell organization. Additionally, a spray-based method was developed to increase the receiver's coating manufacturing speed while improving its homogeneity and reproducibility.

This dual-process method was finally applied to create muscle disease models, allowing precise alignment and differentiation of healthy and dystrophic myoblasts. By revealing significant phenotypical differences between models, these new tools open new perspectives for investigation disease-linked alteration at the cellular level.

Results

The complete characterization of the laser ablation of PS surfaces was first done in the picosecond and femtosecond regimes. We analyzed the depth of the created channels depending on laser pulse energy, scan speed, and pulse duration through confocal microscopy and scanning electron microscopy. We determined a set of laser and processing parameters able to reproducibly generate channels on the bottom of commercial PS culture plates **(Fig 15.A,B)**. The channels were further characterized through contact angle measurement to quantify the induced hydrophobicity of the structured areas. The apparent shape of water droplets and the angle measurement confirmed the creation of hydrophobic surfaces, which was explained by the chemical composition of PS. The latter was analyzed using Fourier Transform Infrared Spectroscopy (FTIR) analysis to evaluate the impact of laser structuration. In this regard, no chemical differences were found, and an MTT assay performed with C2C12 murine

myoblasts indicated a perfectly bio-compatible surface. In parallel, it was observed that the laser structuration of PS surfaces induces a massive increase in the natural PS autofluorescence. Once again, this effect is explained by the chemical composition of the PS and can be treated through photobleaching. By exposing the LS surface to UV light for only 10 minutes, we observed that autofluorescence could be reduced by almost 75%, providing an efficient solution to treat large amounts of samples and preserving the quality of the channels.

In a second step, we evaluated the alignment of C2C12 on different channel spacing to further optimize the process. Various brands of culture dishes were also tested to confirm the universality of the process and its independence from specific commercial surface or coatings. An ideal channel spacing of 125 µm was determined to promote cell alignment and myotubes length **(Fig 15.C)**. Strangely, the fusion index did not reveal any improvement induced by laser-structured surfaces compared to the unprocessed original.

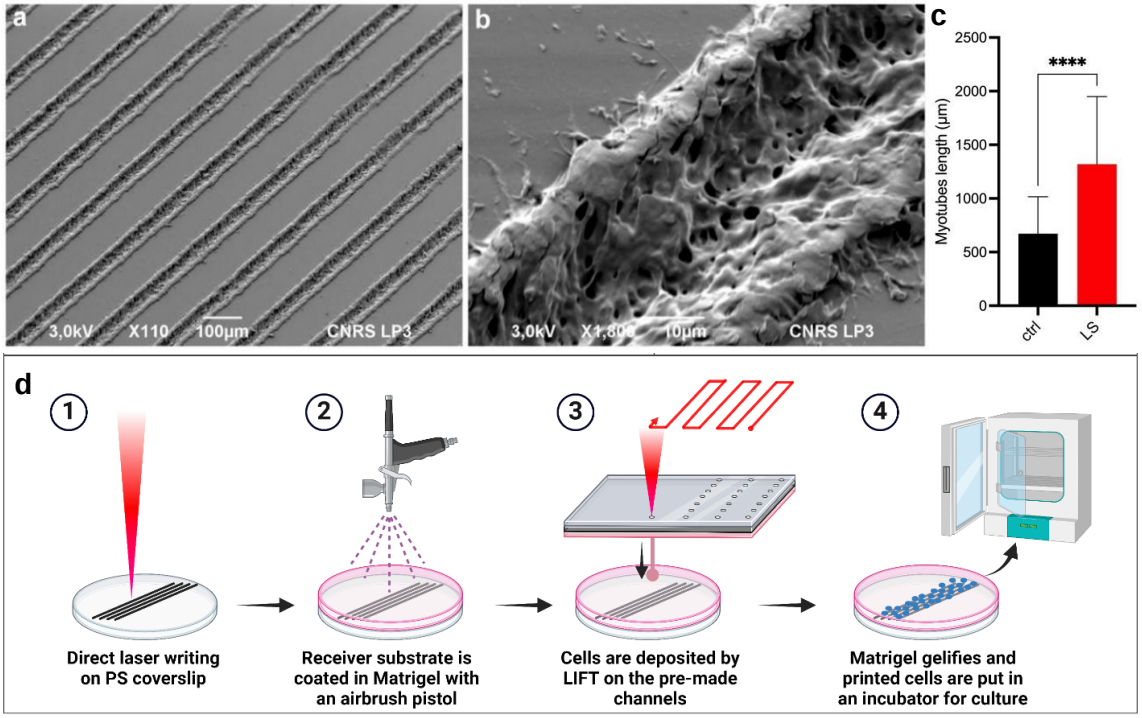

Figure 15: (**a-b**) Scanning electron microscope (SEM) images of laser structured (LS) polystyrene (PS) surfaces. High porosity accompanied by material redeposition on the side of the channels can be observed. (**c**) Analysis of C2C12 myotubes elongation on LS surfaces. The length of myotubes cultured on LS surfaces (red) was significantly higher than that of myotubes on control surfaces (ctrl, black), ($p<0,0001$). (**d**) Workflow combining direct laser structuration and LIFT bioprinting. (1) PS coverslips are structured through laser ablation to create parallel channels. (2) The channels are covered in Matrigel by airbrushing to ensure homogeneity and reproducibility. (3) Cells are printed by LIFT directly in the pre-made channels. (4) Once the Matrigel has gelified, the PS slide is moved from the laser set-up to the incubator for culture.

Once fully characterized, the laser-structured surfaces were combined with LIFT bioprinting. As explained in previous articles, to guarantee cell survival, a coating of hydrogel (here Matrigel) is required on the receiver substrate. Given the hydrophobicity of the channels created and to improve the reproducibility of this step, we developed an airbrush system based on the use of a commercial, inexpensive airbrush paint gun. The latter was extensively modified to spray short pulses of Matrigel while avoiding premature gelation and clogging. This way, the laser-structured surfaces can be coated with a thin layer of Matrigel quickly, efficiently, and reproducibly. We used this method to deposit in lines, aligned with the previously ablated pattern, healthy and dystrophic human myoblasts **(Fig 15.D)**. The morphological characterization of the printed cells revealed a clear difference between the healthy and pathological cell types. Immunofluorescence with appropriate dyes also reveals phenotypical differences for both diseases in the fabricated skeletal muscle model (myotubes diameter and length, fusion index) **(Fig 16)**.

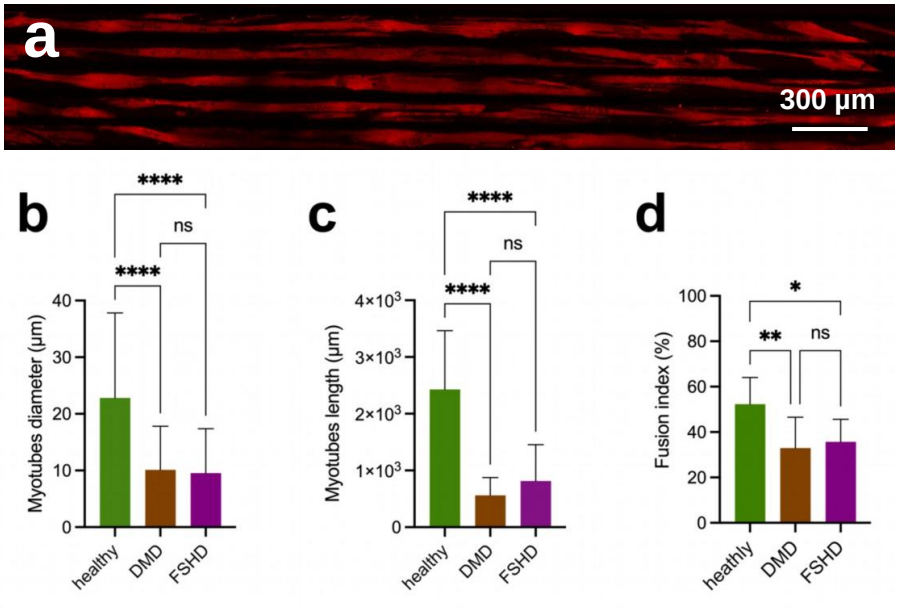

Figure 16: (**a**) Immunofluorescence analysis of post-printed healthy myotubes on PS structured surfaces. The pictures represent the myotubes, positive for Myosin Heavy Chain (Red). (**b-c-d**) Quantitative analysis of maturation and differentiation of healthy (green), DMD (brown) and FSHD affected cells (purple). The diameter (**b**) length (**c**) and fusion index (**d**) of cultured myotubes are all significantly higher for the healthy control.

Conclusions

Laser-induced channels on PS surfaces constitute a solid method to guide cell development and partially improve the maturation of cultured myoblast. These

characteristics are reinforced by the efficiency, rapidity, and versatility of the process. The use of traditional culture boxes allows for rapid integration in cell culture workflow and is perfectly suited for large-scale standardized analysis. Given its reproducibility, we chose this strategy to combine LIFT bioprinting. LIFT brings the ability to precisely position cells on a culture plate while surface structuration improves surface guidance and promotes the proper organization of the engineered muscle model.

Contribution

In this study, I performed the parametrical analysis and characterization of the laser-structured PS surfaces. The autofluorescence induced by the laser ablation was again characterized, and I implemented solutions based on active photobleaching to extensively reduce it. I designed, fabricated, and implemented a spray-based solution to smoothly combine the LIFT bio-printing to the structuration process. I performed the bio-printing experiments and managed cell cultures. Finally, I analyzed dystrophic cell morphology and automated some of this characterization through Matlab.

Publication

Ultrafast infrared laser application for highly organized skeletal muscle tissue modeling: from micrometric laser structuring to LIFT bioprinting

Lucas Duvert[a,b], Clarissa Murru[a], Adrien Casanova[a], Daniel Ferry[c], Pierre Perrin[b], Frederique Magdinier[b], Anne-Patricia Alloncle[a], Stefano Testa[b].

a. Aix-Marseille University, CNRS, LP3 UMR 7341, Campus de Luminy, C13288, Marseille, France.

b. Aix-Marseille University, INSERM, MMG, Marseille Medical Genetics, 13385 Marseille, France.

c. Aix-Marseille University, CNRS, CINaM UMR 7325 - Campus de Luminy, 13288, Marseille, France.

Abstract

Engineered culture surface topography has proven to be an efficient way to guide and organize cell cultures, making it particularly valuable for tissue engineering. By controlling the alignment and spatial organization of cells, it is possible to replicate in vitro the physiological architecture of highly organized tissues, such as skeletal muscle. In this study, we examine the ability of femtosecond-laser-induced topography to guide muscle cells and improve differentiation on commercial polystyrene culture plates. We characterized the modified surface and studied its capacity to induce cell alignment and improve terminal differentiation and maturation. Based on laser ablation, the employed method allows the creation of highly porous channels that exhibit enhanced hydrophobicity while offering strong mechanical cues for cell guidance. Combined, these conditions led myoblasts cultured on laser-structured surfaces to fuse into highly aligned multinucleated myotubes, with a significantly improved yield compared to classical 2D-culture conditions. To further refine the model, we exploited the full capacity of ultra-fast lasers by combining laser ablation with Laser Induced Forward Transfer, a 3D laser-based bioprinting method. The two techniques were efficiently merged to allow for the precise positioning of cells directly on topographical pre-designed patterns. We applied this strategy to disease modeling by considering two of the most common muscular dystrophies, Duchenne muscular dystrophy (DMD) and Facioscapulohumeral dystrophy (FSHD). The printed cells successfully recapitulated pathological defects with significant differences in myotubes morphology and the observation of disease hallmarks. Here, we propose an integrated laser-based processing of commercial culture plates for induced cell alignment combined with a bio-printing method extending the tissue modeling applications. The techniques proposed in this study will be necessary for accessible and standardized 2D tissue engineering approaches. Its effectiveness and versatility widen its application to high throughput screening for therapeutic development and personalized medicine.

1- Introduction

Effective *in vitro* reproduction of tissues and organs requires a deep understanding of their respective cellular components and relative involvement in maintaining tissue homeostasis [1]. Added to the reproduction of tissue function, this set of conditions constitutes a milestone in tissue engineering [2]. Yet, biological complexity is not the only issue to be addressed in *in vitro* modeling [3]. The specific spatial organization of different cell populations and the replication of the typical tissue/organ architecture are as important as the biological counterpart to obtain a reliable *in vitro* model. For example, skeletal muscle tissue is characterized by an isotropic structure of aligned muscle fibers fundamental for the isometric or eccentric contractility and transmission of effective force [4].

Nowadays, several approaches aim to mimic tissue-specific architecture in both 2D and 3D, mainly by replicating the organization of the extracellular matrix (ECM). In this context, various tissue engineering strategies can either replace or be implemented in traditional 2D cell culture to achieve a higher cell organization.
Among these methods, the most widely used for its accessibility and easy workflow integration is the addition of 2D/3D topographical cues to the surface of cell culture supports. Micropatterned surfaces have indeed proven to be a suitable support for modeling different tissues, from endothelium [5] to neural [6] and muscle tissue [7,8]. For the latest, micropatterned surfaces are able to influence myoblast orientation, differentiation, and maturation [9,10]. Photopatterning (or soft lithography) and melt-casting systems constitute the two most widespread surface micropatterning methods used to create micro-grooved and topographical modifications on natural or synthetic polymer surfaces [9,11].
Currently, only a few solutions are commercially available to replicate this specific organization in 2D cell cultures, ranging from thin matrix of aligned nanofibers to nano/micro-structured surfaces treated to modulate the adhesion/non-adhesion of the cells on the dish surface. Due to complex multi-step manufacturing techniques, these solutions remain expensive to integrate into traditional cell biology workflow and can yield varying results depending on the brand and cell types to be used.
The recent advent of ultrafast lasers has democratized the use of laser ablation as a solid, easily accessible approach for micro-to-nano structuration. In this context, its utilization to create bioinspired laser-structured (LS) surfaces has been increasingly studied [12,13] because of its versatility and ability to process a wide range of synthetic and natural materials. Similarly to the previously described methods, the so-obtained LS surfaces are able to influence cell behavior and intrinsic mechanisms such as adhesion, proliferation, and alignment [14,15], creating, for example, an environment conducive to cell interaction and osteogenic differentiation [16].
Laser-ablation techniques allow the generation of complex structured surfaces of any designed pattern with extreme rapidity and reproducibility. When a laser is focused on a polymer substrate, material removal through ablation occurs once the laser fluence exceeds a threshold, which is determined by the material's composition, as well as the laser wavelength and pulse duration [17]. Due to the use of extremely short pulse duration, femtosecond laser processing is done through nonlinear multiphoton absorption [18]. This mechanism allows sufficient peak energy for the laser to interact with materials transparent to its wavelength. Additionally, the ultra-short pulses are shorter than the heat diffusion time (>10 ps), leading to a minimal heat-affected zone [19]. For these reasons, the choice is here to exploit the optical characteristics of a femtosecond laser for structuring the polymeric surfaces of standard commercially available cell culture plates for ease of use and integrability. The laser irradiation of polystyrene (PS), the most widespread polymer used for culture labware, was thoroughly investigated. The resulting structured substrates are studied to evaluate their impact on the survival of myogenic cells and their ability to guide cellular organization, promoting the alignment of the resulting myotubes to give rise to a highly organized 2D skeletal muscle model. We present a fast, single-step, chemical-free method to produce laser-structured surfaces with micrometric topography adapted to skeletal muscle cell culture.

To further improve the model's relevancy and fabricate an extracellular environment that will promote physiological-like processes together with better maturation of cultured myotubes [20], we investigated the implementation of bioprinting to the previously developed technique.

Bioprinting has become increasingly present in tissue engineering research because of its ability to precisely position living cells and ECM components, recreating the hierarchical organization of tissues and organs [21–25]. Different bioprinting approaches can be chosen depending on the researched objective, each with its own potential, field of predilection, and limitations. Among these methods, extrusion-based printing is the most widely used technique to reproduce the 3D anisotropic organization of skeletal muscle tissue. Its ability to efficiently produce continuous printing fibers naturally mimics the muscle architecture [26,27], making it the first choice in this application. However, this technique is quickly limited by a resolution that hardly drops below 100 µm, a limited amount of usable biomaterials, and arguable reliability [28–30].
In this context, laser-based methods such as the Laser-Induced Forward Transfer (LIFT) technique offers a suitable alternative to precisely organize cells with superior resolution and accuracy. This method is based on the laser-matter interaction of a laser pulse to transfer a small quantity of matter from a donor substrate to a receiver slide placed a few hundred microns apart [31–33]. The donor substrate comprises a thin glass slide with a metallic dynamic release layer (DRL), onto which the bio-ink was spread as a thin ribbon. The laser pulse vaporizes the DRL to induce the creation of a jet that will deposit a small amount of the bio-ink at the precise location of the laser interaction with the donor. At its origin, the method was extensively employed for electronic applications [34–36] and the printing of conductive material. It was democratized in tissue engineering by its ability to deposit an extensive range of cell types [37–40] and biomaterials [41–43] with excellent cell survival rates and high resolution. Numerous studies report on the use of LIFT for patterning endothelial cells, fibroblasts, and keratinocytes used for skin modeling, and even induced pluripotent stem cells with extremely high post-printing survival rates [44].
Compared to extrusion bio-printing that creates pre-constraint fibers embedded with cells, the LIFT process falls short of providing a scaffold to constrain and guide cell development. To overcome this limitation, we merged advanced laser-based bio-printing methods with laser-induced topography to precisely deposit cells in pre-designed patterns that will further improve surface guiding and promote maturation. In this way, we make use of LIFT capacities, resolution, and versatility combined with the cell guidance offered by surface topography in a single and efficient process to produce isolated muscle fibers in a highly controlled way. This strategy further motivates the choice of a near-infrared femtosecond laser capable of structuring polymers while minimizing laser-cell interaction during laser-assisted bioprinting [38].

Secondly, the application of this multi-technique procedure to disease modeling is investigated, focusing on two of the most common muscular dystrophies: Duchenne muscular dystrophy (DMD) and Facioscapulohumeral dystrophy (FSHD). DMD is an X-linked muscle-wasting disease that affects 1: 5000 male individuals with lethal consequences due to respiratory and cardiac complications [45]. The disease is caused by mutations in the *DMD* gene that codes for dystrophin, a structural protein involved in the maintenance of muscle fiber integrity. FSHD is an autosomal dominant disease affecting specific facial, shoulder, and pelvic girdle muscles, causing progressive weakness. The incidence rate is 1: 20,000, making FSHD the third most common myopathy. The main FSHD1 variant is due to the deletion of repetitive microsatellite elements (D4Z4) in the 4q35 subtelomeric region, leading to the misexpression of DUX4 protein in adult skeletal muscle with cytotoxic effects and subsequent muscle wasting [46]. Especially for FSHD, existing animal and cellular models cannot fully recapitulate the pathophysiological processes of dystrophy, highlighting the need for reliable disease models based on multidisciplinary approaches [47].

The process combination is thus applied to obtain disease models with a high resolution and reproducibility. In practice, immediately after the laser structuring of the polymer surface, healthy and FSHD/DMD-affected myoblasts are printed in a predefined pattern of parallel lines according to the direction of structuring. The results and effects in alignment, differentiation, and disease hallmarks are evaluated. The proposed concept of merging laser-assisted 3D bioprinting and direct laser writing in a single simple laser-based tissue engineering platform widens the scope of cell culture possibilities and could democratize special strategies to enhance our understanding of tissue function and disease-associated dysfunctions together with high throughput screening.

2- Materials and methods

2.1 Micrometric laser structuring

2.1.1 Laser topography and optical characterization

Generation of the topography was carried out on cell-adhesion treated culture plates (Thermo Fisher) using a pulsed pico to femtosecond laser (Light Conversion Carbide CB-01 Yb:KGW) with a fundamental wavelength of 1030 nm at a frequency of 60 kHz. The laser's average power is 5 W, and its maximum energy per pulse is close to 85 µJ at 60 KHz. A polarizer coupled with a half-wave plate is positioned in the optical path of the laser to reduce and tune the energy deposited on the substrate. The laser beam is finally routed on a high-speed optical scan system (ScanLab intelliSCAN14) coupled with a 70 mm focal length F-Theta lens (Linos F-Theta-Ronar lenses, spot size 2wo = 36µm), which allows us to generate complex marking patterns in a fast and efficient manner. The precise experimental set-up for laser structuring is detailed in **Supplementary Figure 1**. Parallel lines will here be used to ensure the guiding and alignment of the cultured cells. The in between line spacing, as well as the laser pulse overlap, will both be controlled by the scanning system software and the scan speed. Pulse overlap can be determined using the equation [16]:

$$\text{Pulse overlap} = 1 - \frac{\mathrm{v}}{2\mathrm{w}_0 * \mathrm{f}}$$

With v the scan speed, wo the waist of the laser beam, and f the repetition rate of the laser.

The use of an ultrafast laser and its precise focusing on the bottom of commercially available cell culture plates prevent the interaction of the laser with clear polystyrene covers; the box can thus be structured while remaining closed, thereby maintaining sterility. This is only valid for small wells or small structuring patterns, where the vapors generated by ablation remain limited. For larger areas, chemical or autoclave sterilization is entirely possible. The precise beam control allows us to quickly process a large number of samples without additional manipulation or treatment, with the ability to preserve the sterility of the boxes.
In order to study the formation of the created channels and to control their dimensions and characteristics, the influence of pulse duration, laser pulse energy as well as the overlap of the pulses was investigated together with the influence of channel spacing on cell alignment. The characterization of the laser-structured surfaces was achieved using scanning electron microscopy (SEM, JEOL JSM-6390, Tokyo, Japan) working at 3 kV after metalization (gold, 20 nm) of the sample and confocal microscopy (Keyence, VKX-3000). For all the parameters considered, channel depth and width were evaluated by confocal microscopy through the

average of 30 profile lines perpendicularly to the channel orientation. The depth value is calculated between the highest and the lowest point encountered on the profile line (**Suppl. Fig 2**).

2.1.2 Contact angles

Wettability modifications of the laser-structured surface were characterized by studying contact angles. Five µL of distilled water was deposited on the created topography and photographed at two different angles (0° and 90°, Fig. 7a) through a camera (DAHUA) equipped with a 10X zoom lens (Computar). The droplets were illuminated by a white light source (Wild HeerBrugg) placed on the opposite side of the camera to obtain sharp images of their edges. The angle between the droplet and the surface was calculated using the *Contact Angles* plugin for FIJI software. The obtained value was used as an index of hydrophobicity: values ranging from 90° to 0° indicate an increase in hydrophobicity, while values comprised between 90° and 180° an increase in hydrophilicity. Top pictures of the droplets were done by numerical microscopy (Keyence VHX-7000).

2.1.3 Chemical analysis

The surface chemistry and thermal behavior of the laser-structured surfaces were recorded in attenuated total reflectance (ATR, germanium crystal) mode using a Bruker VERTEX70 mid-IR Fourier Transform spectrometer equipped with a temperature-stabilized DLaTGS detector. All spectra were accumulated on the surface of the different areas in a spectral range of 650–4000 cm^{-1} by recording 200 scans at a resolution of 4 cm^{-1}. The spectra were normalized to the maximum absorbance reached.

2.1.4 Cell culture

Murine myoblasts C2C12 (ATCC) were cultured according to a previously published protocol in T-75 Flasks (Sarstedt) at 37 ° C and 5% CO_2 in DMEM GlutaMAX (Gibco) supplemented with 10% heat-inactivated fetal bovine serum (FBS, EuroClone), penicillin (100 IU mL^{-1}, Gibco), and streptomycin (100 mg mL^{-1}, Gibco). To stimulate differentiation, once 90% confluency was reached, cells were transferred to a differentiation medium (DM) composed of DMEM GlutaMAX (Gibco) supplemented with 2% horse serum (Gibco). The images and counting of the cells were obtained with a reverse microscope (EVOS M5000, Invitrogen, Thermo Fisher, America).

Dystrophic immortalized myoblasts (DMD and FSHD) were cultured in Growth Medium (GM) composed of 4 parts of Dulbecco's modified Eagle medium (DMEM, Gibco) and 1 part of Medium 199 (Gibco), supplemented with 20% of FBS (Euroclone), Fetuin (25 µg/mL, Life Technologies), hEGF (5ng/mL, Life Technologies), bFGF (0,5ng/mL, Life Technologies), Dexamethasone (0,2 mg/mL, Sigma) and insulin (5 µg/mL, Sigma). To stimulate differentiation, once 90% confluency was reached, cells were transferred to DM composed of GM supplemented with insulin (10 µg/mL, Sigma).

2.1.5 Proliferation assay

For cell survival assays, C2C12 cells were seeded in laser-structured 12-well plates (Thermo Fisher) at 5 × 10^4 cells per well, respectively. After 24, 48, and 72 hours of exposure to the

channels, cell viability was determined by MTT (3-(4,5-dimethylthiazol-2-yl)-2,5-diphenyltetrazolium bromide) colorimetric assay (Invitrogen, Thermo Fisher Scientific). This test is based on the reduction of the tetrazolium salt by the mitochondria of living cells. The absorbance measured at 600 nm is proportional to the number of living cells.

2.1.6 Differentiation assay

The Fusion Index (FI) is indicative of the level of differentiation of myoblasts into myotubes. It is defined as the ratio of nuclei in Myosin Heavy Chain-expressing myotubes (containing at least three nuclei) over the number of nuclei for each field. To assess the influence of the laser-created topography on myoblasts' myogenic differentiation, FI was manually scored using the Fiji software. C2C12 were seeded at 10^5 cells per well into the laser-structured 12-well plates (Thermo Fisher Scientific). After 48h, the cells reached adequate confluence (90%), and the medium was changed to Differentiation Medium (DM) to induce myotubes formation. DM was changed every 48 hours for up to 1 week to allow for proper myogenic differentiation. Then, after rinsing media residues with Phosphate Buffer Saline (PBS,GIBCO), cells were fixed with 4% Paraformaldehyde in PBS at 4 °C for 10 min and stored at 4°C for subsequent immunostaining analysis.

2.1.7 Immunostaining analysis

Samples were analyzed by immunofluorescence according to the following protocol: cells were permeabilized in a 0.3% solution of Triton X-100 (Sigma) in PBS for 1 h at room temperature (RT) and blocked with a blocking solution consisting of 10% natural goat serum (Thermo Fisher Scientific), 1% glycine (Thermo Fisher Scientific), 0.1% Triton X-100 in PBS for 1 h at RT. Subsequently, cells were incubated with mouse monoclonal anti-Myosin Heavy Chain (MF20, DHSB) primary antibody, diluted 1:100 in blocking solution for 2 h at RT and then rinsed with a washing solution consisting of 1% Bovine Serum Albumin (BSA, Sigma) and 0.2% Triton X-100 in PBS. After washing, cells were incubated with Alexa Fluor 555-conjugated goat anti-mouse IgG secondary antibody (H + L; Thermo Fisher Scientific, diluted 1:400) for 1 h. Finally, nuclei were counterstained with 300 nM DAPI (Thermo Fisher Scientific) in PBS for 10 min.

2.1.8 Cell orientation

After the staining by immunofluorescence, the orientation of the myoblasts was studied using the *Orientation J* plugin for FIJI software. In particular, the *Orientation J distribution tool* allows us to obtain a weighted histogram of the orientation of the analyzed elements, ranging from 0 to 180 degrees. In contrast, the weight of this orientation is indicated by the coherency: a value ranging from 0 (isotropic areas) to 1 (highly oriented surfaces) calculated by the *Orientation J dominant direction tool* [27].

2.1.9 Statistical analysis

All experiments were performed at least in biological triplicate. Data were analyzed using GraphPad Prism 8, and values were expressed as means ± standard error. Statistical significance was tested using one-way ANOVA tests with the appropriate multiple comparison tests. A probability of less than 5% ($p < 0.05$) was considered as statistically significant.

2.2 LIFT bioprinting

2.2.1 - Bio-ink preparation

For bio-ink formulation, cells were harvested using a trypsin/EDTA 1 x solution (GIBCO) and centrifuged in PBS at 115 g for 10 min. PBS was carefully removed and replaced by an adequate volume of a gelatin (Sigma-Aldrich) 2 % solution in DMEM (final concentration 5 x 10^7 cells/ml). The use of gelatin increases the bio-ink viscosity and facilitates the creation of jets during the printing process, leading to an increase in reproducibility and printing resolution (**Article 1**).

2.2.2 - Topography

The process of printing living cells is here divided into three parts: (i) the creation of the topography directly on the receiver substrate, (ii) the deposition of a hydrogel coating on the substrate to guarantee optimal cell survival, (iii) the positioning of the cells onto the specially designed topographical pattern by LIFT.
The receiver substrate is made of a 0.15 mm thick polyethylene terephthalate glycol (PET-G) tissue culture coverslip (Sarstedt). It was first sterilized with a 70% ethanol solution for 30 minutes before being positioned on a specially designed apparatus, which kept it firmly in place by negative pressure. The support, in turn, was positioned under the incident laser beam. The laser's pulse duration was set to 213 femtoseconds, and the laser pulse energy and the scanning speed were adjusted depending on the desired topography. The pattern was programmed on the scanning system software *LaserDesk* and completed in a few milliseconds. Given the use of muscle cells and the anisotropic nature of muscle tissue, a pattern of parallel channels across the entire surface of the receiver slide was designed to better mimic the muscle tissue architecture.

2.2.3 – Airbrushing system for uniform coating of the receiver slide

The second step involved applying a thin layer of Matrigel onto the structured slide. This hydrogel coating is crucial to ensure the survival of the printed cells and their accurate spatial localization. The creation of this layer was automated to guarantee optimal reproducibility and to preserve the positioning of the created topography. To this end, a commercially available airbrush spray (Timbertech, ABPST01) was extensively modified to meet these requirements. The airbrush uses compressed air to atomize and spray a liquid stored in its tank. This tank and the nozzle of the airbrush were coiled with soft tubing into which cold water was being circulated. This homemade water-cooling system allowed the use of Matrigel as a targeted material for the airbrush while avoiding its premature stiffening, which could lead to the clogging of the nozzle. This way, the whole metal assembly can be cooled under 10°C to keep the Matrigel liquid. The supply of compressed air to the airbrush was controlled with a solenoid valve (Heschen). The opening time of this valve corresponds directly to the airbrush spray duration, with control down to 0.2s. The intensity of the spray can be adjusted through the air compressor (Timbertech). The manual movement of the airbrush's internal needle modifies the nozzle size opening, which, in turn, determines the amount of material sprayed. This internal needle was connected to a stepper motor (Stepperonline) to allow its precise and programmable opening. Finally, an Arduino UNO was used to control the motor and the solenoid valve, giving us control of the duration of the spray, its intensity, and the amount of material deposited. The airbrush's nozzle was positioned perpendicularly, 7.5 cm from the receiver substrate. Due to the thickness of pure Matrigel and to limit the risk of

clogging, a solution of 1/2 Matrigel in DMEM was used as coating material. After the creation of the topography, the receiver substrate was moved thanks to an XY translation stage (Newport 150 mm) under the airbrush. Two consecutive sprays of Matrigel, spaced by 120 seconds, were deposited on the substrate, creating a perfectly uniform coating on top of the created channels. The receiver substrate was then moved back under the scan system to receive the cells by LIFT.

2.2.4 - LIFT bioprinting

The LIFT bioprinting method requires a donor substrate from where the cells will be ejected onto the previously prepared receiver. The donor substrate is made of a titanium wafer (LAAS France) onto which individual wells were created to receive the bio-ink and control its layer thickness (**Article 2**). Once the receiver substrate was ready, the bio-ink was deposited in the well and spread homogeneously. A (X, Y, Z) motorized stage (Newport Motion Controller XPS) allows the translation of the donor substrate in the direction of the incident laser beam (vertical direction z) as well as the other perpendicular directions (x and y). After the deposition of the bioink, the donor was positioned inverted with the ink facing down and held by negative pressure in the previously described apparatus. It was then lowered toward the receiver, and the gap between the two substrates was controlled thanks to a camera. The precise experimental set-up for LIFT bioprinting is detailed in **Supplementary Figure 3**.The laser pulse duration was set to 10 ps to promote the formation of the jet. A printing pattern made of lined dots, spaced by 250 µm, matched the previously created topography. Once the cells were printed, the receiver substrate was kept under a small-scale humid chamber to allow for complete gelation of the Matrigel. After a few minutes, the receiver slide was moved from under the laser set-up to a 12-well culture plate. After 15 minutes of incubation at 37°C, growth medium was added to the wells, and the cells were kept in the incubator to allow them to grow and differentiate.

3- Results

3.1 Topographical modification of polystyrene culture plates and cell guidance

Polystyrene (PS) culture plates are predominant in cell culture labware and were thus first used to evaluate the potentialities of laser-induced topography. Given the absorption spectrum of the PS, primarily situated in the UV around 260 nm, the use of an infrared laser leads to a reduced amount of energy absorbed by the polymer. This issue was addressed by the use of ultrashort pulses in the order of pico to femtosecond to maximize the interaction between the pulse and the bulk of the material via nonlinear absorption. Two distinct laser pulse durations accessible with our laser source, 10 ps and 213 fs, were thus considered to create the topography and further evaluated.

3.1.1 Channel characterization

For both pulse durations, pulse energy was investigated from 4.8 to 36.3µJ, and the overlap of the pulses ranged from 48% to 95%, with 100% overlap corresponding to the complete superposition of two consecutive laser pulses. For this analysis, the channel spacing was set to 125 µm **(Fig 1.a)**.

The observation of the resulting structured surfaces with SEM revealed a highly organized pattern of channels with consistent results throughout the processed sample (**Fig 1.b**). The interaction of the laser with the polymeric surface induced a partial and localized melting and vaporization of the material, altering the topography from a smooth surface to an irregular and porous one. The partial redeposition of the melted material could be noticed on the side of the created channels. Confocal microscopy topographical analysis revealed that this material redeposition can account for almost 50% of the total height of the created topography. This amount logically varied depending on the energy density deposited on the substrate, either by a higher pulse energy and/or overlap. Based on the objectives of our work and their potential benefits to guide cell organization, the depth measurement of the channels took into account the creation of these protrusions. These depths are reported in **Figure 1.c,d** for both pulse durations considered and divided into four categories depending on their quality. Green dots represent well-defined and reproducible channels of sufficient depth **(Fig 1.e)**, and yellow dots symbolize highly porous channels of limited depth **(Fig 1.f)**, both suited for cell culture and alignment. Red dots represent the creation of porosity on the surface of the polymer without any actual depth being created. As illustrated by the negative depth values, given these marking parameters, the interaction of the laser with the PS only induces partial in-situ melting of the material. The result is a protrusion band of high porosity and low reproducibility on the surface of the cell culture well **(Fig 1.g)**. Finally, blue dots designate the absence of marking.

As expected, femtosecond pulses offered a large number of energy/overlap couples suitable for the creation of channels with adjustable depth. For both parameters considered, the evolution of its complement was logically accompanied by a progressive decrease of the channel depths, going, for a large majority of them, through all four conditions previously described. The achievable channel depth varied from 6 to 65 µm with an associated width varying from 30 (size of the laser beam) to 127 µm.

On the other hand, picosecond pulses naturally presented less viable options: 20% of the conditions tested resulted in well-defined channels, while femtosecond pulses reached 43%. Contrary to femtosecond ablation, we could also notice a clear marking threshold, beyond which not enough energy was deposited on the polymeric surface to induce topographical changes or create porosity. The range of achievable depth thus varied from 19 to 51 µm. Given poorer energy deposition due to a limited nonlinear absorption, more energy was required with picosecond pulses to achieve the required intensity for breakdown [19]. This absorption difference also appeared in the appearance of the channel's porosity (**Suppl. Fig 4**).

Based on these results, the following study of the created topography was done with a pulse duration of 213 femtoseconds, an overlap of 79%, and a pulse energy of 22.8 µJ. These parameters allowed the creation of 11.5 µm deep channels of 45 µm width. The protrusion of melted material accounted for 41% of the total height of the induced topography.

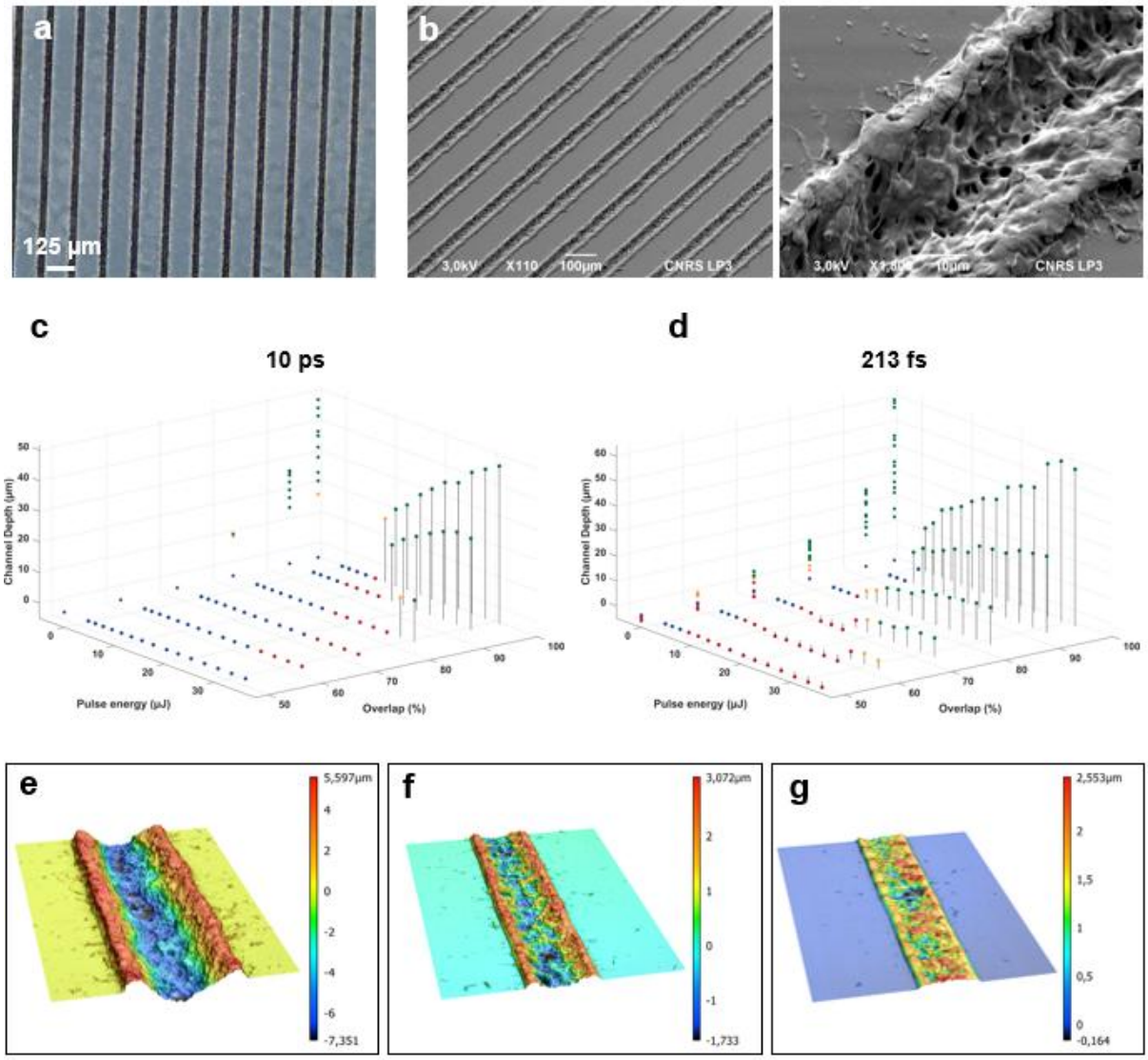

Fig. 1: **(a)** Macroscopic observation of structured culture plate by optical microscope, channel spacing is set at 125 µm.(**b**) Scanning electron microscope (SEM) pictures. **(c-d)** Parametric study of the laser-created channel depth depending on the laser pulse energy and the shot-to-shot overlap for 213 fs (Left) and 10 ps (Right). The depth values are projected on the z axis for easier reading. Green dots indicate well-formed channel with pronounced topographical modifications (**e**), yellow dots indicate the creation of porosity with a slightly indented surface (**f**), red dots indicate only the creation of porosity with a final topography protruding from the surface (**g**). Blue dots indicate the absence of marking by the laser pulses.

3.1.2 Autofluorescence

Polymer surfaces are known to be autofluorescent, especially near the UV light spectrum. The laser-structured (LS) surfaces displayed increased autofluorescence near UV light (DAPI emission peak, 454 nm), a phenomenon that decreased moving toward infrared light (CY5 emission peak, 670 nm). To determine the role of the structuring process in the increase of PS autofluorescence, we analyzed the effect of stronger laser-PS interaction through an incremental number of deposited laser pulses on the PS surface (**Fig 2**). We noticed that one laser pulse only creates limited damage to the PS surface and is not enough to induce porosity (**Fig 2.a**). The associated fluorescence level in DAPI wavelength, where autofluorescence is the

strongest, did not increase. From 2 laser pulses, we observed an increase in porosity and damaged area following the laser pulses interaction (**Fig 2.b-g, h, m**), with a direct correlation between the increase of the area and the fluorescence levels (**Fig 2. i,n**). The latter was calculated as the Mean Gray Value of a defined Region of Interest (ROI, yellow square, **Fig 2.i**) surrounding the laser pulse interaction zone. On the other hand, from the third pulse, the fluorescence value, if measured in the center of the damaged area, remained relatively stable (**Fig 2.l,o**). The previously observed increase in fluorescence with ROI measurements was thus only due to the increase in the fluorescent area associated with the accumulation of laser pulses rather than stronger PS autofluorescence (**Suppl Fig 1**).

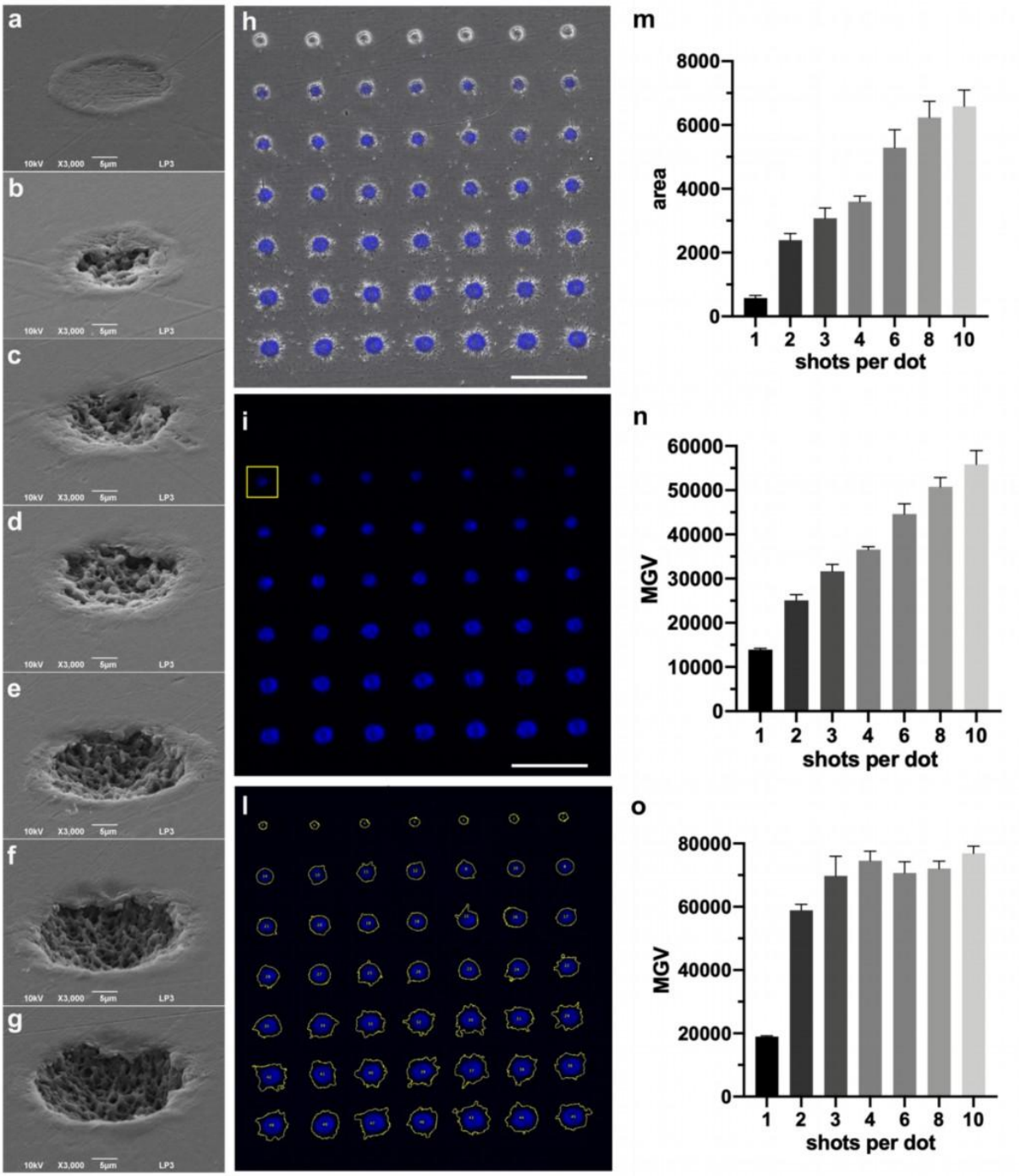

Fig. 2: Systematic study of the effect of multiple laser shots on plastic surface autofluorescence. The effect of laser shot in modifying the porosity of plastic surface is studied by SEM at a different number of pulses per spot: 1 (**a**), 2 (**b**), 3 (**c**), 4 (**d**), 6 (**e**), 8 (**f**), 10 (**g**). The area of the laser hit spots (**h**) is

calculated (**m**). The fluorescence levels at each condition (**i**) are calculated as MGV per ROI of 100x100 pixels (**i, yellow square**) and reported (**n**). The fluorescent particles are identified by Fiji software (**l**), and the resulting MGV per particle is reported (**o).** Scale bar = 150 µm.

To resolve this issue, a photobleaching step was added immediately after the laser structuring process. It has, in fact, been widely demonstrated that exposing auto-fluorescent material, biological or polymeric, to focused illumination can reduce the autofluorescence of the material itself. Following the bleaching procedure set up by Tsuneoka and colleagues [48], the LS surfaces were exposed to an arrangement of 8 50 W cool-white LEDs with a color temperature of 6500K and a luminosity of 5000 lm (Chanzon) (**Suppl. Fig 5.a**) for increasing times up to 5 hours, calculating the fluorescence levels of DAPI wavelength as Mean Gray Values (MGV) by FIJI software (**Fig 4**). Finally, 4 hours was chosen as the exposure time because the MGV line reached a plateau level (**Fig 4**).

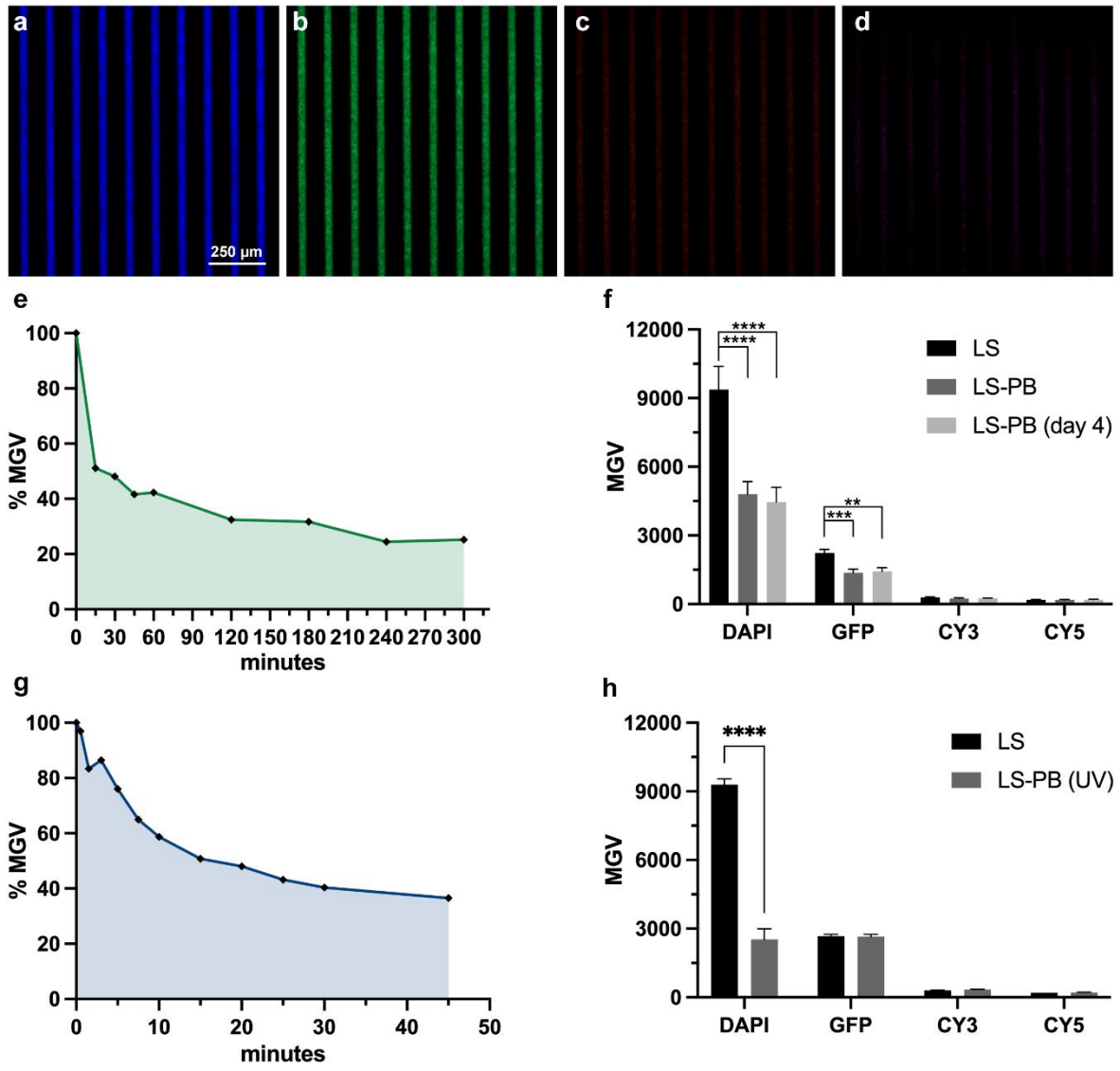

Fig. 3: Autofluorescence of the LS surfaces. The autofluorescence values for Dapi (**a**), GFP (**b**), CY3 (**c**), and CY5 (**d**) wavelength were calculated (**f**) just after laser structuring (LS), after 4 hours of photobleaching (LS-PB) and 4 days after the photobleaching treatment (LS-PB 4 days). Fluorescence level of Dapi over time. Curve of the autofluorescence values for Dapi calculated over time during the continuous exposure to cool-white LED light (**e**) and to UV LEDs (**g**). Autofluorescence for Dapi, GFP,

CY3 and CY5 calculated (**h**) just after laser structuring (LS) and after 10 minutes of exposure to a LED with a wavelength of 365 nm (LS-UV P.B.). (p values: **** p < 0,0001, *** p = 0,0008, ** p = 0,0019).

The analysis conducted on LS surfaces after the photobleaching step showed a drastic reduction in autofluorescence levels for the two more fluorescent fluorophores, a reduction that is also stable over time, as shown by the level measured four days after the photobleaching (**Fig 5.e**).

The downside of this method lies in the temperature increase of the treated samples. The use of powerful LEDs, combined with the increased absorbance due to the presence of the channels, can lead to the melting and deformation of thin polystyrene culture slides. Once again, given the absorbance spectra of the polystyrene (**Suppl. Fig 5.e**), the 50 W white LEDs were switched to a 3 W UV-led (Chanzon, spectra centered at 365 nm) (**Suppl. Fig 5.b**). In this way, as described in **Figure 6**, the overlap between the polymer's absorption band and the UV LED's emission spectra is greater than with the broad-spectrum white LED. Using this method, the fluorescence for DAPI was considerably reduced (73%) in a very short period of 10 minutes (**Fig 6**) without damage to the sample. We can, nevertheless, see no effect of the UV-LED on the fluorescence of other fluorophores.

3.1.3 Contact Angles

To better characterize the changes in the physical properties of the LS surfaces, we decided to perform a contact angle analysis to study the wetting properties of the treated samples. The analysis was conducted for four different channel spacings: ctrl, 75, 100, 125, and 150 µm, according to the laser parameters previously established (pulse energy, duration, and overlap).
This study revealed an increase in the level of surface hydrophobicity in the presence of laser-structured channels, as demonstrated by the different shapes of the droplets when photographed in parallel (**Fig 4.g**) or perpendicular (**Fig 4.e**) to the channels. For all tested conditions, the deposited droplet stretches along the direction of the channel, which creates a hydrophobic barrier. This observation was confirmed by measuring contact angle values perpendicularly (90°) and parallel to the channels (0°). For all LS conditions, these values differed according to the orientation, with differences reaching almost 80% of the original angle. The control, however, presented two identical values (**Fig 4.h**), confirming the influence of the created channels. Finally, the top view of the droplets on control (**Fig 4.b**) and LS (**Fig 4.c**) surfaces revealed the influence of the hydrophobicity of the channels on their sphericity, with a perfect circular shape in the control that became an ellipse with the major axis parallel to the channels on LS surfaces.

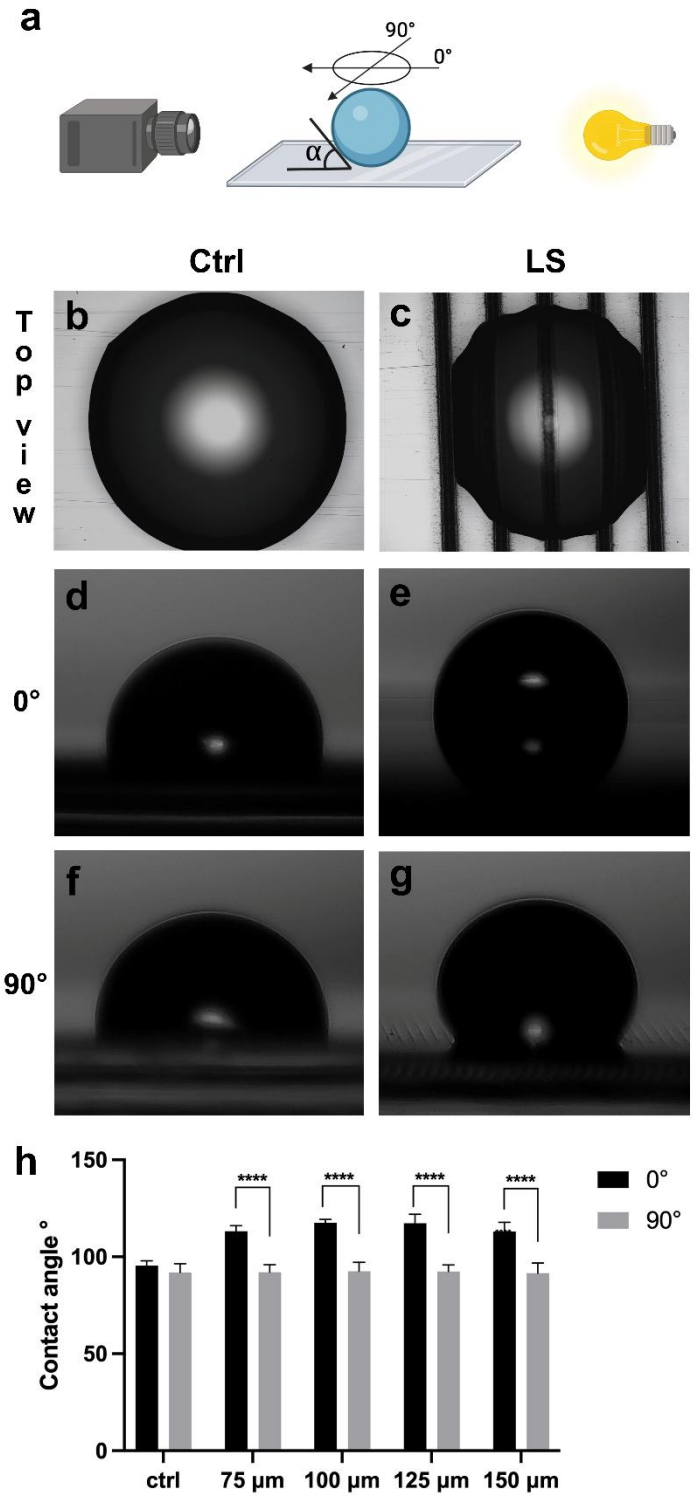

Fig. 4: Contact angle analysis. Scheme of the experimental settings (**a**); Top view of the droplet on control (**b**) and LS (**c**) surfaces; side view at 0° and 90° for the control (**d,f**) and LS (**e,g**) surfaces; histogram of the contact angle values for the different conditions at both 0° and 90° with their relative significance compared to the respective control ($) and between each experimental group (*). (p values: **** $p < 0{,}0001$, $^{\$\$\$\$}$ $p < 0{,}0001$).

3.1.3 FTIR and MTT assay

To verify whether the interaction of the laser with the plastic surface could give rise to the formation of functional groups potentially toxic for cell survival, structured and unstructured samples were analyzed through ATR-FTIR spectroscopy. As shown in **Figure 5** the absorption peaks at the wave numbers of 2942 and 2858 cm^{-1} can be attributed to the asymmetric and symmetric stretching vibrations of the CH_2 methylene groups (saturated C–H). Furthermore, a notable absorption peak at 1460 cm^{-1} can be associated with the stretching vibrations of the aromatic C=C bonds while the peak at the wave numbers of 725 cm^{-1} corresponds to C-H out-of-plane bending vibration [49]. Interestingly, the curves of the two absorbance spectra overlapped, indicating the absence of side products due to laser ablation (**Fig 5.a**).
Secondly, to assess the effect of the laser-structured surfaces on cell viability and proliferation, we performed an MTT (3-(4,5-dimethylthiazol-2-yl)-2,5-diphenyltetrazolium bromide) colorimetric assay.

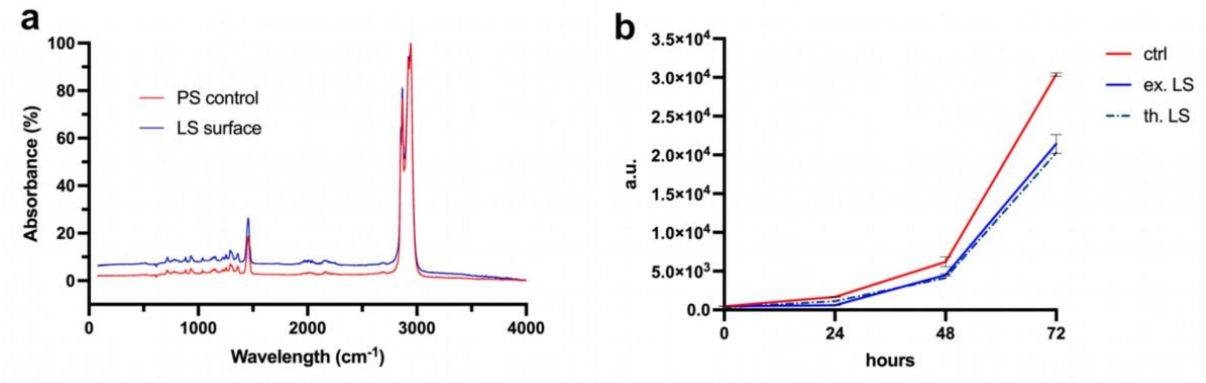

Fig. 5: (a) Infrared spectra of the plastic surface before (PS control, red line) and after (LS surface, blue line) laser structuring; **(b)** MTT assay. The cell growth at three experimental time points (24, 48, and 72 hours) is plotted for the cells seeded on a classical surface (ctrl, red line), laser-structured one (ex. LS, blue line) and the laser-structured theoretical curve (th. LS, dashed dark blue line). (a.u. = arbitrary unit).

A 96-well culture plate (ThermoFisher) was structured according to the previously described protocol and established laser parameters. Cells (C2C12 murine myoblasts) were seeded, and their growth was followed for 72 hours. The absorbance analysis revealed an increase in myoblasts number for both the structured surface and control, with a similar trend (**Fig 5.b**). We can note that the values obtained for the structured surface are lower than the control, an effect that can be explained by the reduction of the total area available for cell adhesion due to the presence of the structured channels and their associated hydrophobicity. To verify this hypothesis, a theoretical curve was calculated, normalizing the values of the control with the percentage of available area on the structured surface (**Fig 5.b** dashed dark-blue line). The surface ratio confirms the safety of the laser-structured surfaces on the cell development, confirming the data obtained experimentally (**Fig 5.b** blue line) with a matching control curve.

3.1.4 Cell Alignment

Once the safety of LS surfaces on cell viability and proliferation was verified, we investigated their ability to drive cell organization. C2C12 myoblasts were cultured on control and LS surfaces, testing the four previously established channel spacing values (75, 100, 125, and 150 µm) to determine the best parameter to obtain aligned myotubes. After the differentiation of

myoblasts into elongated myotubes, the orientation of the latter was studied using the *Orientation J* plugin for FIJI software.

Importantly, LS surfaces induced an increment in myotubes organization (**Fig 6.b,c**) for all the spacing tested compared to control unstructured surfaces (**Fig 6.a**), as confirmed by the analysis of their orientation (**Fig 6.d**). Moreover, even though the organization for the four conditions was significantly higher than the control, as shown in the coherency graphic (**Fig 6.e**), the value for the smaller spacing (75 µm) was significantly lower than the other three. The best coherency value was obtained for the 125 µm spacing, which was then chosen and used for the subsequent experiments. On the LS surfaces, we further showed that the cells were more prone to elongate along the interspace between two consecutive channels rather than into the channel itself. In this context, channels 75 µm apart appeared to be too close for the myotubes to perceive the spatial constraint, resulting in shorter, less organized myotubes that had a tendency to cross channels (**Fig 6.b**), explaining the poor alignment and coherency. On the contrary, increasing the spacing between channels led to greater control over the organization of myotubes, providing them with enough space to grow in width and length while guiding them through the edge of the channels (150 µm, **Fig 6.c**).

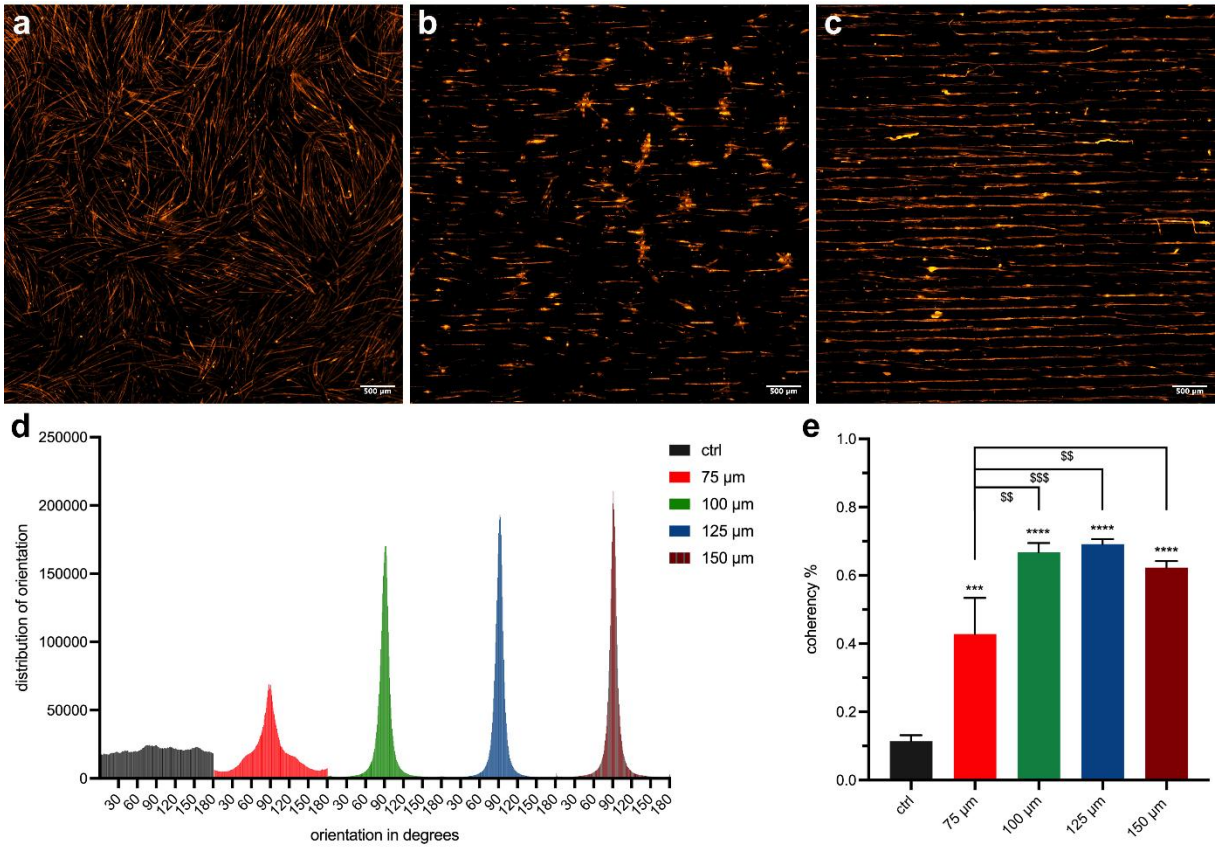

Fig. 6: Top: Immunofluorescence analysis. The myotubes, positive for Myosin Heavy Chain (Red), are randomly oriented in the control (**a**) while properly aligned on the LS surface (channel spacing of 75 µm (**b**) and 150 µm (**c**)). **Bottom: Orientation of the muscular elements.** The distribution of orientation is plotted for all spacing conditions tested (75, 100, 125, and 150 µm), revealing the presence of a prevalent peak for all the LS surfaces (**d**); the quantification of the orientation through the coherency value (**e**) revealed a significative increment for all the LS surfaces compared to the control (*), with the three higher values being significative compared to the 75 µm ($). (p values: **** $p < 0{,}0001$, *** $p = 0{,}0001$, $^{\$\$\$}$ $p = 0{,}0006$, $^{\$\$}$ $p = 0{,}0013$ (75 µm vs 100 µm), $^{\$\$}$ $p = 0{,}0059$ (75 µm vs 150 µm)).

To be sure that the results obtained were not due to a specific cell culture plate in terms of size and brand, a systematic study on myotubes orientations was conducted on culture plates from 6 different commercial brands (NuncTM, Falcon®, CLEARline®, SPL, Costar®, SARSTEDT) ranging from 6 to 96-well dishes to chamber slides laser-structured with a channel spacing of 125 µm. The results were compared with an unstructured control (NuncTM, 12 well). The resulting myotubes presented a better organization than the control in each tested condition (**Fig. 7**).

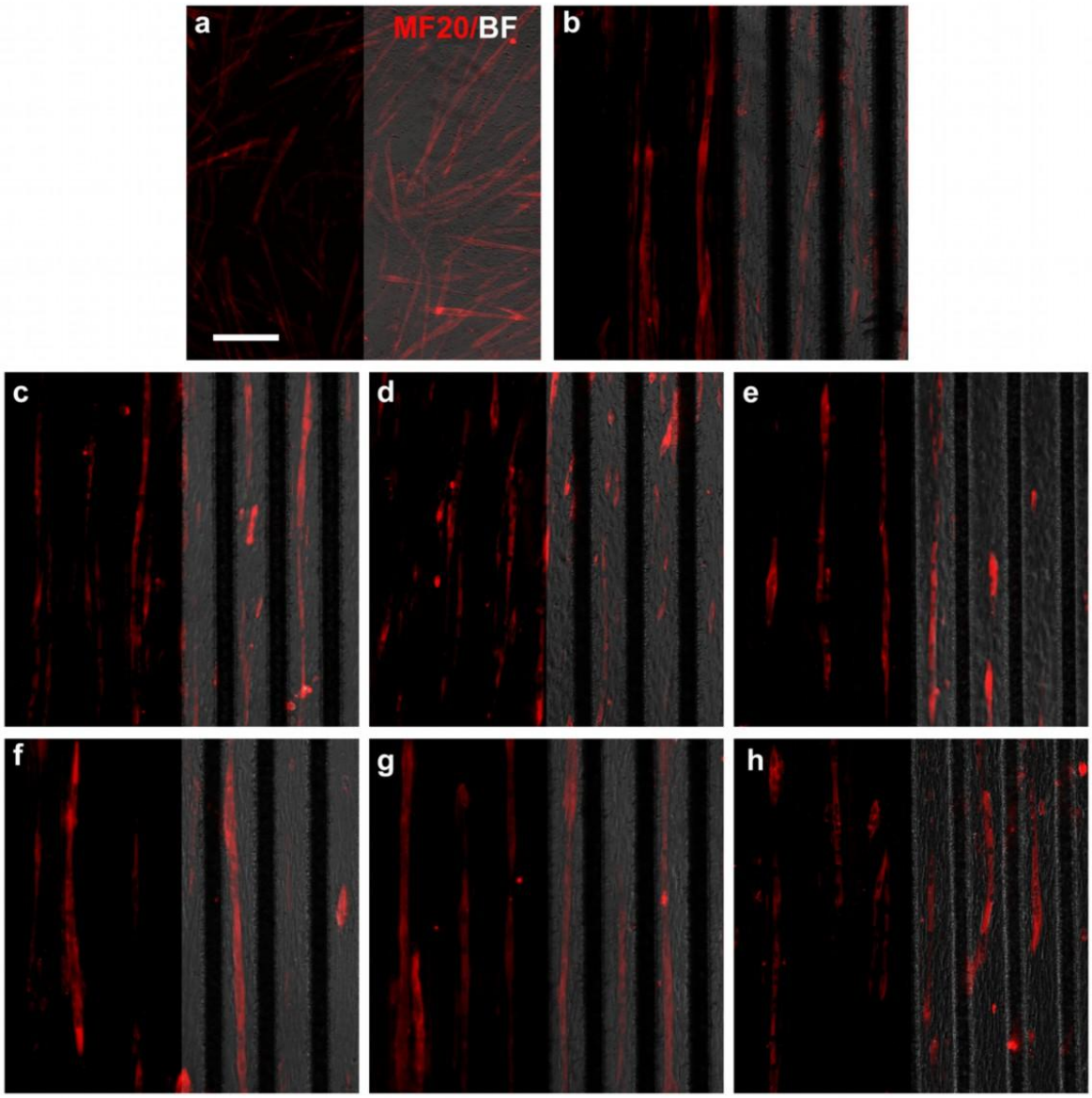

Fig. 7: Immunofluorescence analysis for all the analyzed brands and types of culture plates. The pictures represent the myotubes, positive for Myosin Heavy Chain (Red), with the juxtaposition of the respective bright-field pictures (light gray) to visualize LS channels. Control 12-well plate Nunc™ (**a**), LS 6-well plate Falcon® (**b**), LS 12-well plate Nunc™ (**c**), LS 12-well plate CLEARline (**d**), LS 24-well plate SPL (**e**), LS 48-well plate Costar® (**f**), LS 96-well plate Falcon® (**g**), LS chamber-slide SARSTEDT (**h**). Scale bar = 150 µm.

Moreover, the orientation analyses conducted on these pictures (**Fig 8.a**) clearly show the independence of the laser structuration process from the brand or size of the supports (**Fig 8.b**). Distribution associated with all LS surfaces shows a predominant peak compared to the control plate (**Fig 8.a**). A significative increment of the coherency values can also be observed

for all the LS surfaces compared to the control (**Fig 8.c**). The differences between the LS surfaces themselves are not significant, supporting the universality of the structuring process, regardless of the type of surface (or brand) and the surface of the culture dish.
It is also worth noting that the structuring process has been tested on tissue culture polymeric coverslips such as polyethylene terephthalate glycol (PET-G) (Sarstedt). These materials being similar to polystyrene in terms of chemical composition, we obtained analogous results regarding channel formation and cell alignment. (**Suppl. Fig 6**).

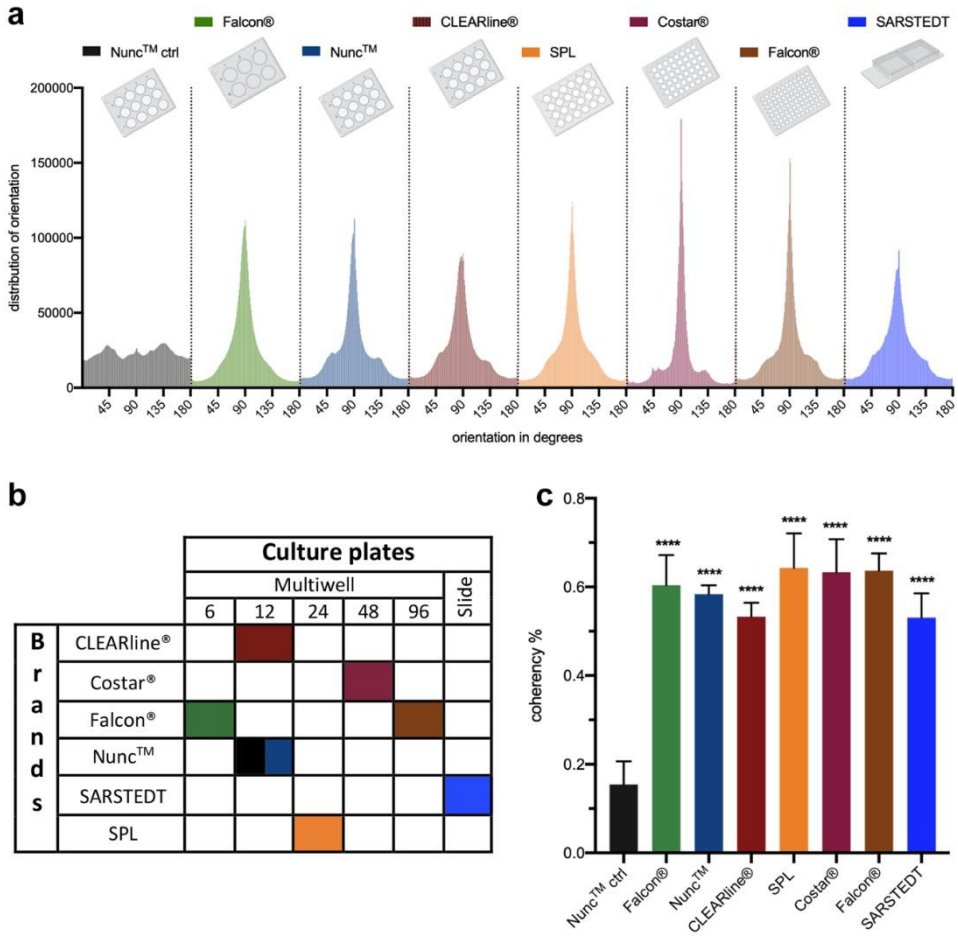

Fig. 8: Systematic study of the effect of laser structuring of culture plates of different brands and sizes on the orientation of myotubes. Distribution of orientation for all the analyzed culture plates (a); table of the different brands and sizes of culture supports analyzed (**b**); Coherency values for all the analyzed samples (**c**) with respective significances (* compared to the control). (p values: **** p < 0,0001).

Finally, we tested different patterns, such as concentric circles and squares, and zig-zag lines at different angles, observing a clear tendency of the cells to follow the designed pattern (**Suppl. Fig 7**).

3.1.4 Influence of laser structuring and photobleaching on myoblast development

Control and LS surfaces with a channel spacing of 125 µm were chosen for analyses. Significantly longer myotubes were found in the presence of structured channels than in the control (**Fig 9.a**). However, fusion index analysis revealed no effect of structuring on C2C12 differentiation (**Fig 9.b**). In addition, to verify that the photobleaching process did not affect

the properties of the laser-structured surface, the differentiation and orientation levels of myoblasts were evaluated (**Fig 9.b,c**), and no differences were found.

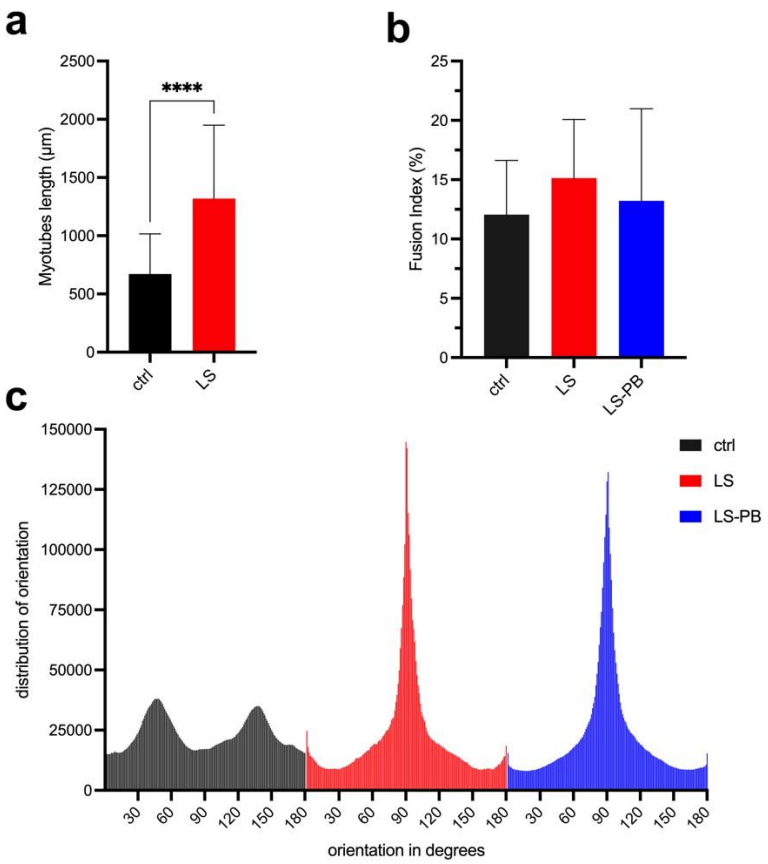

Fig. 9: Analysis of elongation, differentiation, and orientation of C2C12. (**a**) The length of myotubes cultured on laser-structured surfaces (LS, red) was significantly higher than that of myotubes on control surfaces (ctrl, black), (p<0,0001); (**b**) Fusion index analysis revealed no significant differences between myotubes differentiated on control (black), LS (red) and laser-structured and photobleached (LS-PB, blue) surfaces; (**c**) Orientation analysis showed no difference in alignment between the myotubes cultured on LS (red) and LS-PB (blue) surfaces, both of which had a single orientation peak compared with control (black). (p values: **** p < 0,0001).

3.2 Cell bioprinting

To increase the sophistication of muscle models, we decided to combine the laser-structuring of surfaces with LIFT bioprinting. This method allows for the deposition and creation of precise cell patterns to maximize and enhance tissue culture organization (**Fig 10.a**). Moreover, thanks to the accurate micrometric control of cell deposition, LIFT can be used to print different cell populations on the same sample in pre-designed patterns (**Suppl. Fig 8**). Thus, merged with laser-induced topography, LIFT enables us to create isolated muscle fibers in a controlled environment. As demonstrated in precedent studies, cell deposition by LIFT requires a coating layer on the receiver surfaces to achieve high survival rates and maintain print resolution (**Article 2**). This coating is usually poured on the substrate to create a thick layer of gel into which cells are embedded in precise locations. The uniformity of the coating surface highly influences the quality of the process. Indeed, as illustrated in **Figure 10.b**, the "dome" effect

caused by surface tension alters the distance between the donor and receiver substrate, thus affecting the jetting and printing conditions depending on the receiver's location. Additionally, the hydrophobic regions formed by the induced topography further jeopardize the creation of a uniform gel layer.
To overcome this limitation, we developed an airbrush-based system (**Suppl. Fig 9**) to ensure a precise and homogenous deposition of a small amount of coating solution on the receiver surface. Our previous studies have demonstrated the suitability of Matrigel as a coating layer to enable high cell viability and excellent resolution due to its rapid gelling ability. To meet the requirements of Matrigel, a cooling system was developed to maintain a temperature of 4°C during the airbrushing process, avoiding premature Matrigel gelation and consequent clogging of the system. This method uses less initial material (50 µL), leading to thinner coatings of the receiver substrate while being cost-effective (**Suppl. Fig 10**). By using a small quantity of coating, printed cells are directly in contact with the laser-induced topography, promoting their guidance and organization. This improved homogeneity of the coating translates into an equal donor-receiver distance throughout the receiver's surface and thus more homogenous and reproducible LIFT printing.

We report here on the creation of a multi-step process (**Fig 10,c; Suppl. Fig 11**) combining direct laser structuration and laser-induced bioprinting using a single laser source in a time and space-efficient manner. Both methods are done in the same set-up, and the process can be divided into four distinct and consecutive parts: (**1**) Laser structuring of the receiver substrate, (**2**) Creation of the Matrigel coating, (**3**) Bio-printing of the cells by LIFT and (**4**) Gelation of the Matrigel and culture of the cells (**Fig 10.c**).

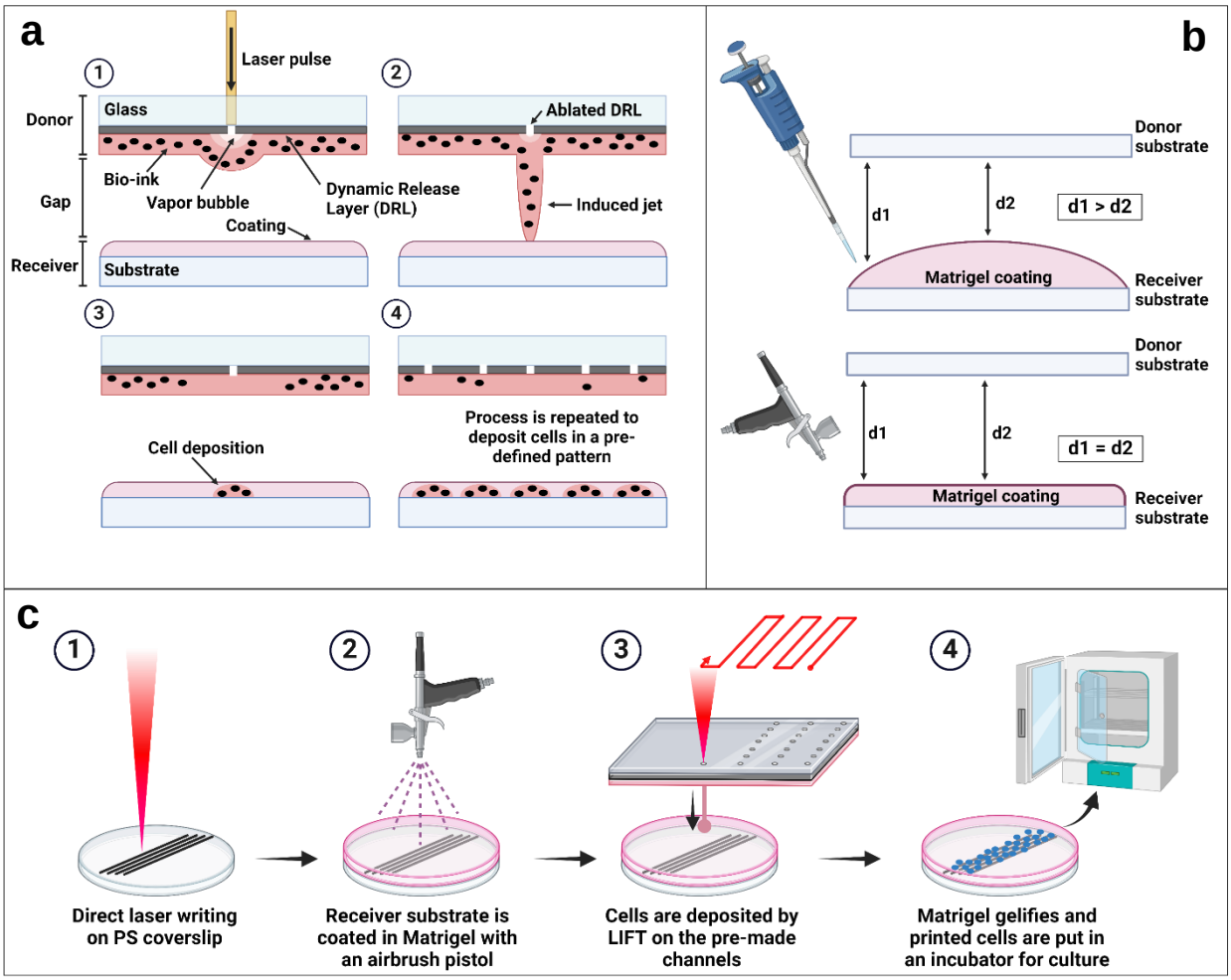

Fig. 10: (a) Lift bio-printing principle of operation (1) The laser pulse interacts with the Dynamic Release Layer (DRL, titanium), creating a vapor bubble inside the bio-ink. (2) The bubble expands and collapses, inducing the creation of a jet that propels the cells contained in the bio-ink. (3) The jet deposits the cells on the receiver's coating and retracts on the donor slide (4) The process is repeated to multiply the number of deposited droplets and complexify the printed pattern. **(b)** The receiver coated by pipetting creates a thick layer of Matrigel in the form of a dome due to the surface tension on the edge of the slide. By airbrushing, the amount of material is reduced and directly applied uniformly onto the receiver substrate. The homogeneity of the coating translates into an equal donor-receiver distance throughout the receiver's surface. **(c)** Workflow combining direct laser structuration and LIFT bioprinting. (1) PS coverslips are structured through laser ablation to create parallel channels. (2) The channels are covered in Matrigel by airbrushing to ensure homogeneity and reproducibility. (3) Cells are printed by LIFT directly in the pre-made channels. (4) Once the Matrigel forms a gel, the PS slide is moved from the laser set-up to the incubator set at 37°C for cell culture.

3.2.1 Disease modeling

The developed system was applied to human cells, including cells from patients affected with muscular dystrophy (DMD and FSHD), to assess whether the system might reveal cellular defects associated with the disease's phenotype. Immortalized myoblasts from healthy and affected donors were printed using a gelatin-based bio-ink and deposited along the created topography. As described using mouse C2C12 cells, we noticed a clear and preferential alignment of the printed cells along the orientation of the laser-induced topography (**Fig 11 a,b,c**). The use of genetically affected cells did not influence already established printing parameters; cells were successfully printed and followed the expected behavior with an alignment along the created channels (**Fig 11.d**).

Clear morphological differences were observed between cell types (**Fig 11.a, b, c**). Healthy cells exhibited myotubes diameter and length almost twice as big as their affected counterparts (**Fig 11.e,f**). They displayed continuous myotubes that maximized their surface extension along the channels, with myotubes widths up to 60 µm and lengths up to 3.6 mm on a single culture slide (**Fig 11.a**). DMD and FSHD printed cells (**Fig 11.b, c**) exhibited myotubes of reduced length (**Fig 11.f**) and width (**Fig 11.e Suppl. Fig 12**) and an overall decreased fusion capacity compared to the control (**Fig 11.g**).

In addition, immunostaining analyses were conducted to study disease-specific markers, revealing, on the one hand, the presence of a typical dystrophin protein network surrounding healthy myosin-positive myotubes (**Fig. 11.h,i**), dystrophin that was totally absent in DMD myotubes (**Fig. 11.l,m**). On the other hand, nuclei positive for the DUX4 protein were found in FSHD myotubes (**Fig. 11.n,o,p**), clearly indicating the pathological nature of the muscle model.

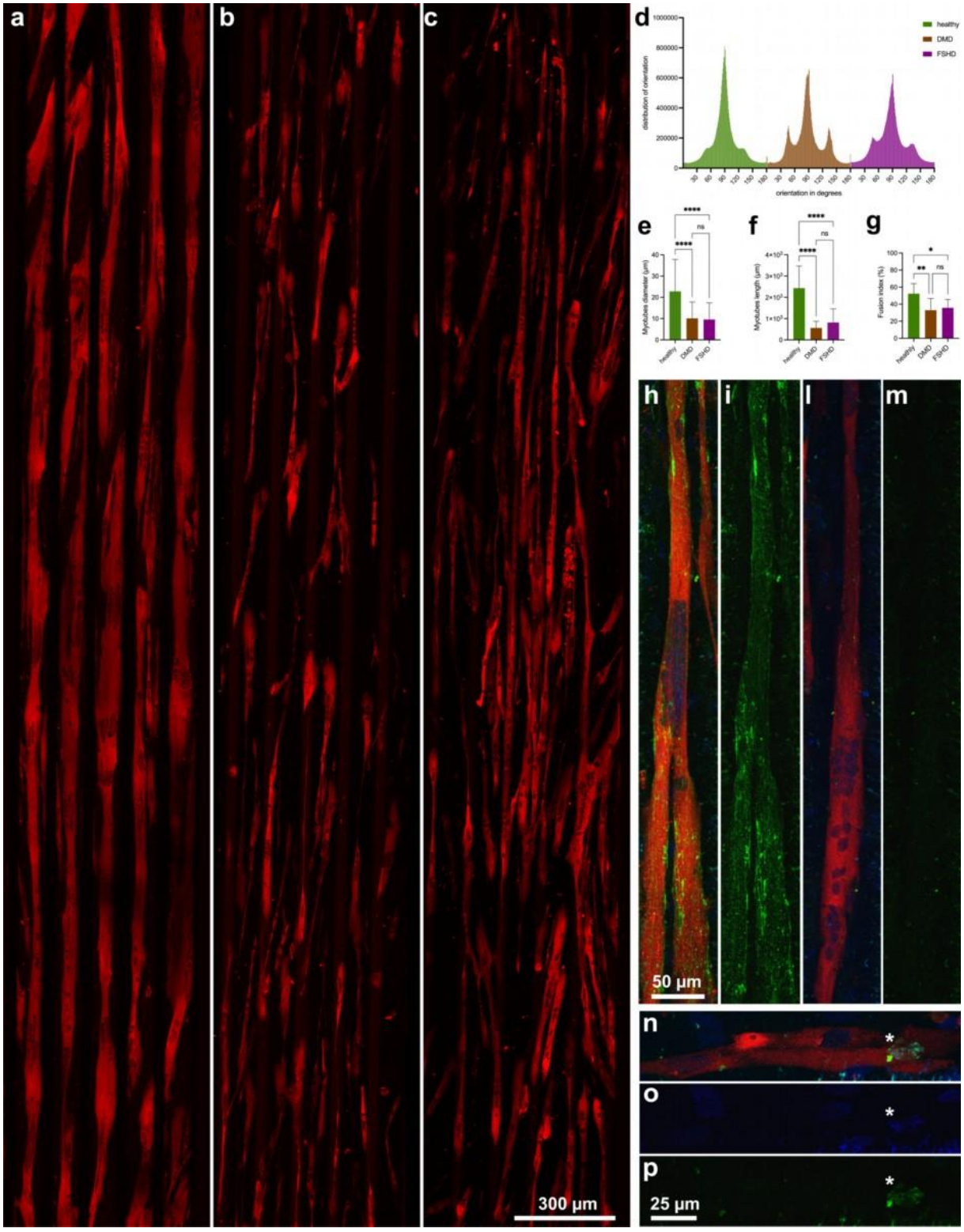

Fig. 11: Immunofluorescence and imaging analyses of LIFT-bioprinted human myoblasts differentiated on LS surfaces. The pictures represent the myotubes, positive for Myosin Heavy Chain (Red) obtained from healthy **(a)** DMD **(b)** and FSHD **(c)** immortalized human myoblasts. The orientation (**d**), diameter (**e**) and length (**f**) of the myotubes are displayed for each cell line (healthy, DMD, FSHD), as well as the relative fusion index (**g**); the healthy (**h,i**) and DMD affected (**l,m**) myotubes were stained for Myosin Heavy Chain (Red) and Dystrophin (green) Nuclei are counterstained in Dapi (Blue). The FSHD affected myotubes were stained for Myosin Heavy Chain in red, nuclei in blue and DUX4 positive nuclei in green (**n,o,p**); The asterisks indicate the same DUX4 positive nucleus in merged (**a**), Dapi (**b**) and GFP (**c**) pictures. (p values: diameters, **** $p < 0{,}0001$; length, **** $p < 0{,}0001$; fusion index, ** $p = 0{,}0032$, * $p = 0{,}0115$).

Discussion

So far, different solutions are commercially available to obtain organized and aligned 2D cultures, mostly based on complex manufacturing methods and requiring additional treatments or coatings to enable cell adhesion. Although effective in obtaining organized cell cultures, these methods force researchers to use a limited range of cell culture supports, many of them in the presence of an ECM protein coating, making their use less flexible and accessible to the scientific community.
In this work, we thoroughly investigated the capacity of a laser-based structuring process to create topographic cues on the surface of standard, commercially available cell culture substrates. We then evaluated and analyzed their associated ability in guiding muscle cell contact, orientation, and differentiation. The use of a high-speed scanning system allowed us to perfectly control the patterning design in a fast and efficient manner. At the same time, the use of an ultra-fast laser minimized the energy required to modify PS surfaces, consequently reducing induced thermal effects and subsequent generation of possible toxic compounds (**Fig 5.a**).
We further showed that the fabrication process proposed here provides effective, highly reproducible, and cell-safe supports for highly organized cell culture systems, with a focus on anisotropic 2D cell patterns applied to skeletal muscle differentiation.

- Physical characterization of LS surfaces

As it is the case for many other polymers, solid polystyrene exhibits extensive absorption up to 350 nm due to the formation of charge-transfer contact complexes with oxygen [50,51]. Naturally, numerous studies have focused on the UV laser irradiation of polymers for patterning approaches, micro/nano structuration, and tunable wettability modification. Depending on laser parameters, the ablation of PS can be done through several mechanisms based on photochemical and photothermal phenomena [18]. The use of an IR femtosecond laser limits the ablation of the polymeric surface to photothermal mechanisms with limited photochemical effects and photodegradation [52], as Wang and colleagues demonstrated [53] by simulating the interaction of a 795 nm 130 fs laser with a PS surface. They showed a large percentage of laser energy converted into heat, which dissipated in the bulk of the material, induced plasma generation, and ablation of the material itself, corroborating our observations. Topography is created here through ablation by nonlinear vaporization of the PS surface and substantial melting, leading to the swelling of the targeted material. Suriano and colleagues [18] irradiated PS samples with 800 nm femtosecond pulses up to 44.2 J/cm². At such intensity, they reported a substantial darkening of the PS. These changes in appearance were explained by oxidative degradation of the polymer under strong laser irradiation. They finally confirmed this hypothesis by displaying the evolution of the IR PS absorbance during µ-ATR-FTIR spectrum analysis depending on the incident laser fluence, which, for high fluence, indicated the apparition of -OH (3400-3600 cm^{-1}) groups and broad bands due to carbonylic species (1700 cm^{-1}). In our case, laser fluence is limited to 2.3 J/cm² at 1030 nm, and, given the obtained IR absorbance spectra of the treated surfaces and further corroborated by the lack of the C=O group absorption band at 1730 cm^{-1}, usually associated with photodegradation [54], we can confidently assume the limited oxidation generated by our process. The darkening of the observed channels is here only due to the creation of a porous surface. In this regard, the increased surface area associated with the porosity created by laser irradiation amplifies the number of exposed non-polar functional groups and, thus,

the hydrophobicity of the polystyrene [55]. This effect is further amplified by the removal of the culture plate surface treatment and, as demonstrated by Wang and colleagues, by the potential chemical bond modifications within the polymer at low fluences [56]. By introducing a partial topographical modification of the cell culture plate (parallel lines spaced from 75 to 150 µm), we, therefore, created strong hydrophobic areas acting as barriers, which explains the difference in contact angles between the different observations of orientations. Additionally, the presence of deep channels and protrusions combined with the generated hydrophobicity reinforce the physical cues, allowing cell topographical guidance.

- Topographical cues for organized cell culture

Experiments with murine myoblasts revealed that geometric constraints on the cultured surface in the form of laser-ablated channels combined with modifications in local porosity (**Fig 1.c,d**) and hydrophobicity (**Fig 4**) were able to drive cell adhesion and orientation, hence promoting the alignment of the resulting myotubes (**Fig 6.c**). The different channel spacing tested highlighted the underlying mechanisms influencing cell organization. Closely spaced hydrophobic channels do not provide enough suitable areas for proper cell adhesion and growth (**Fig 6.b,d**), resulting in a loss of alignment and the formation of cell clusters. In contrast, wider channel spacing allowed sufficient space for cell development, promoting better alignment and organization (**Fig 6.c,d**). The improved, large-scale organization also led to a significant increase in the average length of myotubes when compared with not-structured support (**Fig 9.a**). These results showed that although LS surfaces were not able to directly increase the myogenic potential of myoblasts (**Fig 9.c**), the anisotropic environment promoted better surface utilization with myotubes that, when forced to elongate in a preferential direction, reached a least twice the length of classical culture conditions.

In addition, we ensured that the observed results were not related to a specific plate manufacturing process, culture support size, or cell culture treatment. To this end, the structuring process and subsequent cell analysis were repeated on some of the most common brands of culture plates of ranging sizes, from 96- to 6-multiwells, through chamber slides and to polymeric coverslips treated for cell culture. We obtained significantly higher alignment values for each tested sample compared to the unstructured cell culture surface. On the other hand, we observed no significant differences between the brands and sizes tested (**Fig 9,10**). Altogether, these results demonstrate the validity and versatility of the laser structuring technique to functionalize cell culture substrates. The proposed laser-structuring technique is thus an effective and reliable solution for the large-scale production of standardized and organized cell cultures and tissue models.

- Characterization of autofluorescence and solutions

In contrast to promising cell control, some limitations inherent to the use of laser ablation were observed. As it is well documented in the literature, mechanical and thermal modifications of polymers can lead to increased autofluorescence. This phenomenon could limit the range of application of LS surfaces, especially for immunofluorescence analysis [57]. Therefore, this aspect was thoroughly investigated to define a strategy to reduce, if not eliminate, its impact on laser-structured PS surfaces.

Polystyrene is a synthetic aromatic polymer with monomer units linked by covalent bonds to form macromolecular chains [58]. Its chemical composition and, notably, the presence of

aromatic benzene rings lead to some degree of intrinsic fluorescence [59]. This fluorescence can emanate from monomer emission with a fluorescence peak at 280-285nm or excimer emission at 335 nm [60]. The localized reconfiguration of the material and the increased surface area caused by the creation of high porosities eliminate any surface treatment and special manufacturing processes aiming at reducing the fluorescence abilities of the benzene ring. The increase in fluorescence can also be explained by the reorganization of polymer chains and the formation of excimers following direct laser writing [57]. Given the proximity of PS autofluorescence peak to the absorption and emission of DAPI, this strongly limits nuclei counterstaining. As we observed and as confirmed by Young and colleagues [57], this autofluorescence decreases at longer wavelengths.

In this context, the use of fluorophores far from the affected color channels constitutes only a partial solution to this issue because it constrains applicable experiments and analysis on the processed surfaces. Confocal microscopy proved itself a straightforward and commonly accessible tool to get around the PS auto-fluorescence problem. The extensive majority of the cells cultured on the designed substrates are located between the created channels. Moreover, the autofluorescence of the PS emanates directly from the surface with minimal bleeding toward the z-axis. Thanks to confocal microscopy, the focus depth difference between the three-dimensional cells and the bottom plate is enough to considerably reduce the negative impact of the autofluorescence. This enables us to collect fluorescent data from the cells directly in the channels for all fluorophores.

Photobleaching is a form of photodegradation that involves a gradual loss of fluorescence due to a prolonged exposure to light, particularly at high intensities. This process occurs because the energy absorbed by the fluorescent molecules within the polymer (the benzene ring for PS) can cause chemical reactions, such as bond breakage or the formation of new, non-fluorescent chemical species. These changes degrade the molecular structure that originally emitted fluorescence, leading to a decrease in the overall fluorescence intensity over time. In the case of PS, the exposure to light, especially at UV wavelength, leads to the creation of radicals whose nature depends on the spectral composition of the light, and to overall photooxidation [61]. Hawkins and colleagues [62] reported a decrease in PS auto-fluorescence under continuous illumination at a wavelength comprised between 500nm and 645nm. The observed nonlinear decrease joins the observations of Piruska and colleagues [63]. The first study exhibited a reduction of autofluorescence over several hours, as it was the case with our first considered broad white LEDs, which was itself inspired by the work of Tsuneoka on biological autofluorescent material [48]. Sullivan and colleagues [64] investigated the undesired loss of fluorescence in microplastic by illuminating various polymers to a 405 nm light produced by a solid-state laser. They noticed a similar nonlinear curve with a drastic reduction of fluorescence (minus 70%) plateauing after 30 min exposure. Here, we turn these results and their use to our advantage and report a comparable loss of auto-fluorescence (minus 75%) using UV LEDs centered at 365 nm in about 10 minutes of exposure. The slight wavelength shift toward the natural absorption of polystyrene explains the difference in the photobleaching kinetic. The oxidation of the PS surface and associated rearrangement of the benzene ring due to photooxidation is a direct consequence of the UV exposition, as demonstrated by Pfleging and colleagues [65]. The use of LEDs allows for an accessible and affordable solution, and their broad illumination guarantees the quick processing of structured commercial culture plates. Therefore, the combination of efficient photobleaching and confocal microscopy negates the detrimental autofluorescence induced by the creation of the topography.

- Combination of LS surfaces and LIFT bioprinting for skeletal muscle disease modeling

To further investigate the application of the LS surfaces to muscle tissue modeling, we decided to focus on two of the most common myopathies, Duchenne muscular dystrophy (DMD) and Facioscapulohumeral muscular dystrophy (FSHD), with the intent to develop highly organized human disease models.
Nowadays, there is increasing pressure to reduce and even replace animal testing, motivated by its inadequacy in replicating the pathophysiological aspects of human diseases. The issue is underlined by the failure of over 90% of new drugs tested on animals during clinical trials [66], making the need to develop reliable human disease models even more evident. To this aim, we decided to exploit the full potential of the ultrafast laser system by combining surface structuring and the LIFT bioprinting process. Both methods are seamlessly integrated into a single experimental set-up and utilize the same laser source. This configuration integrates the accurate positioning of cells offered by LIFT with the contact guidance of LS surfaces, making it possible to design both the topography and subsequent cell printing patterns. Equally, the process combination paves the way for the creation of more complex biological models by exploiting the ability of LIFT to efficiently print different cell populations in specific pre-designed patterns on LS surfaces (**suppl. Fig 8**). This methodology could also be integrated with tailored sensors and multi-electrode arrays (MEA) for advanced organ-on-chip applications.

Some adaptations were, however, required to guarantee a practical connection between the laser structuration process and the LIFT bioprinting. Indeed, as indicated by numerous studies and previous work, LIFT-bioprinting is mainly done on a substrate previously coated by a material, most commonly natural hydrogels, to protect the cells from the mechanical stress of the printing [67]. The modification of the LS surface hydrophobicity, and subsequent poor layer homogeneity, led to the development of a new device able to create thin layers of biomaterials on such complicated surfaces. The modified airbrush is here cooled down for its suitability with Matrigel, and a warm, humid chamber acts as a recipient to promote its gelation. These properties can nonetheless be modified and adjusted to different bio-material properties and associated gelation requirements with, for example, a warmed airbrush coupled with a cold recipient chamber. The proposed homemade system is thus an inexpensive, efficient, and fast way to create reproducible coatings on LS surfaces, linking the laser-based structuration and bio-printing process. The implementation of this method also allowed improved uniformity of the coating and, thus, better printing.

The printing results on LS surfaces confirmed the validity of the combined method in producing muscle models starting from healthy and affected human myoblasts. In particular, the healthy muscle model presented highly elongated myotubes (up to 3.6 mm) associated with a significantly higher width, indicating a good level of differentiation and maturation (**Fig 11.a**). On the contrary, both DMD and FSHD models exhibited a reduction in myotubes length and width (**Fig 11.f,e**), together with impaired differentiation ability (**Fig 11.g**), matching the overall aspect of an affected muscle. In addition, immunofluorescence analysis of DMD models confirmed the absence of Dystrophin (**Fig 11.b**), an observation that matches the pathological phenotype of DMD patients. Similarly, we were able to observe the presence of DUX4-positive nuclei in the FSHD model (**Fig 11.p**). Our results are consistent with the hypothesis that in FSHD-affected patients, the ratio of DUX4-positive nuclei to the total number of nuclei is 1/1000 [46]. The observation of such disease hallmarks emphasizes the ability of the proposed model to recapitulate the pathophysiological aspects of the diseases studied and opens new avenues for pathophysiological investigations.

The proposed system efficiently combines two distinct laser-based processes with an automated coating procedure to create tailored topography and precise multi-type cell printing on various commercially available culture substrates. To this end, we use a single laser source and inexpensive homemade techniques concentrated in a compact experimental set-up to execute the previously described procedure quickly and efficiently. The effective duration of the complete process is currently less than one minute **(Suppl. Video).** This time is directly linked with the nature of the biomaterial used and its possible gelation/crosslinking properties. Considering the scalable and amendable nature of the structured devices and the results obtained in skeletal muscle tissue and related disease modelling, one can easily imagine their extension to other diseases and high throughput screening.

Conclusions

Here, we report the development, characterization, and validation of a micrometric laser-structuring process designed for commercial culture plates and applied to 2D skeletal muscle modeling.
The creation of cell-guiding topographical cues through laser ablation constitutes a rapid, reliable, and reproducible process applicable to a whole range of culture supports, with potentially no limitations in the size and complexity of the desired LS pattern. The system currently optimized for skeletal muscle modeling could, therefore, be exploited to mimic the peculiar topography and architecture of different organs and tissues.
By exploiting the LIFT ability to accurately position cells on the surface of culture plates together with the contact guidance of LS surfaces, it would be possible to design both complex structuring geometries and printing patterns, paving the way to the creation of biologically and architecturally complex models combining different cell populations deposed in a pre-designed and reproducible manner on the LS surface. Finally, the tissue and disease modeling strategy developed and validated in this paper could be easily adapted to other myopathies and cell types. The proposed systems could be integrated into a compact and versatile laser-based platform directly accessible in biology laboratories to promote the integration of tissue-engineering strategies into routine cell culture and traditional workflow.

Acknowledgments

This work was funded by the French National Research Agency (ANR Medilibs and Diagem projects) together with the French Defense Innovation Agency (ANR—DGA/AID—ICELARE Project ID ANR—20—ASTR—0004). The PhD thesis of Lucas Duvert was co-funded by Aix-Marseille university and the French Defense Innovation Agency. This work received support from the French government under the France 2030 investment plan, as part of the Initiative d'Excellence d'Aix-Marseille Université – A*MIDEX "AMX-23-CPJ-05". The project leading to this publication has received funding from the Excellence Initiative of Aix-Marseille University-A*Midex, a French "investissement d'avenir programme" AMX-19-IET-007, through the MarMaRa funding scheme. This work was conducted using LaMP facilities at LP3 and MMG imaging facility. The authors also acknowledge the "Region SUD". We also thank MyoLine, the human cell immortalization platform of the Institut de Myologie, for providing us with the immortalized human myoblasts used for our experiments.

Bibliography

1. A. Atala, "Engineering organs," Curr. Opin. Biotechnol. **20**(5), 575–592 (2009).

2. D. E. Ingber, V. C. Mow, D. Butler, L. Niklason, J. Huard, J. Mao, I. Yannas, D. Kaplan, and G. Vunjak-Novakovic, "Tissue engineering and developmental biology: going biomimetic," Tissue Eng. **12**(12), 3265–3283 (2006).

3. E. Lavik and R. Langer, "Tissue engineering: current state and perspectives," Appl. Microbiol. Biotechnol. **65**(1), 1–8 (2004).

4. "Anisotropic Materials for Skeletal-Muscle-Tissue Engineering - Jana - 2016 - Advanced Materials - Wiley Online Library," https://onlinelibrary.wiley.com/doi/abs/10.1002/adma.201600240.

5. O. Bjorgvinsdottir, S. J. Ferguson, B. S. Snorradottir, T. Gudjonsson, and K. Wuertz-Kozak, "The influence of physical and spatial substrate characteristics on endothelial cells," Mater. Today Bio **26**, 101060 (2024).

6. A. Mobasseri, A. Faroni, B. M. Minogue, S. Downes, G. Terenghi, and A. J. Reid, "Polymer Scaffolds with Preferential Parallel Grooves Enhance Nerve Regeneration," Tissue Eng. Part A **21**(5–6), 1152–1162 (2015).

7. "Engineering Muscle Tissues on Microstructured Polyelectrolyte Multilayer Films | Tissue Engineering Part A," https://www.liebertpub.com/doi/abs/10.1089/ten.tea.2012.0079.

8. J. L. Charest, A. J. García, and W. P. King, "Myoblast alignment and differentiation on cell culture substrates with microscale topography and model chemistries," Biomaterials **28**(13), 2202–2210 (2007).

9. H. Gao, J. Xiao, Y. Wei, H. Wang, H. Wan, and S. Liu, "Regulation of Myogenic Differentiation by Topologically Microgrooved Surfaces for Skeletal Muscle Tissue Engineering," ACS Omega **6**(32), 20931–20940 (2021).

10. J. Brunetti, S. Koenig, A. Monnier, and M. Frieden, "Nanopattern surface improves cultured human myotube maturation," Skelet. Muscle **11**(1), 12 (2021).

11. J. T. Vecchi, M. Rhomberg, C. A. Guymon, and M. R. Hansen, "The geometry of photopolymerized topography influences neurite pathfinding by directing growth cone morphology and migration," J. Neural Eng. **21**(2), 026027 (2024).

12. A. Žemaitis, M. Gaidys, M. Brikas, P. Gečys, G. Račiukaitis, and M. Gedvilas, "Advanced laser scanning for highly-efficient ablation and ultrafast surface structuring: experiment and model," Sci. Rep. **8**(1), 17376 (2018).

13. R.-Z. Leng, B. Yun, Z.-H. Chen, C. Chai, W.-W. Xu, Y.-H. Yu, and L. Wang, "High-Transmission Biomimetics Structural Surfaces Produced via Ultrafast Laser Manufacturing," Biomimetics **8**(8), 586 (2023).

14. E. Rebollar, I. Frischauf, M. Olbrich, T. Peterbauer, S. Hering, J. Preiner, P. Hinterdorfer, C. Romanin, and J. Heitz, "Proliferation of aligned mammalian cells on laser-nanostructured polystyrene," Biomaterials **29**(12), 1796–1806 (2008).

15. E. Babaliari, P. Kavatzikidou, D. Angelaki, L. Chaniotaki, A. Manousaki, A. Siakouli-Galanopoulou, A. Ranella, and E. Stratakis, "Engineering Cell Adhesion and Orientation via Ultrafast Laser Fabricated Microstructured Substrates," Int. J. Mol. Sci. **19**(7), 2053 (2018).

16. S. Kedia, R. Checker, S. K. Sandur, and J. P. Nilaya, "Picosecond laser-induced hybrid groove structures on Ti-6Al-4V bio-alloy to accelerate osseointegration," J. Biomed. Mater. Res. B Appl. Biomater. **111**(10), 1775–1784 (2023).

17. N. Ahmed, S. Darwish, and A. M. Alahmari, "Laser Ablation and Laser-Hybrid Ablation Processes: A Review," Mater. Manuf. Process. **31**(9), 1121–1142 (2016).

18. R. Suriano, A. Kuznetsov, S. M. Eaton, R. Kiyan, G. Cerullo, R. Osellame, B. N. Chichkov, M. Levi, and S. Turri, "Femtosecond laser ablation of polymeric substrates for the fabrication of microfluidic channels," Appl. Surf. Sci. **257**(14), 6243–6250 (2011).

19. S. M. Eaton, C. De Marco, R. Martinez-Vazquez, R. Ramponi, S. Turri, G. Cerullo, and R. Osellame, "Femtosecond laser microstructuring for polymeric lab-on-chips," J. Biophotonics **5**(8–9), 687–702 (2012).

20. L. Caron, S. Testa, and F. Magdinier, "Induced Pluripotent Stem Cells for Modeling Physiological and Pathological Striated Muscle Complexity," J. Neuromuscul. Dis. **10**(5), 761–776 (2023).

21. I. Matai, G. Kaur, A. Seyedsalehi, A. McClinton, and C. T. Laurencin, "Progress in 3D bioprinting technology for tissue/organ regenerative engineering," Biomaterials **226**, 119536 (2020).

22. W. Aljohani, M. W. Ullah, X. Zhang, and G. Yang, "Bioprinting and its applications in tissue engineering and regenerative medicine," Int. J. Biol. Macromol. **107**(Pt A), 261–275 (2018).

23. D. Choudhury, S. Anand, and M. W. Naing, "The arrival of commercial bioprinters - Towards 3D bioprinting revolution!," Int. J. Bioprinting **4**(2), 139 (2018).

24. J. Li, M. Chen, X. Fan, and H. Zhou, "Recent advances in bioprinting techniques: approaches, applications and future prospects," J. Transl. Med. **14**(1), 271 (2016).

25. C. Mandrycky, Z. Wang, K. Kim, and D.-H. Kim, "3D bioprinting for engineering complex tissues," Biotechnol. Adv. **34**(4), 422–434 (2016).

26. E. Fornetti, F. De Paolis, C. Fuoco, S. Bernardini, S. M. Giannitelli, A. Rainer, D. Seliktar, F. Magdinier, J. Baldi, R. Biagini, S. Cannata, S. Testa, and C. Gargioli, "A novel extrusion-based 3D bioprinting system for skeletal muscle tissue engineering," Biofabrication **15**(2), (2023).

27. M. Costantini, S. Testa, P. Mozetic, A. Barbetta, C. Fuoco, E. Fornetti, F. Tamiro, S. Bernardini, J. Jaroszewicz, W. Święszkowski, M. Trombetta, L. Castagnoli, D. Seliktar, P. Garstecki, G. Cesareni, S. Cannata, A. Rainer, and C. Gargioli, "Microfluidic-enhanced 3D bioprinting of aligned myoblast-laden hydrogels leads to functionally organized myofibers *in vitro* and *in vivo*," Biomaterials **131**, 98–110 (2017).

28. W. Zhu, X. Ma, M. Gou, D. Mei, K. Zhang, and S. Chen, "3D printing of functional biomaterials for tissue engineering," Curr. Opin. Biotechnol. **40**, 103–112 (2016).

29. Ž. Kačarević, P. Rider, S. Alkildani, S. Retnasingh, R. Smeets, O. Jung, Z. Ivanišević, and M. Barbeck, "An Introduction to 3D Bioprinting: Possibilities, Challenges and Future Aspects," Materials **11**(11), 2199 (2018).

30. S. V. Murphy and A. Atala, "3D bioprinting of tissues and organs," Nat. Biotechnol. **32**(8), 773–785 (2014).

31. M. Colina, M. Duocastella, J. M. Fernández-Pradas, P. Serra, and J. L. Morenza, "Laser-induced forward transfer of liquids: Study of the droplet ejection process," J. Appl. Phys. **99**(8), 084909 (2006).

32. J. M. Fernández-Pradas, C. Florian, F. Caballero-Lucas, P. Sopeña, J. L. Morenza, and P. Serra, "Laser-induced forward transfer: Propelling liquids with light," Appl. Surf. Sci. **418**, 559–564 (2017).

33. P. Serra and A. Piqué, "Laser-Induced Forward Transfer: Fundamentals and Applications," Adv. Mater. Technol. **4**(1), 1800099 (2019).

34. J. Bohandy, B. F. Kim, and F. J. Adrian, "Metal deposition from a supported metal film using an excimer laser," J. Appl. Phys. **60**(4), 1538–1539 (1986).

35. P. Delaporte, A. Ainsebaa, A.-P. Alloncle, M. Benetti, C. Boutopoulos, D. Cannatà, F. Di Pietrantonio, V. Dinca, M. Dinescu, J. Dutroncy, R. Eason, M. Feinaugle, J.-M. Fernández-Pradas, A. Grisel, K. Kaur, U. Lehmann, T. Lippert, C. Loussert, M. Makrygianni, and I. Zergioti, "Applications of laser printing for organic electronics," in (2013), **8607**, p. 86070Z.

36. E. Breckenfeld, H. Kim, R. C. Y. Auyeung, N. Charipar, P. Serra, and A. Piqué, "Laser-induced forward transfer of silver nanopaste for microwave interconnects," Appl. Surf. Sci. **331**, 254–261 (2015).

37. J. A. Barron, B. J. Spargo, and B. R. Ringeisen, "Biological laser printing of three dimensional cellular structures," Appl. Phys. A **79**(4–6), 1027–1030 (2004).

38. B. Hopp, T. Smausz, N. Kresz, N. Barna, Z. Bor, L. Kolozsvári, D. B. Chrisey, A. Szabó, and A. Nógrádi, "Survival and Proliferative Ability of Various Living Cell Types after Laser-Induced Forward Transfer," Tissue Eng. **11**(11–12), 1817–1823 (2005).

39. L. Koch, S. Kuhn, H. Sorg, M. Gruene, S. Schlie, R. Gaebel, B. Polchow, K. Reimers, S. Stoelting, N. Ma, P. M. Vogt, G. Steinhoff, and B. Chichkov, "Laser Printing of Skin Cells and Human Stem Cells," Tissue Eng. Part C Methods **16**(5), 847–854 (2010).

40. M. Gruene, A. Deiwick, L. Koch, S. Schlie, C. Unger, N. Hofmann, I. Bernemann, B. Glasmacher, and B. Chichkov, "Laser Printing of Stem Cells for Biofabrication of Scaffold-Free Autologous Grafts," Tissue Eng. Part C Methods **17**(1), 79–87 (2011).

41. A. Karaiskou, I. Zergioti, C. Fotakis, M. Kapsetaki, and D. Kafetzopoulos, "Microfabrication of biomaterials by the sub-ps laser-induced forward transfer process," Appl. Surf. Sci. **208–209**, 245–249 (2003).

42. M. Colina, P. Serra, J. M. Fernández-Pradas, L. Sevilla, and J. L. Morenza, "DNA deposition through laser induced forward transfer," Biosens. Bioelectron. **20**(8), 1638–1642 (2005).

43. M. Gruene, C. Unger, L. Koch, A. Deiwick, and B. Chichkov, "Dispensing pico to nanolitre of a natural hydrogel by laser-assisted bioprinting," Biomed. Eng. OnLine **10**(1), 19 (2011).

44. L. Koch, A. Deiwick, A. Franke, K. Schwanke, A. Haverich, R. Zweigerdt, and B. Chichkov, "Laser bioprinting of human induced pluripotent stem cells—the effect of printing and biomaterials on cell survival, pluripotency, and differentiation," Biofabrication **10**(3), 035005 (2018).

45. N. Elangkovan and G. Dickson, "Gene Therapy for Duchenne Muscular Dystrophy," J. Neuromuscul. Dis. **8**(s2), S303–S316 (2021).

46. "Facioscapulohumeral dystrophy weakened sarcomeric contractility is mimicked in induced pluripotent stem cells-derived innervated muscle fibres - PubMed," https://pubmed.ncbi.nlm.nih.gov/34859613/.

47. A. M. DeSimone, J. Cohen, M. Lek, and A. Lek, "Cellular and animal models for facioscapulohumeral muscular dystrophy," Dis. Model. Mech. **13**(10), dmm046904 (2020).

48. "Frontiers | Fluorescence quenching by high-power LEDs for highly sensitive fluorescence in situ hybridization," https://www.frontiersin.org/articles/10.3389/fnmol.2022.976349/full.

49. J. Fang, Y. Xuan, and Q. Li, "Preparation of polystyrene spheres in different particle sizes and assembly of the PS colloidal crystals," Sci. China Technol. Sci. **53**(11), 3088–3093 (2010).

50. J. Lucki, J. F. Rabek, B. Rånby, and Y. C. Jiang, "Spectral differences in photodegraded polystyrene in various solvents," Polymer **27**(8), 1193–1200 (1986).

51. T. Li, C. Zhou, and M. Jiang, "UV absorption spectra of polystyrene," Polym. Bull. **25**(2), 211–216 (1991).

52. A. f. Lasagni, D. f. Acevedo, C. a. Barbero, and F. Mücklich, "Direct patterning of polystyrene–polymethyl methacrylate copolymer by means of laser interference lithography using UV laser irradiation," Polym. Eng. Sci. **48**(12), 2367–2372 (2008).

53. B. Wang, X. Wang, H. Zheng, and Y. C. Lam, "Thermal effect of femtosecond laser polystyrene processing," Opt. Laser Technol. **117**, 244–250 (2019).

54. C. Boronat, V. Correcher, J. García-Guinea, and J. C. Bravo-Yagüe, "Effects of UVC irradiation on polystyrene for healthcare packaging: Study by FTIR and Raman spectroscopy with thermoluminescence," Polym. Degrad. Stab. **222**, 110700 (2024).

55. Z. K. Wang, H. Y. Zheng, and Y. C. Lam, "Investigation on femtosecond laser irradiation energy in inducing hydrophobic polymer surfaces," Appl. Surf. Sci. **257**(24), 10427–10433 (2011).

56. Z. K. Wang, H. Y. Zheng, C. P. Lim, and Y. C. Lam, "Polymer hydrophilicity and hydrophobicity induced by femtosecond laser direct irradiation," Appl. Phys. Lett. **95**(11), 111110 (2009).

57. E. W. K. Young, E. Berthier, and D. J. Beebe, "Assessment of enhanced autofluorescence and impact on cell microscopy for microfabricated thermoplastic devices," Anal. Chem. **85**(1), 44–49 (2013).

58. A. Echte, F. Haaf, and J. Hambrecht, "Half a Century of Polystyrene—A Survey of the Chemistry and Physics of a Pioneering Material," Angew. Chem. Int. Ed. Engl. **20**(4), 344–361 (1981).

59. D. Wen, "Review of the relationship between the number of benzene rings within fluorescent dyes and its excitation wavelength," Highlights Sci. Eng. Technol. **17**, 221–227 (2022).

60. E. Abuin, E. Lissi, L. Gargallo, and D. Radic, "Polystyrene fluorescence spectra. Molecular weight dependence in different solvents," Eur. Polym. J. **20**(1), 105–107 (1984).

61. E. Yousif and R. Haddad, "Photodegradation and photostabilization of polymers, especially polystyrene: review," SpringerPlus **2**, 398 (2013).

62. K. R. Hawkins and P. Yager, "Nonlinear decrease of background fluorescence in polymer thin-films – a survey of materials and how they can complicate fluorescence detection in μTAS," Lab. Chip **3**(4), 248–252 (2003).

63. A. Piruska, I. Nikcevic, S. Hwan Lee, C. Ahn, W. R. Heineman, P. A. Limbach, and C. J. Seliskar, "The autofluorescence of plastic materials and chips measured under laser irradiation," Lab. Chip **5**(12), 1348–1354 (2005).

64. K. D. Sullivan and V. Gugliada, "Fluorescence photobleaching of microplastics: A cautionary tale," Mar. Pollut. Bull. **133**, 622–625 (2018).

65. W. Pfleging, M. Torge, M. Bruns, V. Trouillet, A. Welle, and S. Wilson, "Laser- and UV-assisted modification of polystyrene surfaces for control of protein adsorption and cell adhesion," Appl. Surf. Sci. **255**(10), 5453–5457 (2009).

66. M. W. Nicholson, C.-Y. Ting, D. Z. H. Chan, Y.-C. Cheng, Y.-C. Lee, C.-C. Hsu, C.-Y. Huang, and P. C. H. Hsieh, "Utility of iPSC-Derived Cells for Disease Modeling, Drug Development, and Cell Therapy," Cells **11**(11), 1853 (2022).

67. A. Zennifer, A. Subramanian, and S. Sethuraman, "Design considerations of bioinks for laser bioprinting technique towards tissue regenerative applications," Bioprinting **27**, e00205 (2022).

Ultrafast infrared laser application for highly organized skeletal muscle tissue modeling: from micrometric laser structuring to LIFT bioprinting

Supplementary material

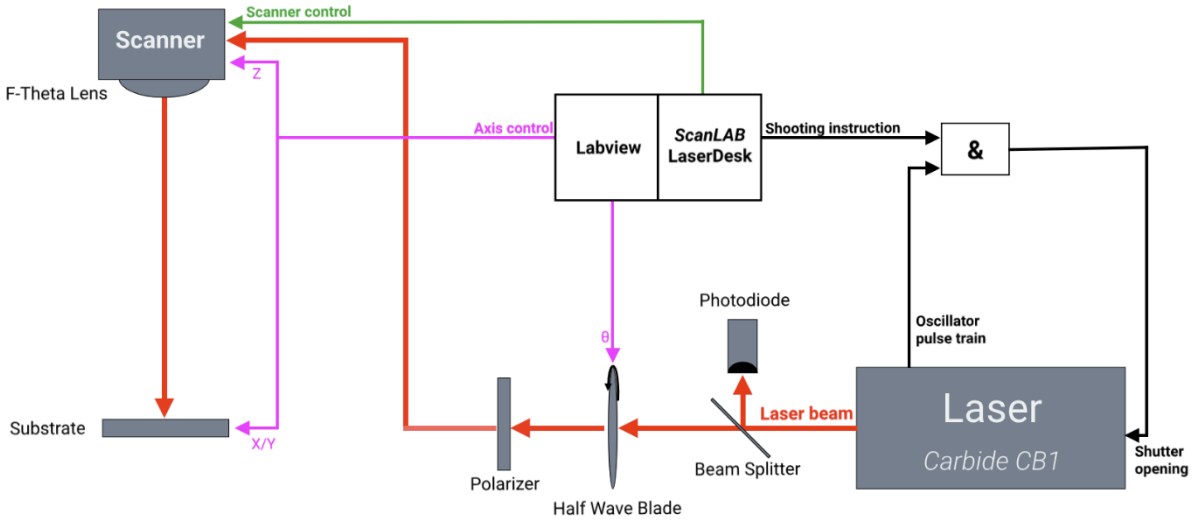

Fig. 1 Experimental set-up for laser structuring.

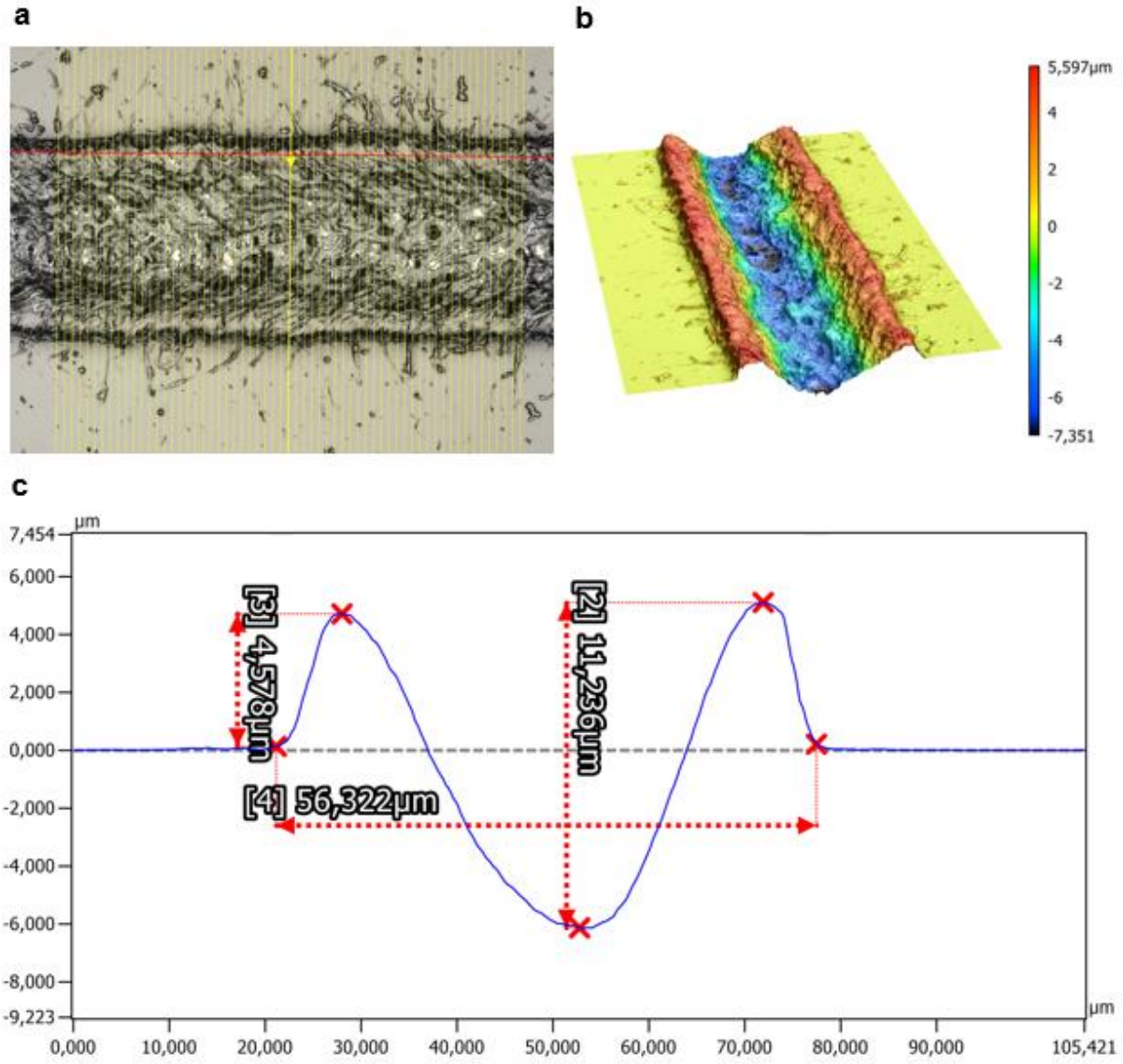

Fig. 2 (**a**) Profile lines for depth and width measurement of the laser-induced channels on polystyrene (PS) surfaces. (**b**) Topographical image of the channel, clear protrusions can be seen on the side of the channel with an indent of the culture surface in the center. (**c**) Detailed measurement of the channel depth, width and height of the protrusions.

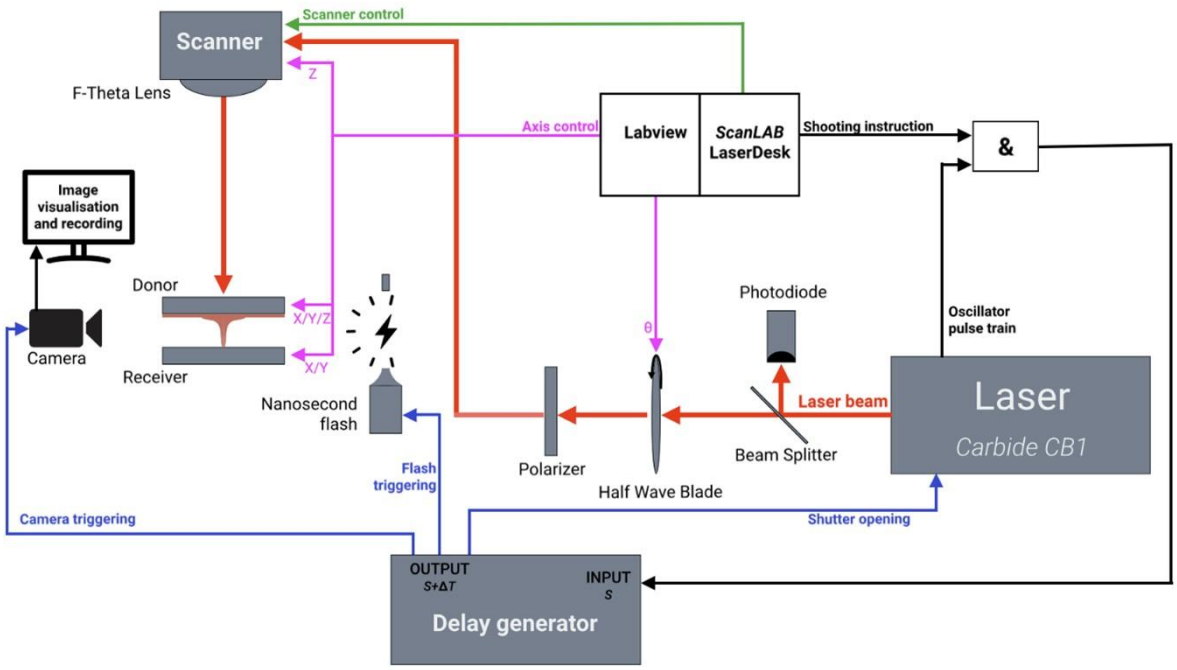

Fig. 3 Experimental set-up for LIFT printing of living cells.

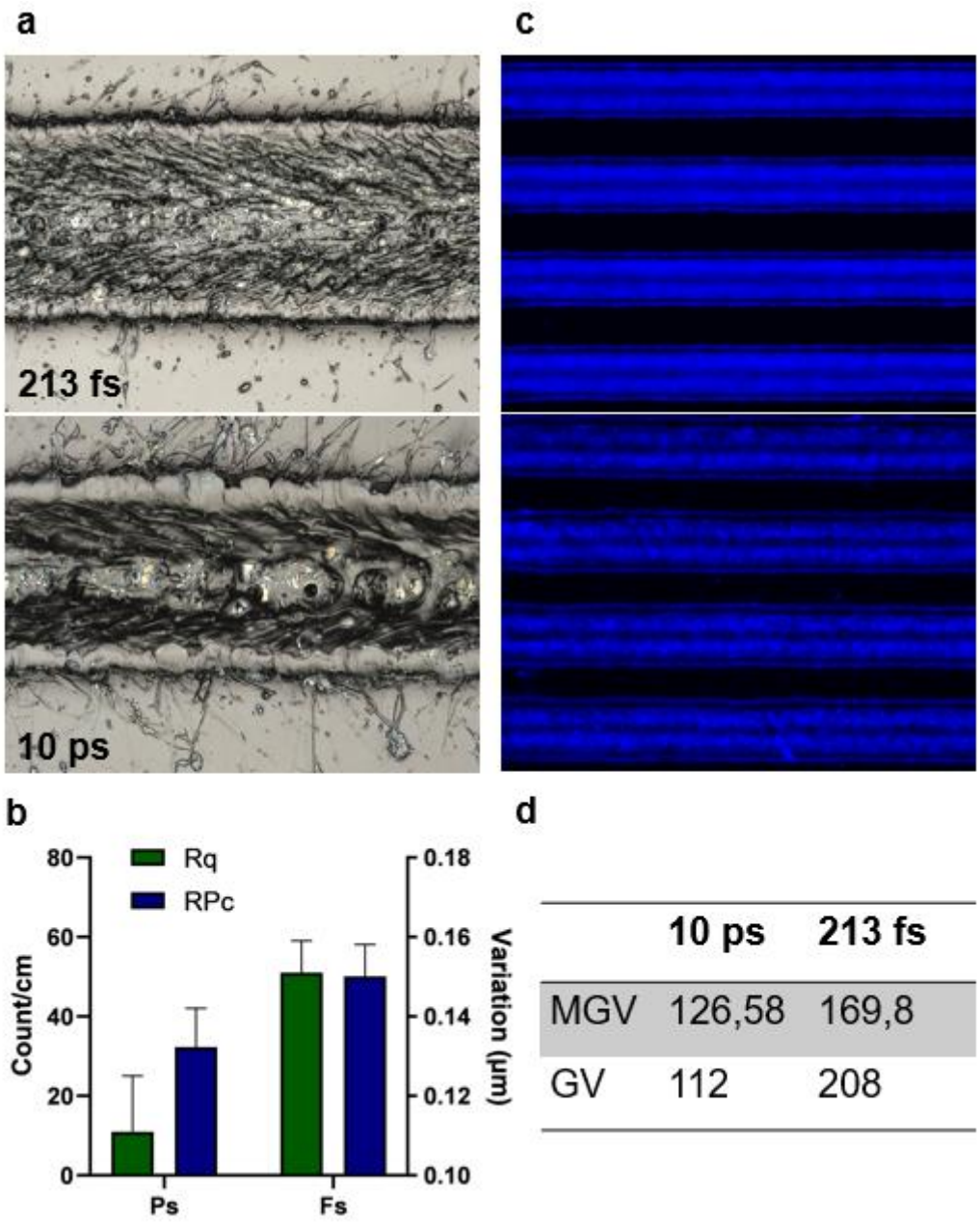

	10 ps	213 fs
MGV	126,58	169,8
GV	112	208

Fig. 4: Influence of porosity on autofluorescence. Channels of similar dimension (18µm depth) were created using laser pulses of 213 femtosecond (**a, top**) and 10 picoseconds (**a, bottom**). Rugosity was investigated by confocal microscopy and two key parameters (Rq mean roughness and RPc peak count number) reported in (**b**) show an increase of porosity with the use of femtosecond pulses. The associated autofluorescence of the channels are displayed in (**c**) and measured mean grey value (MGV) and grey value (GV) are reported in the table (**d**). We can notice a reduction in MGV with lower porosity channels.

The link between polystyrene porosity and its autofluorescence level was further studied through confocal microscopy and quantitative evaluation of surface roughness. The peak count number (RPc) and Root Mean Square Height (Mean roughness, Rq) were considered for this assessment; 35 roughness profiles were extracted parallel to the channel orientation. Two sets of parameters (energy/overlap) were chosen for pulse durations of 10 ps and 213 fs in order to obtain similarly sized channels (depth and width) of different apparent porosity. Channels' surface roughness and associated fluorescence were measured

for both conditions, and the results are displayed in **Figure 2.** We can first note a statistically significant difference in porosity between picosecond and femtosecond pulses, both in Rq and RPc, confirming our precedent qualitative observation. The chemical decomposition of PS under femtosecond ultrafast laser pulses is done through nonlinear mechanisms [47], which generates less heat, leading to sharper porosity due to the evaporation and vaporization of the material. Picosecond laser ablation entails a prolonged deposition of the energy on the material, giving rise to characteristic smoother melting zones and extensive protrusions on the channel's sides. Additionally, fluorescence analysis in DAPI indicated an MGV of 169.8 and a Modal GV of 208 for femtosecond pulses compared to an MGV of 126.6 and a Modal GV of 112 for picosecond pulses. Considering the similarity in the channel's dimensions and an analog statistical analysis, this notable increase in fluorescence is directly linked to the increase in porosity and exposed surface area.

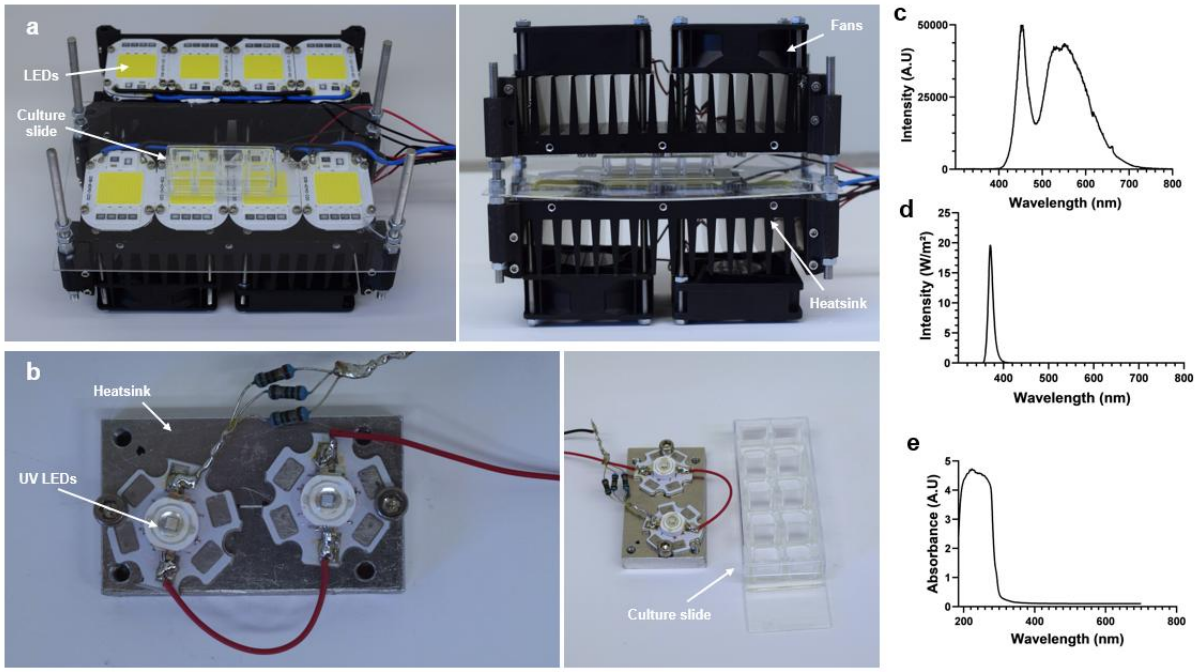

Fig. 5 Photobleaching devices to reduce PS autofluorescence after laser-structuring based on the use of white-LEDs (**a**) and UV LEDs (**b**). The use of extensive heatsinks and fans reduces the heat generated by the high-power white LEDs. Associated light spectra of white LEDs (**c**) and UV-LEDs (**d**) are displayed in comparison with the absorption spectra of PS (**e**)

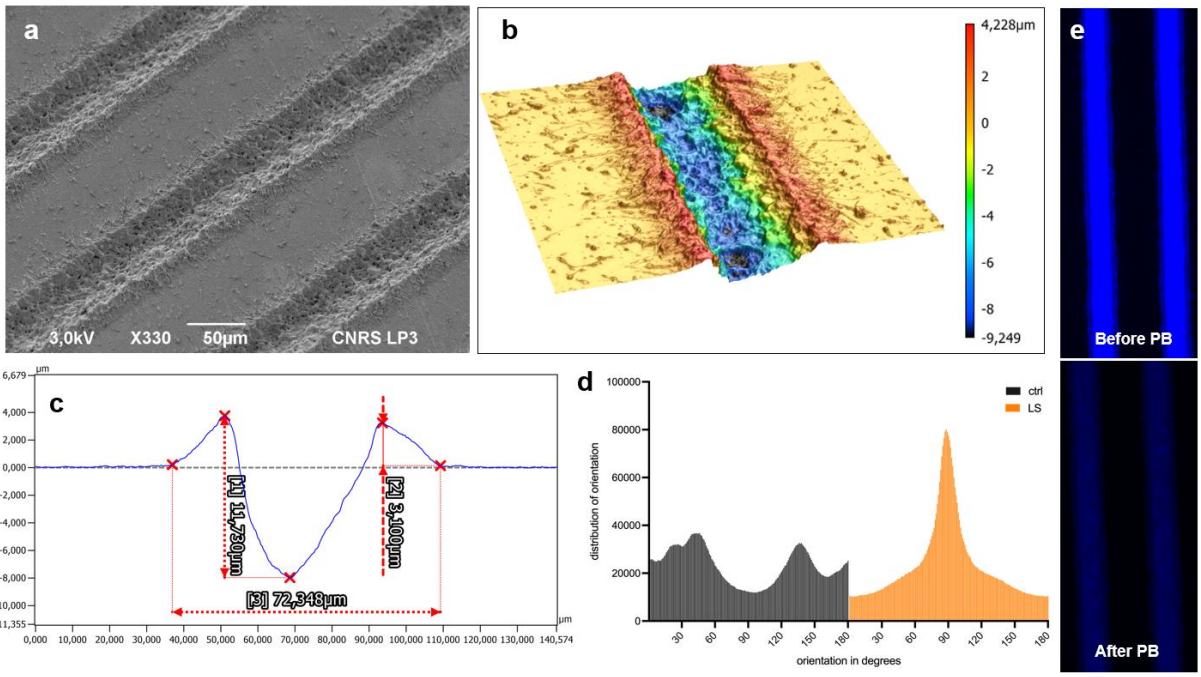

Fig. 6 Characterization of the laser structuration process on PET-G (polyethylene terephthalate glycol-modified) tissue culture coverslips used for LIFT bio-printing. SEM images of the laser-ablated channels(**a**) topographical characterization of the created channel and porosity (**b**). Dimension of the ablated channels, the different dimensions match the one observed on PS (**c**). Murine C2C12 myoblast alignment on structured (LS) and un-structured PET-G surface. Strong cell alignment can clearly be observed on the LS surfaces with one peak (**d**). Natural autofluorescence and result of photobleaching after UV-LEDs exposure, once again following the same pattern as for PS (**e**).

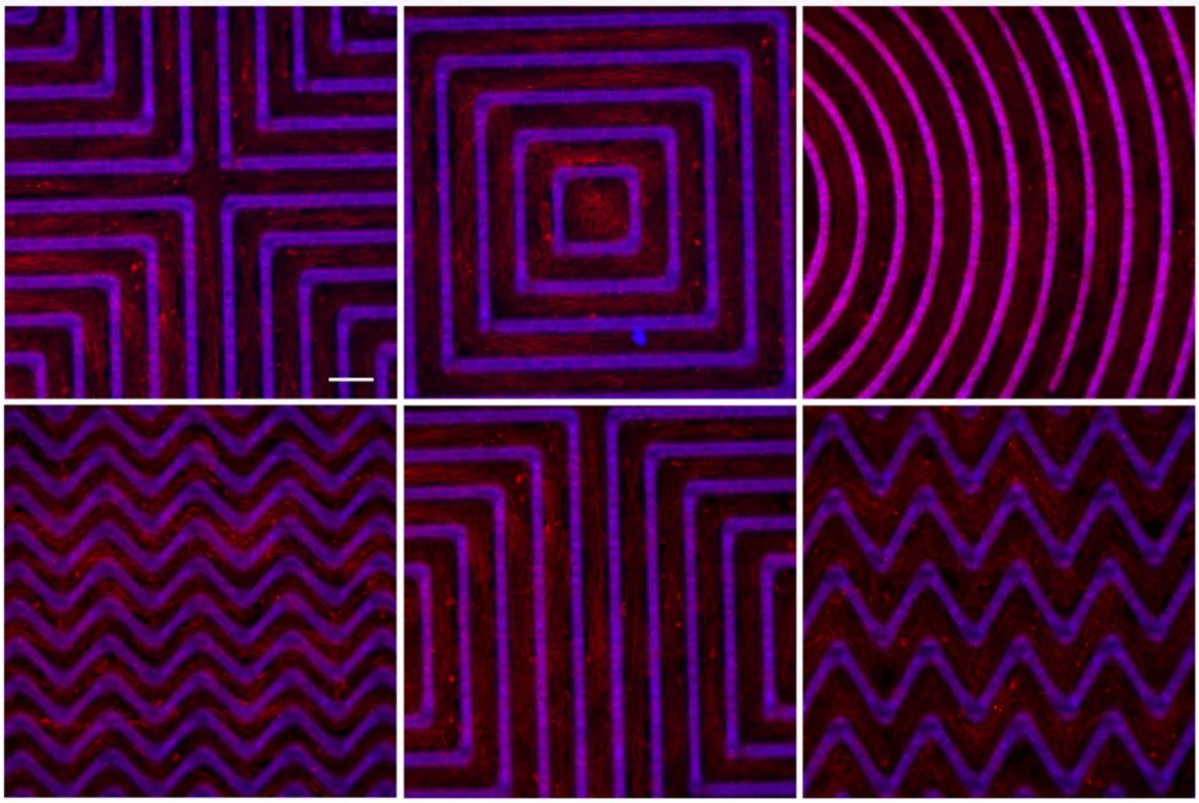

Fig. 7 complex LS patterns. The myoblasts stained for phalloidin (red) follow the laser structured channels (violet) along different complex patterns. Scale bar = 150 µm.

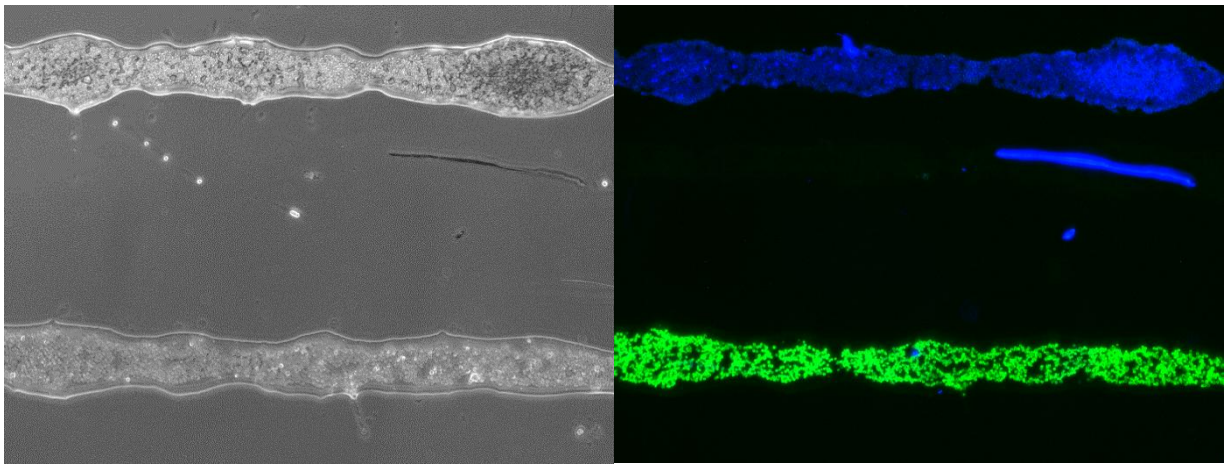

Fig. 8 LIFT bioprinting of two population of C2C12 cells stained in blue and green on a single receiver slide.

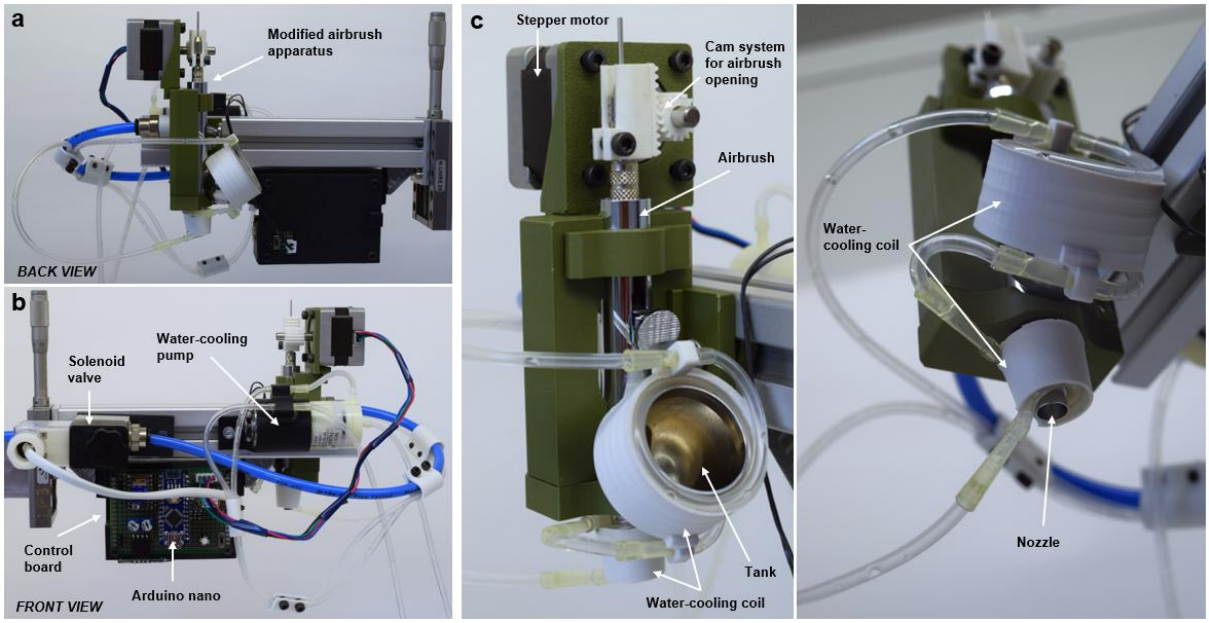

Fig. 9 Modified airbrush and associated apparatus to deposit thin layer of Matrigel on the receiver substrates (**a,c**). The Matrigel is loaded in the water-cooled tank of the airbrush. An Arduino nano is used to operate a solenoid valve that control the air influx (**b**). The control board comprises a stepper motor driver TMC2209 (Bigtreetech) controlling to a Nema 17 (StepperOnline) used to move the needle of the airbrush up and now through a cam system, effectively controlling the amount of material deposited. A box filled with ice water is used as water-cooling agent, the water is circulated by an inkjet printer rolling pump through coiled plastic tubing (Tygon, Saint-Gobain Industrial & Consumer Solutions) to maximize the contact surface area (**c**).

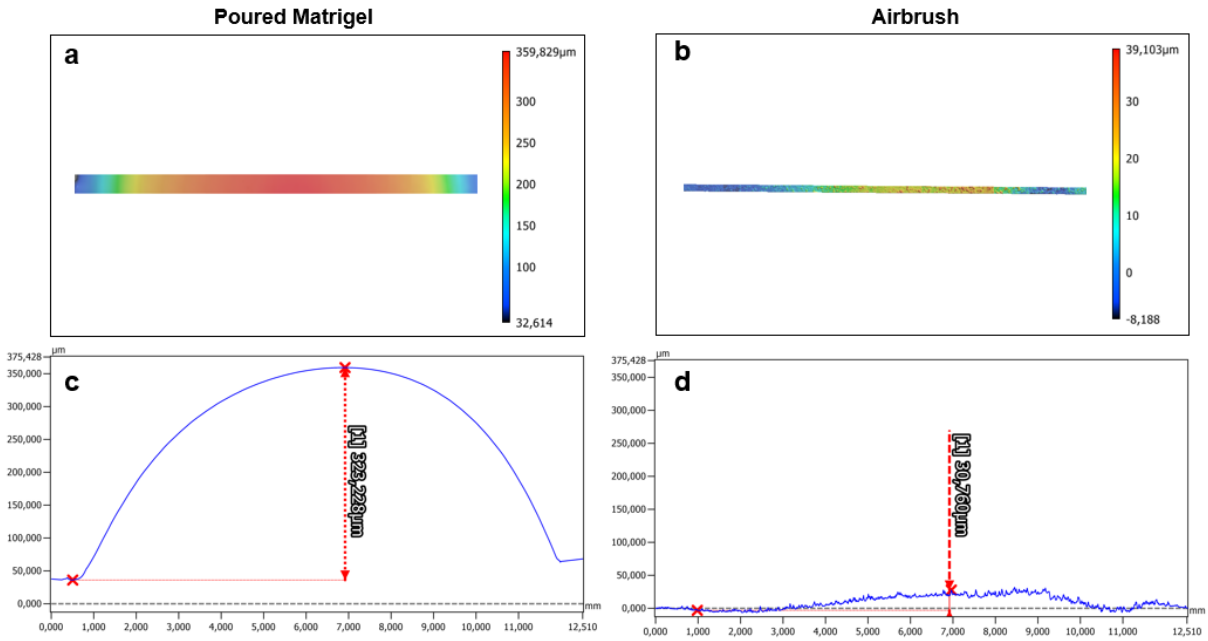

Fig. 10 Analysis of coating surface homogeneity through confocal microscopy. Topographical map for poured Matrigel (**a**) and airbrushed Matrigel (**b**). Associated profile averaged on 30 lines spaced by 2 µm across the entire diameter of a 13mm PET-G culture tissue coverslips for poured (**c**) and airbrush (**d**) Matrigel

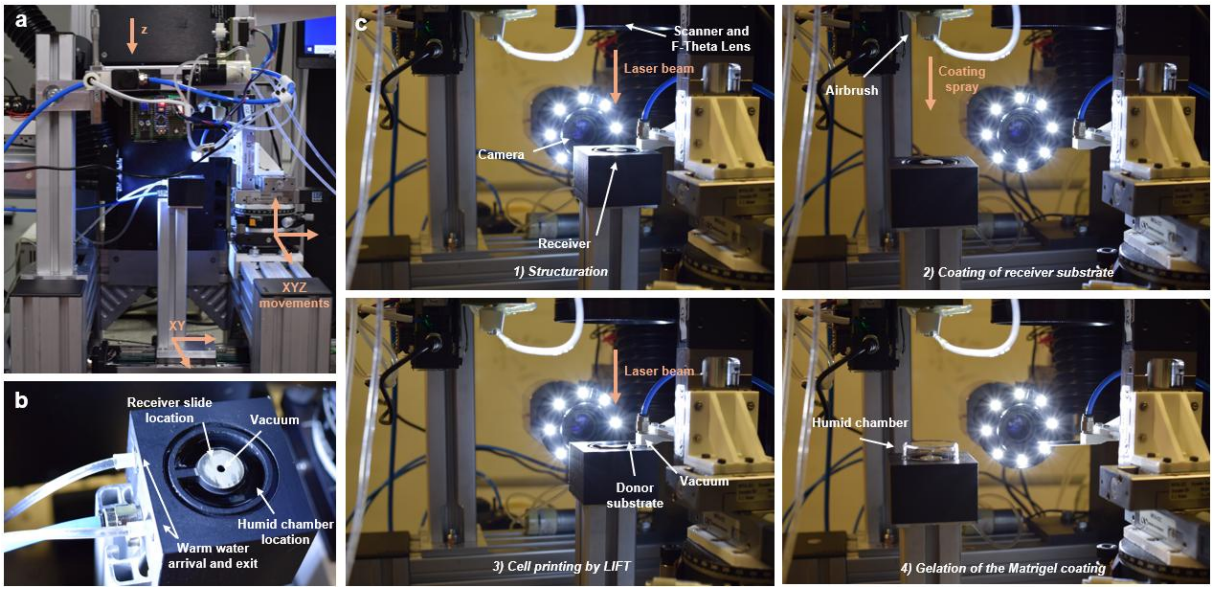

Fig. 11 (**a**) Front view of the full experimental apparatus. (**b**) The receiver is positioned on a 3D printed homemade humid chamber comprising a vacuum intake used to firmly maintain the receiver in position during the whole procedure. Warm water is circulated in close proximity to the receiver slide by an inkjet printer rolling pump. The water passes through plastic tubing which is coiled inside a glass water bottle positioned on top of a heating plate. A circular groove allows for a plastic cover to seal the chamber, effectively promoting condensation and saturating the environment in water vapor. (**c**) Close-up of the experimental set-up with the different step for structuring the receiver slide (**1**), coating it with Matrigel(**2**), printing the cells by LIFT (**3**) and allowing the gelation of the Matrigel (**4**).

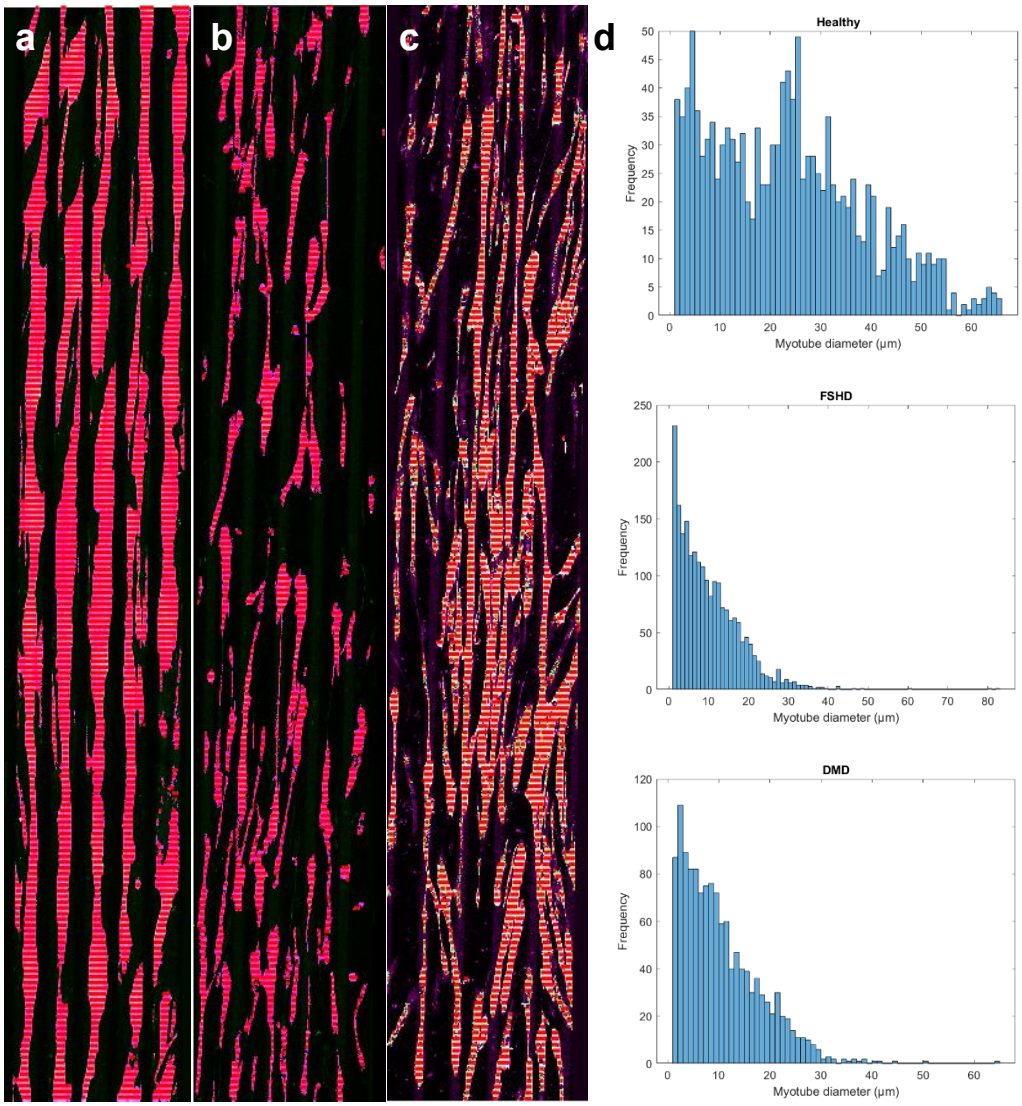

Fig. 12 MATLAB automation of the diameter measurement. Diameter measured on each condition tested are represented in (**a,b,c**). The code is based on the isolation of the myotubes by binarization and morphological operations. The resulting objects are segmented horizontally independently from their sizes. The associated histogram of diameter occurrence are shown in (**d**).

3.5 Article 5: Assessment of laser-synthesized Si nanoparticle effects on myoblast motility, proliferation, and differentiation: towards potential tissue engineering applications

Clarissa Murru[a], **Lucas Duvert**[a,b], Frederique Magdinier[b], Adrien Casanova[a], Anne-Patricia Alloncle[a], Stefano Testa [*b], Ahmed Al-Kattan[a]

a: Aix Marseille University, CNRS, LP3 UMR 7341 , Marseille, France

b: Aix Marseille University, INSERM, Marseille Medical Genetics, Marseille, France

Published Nanoscale Advances (2024)

Context

Nano-sized materials are defined as substance with at least one dimension smaller than 100 nm. Among these, nanoparticles are classified as a zero-dimensional nanomaterials, as all three of their dimensions fall within the nanoscale range (A.K et al., 2019). Nanoparticles are characterized by their small size, large surface area and their ability to undergo surface modification, making them ideal for drug loading. Nanomaterials can serve as effective carriers for the targeted and controlled release of growth factors, cytokines and other bioactive molecules (Han et al., 2023).

Due to their unique properties and abilities, nanoparticles have been widely explored for various applications including drug delivery and tissue engineering (Jeong et al., 2022). Their potential in promoting skeletal muscle regeneration has also been demonstrated, as they enhance cell migration, alignment, and differentiation. However, the factors influencing nano-bio interactions and their precise effects on cell physiology remain subject of interrogations and rigorous investigations (Carnovale et al., 2019).

Gold nanoparticles (AuNPs) are commonly used in biomedical applications for their relative biocompatibility (Leite et al., 2015) and ability to bind with proteins. Research has shown that AuNPs can enhance C2C12 cell proliferation and differentiation through different signaling pathways, while gold-silver alloys have been reported to improve *in vivo* skeletal muscle regeneration (Ge et al., 2018). Biocompatible polymer-based NPs have also been utilized in clinical settings for the delivery of therapeutic agents

combined with active targeting of specific cells and tissues. These NPs encapsulate drugs to ensure temporal and spatial control over their delivery. The polymeric composition of the NP, along with their functionalization, enhances the safety and efficacy of already FDA-approved drugs (Gokarn et al., 2012; D. Huang et al., 2020).

In the context of developing a laser platform for skeletal muscle tissue engineering, we explored the use of femtosecond lasers to fabricate ultra-pure nanoparticles (NPs) aimed at enhancing the myogenic potentiality of progenitor cells.

Laser-based NP production presents a flexible and fast alternative to conventional chemical and electrochemical production methods that often involve additional potentially dangerous reagents. By directing the laser beam at a solid target immersed in liquid, nanoclusters form and coalesce in the medium, resulting in a stable colloidal NP solution. This method allows for the creation of functional nanoparticles from various materials, each with the potential to influence cell maturation in different ways.

Here, we first investigated the use of titanium NP (data not shown), which proved to be non-toxic but did not enhance cell performance. We then shifted to silicon nanoparticles, which have shown promises in the literature. We investigated their ability to improve the proliferation, motility, and differentiation of murine C2C12 cells.

The strength of this approach lies in its simplicity and versatility. We demonstrated the generation of nanoparticles using the same laser setup previously applied in our other experiments, highlighting the adaptability of this platform.

Results

We characterized the physicochemical properties of Si-NPs, which had an average size of 50 nm, and selected concentrations ranging from 14 to 224 µg/mL for testing. However, an MTT colorimetric assay revealed high cytotoxicity at concentrations above 56 µg/mL. As a result, the range for biological tests was narrowed to four concentrations: 0, 14, 28, and 56 µg/mL.

SEM and EDX measurements proved the internationalization of the Si-NP by myoblasts and the abundance of the silicon element in the cells. Further biological testing showed that the 28 µg/mL concentration significantly enhanced cell proliferation and promoted myoblast differentiation into multinucleated myotubes. Quantitative real-time PCR analysis supported these findings, demonstrating that Si-NPs, particularly at 28 µg/mL, increased the expression of differentiation-related genes such as MyoD, Desmin, and Myosin Heavy Chain over time.

Conclusions

In this work, we demonstrated that ultra-pure laser-induced Si-NPs improved the myogenic capabilities of myoblasts. The laser generation process efficiently produces stable abiotic factors usable for improved differentiation and tissue engineering applications.

Contribution

In this work, I participated in the elaboration of the nanoparticle solutions and implemented technical solutions to improve the process performance and efficiency.

Publication

Nanoscale Advances

ROYAL SOCIETY OF CHEMISTRY

PAPER

View Article Online
View Journal

Check for updates

Cite this: DOI: 10.1039/d3na01020a

Assessment of laser-synthesized Si nanoparticle effects on myoblast motility, proliferation and differentiation: towards potential tissue engineering applications†

Clarissa Murru,[a] Lucas Duvert,[ab] Frederique Magdinier,[b] Adrien Casanova,[a] Anne-Patricia Alloncle,[a] Stefano Testa *[b] and Ahmed Al-Kattan *[a]

Due to their biocompatibility and biodegradability and their unique structural and physicochemical properties, laser-synthesized silicon nanoparticles (Si-NPs) are one of the nanomaterials which have been most studied as potential theragnostic tools for non-invasive therapeutic modalities. However, their ability to modulate cell behavior and to promote proliferation and differentiation is still very little investigated or unknown. In this work, ultrapure ligand free Si-NPs of 50 ± 11.5 nm were prepared by femtosecond (fs) laser ablation in liquid. After showing the ability of Si-NPs to be internalized by murine C2C12 myoblasts, the cytotoxicity of the Si-NPs on these cells was evaluated at concentrations ranging from 14 to 224 μg mL^{-1}. Based on these findings, three concentrations of 14, 28 and 56 μg mL^{-1} were thus considered to study the effect on myoblast differentiation, proliferation and motility at the molecular and phenotypical levels. It was demonstrated that up to 28 μg mL^{-1}, the Si-NPs are able to promote the proliferation of myoblasts and their subsequent differentiation. Scratch tests were also performed revealing the positive Si-NP effect on cellular motility at 14 and 28 μg mL^{-1}. Finally, gene expression analysis confirmed the ability of Si-NPs to promote proliferation, differentiation and motility of myoblasts even at very low concentration. This work opens up novel exciting prospects for Si-NPs made by the laser process as innovative tools for skeletal muscle tissue engineering in view of developing novel therapeutic protocols for regenerative medicine.

Received 20th November 2023
Accepted 23rd February 2024

DOI: 10.1039/d3na01020a

rsc.li/nanoscale-advances

Open Access Article. Published on 18 March 2024. Downloaded on 3/18/2024 2:54:46 PM.
This article is licensed under a Creative Commons Attribution-NonCommercial 3.0 Unported Licence.

1 Introduction

The possibility of monitoring cell behaviour and fate can dramatically help in the development of novel tissue engineering technology and therapeutic protocols in view of repairing and regenerating damaged tissues, occurring after injury or other degenerative diseases.[1] In this context, several approaches are currently investigated, including bio-inspired surface topography,[2] engineered functional nanoparticles[3,4] and chemical surface functionalization.[5] Similarly, due to their particular physicochemical properties (size, porosity, hydrophobicity, chemical composition, *etc.*), nanoparticles (NPs) have attracted great interest in the design of innovative theragnostic tools for drug delivery,[6] cell tracking[7,8] and therapy[9,10] with a particular focus on non-invasive anticancer therapeutics (*e.g.*, light-induced generation of singlet oxygen and related photodynamic therapy, radio frequency-induced hyperthermia, *etc.*).[11] On the other hand, their ultra-small size, down to 100 nm, and their high surface reactivity could offer remarkable interactions with biological environments which can be evaluated for their ability to modulate cell behaviour or to influence aspects such as cell differentiation and proliferation.[12,13] The control of the different cellular mechanisms listed above can both improve the fabrication of innovative nanocomposite materials for biomedical applications and promote the use of improved strategies towards therapeutic protocols in order to restore functionality of tissues damaged due to trauma, degenerative diseases or aging.[14] To date, several types of NPs based on polymers, metals and ceramics have been investigated in this respect; most of these studies were thus performed using a variety of stem cells including induced pluripotent stem cells (iPSCs).[15–18] For instance, Au-NPs functionalized with citrate, chitosan or fibronectin, are able to enhance the differentiation of human mesenchymal stem cells (MSCs) and adipose-derived stem cells (ADSCs), respectively, into cardiomyocytes and osteoblasts.[19,20] Ag-NPs can promote osteogenic differentiation of human urine-derived stem cells (USCs) and the proliferation of MSCs,[21] while graphene-based NPs enhance the

[a]Aix-Marseille University, CNRS, LP3 UMR 7341, Campus de Luminy, C13288, Marseille, France. E-mail: ahmed.al-kattan@univ-amu.fr

[b]Aix-Marseille University, INSERM, MMG, Marseille Medical Genetics, 13385 Marseille, France. E-mail: stefano.testa@univ-amu.fr

† Electronic supplementary information (ESI) available. See DOI: https://doi.org/10.1039/d3na01020a

© 2024 The Author(s). Published by the Royal Society of Chemistry

Open Access Article. Published on 18 March 2024. Downloaded on 3/18/2024 2:54:46 PM.
This article is licensed under a Creative Commons Attribution-NonCommercial 3.0 Unported Licence.

cardiomyogenic and angiogenic differentiation capacity of MSCs for cardiac tissue regeneration.[22] Due to their biocompatibility and biodegradability, SiO_2-NPs were also investigated for their ability to modulate murine myoblast (C2C12) behaviour by improving the differentiation of C2C12 myoblasts into myotubes with a beneficial effect on muscle growth.[23] Despite these promising results, the major concerns about the NPs employed in these research studies are their conventional chemical and electrochemical production methods, which involve hazardous products (*e.g.*, HF, nitrate salts, chloride, citrate, *etc.*) and various ligands. The presence of potentially dangerous reagents generally leads to surface contamination by residual toxic products, which can negatively influence the interaction with the biological matrix.[24] Moreover, in some cases the elaboration of NPs takes place under extreme physicochemical conditions (*e.g.*, pH, pressure, temperature, *etc.*) which requires a rigorous control of the synthesis procedure. These reactions frequently necessitate different organic solvents (*e.g.*, ethanol, THF, *etc.*) leading to switching steps between organic and aqueous solutions that complicates the fabrication and purification procedures.[25] Driven by its flexibility, simplicity and rapidity, we have recently introduced an ultra-short femtosecond (fs) laser ablation approach in liquid as a relevant process to design ultra-pure crystalline NPs for biomedical applications. Thanks to the interaction of a fs laser beam with a solid target initially immersed in a liquid, this method allows the formation of nanoclusters which coalesce in a liquid medium to produce a very stable colloidal NP solution.[26] Moreover, by playing with several parameters of the laser (*e.g.*, fluence, beam time duration, ablation/fragmentation sequence, *etc*), the possibility to monitor their physicochemical properties including size, size-distribution and chemical composition has been demonstrated.[27,28] In this context, we have recently used Si (silicon), already known to be involved in many physiological activities such as bone mineralization[29] and transduction mechanisms,[30] to elaborate Si-NPs by fs laser ablation in liquid for biomedical applications. Our study proved their biocompatibility and biodegradability into orthosilicic acid $Si(OH)_4$ without specific induced toxicity.[31] We thus demonstrated their complete safety properties thanks to systematic *in vitro* and *in vivo* tests,[32] while their therapeutic potential was assessed by a variety of non-invasive testes including intra-tumour radiofrequency (RF)-induced hyperthermia[33] and two-photon excited photodynamic therapy (TPE-PDT).[34] Furthermore, we tested Si-NPs as functional additives in innovative electrospun-nanofiber platforms for tissue engineering applications.[35] Nanoparticles can lead to the development of novel tissue engineering technologies and therapeutic protocols to regenerate damaged tissues. Hence, their ability to modulate different aspects of cellular programs is still very little investigated or unknown. In this work, we assessed the effect of laser-synthesized Si-NPs on murine C2C12 myoblast differentiation, proliferation and motility both at the molecular and phenotypical levels. This work is conceived as a first step towards the possible use of these types of Si-NPs in skeletal muscle cells for future applications in tissue engineering and regenerative medicine.

2 Materials and methods

2.1 Synthesis of Si-NPs and characterization

Fabrication of the Si-NPs was carried out with a femtosecond laser (Light Conversion Carbide CB1-05 Yb:KGW), working with a pulse duration of 430 fs, an energy per pulse of 40.3 μJ and a repetition rate of 10 kHz at 1028 nm. Precisely, a Si wafer was placed at the bottom of a glass vessel filled with 10 mL of ultrapure water, and then subjected to a fs laser beam for 10 min with a fluence of 5.081 J cm^{-2}. To promote optimal surface ablation, a scanner system was coupled with the fs laser beam. The characterization of the structural properties of the Si-NPs was achieved through a high-resolution transmission electron microscopy (HR-TEM) system (JEOL JEM 3010) in imaging and diffraction modes working at 200 kV. In parallel dynamic light scattering (DLS) measurements were also performed on Si-NPs solution with a Zetasizer Nano ZS instrument (Malvern Instruments) to assess their hydrodynamic size and zeta potential surface charge. To proceed to biological *in vitro* studies, calibrated Si-NP solutions at increased concentrations in the range of 14 to 224 μg mL^{-1} were prepared through a centrifugation process (14 200 rpm for 10 min). The concentration of the Si-NPs was measured by an inductively coupled plasma mass spectrometry (ICP-MS) method.

2.2 Cell cultures

Murine myoblasts C2C12 (ATCC) were cultured according to a previously published protocol[36] in T-75 Flasks (Sarstedt) at 37 °C and 5% CO_2 in DMEM GlutaMAX (Gibco) supplemented with 10% heat-inactivated fetal bovine serum (FBS, EuroClone), penicillin (100 IU mL^{-1}, Gibco), and streptomycin (100 mg mL^{-1}, Gibco). To stimulate differentiation, once 90% confluency was reached, cells were transferred to differentiation medium (DM) composed of DMEM GlutaMAX (Gibco) supplemented with 2% horse serum (Gibco). The images and counting of the cells were obtained with a reverse microscope (EVOS M5000, Invitrogen, Thermo Fisher, America).

2.3 Cell survival assay

For cell survival assays, C2C12 cells were seeded in 12-well plates (Thermo Scientific) at 5×10^4 cells per well respectively. After 24 h, the culture medium was replaced by 1 mL of fresh medium containing different concentrations of Si-NPs (14 to 224 μg mL^{-1}). After 72 h of exposure, cell viability was determined by MTT (3-(4,5-dimethylthiazol-2-yl)-2,5-diphenyltetrazolium bromide) colorimetric assay. This test is based on the reduction of the tetrazolium salt by the mitochondria of living cells. The absorbance measured at 600 nm is proportional to the number of living cells.

2.4 Differentiation assay

The fusion index (FI) is defined as the ratio between the number of nuclei included in myosin heavy chain-expressing cells (containing at least three nuclei) and the number of nuclei for each field. To assess the influence of Si-NPs on C2C12 myoblast

© 2024 The Author(s). Published by the Royal Society of Chemistry

Open Access Article. Published on 18 March 2024. Downloaded on 3/18/2024 2:54:46 PM.
This article is licensed under a Creative Commons Attribution-NonCommercial 3.0 Unported Licence.

myogenic differentiation,[37] FI was manually calculated using Fiji software, on samples prepared as described below. C2C12 cells were seeded into 12-well plates (Thermo Scientific) at 10^5 cells per well. After 24 h the culture medium was replaced by 1 mL of fresh medium containing different concentrations of Si-NPs (0, 14, 28, and 56 μg mL^{-1}). After 48 h the cells reached adequate confluence (90%), and the medium was replaced with a differentiation medium to induce myotube formation. DM was changed every 48 h for up to 1 week, to allow for proper myogenic differentiation. Then, after rinsing medium residues with PBS, cells were fixed with 4% paraformaldehyde in PBS at 4 °C for 10 min and stored at 4 °C for subsequent immunofluorescence analysis.

2.5 Immunofluorescence analysis

The samples were analyzed by immunofluorescence according to a previously described protocol.[38] Briefly, cells were permeabilized in a solution of Triton X-100 0.3% in PBS for 1 h at room temperature (RT) and blocked with a blocking solution consisting of 10% goat serum, 1% glycine, and 0.1% Triton X-100 in PBS for 1 h at RT. Subsequently, the cells were incubated with mouse monoclonal anti-myosin heavy chain (MF20, DHSB) primary antibody, diluted 1 : 100 in a blocking solution for 2 h at RT and then rinsed with a washing solution consisting of 1% bovine serum albumin (BSA) and 0.2% Triton X-100 in PBS. After washing, the cells were incubated with Alexa Fluor 555-conjugated goat anti-mouse IgG secondary antibody (H + L; Thermo Fisher Scientific, diluted 1 : 400) for 1 h. Finally, the nuclei were counterstained with 300 nM DAPI (Thermo Fisher Scientific) in PBS for 10 min.

2.6 Sample preparation for high-resolution scanning electron microscopy imaging (HR-SEM) coupled with energy dispersive X-ray (EDX) analysis

The adhesion of the Si-NPs to the cell wall was monitored through images obtained using HR-SEM (Jeol JSM-7900F) working at 30 kV. C2C12 myoblasts were seeded on glass coverslips (10^5 per sample) and 24 h later exposed to 56 μg mL^{-1} Si-NPs for 72 h. Then, the culture medium was removed and the cells were washed 3 times with PBS in order to eliminate the NPs in the suspension. Subsequently, the samples were fixed with 5% glutaraldehyde solution over 2 h, then washed with increasing concentrations of ethanol (25, 50, 75, and 95%) and finally stored at 2 °C until analysis. HR-SEM coupled with EDX measurements were also performed on cell sections of C2C12 cells to confirm Si-NP internalization. Basically, C2C12 myoblasts were seeded in 6-well plates (Thermo Scientific) (10^5 per sample) and 24 h later exposed to 56 μg mL^{-1} Si-NPs for 72 h. The culture medium was removed and the cells were washed with a 0.1 M phosphate buffer solution. Subsequently the myoblasts were fixed with 2 mL of a glutaraldehyde 2.5% and 0.1 M phosphate buffer mixture for one hour under gentle stirring conditions. After the removal of glutaraldehyde, the samples were washed and fixed with 2 mL of a 1% osmium solution diluted in phosphate buffer and kept in total darkness for 30 minutes. Several washing steps were then carried out with increasing concentrations of ethanol (50, 70, 80, 90, and 100%) in order to promote a gradual dehydration of the specimens. The fixed and dehydrated cells were finally removed from the multi-well plate, soaked in the resin and polymerized at 60° for 24 hours. The use of a microtome cutter and a diamond blade was crucial to obtain resin segments with a thickness of 30 μm that allow the analysis of cell sections which were deposited on TEM grids to perform SEM analysis. EDX measurements were performed to confirm the chemical nature of the Si-NPs detected.

2.7 Proliferation assay

Growth curves were obtained according to Testa *et al.*[39] method. Briefly, C2C12 cells were seeded into 24-well plates (Thermo Scientific) at 10^4 cells per well. Three wells were prepared for each experimental time point (1, 3, 6, and 8 days) and each Si-NP concentration (0, 14, 28, and 56 μg mL^{-1}). Cellular proliferation was evaluated by harvesting cells at each time point and calculating the average cell number by means of a Burker counting chamber.

2.8 Scratch-wound healing assay

Scratch-wound assays were performed according to the Gargioli *et al.* study.[40] C2C12 cells were seeded in 12-well plates (Thermo Scientific) at 10^5 cells per well. Three wells for each concentration of Si-NPs (0, 14, 28, and 56 μg mL^{-1}) were prepared. After 48 h, the confluent C2C12 monolayer was scratched by using a 10 μL pipette tip. The cells were washed with DMEM (Gibco) to remove any detached cells, and 1 mL of fresh medium containing the right concentration of Si-NPs was added. Time lapse imaging was recorded for each well, taking photographs every 30 minutes for 24 hours.

2.9 Quantitative RT-PCR analysis

C2C12 cells were seeded in 6-well plates (Thermo Scientific) at 3 × 10^5 cells per well, with three wells for each concentration of Si-NPs (0, 14, 28, and 56 μg mL^{-1}) and each experimental time point (early – 80% of cell confluence – day 1; medium – 100% of cell confluence – day 2; late – differentiated myotubes – day 4). Once full confluence was reached (medium point), the growth medium was changed to the differentiation medium, to allow the correct differentiation of myoblasts. RNA was extracted using an RNeasy mini kit (Qiagen), and then 2 μg of RNA for each sample was retrotranscribed using SuperScript IV reverse transcriptase (Invitrogen), according to the manufacturers' instructions. Glyceraldehyde 3-phosphate dehydrogenase (GAPDH) was selected as the endogenous control after verifying its stable expression. Quantitative RT-PCR analysis was performed with a QuantStudio™ 5 Real-Time PCR System (96-wells, Applied Biosystems). Each cDNA sample was amplified using a LightCycler 480 SYBR Green I Master (Roche). Relative mRNA levels were calculated by the delta CT method (ΔΔCt).[41] Primer specificity was confirmed by melting curve analysis.

The primers used are listed below:

(1) GAPDH (80): Fw: ACTGAGCAAGAGAGGCCCTA; Rv: TATGGGGGTCTGGGATGGAA

(2) MHC (85): Fw: AACTGAAGAATGCCTATGAAG; Rv: TCTGCTATCTCTTGTTCTAAGT

Open Access Article. Published on 18 March 2024. Downloaded on 3/18/2024 2:54:46 PM.
This article is licensed under a Creative Commons Attribution-NonCommercial 3.0 Unported Licence.

(3) MyoD1 (82): Fw: GGAAGGGAAGAGCAGAAG; Rv: AAGGACTACAACAACAACAAC

(4) Desmin (82): Fw: CGTGACAACCTGATAGAC; Rv: TGTTCTCTGCTTCTTCTC

(5) Myomaker (94): Fw: GTTGCTTCACTCTGTTCA; Rv: TATTTACTGGTCTAGGGTTCT

(6) MKi67 (75): Fw: GGCATTCACAGCAACTTA; Rv: CACCTTCATCCAGATTCAC

(7) C-met (148): Fw: AGTCCTATATTGATGTCTTAC; Rv: AACCTGATTATTCTTGTATGA

2.10 Statistical analysis

All experiments were performed at least in biological triplicate. Data were analyzed using GraphPad Prism 8, and values were expressed as means ± standard error. Statistical significance was tested using one-way ANOVA tests with the appropriate multiple comparison tests. A probability of less than 5% ($p < 0.05$) was considered as statistically significant.

3 Results

3.1 Physicochemical characterization of Si-NPs

As described above, Si-NPs elaborated by the femtosecond laser process were characterised by HR-TEM coupled with X-ray diffraction measurements. As shown in Fig. 1, Si-NPs appeared typically spherical (Fig. 1a) with an average diameter of 50 ± 11.5 nm (Fig. 1b). Moreover, electron diffraction analysis confirmed the polycrystalline structure of Si-NPs with the presence of diffraction rings, corresponding to the (111), (220), and (311) and (331) crystalline planes of the cubic diamond structure (Fig. 1c).

ζ-Potential measurements were also carried out revealing negative surface −45 ± 1.5 mV due to partial oxidation of the surface. The concentration of Si-NPs was systematically determined by inductively coupled plasma mass spectroscopy (ICP-MS) at an average of 14 ± 1 μg mL^{-1}. To proceed to biological *in vitro* studies, calibrated Si-NP solutions at increased concentrations in the range of 14 to 224 μg mL^{-1} were prepared based on centrifugation at 14 200 rpm for 10 min. The value of 0 μg mL^{-1} of Si-NPs was taken as the control.

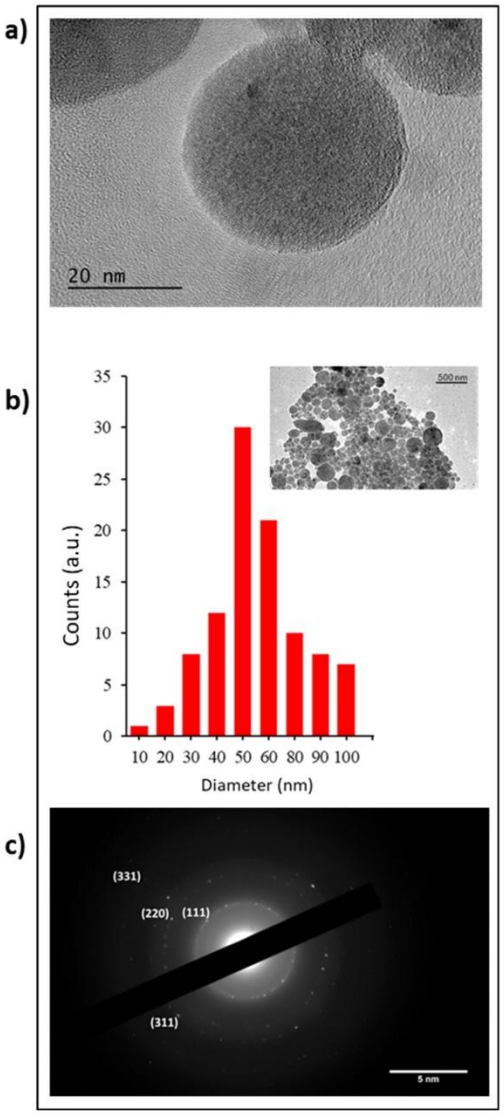

Fig. 1 Morphological characterization of Si-NPs. Si-NPs were characterized by HR-TEM analysis (a). Si-NP size distribution is displayed in histogram (b) where the bars show the percentage of Si-NPs for the different sizes indicated on the *x*-axis. (c) Electron diffraction pattern of Si-NPs.

3.2 *In vitro* cytotoxic assays

In order to evaluate the cytotoxic impact of Si-NPs on C2C12 myoblasts, cell survival was quantified by using the MTT colorimetric assay, which is used to evaluate the metabolic activity of mitochondria. C2C12 murine myoblasts were incubated for 72 h with different concentrations of Si-NPs ranging from 14 to 224 μg mL^{-1}. The cell viability profile shows a survival around 70% for a concentration of 28 μg mL^{-1} and 50% for a concentration of 56 μg mL^{-1}. However, higher concentrations of Si-NPs dramatically reduce cell survival to less than 20% at a concentration of 224 μg mL^{-1} (Fig. 2).

For this reason, further biological tests were performed in a range between 14 and 56 μg mL^{-1}. The mechanical adhesion and internalization of NPs into the myoblasts were investigated through SEM microscopy after fixation of the samples (Fig. 3). Before proceeding with the observation, the samples were

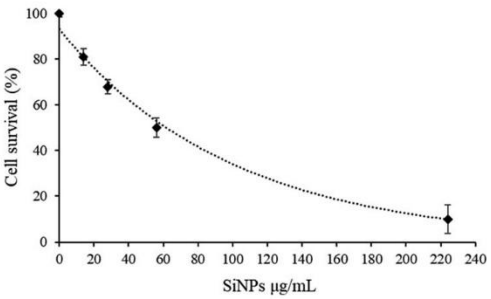

Fig. 2 MTT assay in C2C12 myoblasts. Cell viability was determined following exposure to different concentrations of Si-NPs (14–224 μg mL^{-1}, *x*-axis) for 72 h. The percentage of viable cells is indicated on the *y*-axis.

© 2024 The Author(s). Published by the Royal Society of Chemistry

Open Access Article. Published on 18 March 2024. Downloaded on 3/18/2024 2:54:46 PM.
This article is licensed under a Creative Commons Attribution-NonCommercial 3.0 Unported Licence.

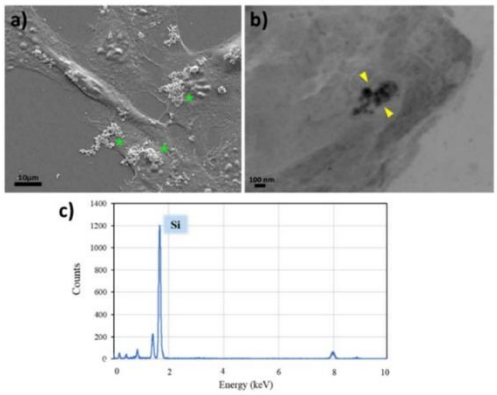

Fig. 3 Images of C2C12 internalization after 72 h of incubation with 56 μg mL^{-1} of Si-NPs. Si-NPs adhere to the cell surface (a) forming aggregates (see the green asterisk). Si-NPs internalized by the myoblasts (b, yellow arrow heads). EDX confirmed the presence of Si-NPs within the cells (c).

rinsed several times with ethanol and water to eliminate the excess non-adhered suspended nanoparticles. The absence of the solvent before fixation led to a rearrangement of the Si-NPs which tend to aggregate on the cell surface (Fig. 3a). By analysing cell sections, Si-NPs were also detected in the aggregate form, confirming the internalization of Si-NPs by the myoblast cells (Fig. 3b). In addition, EDX measurements were carried out in the sample fragment containing the NPs, confirming the presence of the silicon element related to the Si-NPs (Fig. 3c). The totality of the elements displayed on the spectrum derived from the composition of the resin and the reagents used for fixing the sample is provided in the ESI (ESI Fig. 1).†

3.3 Effects of the exposure to Si-NPs on C2C12 cellular processes

In order to evaluate the biological response of Si-NPs, C2C12 myoblasts were exposed to increasing doses of Si-NPs (14, 28, and 56 μg mL^{-1}). In particular, we evaluated the impact of Si-NPs on differentiation of myoblasts to myotubes, the proliferation of myoblasts and cellular motility. Myoblast differentiation is a highly controlled multistep process in which individual mononucleated myoblasts fuse to form multinucleated myotubes. Several genes are involved in this process and their transcription is finely regulated over time. Different types of nanoparticles can promote the formation of myotubes, as reported in the literature.[42,43] We first studied the influence of the exposure to different concentrations of Si-NPs on the differentiation of C2C12 cells by determining the fusion index (FI). The Si-NPs significantly increased the FI value for all concentrations tested compared to the control, with a higher FI obtained for a concentration of 28 μg mL^{-1} (Fig. 4a and b and ESI Table 1†).

The proliferation rate was calculated by analysing cell growth curves obtained during 8 days of continuous exposure to three concentrations of Si-NPs. The experiment was stopped on the eighth day when the cells reached confluence (Fig. 5).

Compared to controls, the treatment with the lowest concentration (14 μg mL^{-1}) did not change the proliferation rate. On the other hand, the highest concentration (56 μg mL^{-1}) significantly decreased the proliferation rate, in particular between day 3 and 6. At the medium range concentration (28 μg mL^{-1}), we observed a significant increase in cell number at day 3 compared to that of the control and to the two other concentrations tested (ESI Table 2† and Fig. 5). To assess whether the exposure to Si-NPs also affected the cellular motility, a scratch-wound healing assay was performed. The curves indicating the percentage of wound closure were obtained every 30 minutes for 24 hours by calculating the surface deprived of cells at each time point. We observed a trend with faster healing for the first two concentrations (14 and 28 μg mL^{-1}) with a closure of the wound between 6 and 21 hours post scratch, compared to the control (Fig. 6 and ESI Table 3†).

Consistent with the other observations on cell proliferation and cell differentiation, we observed a lower healing rate at a higher concentration (56 μg mL^{-1}) suggesting that a high concentration of Si-NPs might impair a number of cellular

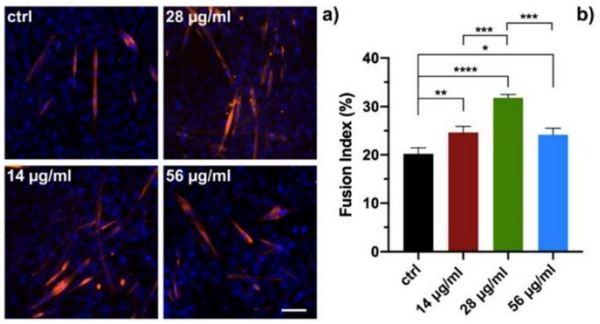

Fig. 4 Fusion index analysis. Representative immunofluorescence images under each experimental condition (a). Myotubes positive for the myosin heavy chain are stained in red, while nuclei are stained in blue with DAPI (scale bar = 50 μm). The graph displays the percentage of the fusion index of differentiated C2C12 myoblasts exposed to different concentrations of Si-NPs (b). Each bar represents an average of 3 independent experiments (for each experiment, $n = 6$ fields were analysed) with experimental variation displayed by error bars.

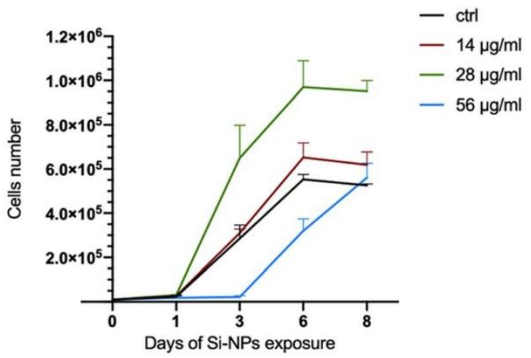

Fig. 5 Analysis of proliferation. Growth curves of C2C12 myoblasts exposed to increasing concentrations of Si-NPs for 8 days. The *x*-axis displays the number of days of Si-NP exposure. The *y*-axis displays the number of cells counted at each time point. Each time point is the average of 3 experiments with experimental variation displayed by error bars. A concentration of 28 μg mL^{-1} (green line) showed the highest proliferation rate.

Open Access Article. Published on 18 March 2024. Downloaded on 3/18/2024 2:54:46 PM.
This article is licensed under a Creative Commons Attribution-NonCommercial 3.0 Unported Licence.

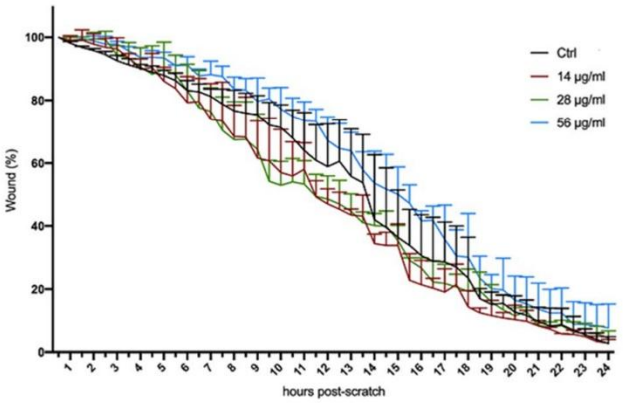

Fig. 6 Scratch-wound healing assay. The *y*-axis displays the percentage of wound at the surface of the culture plate. The *x*-axis displays the time of recording, 1 to 24 h post-scratch. The lines indicate the percentage of wound closure in 24 h for the different concentrations of Si-NPs tested. Each time point is the average of 3 experiments with experimental variation displayed by error bars.

processes together with cell viability. In order to evaluate the effect of the exposure to Si-NPs on the expression of genes related to muscle function, quantitative real-time PCR analysis (qRT-PCR) was performed on C2C12 cells. The expression levels of 6 genes (4 related to muscle differentiation, 1 to proliferation and 1 to cellular motility) were calculated for each concentration of Si-NPs tested (0, 14, 28 and 56 µg mL^{-1}), during three experimental time points (early, medium and late exposure). At the early stage (1 day post exposure to Si-NPs), no differences were observed between cells exposed to Si-NPs and controls for all genes studied. At the medium experimental point (3 days post exposure to Si-NPs), muscle-related genes started to be overexpressed under the 28 and 56 µg mL^{-1} conditions, with a significant increase in the expression of MyoD (the master gene of muscle differentiation) and desmin (28 µg mL^{-1}), an early marker of muscle differentiation. Myomaker (marker of the myotube fusion process) expression was higher for the samples exposed to 28 and 56 µg mL^{-1}, while expression of myosin heavy chain (MHC, a late marker of muscle differentiation) started to increase at a concentration of 28 µg mL^{-1} Si-NPs. Moreover, expression of Ki-67 (a marker of proliferation) and C-met (a marker of cellular motility) progressively increased for all concentrations tested, being significantly higher under the 28 and 56 µg mL^{-1} conditions. At the late stage (5 days post exposure), MyoD was significantly overexpressed under all conditions. Desmin and MHC expression also increased for all concentrations tested (being significantly higher only at 56 µg mL^{-1}) while Myomaker expression significantly increased at 14 and 56 µg mL^{-1}. The expression of the proliferation marker started to decrease at the first two concentrations, remaining significantly overexpressed at 56 µg mL^{-1}, while C-met expression strongly decreased for all the concentrations tested (Fig. 7 and ESI Table 4†).

The trend in the level of expression of each gene for each concentration of Si-NPs tested during the three experimental

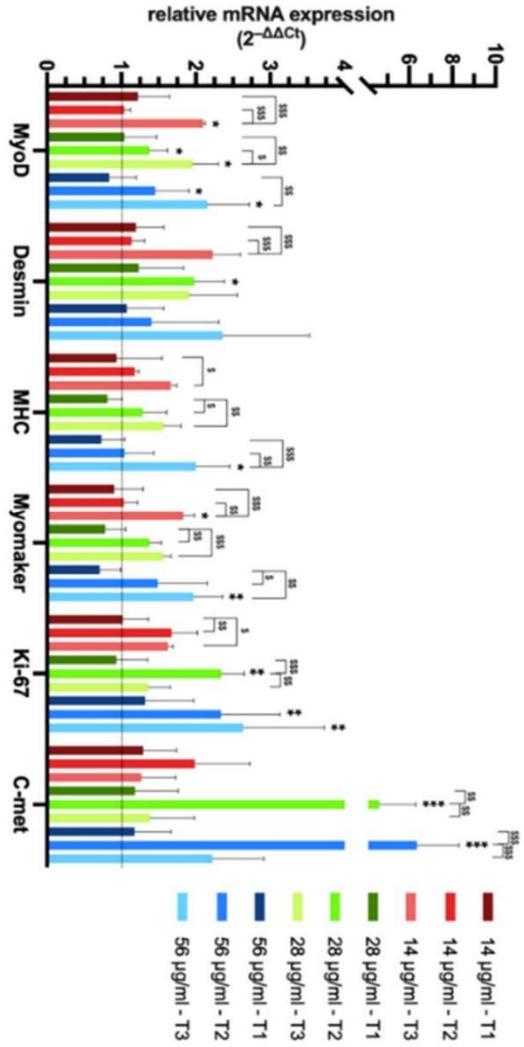

Fig. 7 Relative gene expression. The *y*-axis displays the relative values of the mRNA levels, calculated with the $2^{-\Delta\Delta Ct}$ method. Each bar is the average of 3 experiments with experimental variation displayed by error bars. The *x*-axis displays the genes studied for each concentration of Si-NPs at each experimental time point.

time points was also studied. Interestingly, the expression of muscle-related genes increased over time, while proliferation- and motility-related genes peaked in the medium stage, to decline in the late stage (Fig. 7). This significant trend in the kinetics of gene expression is consistent with a decrease in cell proliferation and migration associated with muscle commitment and differentiation (ESI Table 5†).

4 Discussion

In our previous studies we have shown the benefit of employing laser-synthesized Si-NPs as a potential biocompatible and biodegradable therapy tool for oncology applications.[31] In this context, it appears relevant to assess the effect of such NPs as novel functional additives on modulation of cell behavior and promotion of proliferation, differentiation and motility both at the molecular and phenotypical levels. The possibility of influencing cell behavior can be useful for developing therapeutic

© 2024 The Author(s). Published by the Royal Society of Chemistry

Open Access Article. Published on 18 March 2024. Downloaded on 3/18/2024 2:54:46 PM.
This article is licensed under a Creative Commons Attribution-NonCommercial 3.0 Unported Licence.

protocols and models for tissue engineering applications. However, so far, the most widely used processes to obtain NPs involve the use of different solvents and multi-step approaches, resulting in time-consuming and expensive procedures that can lead to the chemical contamination of the NP surface, a condition that undermines their effect when applied to living matter. In this work, ultra-pure ligand free Si-NPs of 50 ± 11.5 nm were generated by a laser ablation process to by-pass such limitations. It has been largely studied and shown that the interaction between nanoparticles and cells triggers a cascade of molecular events which could induce toxicity and cell death.[44] These mechanisms are associated with the uptake of nanoparticles, their persistence at the cellular level, and their ability to release free radicals and to induce oxidative stress.[45] In our study cytotoxicity was maintained up to a limit of 56 μg mL^{-1} of Si-NPs with a cell survival of 50%, and their internalization was assessed by electron microscopy. At the extracellular membrane, NPs can interact with components of the plasma membrane or extracellular matrix to be internalized, mainly by endocytosis.[46] Shin-Woo Ha *et al.* demonstrated that once internalized, Si-NPs are quickly sequestered by the autophagosome, an organelle designed to isolate and eliminate potentially toxic agents. This internalization might generate a stress response that would in turn stimulate one or more of the common mitogen-activated protein kinase (MAPK) signaling pathway cascades that can lead to the conversion of extracellular stimuli into a wide range of cellular responses.[47] MAP kinase-associated signal transduction cascades are among the most thoroughly studied signal transduction systems and have been shown to participate in cell differentiation, cell movement, cell division, and cell death.[48,49] In this work we used a defined range of Si-NP concentrations to demonstrate their significant stimulatory effects on several cellular processes. The experiments conducted on cellular proliferation proved a positive influence of Si-NPs, with a proliferation rate after 8 days of continuous exposure which is almost the double compared to that of the controls (Fig. 5, 28 μg ml^{-1}). Gene expression analysis confirmed these data, showing a peak of Ki-67 expression at the medium experimental time point for each concentration of NPs tested, with a significant decrease at the late point (28 μg mL^{-1}) consistent with the full confluence of the cell monolayer and the switching to a differentiation medium, both known to promote exit from the replicative cycle (Fig. 7). The study of cellular motility was conducted by using a scratch-wound healing assay. This assay revealed a trend for the samples exposed to low and medium concentrations of Si-NPs to migrate to the wound area faster than the control (Fig. 6). Gene expression analysis confirmed this result, showing a common trend for each concentration used with a peak at the medium point and a strong decrease at the late point, when the surface of the wound is filled with cells. This effect is significantly higher at the medium and high concentrations (Fig. 7, C-met). Interestingly, while in the scratch-test assay, the best results are obtained with exposure to low and medium concentrations of Si-NPs, the most significant results were obtained for the medium and high concentrations regarding the quantification of gene expression. However, the sensitivity of the two approaches is different as the exposure time differs between the two experiments, 24 h for the scratch assay and 4 days for the qRT-PCR. Regarding myogenic differentiation, Si-NPs showed a robust positive effect at each concentration as indicated by the fusion index (Fig. 4) and confirmed by gene expression patterns. For qRT-PCR experiments, we summarized key steps of the myogenic program by observing the expression trend of 3 genes sequentially expressed during myoblast to myotube differentiation (MyoD, Desmin and MHC, repectively) and a marker of myoblast fusion (Myomaker). The results showed that each concentration of Si-NPs tested can increase the expression levels of each gene over time, with the more significantly relevant results obtained at 28 μg mL^{-1}. Of note, this concentration is the only one able to promote the overexpression of desmin at the medium point (Fig. 7). Overall, the results presented here confirm and deepen the observations regarding the positive effect of using Si-NPs to increase the myogenic capabilities of myoblasts, demonstrating a positive effect not only on differentiation but also on proliferation and migration. Interestingly, although each concentration of Si-NPs used for these experiments has proven to have a positive effect on the cellular fitness of C2C12 myoblasts, a concentration of 28 μg mL^{-1} yielded the best results when comparing the phenotypic and molecular experiments.

5 Conclusion

Here, the effect of ultra-pure ligand-free Si-NPs (50 ± 11.5 nm) obtained by fs laser ablation in liquid was evaluated. This research demonstrated the positive outcomes of the exposure of C2C12 myoblasts to Si-NPs, leading to significant improvements in their proliferation, differentiation and motility, even at the lowest concentration, both in phenotypic and molecular analyses. Si-NPs could be considered an optimal candidate as an alternative to classical growth and differentiation factors with interesting features: (i) excellent stability over time at room temperature; (ii) no species-specificity (abiotic factor); (iii) advantageous production procedures in terms of time and costs. Overall, the Si-NPs can be considered an useful and easy-to-use tool for biomedical investigation ranging from the establishment of novel differentiation protocols to tissue engineering applications.

Author contributions

C. M., S. T. and A. A. K. conceived the work; C. M., L. D. and A. A. K. designed and characterized the NPs; C. M., S. T. and F. M. performed biological experiments and analysed the obtained data. C. M., S. T., F. M. and A. A. K. wrote the manuscript. All authors reviewed the article, added comments and corrections in drafting the manuscript. All authors have read and agreed to the published version of the manuscript.

Conflicts of interest

The authors declare that they have no competing interest.

Open Access Article. Published on 18 March 2024. Downloaded on 3/18/2024 2:54:46 PM.
This article is licensed under a Creative Commons Attribution-NonCommercial 3.0 Unported Licence.

Acknowledgements

The work was funded by the French National Research Agency (ANR Medilibs and Diagem projects) together with the French Defence Innovation Agency (ANR—DGA/AID—ICELARE Project ID ANR—20—ASTR—0004). The authors express thanks to Damien Chaudenson and Alexandre Altié for their assistance in microscopy measurements and sample preparations.

References

1 F. Han, J. Wang, L. Ding, *et al.*, Tissue Engineering and Regenerative Medicine: Achievements, Future, and Sustainability in Asia, *Front. Bioeng. Biotechnol.*, 2020, **8**, 83, DOI: **10.3389/fbioe.2020.00083**.

2 S. Arango-Santander, Bioinspired Topographic Surface Modification of Biomaterials, *Materials*, 2022, **15**(7), 2823, DOI: **10.3390/ma15072383**.

3 G. R. Rudramurthy and M. K. Swamy, Potential applications of engineered nanoparticles in medicine and biology: an update, *JBIC, J. Biol. Inorg. Chem.*, 2018, **23**(8), 1185–1204, DOI: **10.1007/s00775-018-1600-6**.

4 K. Upadhyay, R. K. Tamrakar, S. Thomas and M. Kumar, Surface functionalized nanoparticles: A boon to biomedical science, *Chem.-Biol. Interact.*, 2023, **380**, 110537, DOI: **10.1016/j.cbi.2023.110537**.

5 A. Casanova, M. C. Blatche, C. A. Ferre, *et al.*, Self-Aligned Functionalization Approach to Order Neuronal Networks at the Single-Cell Level, *Langmuir*, 2018, **34**(22), 6612–6620, DOI: **10.1021/acs.langmuir.8b00529**.

6 M. J. Mitchell, M. M. Billingsley, R. M. Haley, M. E. Wechsler, N. A. Peppas and R. Langer, Engineering precision nanoparticles for drug delivery, *Nat. Rev. Drug Discovery*, 2021, **20**(2), 101–124, DOI: **10.1038/s41573-020-0090-8**.

7 J. Kim, P. Chhour, J. Hsu, *et al.*, Use of Nanoparticle Contrast Agents for Cell Tracking with Computed Tomography, *Bioconjugate Chem.*, 2017, **28**(6), 1581–1597, DOI: **10.1021/acs.bioconjchem.7b00194**.

8 Q. Wang, X. Ma, H. Liao, *et al.*, Artificially Engineered Cubic Iron Oxide Nanoparticle as a High-Performance Magnetic Particle Imaging Tracer for Stem Cell Tracking, *ACS Nano*, 2020, **14**(2), 2053–2062, DOI: **10.1021/acsnano.9b08660**.

9 F. Chen, E. R. Zhao, G. Hableel, *et al.*, Increasing the Efficacy of Stem Cell Therapy via Triple-Function Inorganic Nanoparticles, *ACS Nano*, 2019, **13**(6), 6605–6617, DOI: **10.1021/acsnano.9b00653**.

10 S. Vosen, S. Rieck, A. Heidsieck, *et al.*, Vascular repair by circumferential cell therapy using magnetic nanoparticles and tailored magnets, *ACS Nano*, 2016, **10**(1), 369–376, DOI: **10.1021/acsnano.5b04996**.

11 M. Dessale, G. Mengistu and H. M. Mengist, Nanotechnology: A Promising Approach for Cancer Diagnosis, Therapeutics and Theragnosis, *Int. J. Nanomed.*, 2022, **17**, 3735–3749, DOI: **10.2147/IJN.S378074**.

12 J. Ge, K. Liu, W. Niu, *et al.*, Gold and gold-silver alloy nanoparticles enhance the myogenic differentiation of myoblasts through p38 MAPK signaling pathway and promote in vivo skeletal muscle regeneration, *Biomaterials*, 2018, **175**, 19–29, DOI: **10.1016/j.biomaterials.2018.05.027**.

13 R. Zhang, P. Lee, V. C. H. Lui, *et al.*, Silver nanoparticles promote osteogenesis of mesenchymal stem cells and improve bone fracture healing in osteogenesis mechanism mouse model, *Nanomedicine*, 2015, **11**(8), 1949–1959, DOI: **10.1016/j.nano.2015.07.016**.

14 J. Bramhill, S. Ross and G. Ross, Bioactive nanocomposites for tissue repair and regeneration: A review, *Int. J. Environ. Res. Public Health*, 2017, **14**(1), 66, DOI: **10.3390/ijerph14010066**.

15 M. A. Yamoah, M. Moshref, J. Sharma, *et al.*, Highly efficient transfection of human induced pluripotent stem cells using magnetic nanoparticles, *Int. J. Nanomed.*, 2018, **13**, 6073–6078, DOI: **10.2147/IJN.S172254**.

16 M. A. Yamoah, P. N. Thai and X. D. Zhang, Transgene Delivery to Human Induced Pluripotent Stem Cells Using Nanoparticles, *Pharmaceuticals*, 2021, **14**(4), 334, DOI: **10.3390/ph14040334**.

17 H. I. Seo, A. N. Cho, J. Jang, D. W. Kim, S. W. Cho and B. G. Chung, Thermo-responsive polymeric nanoparticles for enhancing neuronal differentiation of human induced pluripotent stem cells, *Nanomedicine*, 2015, **11**(7), 1861–1869, DOI: **10.1016/j.nano.2015.05.008**.

18 A. Ito, K. Yoshioka, S. Masumoto, *et al.*, Magnetic heating of nanoparticles as a scalable cryopreservation technology for human induced pluripotent stem cells, *Sci. Rep.*, 2020, **10**(1), 13605, DOI: **10.1038/s41598-020-70707-6**.

19 R. Ravichandran, R. Sridhar, J. R. Venugopal, S. Sundarrajan, S. Mukherjee and S. Ramakrishna, Gold nanoparticle loaded hybrid nanofibers for cardiogenic differentiation of stem cells for infarcted myocardium regeneration, *Macromol. Biosci.*, 2014, **14**(4), 515–525, DOI: **10.1002/mabi.201300407**.

20 W. K. Ko, D. N. Heo, H. J. Moon, *et al.*, The effect of gold nanoparticle size on osteogenic differentiation of adipose-derived stem cells, *J. Colloid Interface Sci.*, 2015, **438**, 68–76, DOI: **10.1016/j.jcis.2014.08.058**.

21 H. Qin, C. Zhu, Z. An, *et al.*, Silver nanoparticles promote osteogenic differentiation of human urine-derived stem cells at noncytotoxic concentrations, *Int. J. Nanomed.*, 2014, **9**(1), 2469–2478, DOI: **10.2147/IJN.S59753**.

22 M. Sekuła-Stryjewska, S. Noga, M. Dźwigońska, *et al.*, Graphene-based materials enhance cardiomyogenic and angiogenic differentiation capacity of human mesenchymal stem cells in vitro – Focus on cardiac tissue regeneration, *Mater. Sci. Eng. C*, 2021, **119**, 111614, DOI: **10.1016/j.msec.2020.111614**.

23 S. Poussard, M. Decossas, O. Le Bihan, S. Mornet, G. Naudin and O. Lambert, Internalization and fate of silica nanoparticles in C2C12 skeletal muscle cells: Evidence of a beneficial effect on myoblast fusion, *Int. J. Nanomed.*, 2015, **10**, 1479–1492, DOI: **10.2147/IJN.S74158**.

24 S. Shamaila, A. K. L. Sajjad, A. Ryma N ul, *et al.*, Advancements in nanoparticle fabrication by hazard free eco-friendly green routes, *Appl. Mater. Today*, 2016, **5**, 150–199, DOI: **10.1016/j.apmt.2016.09.009**.

 © 2024 The Author(s). Published by the Royal Society of Chemistry

Open Access Article. Published on 18 March 2024. Downloaded on 3/18/2024 2:54:46 PM.
This article is licensed under a Creative Commons Attribution-NonCommercial 3.0 Unported Licence.

25 A. V. Rane, K. Kanny, V. K. Abitha, S. Thomas and S. Thomas, Methods for Synthesis of Nanoparticles and Fabrication of Nanocomposites, in *Synthesis of Inorganic Nanomaterials: Advances and Key Technologies*, Elsevier, 2018, pp. 121–139, DOI: 10.1016/B978-0-08-101975-7.00005-1.

26 T. Baati, A. Al-Kattan, M. A. Esteve, *et al.*, Ultrapure laser-synthesized Si-based nanomaterials for biomedical applications: In vivo assessment of safety and biodistribution, *Sci. Rep.*, 2016, **6**, 2045–2322, DOI: 10.1038/srep25400.

27 D. Zhang, B. Gökce and S. Barcikowski, Laser Synthesis and Processing of Colloids: Fundamentals and Applications, *Chem. Rev.*, 2017, **117**(5), 3990–4103, DOI: 10.1021/acs.chemrev.6b00468.

28 A. Al-Kattan, D. Grojo, C. Drouet, *et al.*, Short-Pulse Lasers: A Versatile Tool in Creating Novel Nano-/Micro-Structures and Compositional Analysis for Healthcare and Wellbeing Challenges, *Nanomaterials*, 2021, **11**(3), 712, DOI: 10.3390/nano11030712.

29 M. Arora and E. Arora, The Promise of Silicon: bone regeneration and increased bone density, *J. Arthrosc. Jt. Surg.*, 2017, **4**(3), 103–105, DOI: 10.1016/j.jajs.2017.10.003.

30 C. RoyChaudhuri, A review on porous silicon based electrochemical biosensors: Beyond surface area enhancement factor, *Sens. Actuators, B*, 2015, **210**, 310–323, DOI: 10.1016/j.snb.2014.12.089.

31 A. Al-Kattan, Y. V. Ryabchikov, T. Baati, *et al.*, Ultrapure laser-synthesized Si nanoparticles with variable oxidation states for biomedical applications, *J. Mater. Chem. B*, 2016, **4**(48), 7852–7858, DOI: 10.1039/c6tb02623k.

32 A. Al-Kattan, G. Tselikov, K. Metwally, A. A. Popov, S. Mensah and A. V. Kabashin, Laser Ablation-Assisted Synthesis of Plasmonic Si@Au Core-Satellite Nanocomposites for Biomedical Applications, *Nanomaterials*, 2021, **11**(3), 592, DOI: 10.3390/nano11030592.

33 K. P. Tamarov, L. A. Osminkina, S. V. Zinovyev, *et al.*, Radio frequency radiation-induced hyperthermia using Si nanoparticle-based sensitizers for mild cancer therapy, *Sci. Rep.*, 2014, **4**(1), 7034, DOI: 10.1038/srep07034.

34 A. Al-Kattan, M. A. L. Ali, M. Daurat, E. Mattana and M. Gary-Bobo, Biological Assessment of Laser-Synthesized Silicon Nanoparticles Effect in Two-Photon Photodynamic Therapy on Breast Cancer MCF-7 Cells, *Nanomaterials*, 2020, **10**(8), 1462, DOI: 10.3390/nano10081462.

35 A. Al-Kattan, V. Nirwan, A. Popov, *et al.*, Recent Advances in Laser-Ablative Synthesis of Bare Au and Si Nanoparticles and Assessment of Their Prospects for Tissue Engineering Applications, *Int. J. Mol. Sci.*, 2018, **19**(6), 1563, DOI: 10.3390/ijms19061563.

36 S. Testa, P. D'Addabbo, E. Fornetti, *et al.*, Myoblast myogenic differentiation but not fusion process is inhibited via MyoD tetraplex interaction, *Oxid. Med. Cell. Longevity*, 2018, **2018**, 7640272, DOI: 10.1155/2018/7640272.

37 A. Reggio, M. Rosina, N. Krahmer, *et al.*, Metabolic reprogramming of fibro/adipogenic progenitors facilitates muscle regeneration, *Life Sci. Alliance*, 2020, **3**(3), e202000646, DOI: 10.26508/lsa.202000660.

38 E. Fornetti, S. Testa, F. De Paolis, *et al.*, Dystrophic Muscle Affects Motoneuron Axon Outgrowth and NMJ Assembly, *Adv. Mater. Technol.*, 2022, **7**(7), 2101216, DOI: 10.1002/admt.202101216.

39 S. Testa, C. S. Riera, E. Fornetti, *et al.*, Skeletal Muscle-Derived Human Mesenchymal Stem Cells: Influence of Different Culture Conditions on Proliferative and Myogenic Capabilities, *Front. Physiol.*, 2020, **11**, 553198, DOI: 10.3389/fphys.2020.553198.

40 C. Gargioli, G. Turturici, M. M. Barreca, *et al.*, Oxidative stress preconditioning of mouse perivascular myogenic progenitors selects a subpopulation of cells with a distinct survival advantage in vitro and in vivo article, *Cell Death Dis.*, 2018, **9**(1), 1, DOI: 10.1038/s41419-017-0012-9.

41 K. J. Livak and T. D. Schmittgen, Analysis of relative gene expression data using real-time quantitative PCR and the 2-ΔΔCT method, *Methods*, 2001, **25**(4), 402–408, DOI: 10.1006/meth.2001.1262.

42 V. Ramalingam and I. Hwang, Zinc oxide nanoparticles promoting the formation of myogenic differentiation into myotubes in mouse myoblast C2C12 cells, *J. Ind. Eng. Chem.*, 2020, **83**, 315–322, DOI: 10.1016/j.jiec.2019.12.004.

43 D. Böcking, O. Wiltschka, J. Niinimäki, *et al.*, Mesoporous silica nanoparticle-based substrates for cell directed delivery of Notch signalling modulators to control myoblast differentiation, *Nanoscale*, 2014, **6**(3), 1490–1498, DOI: 10.1039/C3NR04022D.

44 Y. W. Huang, M. Cambre and H. J. Lee, The Toxicity of Nanoparticles Depends on Multiple Molecular and Physicochemical Mechanisms, *Int. J. Mol. Sci.*, 2017, **18**(12), 2702, DOI: 10.3390/ijms18122702.

45 M. Kersting, M. Olejnik, N. Rosenkranz, *et al.*, Subtoxic cell responses to silica particles with different size and shape, *Sci. Rep.*, 2020, **10**(1), 21591, DOI: 10.1038/s41598-020-78550-5.

46 S. Behzadi, V. Serpooshan, W. Tao, *et al.*, Cellular uptake of nanoparticles: Journey inside the cell, *Chem. Soc. Rev.*, 2017, **46**(14), 4218–4244, DOI: 10.1039/c6cs00636a.

47 S. W. Ha, M. Neale Weitzmann and G. R. Beck, Bioactive silica nanoparticles promote osteoblast differentiation through stimulation of autophagy and direct association with LC3 and p62, *ACS Nano*, 2014, **8**(6), 5898–5910, DOI: 10.1021/nn5009879.

48 M. Cargnello and P. P. Roux, Activation and Function of the MAPKs and Their Substrates, the MAPK-Activated Protein Kinases, *Microbiol. Mol. Biol. Rev.*, 2011, **75**(1), 50–83, DOI: 10.1128/mmbr.00031-10.

49 A. Keren, Y. Tamir and E. Bengal, The p38 MAPK signaling pathway: A major regulator of skeletal muscle development, *Mol. Cell. Endocrinol.*, 2006, **252**(1–2), 224–230, DOI: 10.1016/j.mce.2006.03.017.

Electronic Supplementary Material (ESI) for Nanoscale Advances.
This journal is © The Royal Society of Chemistry 2024

Assessment of laser-synthesized Si nanoparticles effects on myoblasts motility, proliferation and differentiation: towards potential tissue engineering applications

Clarissa Murru[a], Lucas Duvert[a,b], Frederique Magdinier[b], Adrien Casanova[a], Anne-Patricia Alloncle[a], Stefano Testa[b]*, Ahmed Al-Kattan[a]*

Supplementary Material

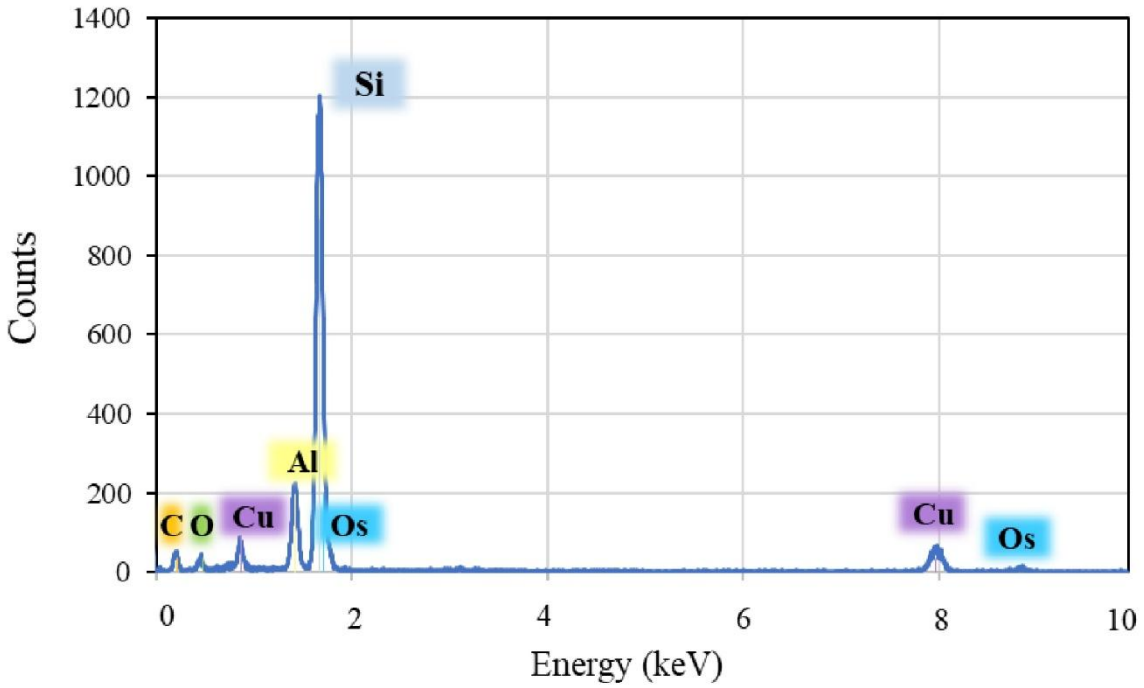

Supplementary Figure 1. Energy-dispersive X-ray spectroscopy of Si-NPs. EDS was performed in the section of the sample where the nanoparticles were detected. The obtained spectrum confirmed the internalization of Si-NPs while the other elements displayed derive by the composition of the resin, the products applied for fixing the cells and the grid used to observe the sample.

	Significativity	**P values**
ctrl vs 14	**	0.0070
ctrl vs 28	****	<0.0001
ctrl vs 56	*	0.0133
14 vs 28	***	0.0003
14 vs 56	**ns**	0.9574
28 vs 56	***	0.0002

Supplementary Table 1. Statistical validation of Fusion Index analysis. For each Si-NPs concentration tested p values and statistical significance are reported. The p values are calculated using a one-way ANOVA with Tukey's multiple comparisons test.

	day 1		**day 3**		**day 6**		**day 8**	
	signif.	P value	signif.	P value	signif.	P value	signif.	P value
ctrl vs 14	ns	0.6909	ns	0.9805	ns	0.4143	ns	0.1818
ctrl vs 28	ns	0.0506	**	0.0025	***	0.0006	****	<0.0001
ctrl vs 56	ns	0.1192	*	0.0165	*	0.0203	ns	0.8206
14 vs 28	ns	0.2382	**	0.0038	**	0.0034	***	0.0002
14 vs 56	*	0.0250	*	0.0100	**	0.0026	ns	0.5256
28 vs 56	**	0.0019	****	<0.0001	****	<0.0001	****	<0.0001

Supplementary Table 2. Statistical validation of the growth curves analysis. For each Si-NPs concentration tested at each experimental point, p values and statistical significance are reported. The concentration of 28 µg/mL is the only one that is significant compared to the other conditions starting on day 3 (light blue lines).

	hours post-scratch																			
	7.5	8	8.5	9	9.5	10	10.5	11	11.5	12	12.5	13	13.5	14	14.5	15	15.5	16	16.5	17.5	18
ctrl vs 14											*										
ctrl vs 28					*	**															
ctrl vs 56																					
14 vs 28																					
14 vs 56		*	*	**	**	**	**	*	***	**	**	**		**	*	*	***	**	**	*	*
28 vs 56	*	*	*	*	****	***	**	**	***	**	*	**	*				**	*	**		

Supplementary Table 3. Statistical validation of the Scratch-wound healing assay. For each Si-NPs concentration tested at each experimental point, p values and statistical significance are reported. Only experimental time points showing a statistically significant result are presented.

Gene	**Time 2**				**Time 3**					
	28 µg/ml		56 µg/ml		14 µg/ml		28 µg/ml		56 µg/ml	
		p value		*p value*		*p value*		*p value*		*p value*
MyoD	*	0.0259	*	0.0124	*	0.0259	*	0.0439	*	0.0324
Desmin	*	0.0126								
MHC									*	0.0127
Myomaker					*	0.0115			**	0.0054
Ki-67	**	0.0058	**	0.0060					**	0.0068
C-met	***	0.0006	***	0.0001						

Supplementary Table 4. Statistical validation of qRT-PCR analysis. For each gene studied at each Si-NPs concentration tested and each experimental time point, p values and statistical significance are reported. Values were calculated using the ΔCt of the target gene *versus* the ΔCt of the control gene. Statistical siginficance was determined using the Ordinary one-way ANOVA with Dunnett's multiple comparisons test.

Gene	**Si-NPs - 14 µg/ml**			**Si-NPs - 28 µg/ml**			**Si-NPs - 56 µg/ml**		
	T1 vs T2	T1 vs T3	T2 vs T3	T1 vs T2	T1 vs T3	T2 vs T3	T1 vs T2	T1 vs T3	T2 vs T3
MyoD		$$$	$$$		$$	$		$$	
p value		0.0005	0.0001		0.0037	0.0448		0.0024	
Desmin		$$$	$$$						
p value		0.001	0.0007						
MHC		$		$	$$			$$$	$$
p value		0.0159		0.0272	0.0019			0.0009	0.0058
Myomaker		$$$	$$	$$	$$$		$	$$	
p value		0.0005	0.0014	0.0015	0.0002		0.0464	0.0034	
Ki-67	$$	$		$$$		$$			
p value	0.0079	0.013		0.0002		0.0023			
C-met				$$$		$$$	$$$		$$$
p value				0.0010		0.0016	0.0001		0.0007

Supplementary Table 5. Significance and p values based on the $2^{-\Delta\Delta Ct}$ values. For each gene studied at each Si-NPs concentration tested and each experimental time point, p values and statistical significance are reported. In particular, for each gene the trend during the 3 experimental time points for each concentration of Si-NPs tested was investigated, using the Ordinary one-way ANOVA with Tukey's multiple comparisons test.

Exploratory work

4. Exploratory work

4.1 A novel laser-based subtractive process for creating highly organized *in vitro* human artificial muscles: a promising tool for FSHD modeling.

Lucas Duvert[a,b], Patricia Alloncle [a], Frederique Magdinier [b], Stefano Testa [b].

a: Aix Marseille University, CNRS, LP3 UMR 7341 , Marseille, France

b: Aix Marseille University, INSERM, Marseille Medical Genetics, Marseille, France

Context

During my thesis I explored an alternative direct laser writing technique for 3D skeletal muscle modeling by micro-drilling hydrogel scaffolds. Contrary to LIFT bioprinting where the targeted tissue is constructed layer by layer through an additive process, we are here subtracting material to shape human artificial skeletal muscle models.

The process is based on a multi-step protocol to obtain volumetric constructs with a predetermined number of muscle fibers aligned and spatially organized in 3D.

a) A biocompatible PEG-fibrinogen (PF) is poured into a cylindrical mold (5 mm diameter by 10 mm height). PF is a hybrid biomaterial composed of denatured fibrinogen, which promote cell adhesion and facilitates degradation and resorption of the biomaterial, and polyethylene glycol, which provides the mechanical support as scaffolding (Almany & Seliktar, 2005).

b) After the addition of a radical photoinitiator (0.1% w/v of Irgacure 2959), the PF is exposed for 5 minutes to a UV source (365 nm) to allow its polymerization and transition from a liquid state to a hydrogel.

c) Channels are dig into the PF structure by focusing 213 femtosecond laser pulses at a frequency of 60KHz. The use of a galvanometric scanner allows for the fast and

reproducible creation of personalized channel patterns. By modifying parameters such as the pulse energy, the laser exposure duration and the focus distance it is possible to modify the diameter and depth of the resulting channels.

d) The channels created are then loaded with a solution of myogenic cells resuspended in a polymerizable biomaterial (PF or Matrigel). Once gelled, the cells form elongated fibers, adequately aligned to replicate the architecture of skeletal muscle tissue.

e) The 3D muscle constructs are finally cultured to allow cell proliferation, elongation and differentiation.

Results

Murine myoblasts (C2C12) were first used to assess the potentiality of the proposed laser-based 3D culture system in replicating the skeletal muscle tissue organization. This way, we determined the best parameters in terms of channel stability, cell development and organization. The myotubes obtained from the C2C12 were properly oriented into elongated bundles with a structure closely mimicking muscle fiber.

Once validated the system was applied to the modeling of human muscle. Human immortalized myoblasts were resuspended in a Matrigel solution (33% v/v in DMEM) and loaded inside the channels. After 3 days of culture, the medium was changed with differentiation medium (DMEM + 2% Horse Serum) and the samples were fixed at day 10. Similar alignment and survival rates were observed than with the murine cells, demonstrating the efficiency of the system to create physiologically relevant 3D contract mimicking human skeletal muscle.

To prove its potential in disease modeling applications, immortalized human FSHD1 myoblasts were loaded into laser-ablated channels and cultured as explained above. Also in this case, the affected cells were able to generate aligned bundles of myotubes, well organized within the channels. Furthermore, immunostaining analysis conducted for DUX4 protein, the main marker of FSHD1, revealed the presence of DUX4-positive cells within the 3D constructs. A very promising result given the very low frequency of affected nuclei (1:10000) and the challenges in visualizing them using immunostaining in traditional 2D cultures.

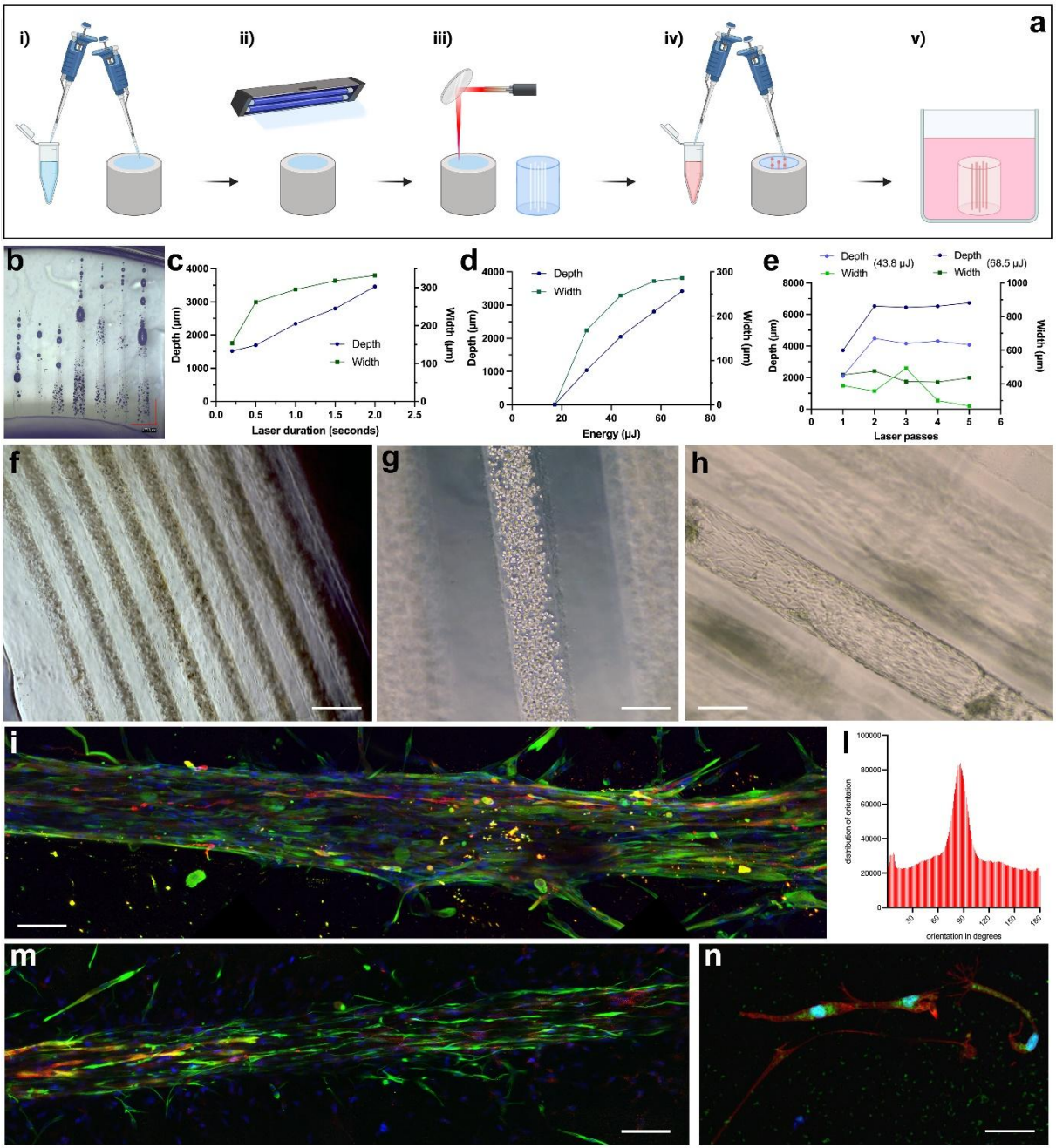

Figure 17 : (**a**) Protocol for the preparation of the constructs. (I) PF is poured inside a mold and (II) polymerized by UV illumination. (III) Channels are created across the PF matrix by laser ablation. (IV) The created channels are filled with a polymerizable bio-ink containing the cells. (V) The cell-loaded matrix is removed from the mold and put in culture for development and maturation. (**b**) Empty channels inside the PF after laser illumination at different parameters. (**c-e**) Influence of laser energy, duration, and focus variation on the depth of the laser-created channels. (**f,g**) PF matrix loaded with C2C12 cells (**h**) Development and alignment of the cells within the channels after 48h in culture (**i**) Immunostaining analysis of healthy human myoblast loaded channels after 1 week of differentiation. In red is stained the Myosin Heavy Chain (MHC), in green the Desmin and in Blue the nucleus; (**l**) Distribution analysis of the myotubes within the channels. (**m**) Immunostaining analysis of FSHD-affected immortalized human myoblast. (**n**) The FSHD affected myotubes were stained for Phalloidin in red, nuclei in blue and DUX4 positive nuclei in green.

Conclusion

Here we report on the design and validation of another laser-based tissue engineering approach for creating human artificial skeletal muscles. The described cell-loaded scaffold has proven ideal for faithfully replicating muscle fiber-like structures with a high level of reproducibility. We demonstrated the possibility of applying this system to disease modeling, with a particular emphasis on facioscapulohumeral muscular dystrophy (FSHD), a pathology for which human modeling is of crucial importance.

While the developed system is promising, it still has to be refined through the investigation of different biomaterials to improve cell behavior consistency within the channels and improve maximum nutrient diffusion throughout the 3D scaffold. Additionally, the channels quality could also be improved by using a Bessel beam for more homogenous ablation across the hydrogel volume. Despite these challenges, this proof of concept demonstrates once again the significant potential and ability of combining laser processes with suitable biomaterials to create efficient scaffolds for complex cell cultures.

Contribution

In this work, I established the protocols for the creation of the channels and performed the parametric study to evaluate the influence of laser parameters on the channel characteristics. I also participated in the development of the protocols for loading the cells into the channels and the necessary precautions to assure their survival and optimal development. Finally, I performed the immunostaining and subsequent imaging analysis of the constructs.

4.2 Development of an electrical stimulation system for modeling neuromuscular pathologies

Manel Benaboura [a], **Lucas Duvert** [a,b], Frederique Magdinier [a], Stefano Testa [a].

a: Aix Marseille University, INSERM, Marseille Medical Genetics, Marseille, France

b: Aix Marseille University, CNRS, LP3 UMR 7341 , Marseille, France

Context

The development and application of the polystyrene laser structuring was further investigated by combining it with electrical stimulation to mimic natural nerve signals. The merging of topographical cues with external stimulation promotes the maturation of muscle cells in culture and improves their contractile properties, offering an ethical alternative to animal models for disease modeling.

In this study, we aimed to develop an electrical stimulation system to model neuromuscular diseases such as FSHD. To achieve this, we designed an affordable and accessible Arduino-based pulse generator, along with electrodes compatible with commercially available cell culture plates. The system was designed on the same principle as laser-induced topography, prioritizing versatility and seamless integration into traditional cell culture workflows. The topographical cues allowed for the alignment of cells in an anisotropic architecture, mimicking skeletal muscle physiology, while the addition of electrical stimuli improved cell maturation and functionality.

Results

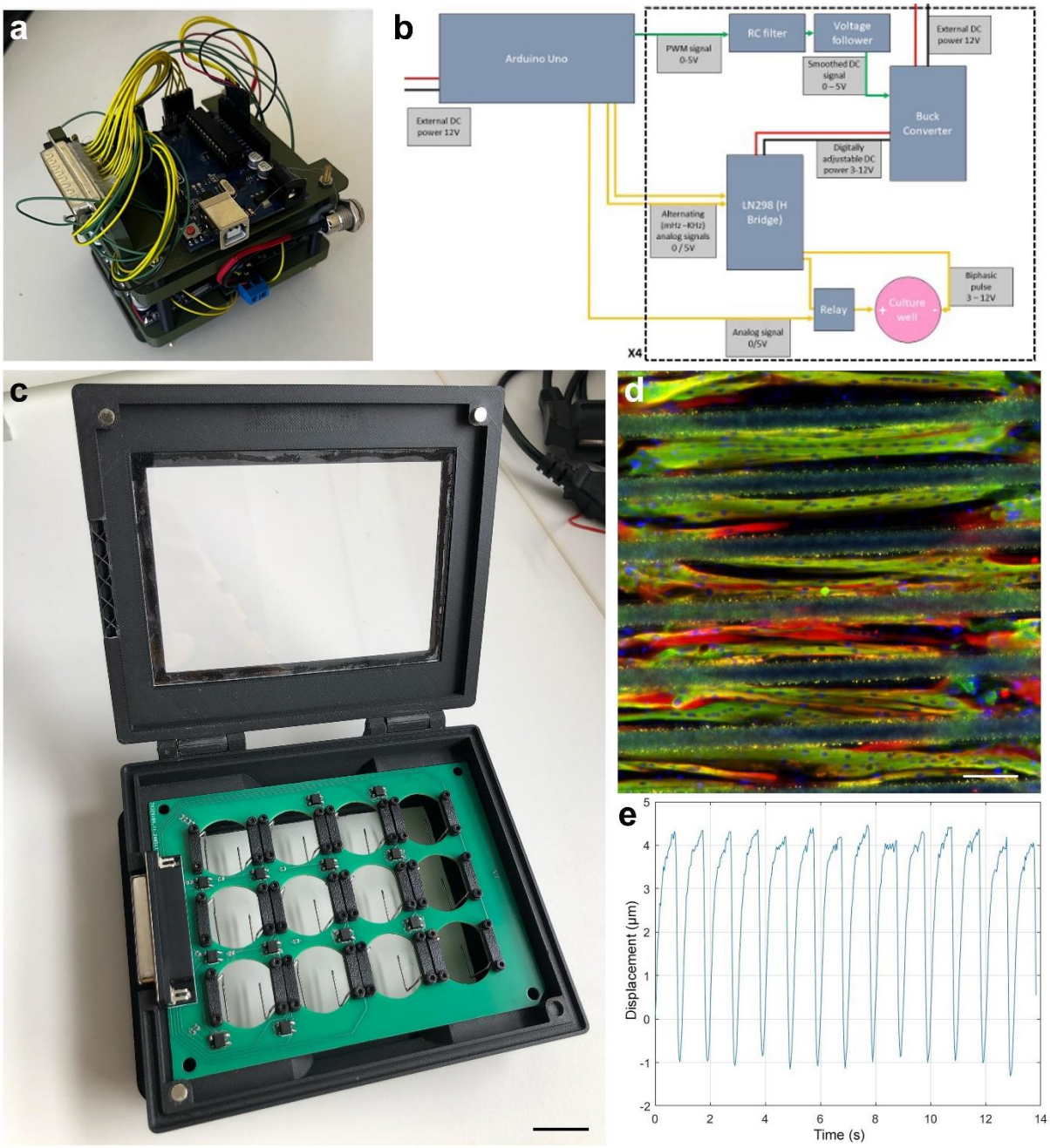

Figure 18: (a) Designed pulse generator for the electrical stimulation of cells and (b) schematic of operation based on affordable and easily accessible electrical components. (c) Housing for 12-well culture plates and electrodes for transmitting the pulses. (d) Immunostaining analysis of human immortalized FSHD-affected myotubes stained for Myosin Heavy Chain in red, titin in green and nuclei in blue after culture on laser-structured channels and maturation by electrical stimulation. (e) Myotubes displacement under a 1Hz 8V bi-phasic electrical stimulation.

We first calibrated the stimulation parameters using murine C2C12 cells before applying them to human myotubes. The effects were assessed through brightfield video analysis and calcium flux measurements. These analyses, supported by statistical data, demonstrated that continuous low-intensity stimulation, or "training," is crucial for the proper functionalization of myotubes. After this training period, the myotubes exhibited

measurable responses to subsequent stimulation, confirming the necessity of pre-conditioning for optimal functionality.

Myotubes stimulated at 1 Hz showed regular and synchronized contractions, with average displacements of about 1 µm. At 2 Hz, the contractions became more pronounced, indicating a stronger response to stimulation. At 20 Hz, significant tetanic contractions (displacement of 24 µm) were observed, although they were quickly followed by muscle fatigue.

Calcium flux analysis revealed variations synchronized with the given stimulation. At 1 and 2 Hz, calcium peaks are in phase with the stimulation frequency. At 20 Hz, fatigue and intracellular calcium depletion were evident, indicating a reduction in the effectiveness of the calcium response at high frequency. These findings confirm that electrical stimulation modulates both contractile and calcium responses, reinforcing the effectiveness of the developed stimulation system for functionalization of the myotubes.

Conclusion

The results obtained demonstrate that training and electrical stimulation significantly influence the contractile and calcium responses of human myotubes. The stimulation system we developed proved to be reliable, enabling muscle contractions to be precisely synchronized with the programmed parameters. Further investigation is needed to assess the system's influence on myotube maturation through morphological analysis and to evaluate its potential to recapitulate the pathological mechanisms of dystrophic muscle cells for disease modeling applications. Finally, preliminary results highlight the effectiveness of laser-structured surfaces in organizing cell cultures and their seamless integration with other tissue engineering approaches, contributing to the development of more mature skeletal muscle models.

Contribution

In this project, I was responsible for all the technical aspects, including the design, construction, and setup of the pulse generator used to stimulate the cultured cells. I also designed the housing and the printed circuit board, enabling parametric studies to be conducted within a single 12-well culture plate. Additionally, I helped setting up the

protocol for standardized analysis of myotube contractions and contributed to the imaging analysis.

Discussion

5. Discussion

5.1 Experimental consideration for LIFT bio-printing

The first article presented in this work demonstrated our ability to control the jetting dynamics of hydrogel-based inks to print living cells. We first focused on the optimization of decellularized alginate-based inks to precisely control the landing conditions of the jets on the receiver substrate. The objective was to set ourselves in the best possible printing conditions by minimizing the mechanical stress on the cells in order to improve survival, proliferation and differentiation. To achieve this, we studied different alginate concentrations and experimental conditions to find optimal cell-printing parameters. Given a range of ink viscosities, we determined special jetting conditions where the receiver substrate can be precisely positioned to reduce mechanical stress. This work allowed for the setup of the experimental process and of all the protocols that subsequently led to a successful cell printing. It also revealed a few significant parameters and experimental difficulties that need to be considered when printing living cells.

5.1.1 Protocols for thin donor layer preparations

Among the experimental considerations of applying LIFT to bio-printing, the deposition of the bio-ink layer of the donor substrate, which is here composed of 0.5 mm glass slides with a 50 nm titanium dynamic release layer (DRL), constituted a major limiting factor in the reproducibility of the printing process.

When used for electronic purposes (Breckenfeld et al., 2015; Piqué & Charipar, 2021; Zacharatos et al., 2021), which it was initially meant for, LIFT can rely on precise techniques such as spin coating or physical vapor deposition to create thin donor layers of conductive paste or pure metals. In the case of sensible biological materials, coating options are reduced to blade-coating and its derivative in order to preserve the integrity of the cells embedded in the ink. The method involves positioning a sharp blade at a set distance from the surface to be coated. The coating solution is applied in front of the blade, which is then moved along the surface, spreading the solution into a uniform wet film (**Figure 19**)(Cherrington & Liang, 2016). This technique is used in most LIFT bioprinting studies (Gruene, Pflaum, Deiwick, et al., 2011; Guillemot et al., 2010; Guillotin et al., 2010;

Koch et al., 2010, 2017; Ovsianikov et al., 2010), yet it mostly remains a manual process subjected to variations between experiments.

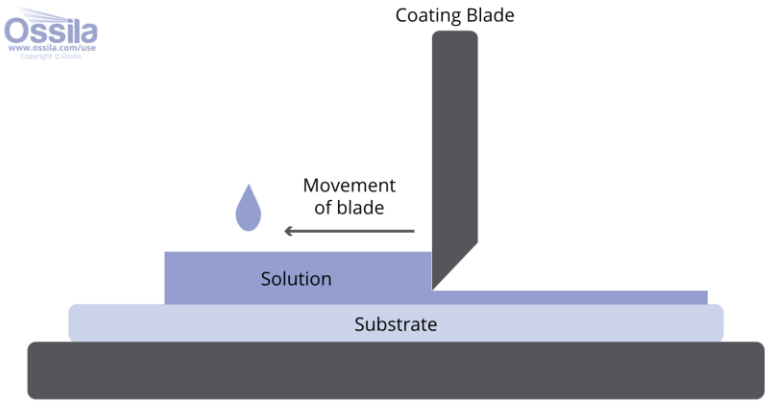

Figure 19: Blade coating process operation. The movement of the blade can be automatized to improve the reproducibility of the thin film thickness

The nature of the ink itself also has to be considered. Unlike solvent-based inks used in electronics such as silver (Munoz-Martin et al., 2016; Sopeña et al., 2020), platinum or copper (A. Das & Ding, 2024), the application of LIFT to bioprinting relies heavily on hydrogel-based solutions. These solutions, in contrast, are prone to drying, deterioration, and rheological modifications (Zennifer et al., 2022). To homogenize these properties and prevent drying, additives like glycerol (Deng et al., 2017) can be incorporated into the solution. However, these bio-inks must also deal with inherent and unpredictable biological variation in a context where the slightest change in cell concentration, homogeneity, and ink viscosity can lead to drastically different printing quality results and outcomes. Therefore, the method for creating a thin bio-ink layer on the donor was adjusted throughout our work to adapt to the ink viscosity and its properties in order to optimize printing conditions.

Blade coating proved efficient for high-viscosity inks, and automating the speed of the blade further improved the process reproducibility. However, when considering this coating method, some aspects remain inevitably operator-dependent, such as the initial deposition of material on the donor substrate before the blade passage, the donor substrate quality, its orientation, and the overall quality of the bio-ink following its preparation. These inconsistent factors lead to major variations in donor quality from one experiment to the other. Additionally, handling small volumes of biological material and the possible presence of cell clusters exacerbated reproducibility issues. The cell

concentration used in this work was set at $50x10^6$ cells/mL and collected in a volume of approximately 50 µL. As we demonstrated, this concentration allowed us to control the number of printed cells from only a few to several dozens of cells per spot. In this context, an underlying issue lies in the combination of small volumes, highly viscous inks, and high cell numbers, which requires more pipetting to effectively combine the hydrogel with the cell pellet. In this way, the number of cell aggregates can be extensively minimized. However, the shear stress brought by pipetting and additional manipulations could constitute another limiting factor for handling sensible cell types such as stem cells (Kato et al., 2019; Uhrig et al., 2022). Inherent variation of cell behavior and unstable base bio-ink can also both significantly impact the homogeneity of the donor layer and thus the quality of the printing; in these conditions, parametric studies on LIFT bio-printing appeared as extremely tedious processes with uncertain outcomes.

The challenges discussed here are not reflected in the previous LIFT bio-printing studies. An extensive majority of them use blade coating to prepare the donor substrate without mention of difficulties or inhomogeneities despite cell concentration higher than $50x10^6$ cells/ml or the use of highly viscous bio-inks such as concentrated alginate solutions(Catros, Guillotin, et al., 2011; Catros et al., 2012; Gruene, Deiwick, et al., 2011; Gudapati et al., 2014), Matrigel (Koch et al., 2018) or collagen (Michael et al., 2013; Pagès et al., 2015). Providing a detailed explanation of the donor substrate preparation protocol and addressing potential associated difficulties would promote the accessibility of the LIFT bioprinting process and improve the reproducibility of the published experiments and transferability from lab to lab by limiting inter-operator variability.

5.1.2 Optimization for low-viscosity inks

Blade-coating of low-viscosity inks proved less effective due to the creation of "waves" of material during the blade passage, leading to uneven cell repartition on the donor substrate, with some areas lacking cells and others containing clumps of cells. The blade-coating technique is also limited to creating relatively thin layers, which exhibited faster drying time when used with low viscosity material, further compromising printing reproducibility. The layer creation method was subsequently adjusted from blade coating to simple pipetting of the bio-ink in pre-constrained wells. After its deposition, the ink is spread over the small area using a pipette tip. Although this method remains imperfect, with noticeable surface tension effects on the sides of the wells, it significantly improved

layer homogeneity. Depositing the ink in a perfectly calibrated well allows for reproducible layer height regardless of slight bio-ink viscosity variation. This approach was particularly well-suited to low-viscosity inks, as their liquid nature enabled smooth cell distribution within the confined area. By using approximately 5 µL of ink per well, we achieved increased layer thickness, which reduced drying, improved reproducibility, and allowed for higher cell concentrations. In those conditions, the addition of glycerol, which showed its benefits in the first article, was dismissed to maximize cell survival and reduce external factors.

Despite reproducibility improvements thanks to the well-based method, cell clusters remain the leading cause of inhomogeneity on the donor substrate ink layer. Additionally, we evaluated and demonstrated the ability of the LIFT printing process to control the number of cells printed through various direct and indirect methods. As currently applied in this work, LIFT bioprinting is a fundamentally statistical process: the number of cells printed depends on their even distribution on the donor substrate. The potential presence of clumps and cell aggregates in the bio-ink may, therefore, undermine this process, further reducing the printing quality and reproducibility.

5.1.3 Set-up optimization and future improvements

Reproducibility issues caused by the complex donor preparation and the sensible nature of bio-inks could be addressed through automation and streamlining a larger part of the process. The blade coating device should include the automatic deposition of the biological material while accounting for the limited available volume. Reducing manual operations and creating perfectly reproducible donors could resolve some of the challenges discussed earlier.

Nonetheless, the presence of cell aggregates is an external variable that can only be controlled to a certain extent. To minimize the impact of this limitation, the bio-ink concentration could be significantly reduced to a few hundred thousand cells per milliliter, reducing pipetting and making the process applicable to more sensitive cell lines. The increased amount of biomaterial for the blade coater would also reduce the operation's complexity and intricacy. On the other hand, using a lower concentration of bio-ink would also reduce the number of deposited cells, or, in the best-case scenario, as shown in the first article, it would require multiple laser passages. This approach

significantly reduces the versatility of the printing process while imposing additional constraints.

In this context, real-time direct visualization of the donor substrate appears absolutely essential for LIFT bio-printing. It would allow the precise focusing of the laser beam on the cell location and avoid clusters that compromise printing accuracy, as used by Zhang and colleagues (J. Zhang et al., 2021) and cleverly perfected by Narrog and colleagues (Narrog et al., 2023). This approach, coupled with a high-speed XY stages for the receiver substrate, could precisely align the receiver under the cells to be printed position before their transfer by the laser pulse. Rather than a single-step process based on a high-speed galvanometric scanner and relying on statistics, the LIFT would become a sequential deposition of cells with a precise and anticipated control of their number. While the added mechanical movement may slow the process, the space footprint of the experimental setup could be reduced by eliminating the scanner in favor of a fixed objective for the laser beam, paired with high-speed XY donor and receiver stages. The donor substrate would be constantly filmed to determine the position of the cells before lining them up under the fixed laser beam. Finally, the receiver positions itself in the right location for the cells to land. Given the small scale of printing patterns, mechanical movements could be minimized, reducing the setup overall footprint and enabling its use within commercially available culture hoods to promote sterility and facilitate application in biology laboratories.

The multi-cell printing ability of LIFT, as shown in **Article 4**, could also be simplified. Currently, multiple cell populations can be printed on a single receiver by multiplying the number of donors or by creating several individual wells, as described in **Article 2**. Each cell population is deposited in its given donor/well, and the receiver is aligned in accordance with the current printed cell line. A potential improvement of this approach would involve mixing the different cell populations in a single universal bio-ink and relying on pre-printing fluorescent staining to differentiate them while still on the donor substrate. With the previously described set-up coupled with image analysis and given a sufficiently diluted bio-ink, the different cell types could be identified and printed in the desired pattern, allowing for the use of a single ink spread autonomously via blade coating to create complex cell models quickly and efficiently.

The mechanisms behind LIFT are well-known, and extensive descriptions and simulations are available in the literature. Its possible application in biology makes no doubt, with an increasing number of publications (Antoshin et al., 2019; Florian & Serra, 2023) and several companies exploiting the method commercially such as Poietis and PhosPrint. Poietis focuses on the production of skin tissues by LIFT, it is for now the only one that has entered clinical trial, further showcasing the applicability of the process. Yet, reducing complexity and promoting the development of small-scale devices could also greatly encourage the application of LIFT in biology applications. For now, this complexity and intricacy of operation are major barriers to broader applications and tissue modeling or drug screening, among others. Many times, the LIFT process has proved itself capable of printing anything, and biological material is no exception; it now has to be done efficiently for it to escape the confine of laboratories and experimental research. Biological printing, therefore, should not be considered a sub-experiment of an electronics-based LIFT setup. It requires a dedicated platform designed to address its unique challenges, such as handling sensitive materials, managing the inherent variability of bio-inks, and more importantly, maintaining sterility for cell biology applications.

5.1.4 Laser choice

The LIFT experimental set-up in this work was based on the utilization of a pico-to-femtosecond laser. The application of ultra-short pulses to LIFT bioprinting is less common in the literature (Chang & Sun, 2023). For this reason, a first and obvious step of our work was to investigate the impact of pulse duration on cell survival rates. To this aim, we compared nanoseconds, which are commonly used in most published LIFT studies, with picosecond pulses to evaluate their ability to effectively transfer biological material. Femtosecond pulses were also investigated, but the laser pulses, in the presence of the titanium DRL and with a thick bio-ink layer, did not induce sufficient jetting to transfer enough cells for statistically relevant comparisons between experimental conditions. This condition was, therefore, omitted from the final work.

In the second article, we demonstrated by isolating the laser process that picosecond pulses yielded higher survival rates than nanosecond ones. Yet the differences were only relevant for the highest energy considered, which is unsuitable for resolute cell printing given its explosive nature in both studied regimes. The difference in laser pulse duration can thus be considered nonsignificant in the survival of the cells. Thermal effects

with pulses at or below the nanosecond range are already negligible when considering the bulk of the ink. Considering only the LIFT process in the condition that we proposed here, picosecond pulses does not seem to bring any noticeable advantages. Ultra-short pulses, however, could offer significant benefits by utilizing non-linear absorption to propel the bio-ink, eliminating the need for a metallic DRL and thereby reducing the risk of metallic contamination on the receiver. In the prospect of accessibility and scalability of the LIFT bio-printing process, while picosecond lasers offer certain advantages, the use of more readily available and cost-effective low-power nanosecond sources should be considered as a viable option.

Similarly, high-frequency lasers are currently underutilized. As previously discussed, the bio-inks used in LIFT bioprinting are particularly prone to degradation over time. They also contain sensible material that must be handled with care and limited exposition. The combination of a high-frequency laser and a high-speed galvanometric scanner allows for exceptionally fast printing, limiting ink degradation. However, as outlined in **Article 1**, obtaining consistent jetting requires both spatial and temporal independence between jets, which considerably limits the achievable printing speed. Consequently, the laser frequency is thus often artificially slowed down to match the underlying physical processes. For cell printing, lasers with achievable frequencies between 10 and 100 Hz are generally sufficient.

In contrast, in the sake of establishing a versatile and multidisciplinary laser-based platform for tissue engineering, the use of ultra-fast lasers become crucial. Their ability to interact with transparent materials while minimizing thermal transfer makes them highly efficient for laser ablation processes. As detailed in Articles 3 and 4, an ultra-fast high-frequency laser coupled with a galvanometric scanner demonstrated its full potential during laser-ablation processes for surface structuring. Ultra-short pulses can be employed to structure natural and synthetic polymers to specifically improve cell organization and myoblast fusion. In Article 5, we further demonstrated how this laser system could generate silicon nanoparticles, which significantly improved murine myoblast motility, proliferation, and differentiation. Moreover, we once again crucially utilized femtosecond pulses to generate 3D scaffolds mimicking the anisotropic 3D structure of physiological human muscle. The creation of channels in the bulk of a hydrogel is only possible with limited thermal transfer, in order to avoid overheating of the constructs (resulting in drying or burning of the hydrogel scaffold). Therefore, here we report four distinct yet combinable tissue engineering strategies - 2D structuring, 3D

structuring, bioprinting, nanoparticle generation - utilizing a single laser source. This emphasizes the versatility, flexibility, and potential of the proposed platform for skeletal muscle tissue engineering, human skeletal muscle modeling and disease study.

5.2 Optimization of LIFT for skeletal muscle bioprinting

5.2.1 Key parameters for cell survival

In addition to considerable variation in donor reproducibility, differences in bio-ink viscosity led to contrasting cell survival results. As demonstrated in the first article, more viscous bio-inks yielded more reproducible layers, more controllable jets, and overall better printing resolution. Under specific printing conditions, we determined and analyzed the speed of the jets, revealing a point where their speed approaches zero. This "zero-velocity jet" is associated with a precise maximum height, where the receiver substrate should be positioned to minimize mechanical stress on the cells. Although theoretically valid, applying this method to cell printing proved highly challenging and difficult to implement. Indeed, as other studies have indicated (Z. Zhang et al., 2017), adding cells to the ink creates considerable turbulences, locally changing the rheological properties of the inks and thus modifying the jetting mechanism. The created jets tend to warp and no longer propagate perpendicularly to the donor substrate. While this effect has limited consequences on the spatial resolution of the LIFT printing method, it does alter the previously analyzed jetting behavior. The precise deposition of cells on the receiver substrate at a speed close to zero is compromised, resulting in poor cell survival rates with the alginate bio-inks studied in the first article.

In contrast, in the second article, we used 2% gelatin as a base for cell printing, which yielded much higher cell survival rates, even without the addition of receiver coatings. Still, the latter proved to be a viable solution to guarantee a maximum survival, reaching 90% for a large range of energies, given that gelatin is used as bio-ink. High-viscosity inks like alginate, on the other hand, resulted in far lower survival rates even when substantial amounts of coating material were applied. The difference in results is likely due to the increase of shear stress during the jetting dynamic, the increased inertia of jets produced from viscous inks, and the overall higher jetting speeds.

The observations made in this work concerning alginate's efficiency as a bio-ink are in complete contradiction with numerous LIFT studies, which report no apparent issues (Khalil & Sun, 2009; Z. Zhang et al., 2016). Such a disparity in our printing results may stem from variations in other underlying parameters such as the cell type, their concentration, the donor-receiver gap, or the overall experimental set-up. Nevertheless, it highlights the sensibility and complexity of the LIFT process and underscores the importance of precise protocols and improved reproducibility to reach initial experimental goals.

The link between viscosity and survival is especially difficult to demonstrate, given the great disparities in layer quality between a low-viscosity ink such as gelatin and a highly viscous one like alginate. For a conclusive cell survival rate comparison, factors such as ink layer, cell distribution, and energy deposited on the donor in regard to the difficulty of creating the jets must all be taken into account. Unfortunately, given the reproducibility issues previously mentioned, this type of analysis was not feasible within the scope of this study.

5.2.2 Receiver coating materials

Various coating materials were tested for their ability and contribution to support cell survival, with all demonstrating perfect cell viability. However, maintaining printing resolution posed another challenge. As detailed in **Article 2**, adding a thin hydrogel layer on the receiver substrate can cause the printed cell droplet to dissolve once the culture media is added, leading to a complete loss of the resolution provided by printing. Two potential solutions were investigated. The first one involves the adhesion of cells to the substrate before addition of the culture media as it is used by Schiele and colleagues (Schiele et al., 2011). While this approach helps to preserve the desired printing resolution, it significantly extends the printing process and increases the exposure of cells to a potential non-sterile environment, as the used LIFT set-up cannot be put in a sterile chamber/hood, and to the subsequent drying of the thin coating with consequent cell death. Additionally, slight movements after printing can displace the cells, making the transfer to an incubator difficult.

The second solution is to use cross-linkable biomaterials like Matrigel. Other materials, such as gelatin methacrylate end PEG-fibrinogen, were also tested, utilizing a

photoinitiator and short UV exposition to crosslink the gel. Although both biomaterials enabled a good cell survival, their adhesion to the glass coverslip was inconsistent. Furthermore, the addition of a photoinitiator presents limitations for certain applications due to cell cytotoxicity (B. Zeng et al., 2021). Crosslinking sodium alginate with calcium chloride was also evaluated, but the deformations provoked by the addition of the crosslinking agent led to a loss of resolution and detachment the substrate from the glass coverslip. For these reasons, Matrigel met all the requirements for effectively coating the receiver substrate. Its properties, including gelation at room temperature and strong adherence to the glass substrate, make it an ideal material for LIFT bioprinting. Using Matrigel, we achieved both high cell survival and an excellent printing resolution.

We also noted the possibility of depositing cells within the bulk of the gel for precise three-dimensional printing, further enhancing its suitability for bioprinting applications.

5.2.3 Optimization of the coating layer protocol

The production of reproducible coating layers on the receiver substrate has been subjected to similar challenges as those faced with the donor. Initially, Matrigel was deposited on the glass substrate via pipetting. However, as highlighted in **Article 4**, this approach resulted in increased surface tension due to the large volume of material required to create reproducible layers. We also observed a rapid shrinkage of the material during its gelation.

To address these issues, we developed a spray-based method that provided a valid and valuable alternative to manual coating. The pipeline described in **Article 4** reduced the amount of Matrigel deposited on the glass substrate while ensuring an uniform coverage across the glass surface. This method also allowed for two consecutive coatings, thus reducing the shrinkage of the Matrigel. Additionally, it showed additional potentials for constructing 3D structures by layering coatings and cells without the need of a manual intervention. This system could thus constitute an introduction to the LIFT process automatization, which I discussed earlier.

5.3 Surface structuration

Topographical cues on an engineered surface can highly influence cell organization and alignment by mimicking the ECM, ultimately enhancing cell maturation. In this work, we explored the laser structuration of biomaterials and polymeric surfaces to evaluate the ability of the process to successfully guide the development and differentiation of skeletal muscle cells.

5.3.1 Biomaterial choice

Several biomaterials were considered for their structuration by laser ablation. Commonly used materials in tissue engineering, such as gelatin and alginate, as tested in **Article 2**, demonstrated poor stability under cell culture conditions. On the other hand, the adhesion of more complex materials to the underlying glass substrate also posed a significant challenge. For example, gelatin methacrylate demonstrated successful crosslinking and stable performance under cell culture conditions. However, despite extensive pre-processing, it failed to adhere to the glass, making it unsuitable for our purposes and for long term cell culture required to achieve muscle fiber formation.

In contrast, collagen type 1 adhered well for several days with extensive stability. However, it proved fragile, easily breaking under intense pipetting. Its use requires careful consideration of both its strengths and limitations. For long-term cultures involving frequent pipetting and media changes, collagen coatings may not be the most practical choice. Furthermore, the tensions created by the cells during differentiation, combined with the rearrangement of the collagen coating by the cells themselves, could lead to the detachment of the collagen layer from the glass substrate, resulting in the wrapping of the sample.

5.3.2 Surface structuration of biomaterials for myoblast alignment

The structuring of thin layers of collagen type 1 created highly hydrophilic channels that enabled the efficient alignment of human-immortalized myoblasts. The cells were confined on the ridges and within the bottom of the created channels, which allowed them to orient in the desired direction. The laser-structuring of bio-polymer layers offers a simple and perfectly bio-compatible method for cell organization. However, as

described in **Article 4**, depositing large amounts of biomaterial on cell culture coverslips inevitably results in inhomogeneities due to the surface tension on the edge of the base slide. The "dome's" effect transcribes on the quality of the final dried layer with edges noticeably thinner than the center. Additionally, the gelation and drying of the collagen led to the formation of crystals and crystal-like structures randomly distributed across the surface. These inhomogeneities complicate laser processing, as laser ablation is highly dependent on the precise focusing of the laser on the material's surface. By using uneven surfaces, the results of the structuration process lack reproducibility from one sample to the other. The process is also time-consuming as the collagen layers have to completely dry before being processable and highly operator-dependent. With this in mind, this prolonged curing time does not fit well with the extremely fast galvanometric-based laser-structuring process.

In this context, the spray-based method developed in **Article 4** for producing the receiver substrate coating could offer a valuable alternative to the current preparation protocol. Automating the collagen slide production would limit variability and promote the accessibility and scalability of the process. To achieve a thick enough coating that prevents the laser from reaching the glass, the spraying technique could be optimized to deposit multiple short sprays. Although increasing biomaterial consumption, the quick-drying layers could build up thickness while minimizing surface tension effects.

Additionally, one could also envision spraying collagen directly onto the bottom of cell culture plates; the precise and homogenous deposition of thin layers would allow for more precise laser focusing. In this way, and as described in **Article 4**, this approach could enable the large-scale processing of pre-coated culture plates with tailored patterns, paving the way for high-throughput analysis, drug screening, and disease modeling on bio-compatible surfaces that mimic the ECM.

The creation of structured and highly porous topographies on bio-polymers provides an efficient approach to guiding cell development, with promising applications in tissue modeling. However, as with the LIFT experimental setup, the system developed here requires significant refinement to ensure scalability and reproducibility. Optimizing this process presents a substantial engineering challenge, though viable solutions are within reach.

5.3.3 Surface structuration of polymers

To meet the challenges prompted by bio-polymer structuration and to propose a universal and scalable method for producing topographical cues, the laser-structuring of polystyrene (PS) was extensively investigated. PS constitutes the major component of tissue culture labware; for this reason, the ability to promote cell organization following its processing considerably widens the application scale of the process.

The strengths, limitations, and prospects of PS structuration are extensively described in **Article 4**. While the autofluorescence of the channels presents a significant drawback, the method effectively addresses many of the challenges associated with the previously discussed collagen coatings. We demonstrated that photobleaching and the use of confocal microscopy could minimize photobleaching and offer a simple solution for immunostaining analysis of cultured cells.

The laser-based creation of highly porous channels on the PS surfaces allowed for the guiding of murine C2C12, resulting in highly organized and coherent cultures. In contrast to the collagen structuration, the laser is here used to create highly hydrophobic areas on the PS surface to influence the behavior of the cells. The latter thus exhibited preferential adhesion to the unstructured part of the processed surfaces, allowing for a controlled differentiation. Here, we utilize the channels to reproduce the anisotropic organization of the muscle, but these hydrophobic properties could be exploited for a variety of cell types and the production of tissues.

We developed a reproducible method to structure polymeric substrates quickly and efficiently, guaranteeing the scalability and the easy integration of the process in cell culture workflow. While displaying clear advantages compared to the tested biomaterials, the latter must not be disregarded. Indeed, the laser-processing of collagen revealed highly porous and hydrophilic surfaces with cells developing on the entire processed surface. The ability to adjust the composition of the biomaterial offers a chance to tune not only the spatial organization of the cells but also to mimic more profoundly the physiological ECM by adding chemical factors and cues in the scaffold itself.

Laser structuration for tissue engineering purposes can be applied to a wide range of natural and synthetic materials, each with its own advantages and limitations. The choice of material depends on the specific application and research objectives, offering a

wide array of possibilities. Despite the variations in substrates, the processing method remains the same while inducing different effects depending on the substrate's nature (hydrophilic/hydrophobic), demonstrating both its versatility and adaptability across different materials.

5.4 Combination of LIFT bioprinting and surface structuration for skeletal muscle modeling

The structuring of PS with the creation of hydrophobic channels effectively guided myoblast orientation and differentiation, providing a customizable substrate ideal for depositing cells by LIFT. We demonstrated the potential of the two processes through the printing of healthy and DMD/FSHD-affected human myoblasts that accurately exhibited physiopathological hallmarks. Combining the two methods also enables the precise placement of different cell types on the receiver substrate with adapted topographical cues, which could be used to recreate complex cell interactions in muscle tissues for relevant disease modeling purposes.

However, it is essential to acknowledge the limitations of the process to better utilize it. LIFT is not designed for fabricating large-scale 3D constructs; the number of cells deposited is insufficient for building proper volumetric tissues. For larger constructs, other bio-printing methods, such as extrusion, are more suitable and to be favored.

While a few studies have explored the use of LIFT for 3D structures, these are generally based on the layering of bio-materials and cells to form a volumetric matrix (Barron et al., 2004; Gruene, Pflaum, Hess, et al., 2011). The dimensions of these constructs can be adequate for specific applications (Gaebel et al., 2011) and even for regenerative medicine, with multiple examples of skin patches being printed and implanted *in vivo* (Manita et al., 2021). Yet, in the case of skeletal muscle, the method remains largely insufficient for potential use in regenerative medicine. LIFT should instead take advantage of its resolution and flexibility to assess specific cell interactions for applications in fields such as disease modeling and drug screening rather than volumetric tissue engineering.

5.5 Future prospects

In this work, we extensively explored the potential of ultra-fast lasers in various tissue engineering applications, including LIFT bioprinting and surface structuring. The laser-based platform developed throughout my doctoral work can also be expanded to include nanoparticle generation, as highlighted in **Article 5**. Their integration could further enhance myogenic differentiation and improve the relevance of the engineered tissue.

All the techniques developed in this work have been proven efficient as standalone tissue engineering strategies. The strength of the so-developed laser platform lies in the ability to combine them in a single protocol to create a model with enhanced relevancy. Here, we have already combined LIFT bioprinting with laser-induced topographical cues for precise guiding of myoblasts. Nanoparticles of different materials could easily be embedded in the matrix of the collagen coatings investigated in **Article 3** to further promote cell differentiation and allow for sustained release over time to extend their effects. Moreover, the addition of electrical stimuli to the patterned cells could once more improve the maturation of the created tissue and enhance its functionality.

This approach offers a versatile laser-based toolkit for tissue engineering applications where each method can be used independently or combined depending on the tissue and the research objective.

It is important to note that this work represents only the first step in developing human skeletal muscle models using laser-based tissue engineering strategies. The next step will involve the advanced integration of all the developed approaches and their application to more complex multicellular models. We envision the precise bioprinting of iPSC-derived neural progenitors in co-culture with affected myoblasts to precisely study the *in vitro* formation of neuro-muscular junction. Additionally, we aim to enhance the three-dimensionality of the constructs by layering cells and incorporating multiple coatings, to print for example, both tenocytes and myoblasts in a carefully tailored 3D configuration for myotendinous junction study.

Conclusion

6. Conclusion

My thesis project aimed to investigate the integration of two laser processes: (i) laser-assisted bioprinting and (ii) laser surface texturing, to create culture microenvironments that promote muscle cell differentiation. The objective was to optimize and control the proliferation, migration, organization, and differentiation of muscle cells into populations of mature myotubes.

To this end, we set up a LIFT printing experiment based on the use of an ultra-fast laser source that allowed us to successfully combine the two methods. We formulated a bio-ink that guaranteed precise printing and characterized the jetting mechanisms to optimize the deposition of living cells. Through various printing strategies, we were able to control the number of printed cells while maintaining high printing accuracy and resolution. We characterized the survival of the cells and evaluated the role and importance of a thin hydrogel layer on the collector substrate. Different materials were investigated to identify the one that best suited our needs. In this way, cells were successfully transferred in a gelatin-based bio-ink onto Matrigel-coated receivers, yielding excellent survival rates.

In parallel to the printing experiment, we evaluated the laser structuring of natural (collagen type 1) and synthetic polymers (polystyrene) for their capacity to guide myoblast development and fusion. We demonstrated that laser-induced hydrophilic channels in collagen and hydrophobic channels in polystyrene both lead to excellent cell organization that mimics the anisotropic nature of the muscle fibers. The two materials studied exhibited strengths and limitations that are suitable for various applications.

The LIFT bio-printing and the structuration processes were successfully combined in a single and efficient protocol that required some additional adaptation in order to improve its efficiency. Healthy and DMD/FSHD-affected myoblasts were printed on structured polystyrene, where they displayed enhanced organization as well as distinct pathological defects, including significant differences in myotubes' morphology and the appearance of disease markers. Additionally, our experimental set-up enabled the generation of silicon nanoparticles, which, when interacting with murine C2C12 cells, enhanced their proliferation, motility, and differentiation. This further enhances the potential of the set-up for improved cell cultures and tissue engineering applications.

The limitations discussed in this work relate more to engineering challenges than to inherent limitations of the processes themselves. Their simple and flexible nature makes them easily scalable for high throughput screening and disease modeling. To conclude, the creation of a compact laser-based platform able to perform bio-printing for precise multi-cell deposition, surface structuring for enhanced tissue organization, and generation of nanoparticles for improved myogenic capabilities - all using a single laser source - opens the door for accessible, tailored tissue engineering solutions.

Bibliography

admin.facellitate. (2022, décembre 20). Évolution de la culture cellulaire 3D. *faCellitate*. https://facellitate.com/fr/evolution-of-3d-cell-culture/

Aguirre, A. S., Astudillo Moncayo, O. M., Mosquera, J., Muyolema Arce, V. E., Gallegos, C., Ortiz, J. F., Andrade, A. F., Oña, S., & Buj, M. J. (s. d.). Treatment of Facioscapulohumeral Muscular Dystrophy (FSHD) : A Systematic Review. *Cureus*, *15*(6), e39903. https://doi.org/10.7759/cureus.39903

Ahmad Raus, R., Wan Nawawi, W. M. F., & Nasaruddin, R. R. (2021). Alginate and alginate composites for biomedical applications. *Asian Journal of Pharmaceutical Sciences*, *16*(3), 280-306. https://doi.org/10.1016/j.ajps.2020.10.001

Ahuja, N., Awad, K., Peper, S., Brotto, M., & Varanasi, V. (2021). Mini review : Biomaterials in repair and regeneration of nerve in a volumetric muscle loss. *Neuroscience Letters*, *762*, 136145. https://doi.org/10.1016/j.neulet.2021.136145

A.K, L., Viswanath, I. V., Bhagavathula, D., Boddeti, G., Venu, R., & Murthy, Y. L. N. (2019). Review on nanomaterials : Synthesis and applications. *Materials Today: Proceedings*, *18*. https://doi.org/10.1016/j.matpr.2019.07.371

Ali, A. S. M., Wu, D., Bannach-Brown, A., Dhamrait, D., Berg, J., Tolksdorf, B., Lichtenstein, D., Dressler, C., Braeuning, A., Kurreck, J., & Hülsemann, M. (2024). 3D bioprinting of liver models : A systematic scoping review of methods, bioinks, and reporting quality. *Materials Today Bio*, *26*, 100991. https://doi.org/10.1016/j.mtbio.2024.100991

Aljohani, W., Ullah, M. W., Zhang, X., & Yang, G. (2018). Bioprinting and its applications in tissue engineering and regenerative medicine. *International Journal of Biological Macromolecules*, *107*(Pt A), 261-275. https://doi.org/10.1016/j.ijbiomac.2017.08.171

Almany, L., & Seliktar, D. (2005). Biosynthetic hydrogel scaffolds made from fibrinogen and polyethylene glycol for 3D cell cultures. *Biomaterials*, *26*(15), 2467-2477. https://doi.org/10.1016/j.biomaterials.2004.06.047

Antoshin, A. A., Churbanov, S. N., Minaev, N. V., Zhang, D., Zhang, Y., Shpichka, A. I., & Timashev, P. S. (2019). LIFT-bioprinting, is it worth it? *Bioprinting*, *15*, e00052. https://doi.org/10.1016/j.bprint.2019.e00052

Arandel, L., Polay Espinoza, M., Matloka, M., Bazinet, A., De Dea Diniz, D., Naouar, N., Rau, F., Jollet, A., Edom-Vovard, F., Mamchaoui, K., Tarnopolsky, M., Puymirat, J., Battail, C., Boland, A., Deleuze, J.-F., Mouly, V., Klein, A. F., & Furling, D. (2017). Immortalized human myotonic dystrophy muscle cell lines to assess therapeutic compounds. *Disease Models & Mechanisms*, *10*(4), 487-497. https://doi.org/10.1242/dmm.027367

Ariyasinghe, N. R., Santoso, J. W., Gupta, D., Pincus, M. J., August, P. R., & McCain, M. L. (2021). Optical Clearing of Skeletal Muscle Bundles Engineered in 3-D Printed Templates. *Annals of Biomedical Engineering*, *49*(2), 523-535. https://doi.org/10.1007/s10439-020-02583-0

Autar, K., Guo, X., Rumsey, J. W., Long, C. J., Akanda, N., Jackson, M., Narasimhan, N. S., Caneus, J., Morgan, D., & Hickman, J. J. (2021). A functional hiPSC-cortical neuron differentiation and maturation model and its application to neurological disorders. *Stem Cell Reports*, *17*(1), 96-109. https://doi.org/10.1016/j.stemcr.2021.11.009

Babaliari, E., Kavatzikidou, P., Angelaki, D., Chaniotaki, L., Manousaki, A., Siakouli-Galanopoulou, A., Ranella, A., & Stratakis, E. (2018). Engineering Cell Adhesion and Orientation via Ultrafast Laser Fabricated Microstructured Substrates. *International Journal of Molecular Sciences*, *19*(7), 2053. https://doi.org/10.3390/ijms19072053

Banks, T. A., Luckman, P. S. B., Frith, J. E., & Cooper-White, J. J. (2015). Effects of electric fields on human mesenchymal stem cell behaviour and morphology using a novel multichannel device. *Integrative Biology*, *7*(6), 693-712. https://doi.org/10.1039/c4ib00297k

Barron, J. A., Spargo, B. J., & Ringeisen, B. R. (2004). Biological laser printing of three dimensional cellular structures. *Applied Physics A*, *79*(4-6), 1027-1030. https://doi.org/10.1007/s00339-004-2620-3

Bentzinger, C., Wang, Y. X. (Will), Maltzahn, J., & Rudnicki, M. (2013). The emerging biology of muscle stem cells : Implications for cell-based therapies. *BioEssays : news and reviews in molecular, cellular and developmental biology*, *35*. https://doi.org/10.1002/bies.201200063

Bohandy, J., Kim, B. F., & Adrian, F. J. (1986). Metal deposition from a supported metal film using an excimer laser. *Journal of Applied Physics*, *60*(4), 1538-1539. https://doi.org/10.1063/1.337287

Bohandy, J., Kim, B. F., Adrian, F. J., & Jette, A. N. (1988). Metal deposition at 532 nm using a laser transfer technique. *Journal of Applied Physics*, *63*(4), 1158-1162. https://doi.org/10.1063/1.340023

Bosmans, C., Rodriguez, N. G., Karperien, M., Malda, J., Teixeira, L. M., Levato, R., & Leijten, J. (2024). Towards single-cell bioprinting : Micropatterning tools for organ-on-chip development. *Trends in Biotechnology*, *42*(6), 739-759. https://doi.org/10.1016/j.tibtech.2023.11.014

Boso, D., Maghin, E., Carraro, E., Giagante, M., Pavan, P., & Piccoli, M. (2020). Extracellular Matrix-Derived Hydrogels as Biomaterial for Different Skeletal Muscle Tissue Replacements. *Materials*, *13*(11), 2483. https://doi.org/10.3390/ma13112483

Bourget, J.-M., Kérourédan, O., Medina, M., Rémy, M., Thébaud, N. B., Bareille, R., Chassande, O., Amédée, J., Catros, S., & Devillard, R. (2016). Patterning of Endothelial Cells and Mesenchymal Stem Cells by Laser-Assisted Bioprinting to Study Cell Migration. *BioMed Research International*, *2016*(1), 3569843. https://doi.org/10.1155/2016/3569843

Breckenfeld, E., Kim, H., Auyeung, R. C. Y., Charipar, N., Serra, P., & Piqué, A. (2015). Laser-induced forward transfer of silver nanopaste for microwave interconnects. *Applied Surface Science*, *331*, 254-261. https://doi.org/10.1016/j.apsusc.2015.01.079

Brown, A. C., & Barker, T. H. (2014). Fibrin-based biomaterials : Modulation of macroscopic properties through rational design at the molecular level. *Acta biomaterialia*, *10*(4), 1502-1514. https://doi.org/10.1016/j.actbio.2013.09.008

Brun, C. E., Chevalier, F. P., Dumont, N. A., & Rudnicki, M. A. (2017). The Satellite Cell Niche in Skeletal Muscle. In *Biology and Engineering of Stem Cell Niches* (p. 145-166). Elsevier. https://doi.org/10.1016/B978-0-12-802734-9.00010-X

Buchberger, G., Muck, M., Plamadeala, C., & Heitz, J. (2023). *Laser Structuring for Biomedical Applications* (p. 1105-1165). https://doi.org/10.1007/978-3-031-14752-4_31

Bulgakova, N. M., & Bulgakov, A. V. (2001). Pulsed laser ablation of solids : Transition from normal vaporization to phase explosion. *Applied Physics A*, *73*(2), 199-208. https://doi.org/10.1007/s003390000686

Bushby, K., Norwood, F., & Straub, V. (2007). The limb-girdle muscular dystrophies—Diagnostic strategies. *Biochimica et Biophysica Acta (BBA) - Molecular Basis of Disease*, *1772*(2), 238-242. https://doi.org/10.1016/j.bbadis.2006.09.009

Buskermolen, A. B. C., Suresh, H., Shishvan, S. S., Vigliotti, A., DeSimone, A., Kurniawan, N. A., Bouten, C. V. C., & Deshpande, V. S. (2019). Entropic Forces Drive Cellular Contact Guidance. *Biophysical Journal*, *116*(10), 1994-2008. https://doi.org/10.1016/j.bpj.2019.04.003

Cao, X., Maharjan, S., Ashfaq, R., Shin, J., & Zhang, Y. S. (2021). Bioprinting of Small-Diameter Blood Vessels. *Engineering*, *7*(6), 832-844. https://doi.org/10.1016/j.eng.2020.03.019

Carnes, M. E., & Pins, G. D. (2020). Skeletal Muscle Tissue Engineering : Biomaterials-Based Strategies for the Treatment of Volumetric Muscle Loss. *Bioengineering*, *7*(3), Article 3. https://doi.org/10.3390/bioengineering7030085

Carnovale, C., Bryant, G., Shukla, R., & Bansal, V. (2019). Identifying Trends in Gold Nanoparticle Toxicity and Uptake : Size, Shape, Capping Ligand, and Biological Corona. *ACS Omega*, *4*(1), 242-256. https://doi.org/10.1021/acsomega.8b03227

Caron, L., Testa, S., & Magdinier, F. (2023). Induced Pluripotent Stem Cells for Modeling Physiological and Pathological Striated Muscle Complexity. *Journal of Neuromuscular Diseases*, *10*(5), 761-776. https://doi.org/10.3233/JND-230076

Catros, S., Fricain, J.-C., Guillotin, B., Pippenger, B., Bareille, R., Remy, M., Lebraud, E., Desbat, B., Amédée, J., & Guillemot, F. (2011). Laser-assisted bioprinting for creating on-demand patterns of human osteoprogenitor cells and nano-hydroxyapatite. *Biofabrication*, *3*(2), 025001. https://doi.org/10.1088/1758-5082/3/2/025001

Catros, S., Guillemot, F., Nandakumar, A., Ziane, S., Moroni, L., Habibovic, P., van Blitterswijk, C., Rousseau, B., Chassande, O., Amédée, J., & Fricain, J.-C. (2012). Layer-by-layer tissue microfabrication supports cell proliferation in vitro and in vivo. *Tissue Engineering. Part C, Methods*, *18*(1), 62-70. https://doi.org/10.1089/ten.TEC.2011.0382

Catros, S., Guillotin, B., Bačáková, M., Fricain, J.-C., & Guillemot, F. (2011). Effect of laser energy, substrate film thickness and bioink viscosity on viability of endothelial cells printed by Laser-Assisted Bioprinting. *Applied Surface Science*, *257*(12), 5142-5147. https://doi.org/10.1016/j.apsusc.2010.11.049

Cè, E., Paracchino, E., & Esposito, F. (2008). Electrical and mechanical response of skeletal muscle to electrical stimulation after acute passive stretching in humans : A combined electromyographic and mechanomyographic approach. *Journal of Sports Sciences*, *26*(14), 1567-1577. https://doi.org/10.1080/02640410802277429

Chandra, P., & Lee, S. J. (2015). Synthetic Extracellular Microenvironment for Modulating Stem Cell Behaviors. *Biomarker Insights*, *10*(Suppl 1), 105-116. https://doi.org/10.4137/BMI.S20057

Chang, J., & Sun, X. (2023). Laser-induced forward transfer based laser bioprinting in biomedical applications. *Frontiers in Bioengineering and Biotechnology*, *11*. https://doi.org/10.3389/fbioe.2023.1255782

Charest, J. L., García, A. J., & King, W. P. (2007). Myoblast alignment and differentiation on cell culture substrates with microscale topography and model chemistries. *Biomaterials*, *28*(13), 2202-2210. https://doi.org/10.1016/j.biomaterials.2007.01.020

Chen, C., Bai, X., Ding, Y., & Lee, I.-S. (2019). Electrical stimulation as a novel tool for regulating cell behavior in tissue engineering. *Biomaterials Research*, *23*(1), 25. https://doi.org/10.1186/s40824-019-0176-8

Chen, Y., Zhang, J., Liu, X., Wang, S., Tao, J., Huang, Y., Wu, W., Li, Y., Zhou, K., Wei, X., Chen, S., Li, X., Xu, X., Cardon, L., Qian, Z., & Gou, M. (2020). Noninvasive in vivo 3D bioprinting. *Science Advances*, *6*, eaba7406. https://doi.org/10.1126/sciadv.aba7406

Cherrington, R., & Liang, J. (2016). 2—Materials and Deposition Processes for Multifunctionality. In V. Goodship, B. Middleton, & R. Cherrington (Éds.), *Design and Manufacture of Plastic Components for Multifunctionality* (p. 19-51). William Andrew Publishing. https://doi.org/10.1016/B978-0-323-34061-8.00002-8

Chi, D., Raman, S., Tawaklna, K., Zhu, W. Y., Keane, A. M., Bruce, J. G., Parikh, R., & Tung, T. H. (2023). Free functional muscle transfer for lower extremity reconstruction. *Journal of Plastic, Reconstructive & Aesthetic Surgery*, *86*, 288-299. https://doi.org/10.1016/j.bjps.2023.09.041

Chichkov, B. N., Momma, C., Nolte, S., Alvensleben, F., & Tünnermann, A. (1996). Femtosecond, picosecond and nanosecond laser ablation of solids. *Applied Physics A Materials Science & Processing*, *63*(2), 109-115. https://doi.org/10.1007/BF01567637

Christopher A. McCuller, McCuller, C., Rishita Jessu, Avery L. Callahan, Callahan, A. L., Jessu, R., & Avery L. Callahan. (2020). *Physiology, Skeletal Muscle*.

Colina, M., Duocastella, M., Fernández-Pradas, J. M., Serra, P., & Morenza, J. L. (2006). Laser-induced forward transfer of liquids : Study of the droplet ejection process. *Journal of Applied Physics*, *99*(8), 084909. https://doi.org/10.1063/1.2191569

Colina, M., Serra, P., Fernández-Pradas, J. M., Sevilla, L., & Morenza, J. L. (2005). DNA deposition through laser induced forward transfer. *Biosensors and Bioelectronics*, *20*(8), 1638-1642. https://doi.org/10.1016/j.bios.2004.08.047

Collins, L. T., Ponnazhagan, S., & Curiel, D. T. (2023). Synthetic Biology Design as a Paradigm Shift toward Manufacturing Affordable Adeno-Associated Virus Gene Therapies. *ACS Synthetic Biology*, *12*(1), 17-26. https://doi.org/10.1021/acssynbio.2c00589

Cordova, G., Negroni, E., Cabello-Verrugio, C., Mouly, V., & Trollet, C. (2018). Combined Therapies for Duchenne Muscular Dystrophy to Optimize Treatment Efficacy. *Frontiers in Genetics*, *9*. https://doi.org/10.3389/fgene.2018.00114

Corona, B. T., Wenke, J. C., & Ward, C. L. (2016). Pathophysiology of Volumetric Muscle Loss Injury. *Cells Tissues Organs*, *202*(3-4), 180-188. https://doi.org/10.1159/000443925

Cox, J. K., Eisenberg*, A., & Lennox, R. B. (1999). Patterned surfaces via self-assembly. *Current Opinion in Colloid & Interface Science*, *4*(1), 52-59. https://doi.org/10.1016/S1359-0294(99)00004-7

Cretoiu, D., Pavelescu, L., Duica, F., Radu, M., Suciu, N., & Cretoiu, S. M. (2018). Myofibers. *Advances in Experimental Medicine and Biology*, *1088*, 23-46. https://doi.org/10.1007/978-981-13-1435-3_2

Das, A., & Ding, C.-F. (2024). Innovative Fabrication of Metal Alloy Structures via Laser-Induced Forward Transfer on Flexible Substrates. *Small Methods*, *8*(9), 2301429. https://doi.org/10.1002/smtd.202301429

Das, A., Ghosh, A., Chattopadhyaya, S., & Ding, C.-F. (2024). A review on critical challenges in additive manufacturing via laser-induced forward transfer. *Optics & Laser Technology*, *168*, 109893. https://doi.org/10.1016/j.optlastec.2023.109893

Das, S., Browne, K. D., Laimo, F. A., Maggiore, J. C., Hilman, M. C., Kaisaier, H., Aguilar, C. A., Ali, Z. S., Mourkioti, F., & Cullen, D. K. (2020). Pre-innervated tissue-engineered muscle promotes a pro-

regenerative microenvironment following volumetric muscle loss. *Communications Biology*, *3*, 330. https://doi.org/10.1038/s42003-020-1056-4

Dave, H. D., Shook, M., & Varacallo, M. (2024). Anatomy, Skeletal Muscle. In *StatPearls*. StatPearls Publishing. http://www.ncbi.nlm.nih.gov/books/NBK537236/

Deenen, J. C. W., Arnts, H., van der Maarel, S. M., Padberg, G. W., Verschuuren, J. J. G. M., Bakker, E., Weinreich, S. S., Verbeek, A. L. M., & van Engelen, B. G. M. (2014). Population-based incidence and prevalence of facioscapulohumeral dystrophy. *Neurology*, *83*(12), 1056-1059. https://doi.org/10.1212/WNL.0000000000000797

Delaporte, P., & Alloncle, A.-P. (2016). [INVITED] Laser-induced forward transfer : A high resolution additive manufacturing technology. *Optics & Laser Technology*, *78*, 33-41. https://doi.org/10.1016/j.optlastec.2015.09.022

Delourme, M., Broucqsault, N., Mazaleyrat, K., & Magdinier, F. (2020). Production of Innervated Skeletal Muscle Fibers Using Human Induced Pluripotent Stem Cells. In A. Nagy & K. Turksen (Éds.), *Induced Pluripotent Stem (iPS) Cells* (Vol. 2454, p. 231-239). Springer US. https://doi.org/10.1007/7651_2020_334

Demirci, S., Leonard, A., & Tisdale, J. F. (2020). Hematopoietic stem cells from pluripotent stem cells : Clinical potential, challenges, and future perspectives. *Stem Cells Translational Medicine*, *9*(12), 1549-1557. https://doi.org/10.1002/sctm.20-0247

Deng, Y., Renaud, P., Guo, Z., Huang, Z., & Chen, Y. (2017). Single cell isolation process with laser induced forward transfer. *Journal of Biological Engineering*, *11*(1), 2. https://doi.org/10.1186/s13036-016-0045-0

DeSimone, A. M., Cohen, J., Lek, M., & Lek, A. (2020). Cellular and animal models for facioscapulohumeral muscular dystrophy. *Disease Models & Mechanisms*, *13*(10), dmm046904. https://doi.org/10.1242/dmm.046904

Dinca, V., Patrascioiu, A., Fernández-Pradas, J. M., Morenza, J. L., & Serra, P. (2012). Influence of solution properties in the laser forward transfer of liquids. *Applied Surface Science*, *258*(23), 9379-9384. https://doi.org/10.1016/j.apsusc.2012.02.007

Dinca, V., Sima, L. E., Rusen, L., Bonciu, A., Lippert, T., Dinescu, M., & Farsari, M. (2016). Bio-Interfaces Engineering Using Laser-Based Methods for Controlled Regulation of Mesenchymal Stem Cell Response In Vitro. In F. K. Parveen (Éd.), *Recent Advances in Biopolymers*. InTech. https://doi.org/10.5772/61516

Dipalo, M., McGuire, A. F., Lou, H.-Y., Caprettini, V., Melle, G., Bruno, G., Lubrano, C., Matino, L., Li, X., De Angelis, F., Cui, B., & Santoro, F. (2018). Cells Adhering to 3D Vertical Nanostructures : Cell Membrane Reshaping without Stable Internalization. *Nano Letters*, *18*(9), 6100-6105. https://doi.org/10.1021/acs.nanolett.8b03163

Eaton, S. M., De Marco, C., Martinez-Vazquez, R., Ramponi, R., Turri, S., Cerullo, G., & Osellame, R. (2012). Femtosecond laser microstructuring for polymeric lab-on-chips. *Journal of Biophotonics*, *5*(8-9), 687-702. https://doi.org/10.1002/jbio.201200048

Eugenis, I., Wu, D., & Rando, T. A. (2021). Cells, scaffolds, and bioactive factors : Engineering strategies for improving regeneration following volumetric muscle loss. *Biomaterials*, *278*, 121173. https://doi.org/10.1016/j.biomaterials.2021.121173

Fadeeva, E., Deiwick, A., Chichkov, B., & Schlie-Wolter, S. (2014). Impact of laser-structured biomaterial interfaces on guided cell responses. *Interface Focus*, *4*(1), 20130048. https://doi.org/10.1098/rsfs.2013.0048

Fan, J., Abedi Dorcheh, K., Vaziri, A., Kazemi-Aghdam, F., Rafieyan, S., Sohrabinejad, M., Ghorbani, M., Rastegar Adib, F., Ghasemi, Z., Klavins, K., & Jahed, V. (2022). A Review of Recent Advances in Natural Polymer-Based Scaffolds for Musculoskeletal Tissue Engineering. *Polymers*, *14*. https://doi.org/10.3390/polym14102097

Fardel, R., Nagel, M., Nüesch, F., Lippert, T., & Wokaun, A. (2010). Laser-Induced Forward Transfer of Organic LED Building Blocks Studied by Time-Resolved Shadowgraphy. *The Journal of Physical Chemistry C*, *114*(12), 5617-5636. https://doi.org/10.1021/jp907387q

Farshidfar, N., Iravani, S., & Varma, R. S. (2023). Alginate-Based Biomaterials in Tissue Engineering and Regenerative Medicine. *Marine Drugs*, *21*(3), Article 3. https://doi.org/10.3390/md21030189

Fernández-Pradas, J. M., Florian, C., Caballero-Lucas, F., Sopeña, P., Morenza, J. L., & Serra, P. (2017). Laser-induced forward transfer : Propelling liquids with light. *Applied Surface Science*, *418*, 559-564. https://doi.org/10.1016/j.apsusc.2016.10.197

Fernández-Pradas, J. M., & Serra, P. (2020). Laser-Induced Forward Transfer : A Method for Printing Functional Inks. *Crystals*, *10*(8), Article 8. https://doi.org/10.3390/cryst10080651

Ferraris, S., Spriano, S., Scalia, A. C., Cochis, A., Rimondini, L., Cruz-Maya, I., Guarino, V., Varesano, A., & Vineis, C. (2020). Topographical and Biomechanical Guidance of Electrospun Fibers for Biomedical Applications. *Polymers*, *12*(12), Article 12. https://doi.org/10.3390/polym12122896

Fischer, J. P., Elliott, R. M., Kozin, S. H., & Levin, L. S. (2013). Free function muscle transfers for upper extremity reconstruction : A review of indications, techniques, and outcomes. *The Journal of Hand Surgery*, *38*(12), 2485-2490. https://doi.org/10.1016/j.jhsa.2013.03.041

Flégeau, K., Puiggali-Jou, A., & Zenobi-Wong, M. (2022). Cartilage tissue engineering by extrusion bioprinting utilizing porous hyaluronic acid microgel bioinks. *Biofabrication*, *14*(3). https://doi.org/10.1088/1758-5090/ac6b58

Florian, C., & Serra, P. (2023). Printing via Laser-Induced Forward Transfer and the Future of Digital Manufacturing. *Materials*, *16*(2), Article 2. https://doi.org/10.3390/ma16020698

Forcina, L., Miano, C., Pelosi, L., & Musarò, A. (2019). An Overview about the Biology of Skeletal Muscle Satellite Cells. *Current Genomics*, *20*(1), 24-37. https://doi.org/10.2174/1389202920666190116094736

Fornetti, E., Paolis, F. D., Fuoco, C., Bernardini, S., Giannitelli, S. M., Rainer, A., Seliktar, D., Magdinier, F., Baldi, J., Biagini, R., Cannata, S., Testa, S., & Gargioli, C. (2023). A novel extrusion-based 3D bioprinting system for skeletal muscle tissue engineering. *Biofabrication*, *15*(2), 025009. https://doi.org/10.1088/1758-5090/acb573

Foyt, D., Norman, M., Yu, T., & Gentleman, E. (2018). Exploiting Advanced Hydrogel Technologies to Address Key Challenges in Regenerative Medicine. *Advanced healthcare materials*, *7*. https://doi.org/10.1002/adhm.201700939

Furth, M. E., & Atala, A. (2014). Chapter 6 - Tissue Engineering : Future Perspectives. In R. Lanza, R. Langer, & J. Vacanti (Éds.), *Principles of Tissue Engineering (Fourth Edition)* (p. 83-123). Academic Press. https://doi.org/10.1016/B978-0-12-398358-9.00006-9

Gaebel, R., Ma, N., Liu, J., Guan, J., Koch, L., Klopsch, C., Gruene, M., Toelk, A., Wang, W., Mark, P., Wang, F., Chichkov, B., Li, W., & Steinhoff, G. (2011). Patterning human stem cells and endothelial cells with laser printing for cardiac regeneration. *Biomaterials*, *32*(35), 9218-9230. https://doi.org/10.1016/j.biomaterials.2011.08.071

Gao, H., Xiao, J., Wei, Y., Wang, H., Wan, H., & Liu, S. (2021). Regulation of Myogenic Differentiation by Topologically Microgrooved Surfaces for Skeletal Muscle Tissue Engineering. *ACS Omega*, *6*(32), 20931-20940. https://doi.org/10.1021/acsomega.1c02347

Ge, J., Liu, K., Niu, W., Chen, M., Wang, M., Xue, Y., Gao, C., Ma, P. X., & Lei, B. (2018). Gold and gold-silver alloy nanoparticles enhance the myogenic differentiation of myoblasts through p38 MAPK signaling pathway and promote *in vivo* skeletal muscle regeneration. *Biomaterials*, *175*, 19-29. https://doi.org/10.1016/j.biomaterials.2018.05.027

George Kolios, Kolios, G., Yuben Moodley, & Moodley, Y. (2013). Introduction to stem cells and regenerative medicine. *Respiration*, *85*(1), 3-10. https://doi.org/10.1159/000345615

Gillispie, G., Prim, P., Copus, J., Fisher, J., Mikos, A. G., Yoo, J. J., Atala, A., & Lee, S. J. (2020). Assessment Methodologies for Extrusion-Based Bioink Printability. *Biofabrication*, *12*(2), 022003. https://doi.org/10.1088/1758-5090/ab6f0d

Gokarn, Y. R., McLean, M., & Laue, T. M. (2012). Effect of PEGylation on Protein Hydrodynamics. *Molecular Pharmaceutics*, *9*(4), 762-773. https://doi.org/10.1021/mp200470c

Goyenvalle, A., Seto, J. T., Davies, K. E., & Chamberlain, J. (2011). Therapeutic approaches to muscular dystrophy. *Human Molecular Genetics*, *20*(R1), R69-R78. https://doi.org/10.1093/hmg/ddr105

Greising, S. M., Corona, B. T., McGann, C., Frankum, J. K., & Warren, G. L. (2019). Therapeutic Approaches for Volumetric Muscle Loss Injury : A Systematic Review and Meta-Analysis. *Tissue Engineering. Part B, Reviews*, *25*(6), 510-525. https://doi.org/10.1089/ten.TEB.2019.0207

Greising, S. M., Warren, G. L., Southern, W. M., Nichenko, A. S., Qualls, A. E., Corona, B. T., & Call, J. A. (2018). Early rehabilitation for volumetric muscle loss injury augments endogenous regenerative aspects of muscle strength and oxidative capacity. *BMC Musculoskeletal Disorders*, *19*, 173. https://doi.org/10.1186/s12891-018-2095-6

Grigoryan, B., Sazer, D. W., Avila, A., Albritton, J. L., Padhye, A., Ta, A. H., Greenfield, P. T., Gibbons, D. L., & Miller, J. S. (2021). Development, characterization, and applications of multi-material stereolithography bioprinting. *Scientific Reports*, *11*(1), 3171. https://doi.org/10.1038/s41598-021-82102-w

Grogan, B. F., Hsu, J. R., & Consortium, S. T. R. (2011). Volumetric Muscle Loss. *JAAOS - Journal of the American Academy of Orthopaedic Surgeons*, *19*, S35.

Grossi, A., Yadav, K., & Lawson, M. A. (2007). Mechanical stimulation increases proliferation, differentiation and protein expression in culture : Stimulation effects are substrate dependent. *Journal of Biomechanics*, *40*(15), 3354-3362. https://doi.org/10.1016/j.jbiomech.2007.05.007

Gruene, M., Deiwick, A., Koch, L., Schlie, S., Unger, C., Hofmann, N., Bernemann, I., Glasmacher, B., & Chichkov, B. (2011). Laser Printing of Stem Cells for Biofabrication of Scaffold-Free Autologous Grafts. *Tissue Engineering Part C: Methods*, *17*(1), 79-87. https://doi.org/10.1089/ten.tec.2010.0359

Gruene, M., Pflaum, M., Deiwick, A., Koch, L., Schlie, S., Unger, C., Wilhelmi, M., Haverich, A., & Chichkov, B. N. (2011). Adipogenic differentiation of laser-printed 3D tissue grafts consisting of

human adipose-derived stem cells. *Biofabrication*, *3*(1), 015005. https://doi.org/10.1088/1758-5082/3/1/015005

Gruene, M., Pflaum, M., Hess, C., Diamantouros, S., Schlie, S., Deiwick, A., Koch, L., Wilhelmi, M., Jockenhoevel, S., Haverich, A., & Chichkov, B. (2011). Laser Printing of Three-Dimensional Multicellular Arrays for Studies of Cell–Cell and Cell–Environment Interactions. *Tissue Engineering Part C: Methods*, *17*(10), 973-982. https://doi.org/10.1089/ten.tec.2011.0185

Gudapati, H., Yan, J., Huang, Y., & Chrisey, D. B. (2014). Alginate gelation-induced cell death during laser-assisted cell printing. *Biofabrication*, *6*(3), 035022. https://doi.org/10.1088/1758-5082/6/3/035022

Guillemot, F., Souquet, A., Catros, S., Guillotin, B., Lopez, J., Faucon, M., Pippenger, B., Bareille, R., Rémy, M., Bellance, S., Chabassier, P., Fricain, J. C., & Amédée, J. (2010). High-throughput laser printing of cells and biomaterials for tissue engineering. *Acta Biomaterialia*, *6*(7), 2494-2500. https://doi.org/10.1016/j.actbio.2009.09.029

Guillotin, B., & Guillemot, F. (2011). Cell patterning technologies for organotypic tissue fabrication. *Trends in Biotechnology*, *29*(4), Article 4. https://doi.org/10.1016/j.tibtech.2010.12.008

Guillotin, B., Souquet, A., Catros, S., Duocastella, M., Pippenger, B., Bellance, S., Bareille, R., Rémy, M., Bordenave, L., Amédée, J., & Guillemot, F. (2010). Laser assisted bioprinting of engineered tissue with high cell density and microscale organization. *Biomaterials*, *31*(28), Article 28. https://doi.org/10.1016/j.biomaterials.2010.05.055

Hakobyan, D., Médina, C., Dusserre, N., Stachowicz, M.-L., Handschin, C., Fricain, J.-C., Guillermet-Guibert, J., & Oliveira, H. (2020). Laser-assisted 3D bioprinting of exocrine pancreas spheroid models for cancer initiation study. *Biofabrication*, *12*(3), 035001. https://doi.org/10.1088/1758-5090/ab7cb8

Han, S., Cruz, S. H., Park, S., & Shin, S. R. (2023). Nano-biomaterials and advanced fabrication techniques for engineering skeletal muscle tissue constructs in regenerative medicine. *Nano Convergence*, *10*(1), 48. https://doi.org/10.1186/s40580-023-00398-y

Heller, K. N., Mendell, J. T., Mendell, J. R., & Rodino-Klapac, L. R. (2017). MicroRNA-29 overexpression by adeno-associated virus suppresses fibrosis and restores muscle function in combination with micro-dystrophin. *JCI Insight*, *2*(9). https://doi.org/10.1172/jci.insight.93309

Huang, C.-F., Colley, M., Lu, L.-S., Chang, C.-Y., Peng, P.-W., & Yang, T.-S. (2019). Performance characterization of continuous-wave laser-induced forward transfer of liquid bioink. *Applied Physics Express*, *12*. https://doi.org/10.7567/1882-0786/ab4caf

Huang, D., Yue, F., Qiu, J., Deng, M., & Kuang, S. (2020). Polymeric nanoparticles functionalized with muscle-homing peptides for targeted delivery of phosphatase and tensin homolog inhibitor to skeletal muscle. *Acta Biomaterialia*, *118*, 196-206. https://doi.org/10.1016/j.actbio.2020.10.009

Iberite, F., Gruppioni, E., & Ricotti, L. (2022). Skeletal muscle differentiation of human iPSCs meets bioengineering strategies : Perspectives and challenges. *Npj Regenerative Medicine*, *7*(1), 23. https://doi.org/10.1038/s41536-022-00216-9

Jang, M., Scheffold, J., Røst, L. M., Cheon, H., & Bruheim, P. (2022). Serum-free cultures of C2C12 cells show different muscle phenotypes which can be estimated by metabolic profiling. *Scientific Reports*, *12*(1), 827. https://doi.org/10.1038/s41598-022-04804-z

Järvinen, T. A. H., Järvinen, T. L. N., Kääriäinen, M., Kalimo, H., & Järvinen, M. (2005). Muscle Injuries : Biology and Treatment. *The American Journal of Sports Medicine*, *33*(5), 745-764. https://doi.org/10.1177/0363546505274714

Järvinen, T. A. H., Kääriäinen, M., Äärimaa, V., Järvinen, M., & Kalimo, H. (2008). Skeletal Muscle Repair After Exercise-Induced Injury. In S. Schiaffino & T. Partridge (Éds.), *Skeletal Muscle Repair and Regeneration* (p. 217-242). Springer Netherlands. https://doi.org/10.1007/978-1-4020-6768-6_11

Jeong, G.-J., Castels, H., Kang, I., Aliya, B., & Jang, Y. C. (2022). Nanomaterial for Skeletal Muscle Regeneration. *Tissue Engineering and Regenerative Medicine*, *19*(2), 253-261. https://doi.org/10.1007/s13770-022-00446-4

Jin, Y., Li, S., Yu, Q., Chen, T., & Liu, D. (2023). Application of stem cells in regeneration medicine. *MedComm*, *4*(4), e291. https://doi.org/10.1002/mco2.291

Jl, C., Sc, S., Da, B., J, S., Mj, M., & Db, C. (2016). Isolated node engineering of neuronal systems using laser direct write. *Biofabrication*, *8*(1). https://doi.org/10.1088/1758-5090/8/1/015013

Joe, A. W. B., Yi, L., Natarajan, A., Le Grand, F., So, L., Wang, J., Rudnicki, M. A., & Rossi, F. M. V. (2010). Muscle injury activates resident fibro/adipogenic progenitors that facilitate myogenesis. *Nature Cell Biology*, *12*(2), 153-163. https://doi.org/10.1038/ncb2015

Kačarević, Ž., Rider, P., Alkildani, S., Retnasingh, S., Smeets, R., Jung, O., Ivanišević, Z., & Barbeck, M. (2018). An Introduction to 3D Bioprinting : Possibilities, Challenges and Future Aspects. *Materials*, *11*(11), 2199. https://doi.org/10.3390/ma11112199

Karpati, G., & Molnar, M. J. (2008). Muscle Fibre Regeneration in Human Skeletal Muscle Diseases. In S. Schiaffino & T. Partridge (Éds.), *Skeletal Muscle Repair and Regeneration* (p. 199-216). Springer Netherlands. https://doi.org/10.1007/978-1-4020-6768-6_10

Kato, Y., Matsumoto, T., & Kino-oka, M. (2019). Effect of liquid flow by pipetting during medium change on deformation of hiPSC aggregates. *Regenerative Therapy*, *12*, 20-26. https://doi.org/10.1016/j.reth.2019.03.004

Kattamis, N. T., Purnick, P. E., Weiss, R., & Arnold, C. B. (2007). Thick film laser induced forward transfer for deposition of thermally and mechanically sensitive materials. *Applied Physics Letters*, *91*(17), Article 17. https://doi.org/10.1063/1.2799877

Khademhosseini, A., Ashammakhi, N., Karp, J. M., Gerecht, S., Ferreira, L., Annabi, N., Darabi, M. A., Sirabella, D., Vunjak-Novakovic, G., & Langer, R. (2020). Chapter 27—Embryonic stem cells as a cell source for tissue engineering. In R. Lanza, R. Langer, J. P. Vacanti, & A. Atala (Éds.), *Principles of Tissue Engineering (Fifth Edition)* (p. 467-490). Academic Press. https://doi.org/10.1016/B978-0-12-818422-6.00027-7

Khalil, S., & Sun, W. (2009). Bioprinting endothelial cells with alginate for 3D tissue constructs. *Journal of Biomechanical Engineering*, *131*(11), 111002. https://doi.org/10.1115/1.3128729

Khodabukus, A., Prabhu, N., Wang, J., & Bursac, N. (2018). In Vitro Tissue-Engineered Skeletal Muscle Models for Studying Muscle Physiology and Disease. *Advanced healthcare materials*, *7*(15), e1701498. https://doi.org/10.1002/adhm.201701498

Kim, C. (2014). Disease modeling and cell based therapy with iPSC : Future therapeutic option with fast and safe application. *Blood research*, *49*(1), 7-14. https://doi.org/10.5045/br.2014.49.1.7

Kim, K. H., Qiu, J., & Kuang, S. (2020). Isolation, Culture, and Differentiation of Primary Myoblasts Derived from Muscle Satellite Cells. *Bio-protocol*, *10*(14), e3686. https://doi.org/10.21769/BioProtoc.3686

Kiran, S., Dwivedi, P., Kumar, V., Price, R. L., & Singh, U. P. (2021). Immunomodulation and Biomaterials : Key Players to Repair Volumetric Muscle Loss. *Cells*, *10*(8), 2016. https://doi.org/10.3390/cells10082016

Koch, L., Brandt, O., Deiwick, A., & Chichkov, B. (2017). Laser-assisted bioprinting at different wavelengths and pulse durations with a metal dynamic release layer : A parametric study. *International Journal of Bioprinting*, *3*(1), 001. https://doi.org/10.18063/IJB.2017.01.001

Koch, L., Deiwick, A., & Chichkov, B. (2021). Capillary-like Formations of Endothelial Cells in Defined Patterns Generated by Laser Bioprinting. *Micromachines*, *12*(12), 1538. https://doi.org/10.3390/mi12121538

Koch, L., Deiwick, A., Franke, A., Schwanke, K., Haverich, A., Zweigerdt, R., & Chichkov, B. (2018). Laser bioprinting of human induced pluripotent stem cells—The effect of printing and biomaterials on cell survival, pluripotency, and differentiation. *Biofabrication*, *10*(3), 035005. https://doi.org/10.1088/1758-5090/aab981

Koch, L., Deiwick, A., Schlie, S., Michael, S., Gruene, M., Coger, V., Zychlinski, D., Schambach, A., Reimers, K., Vogt, P. M., & Chichkov, B. (2012). Skin tissue generation by laser cell printing. *Biotechnology and Bioengineering*, *109*(7), 1855-1863. https://doi.org/10.1002/bit.24455

Koch, L., Kuhn, S., Sorg, H., Gruene, M., Schlie, S., Gaebel, R., Polchow, B., Reimers, K., Stoelting, S., Ma, N., Vogt, P. M., Steinhoff, G., & Chichkov, B. (2010). Laser Printing of Skin Cells and Human Stem Cells. *Tissue Engineering Part C: Methods*, *16*(5), 847-854. https://doi.org/10.1089/ten.tec.2009.0397

Kozan, N. G., Joshi, M., Sicherer, S. T., & Grasman, J. M. (2023). Porous biomaterial scaffolds for skeletal muscle tissue engineering. *Frontiers in Bioengineering and Biotechnology*, *11*, 1245897. https://doi.org/10.3389/fbioe.2023.1245897

Kumar, H., & Kim, K. (2020). Stereolithography 3D Bioprinting. *Methods in Molecular Biology (Clifton, N.J.)*, *2140*, 93-108. https://doi.org/10.1007/978-1-0716-0520-2_6

Kwee, B. J., & Mooney, D. J. (2017). Biomaterials for Skeletal Muscle Tissue Engineering. *Current opinion in biotechnology*, *47*, 16-22. https://doi.org/10.1016/j.copbio.2017.05.003

LaPelusa, A., Asuncion, R. M. D., & Kentris, M. (2024). Muscular Dystrophy. In *StatPearls*. StatPearls Publishing. http://www.ncbi.nlm.nih.gov/books/NBK560582/

Leclech, C., & Barakat, A. I. (2021). Is there a universal mechanism of cell alignment in response to substrate topography? *Cytoskeleton*, *78*(6), 284-292. https://doi.org/10.1002/cm.21661

Leite, P. E. C., Pereira, M. R., do Nascimento Santos, C. A., Campos, A. P. C., Esteves, T. M., & Granjeiro, J. M. (2015). Gold nanoparticles do not induce myotube cytotoxicity but increase the susceptibility to cell death. *Toxicology in Vitro: An International Journal Published in Association with BIBRA*, *29*(5), 819-827. https://doi.org/10.1016/j.tiv.2015.02.010

Leslie Caron, Caron, L., Devaki Kher, Devaki Kher, Kher, D., Kian Leong Lee, Lee, K. L., Robert McKernan, McKernan, R., Biljana Dumevska, Dumevska, B., Alejandro Hidalgo, Hidalgo, A., Jia Li, Jia Li, Jia Li, Li, J., Henry Yang, Yang, H., … Uli Schmidt. (2016). A Human Pluripotent Stem Cell Model of Facioscapulohumeral Muscular Dystrophy-Affected Skeletal Muscles. *Stem Cells Translational Medicine*, *5*(9), 1145-1161. https://doi.org/10.5966/sctm.2015-0224

Li, W., Wang, M., Ma, H., Chapa-Villarreal, F. A., Lobo, A. O., & Zhang, Y. S. (2023). Stereolithography apparatus and digital light processing-based 3D bioprinting for tissue fabrication. *iScience*, *26*(2), 106039. https://doi.org/10.1016/j.isci.2023.106039

Liew, W. L. A., & Zhang, Y. (2018). Laser-based fabrication of 3D hydrogel constructs using bessel beams. *Bioprinting*, *9*, 44-51. https://doi.org/10.1016/j.bprint.2018.02.004

Lim, K. R. Q., Nguyen, Q., & Yokota, T. (2020). DUX4 Signalling in the Pathogenesis of Facioscapulohumeral Muscular Dystrophy. *International Journal of Molecular Sciences*, *21*(3), 729. https://doi.org/10.3390/ijms21030729

Liu, C., Oikonomopoulos, A., Sayed, N., & Wu, J. C. (2018). Modeling human diseases with induced pluripotent stem cells : From 2D to 3D and beyond. *Development (Cambridge, England)*, *145*(5), dev156166. https://doi.org/10.1242/dev.156166

Liu, W., & Chakkalakal, J. V. (2018). Chapter Four—The Composition, Development, and Regeneration of Neuromuscular Junctions. In D. Sassoon (Éd.), *Current Topics in Developmental Biology* (Vol. 126, p. 99-124). Academic Press. https://doi.org/10.1016/bs.ctdb.2017.08.005

Lovering, R. M., Porter, N. C., & Bloch, R. J. (2005). The Muscular Dystrophies : From Genes to Therapies. *Physical therapy*, *85*(12), 1372-1388.

Lyra-Leite, D. M., Gutiérrez-Gutiérrez, Ó., Wang, M., Zhou, Y., Cyganek, L., & Burridge, P. W. (2022). A review of protocols for human iPSC culture, cardiac differentiation, subtype-specification, maturation, and direct reprogramming. *STAR Protocols*, *3*(3), 101560. https://doi.org/10.1016/j.xpro.2022.101560

Machida, S., Spangenburg, E. E., & Booth, F. W. (2004). Primary rat muscle progenitor cells have decreased proliferation and myotube formation during passages. *Cell Proliferation*, *37*(4), 267-277. https://doi.org/10.1111/j.1365-2184.2004.00311.x

Madrid, M., Lakshmipathy, U., Zhang, X., Bharti, K., Wall, D. M., Sato, Y., Muschler, G., Ting, A., Smith, N., Deguchi, S., Kawamata, S., Moore, J. C., Makovoz, B., Sullivan, S., Falco, V., & Al-Riyami, A. Z. (2024). Considerations for the development of iPSC-derived cell therapies : A review of key challenges by the JSRM-ISCT iPSC Committee. *Cytotherapy*, *0*(0). https://doi.org/10.1016/j.jcyt.2024.05.022

Maffioletti, S. M., Sarcar, S., Henderson, A. B. H., Mannhardt, I., Pinton, L., Moyle, L. A., Steele-Stallard, H., Cappellari, O., Wells, K. E., Ferrari, G., Mitchell, J. S., Tyzack, G. E., Kotiadis, V. N., Khedr, M., Ragazzi, M., Wang, W., Duchen, M. R., Patani, R., Zammit, P. S., … Tedesco, F. S. (2018). Three-Dimensional Human iPSC-Derived Artificial Skeletal Muscles Model Muscular Dystrophies and Enable Multilineage Tissue Engineering. *Cell Reports*, *23*(3), 899-908. https://doi.org/10.1016/j.celrep.2018.03.091

Mahdy, M. A. A. (2019). Skeletal muscle fibrosis : An overview. *Cell and Tissue Research*, *375*(3), 575-588. https://doi.org/10.1007/s00441-018-2955-2

Mak, I. W., Evaniew, N., & Ghert, M. (2014). Lost in translation : Animal models and clinical trials in cancer treatment. *American Journal of Translational Research*, *6*(2), 114-118.

Malekpour, A., & Chen, X. (2022). Printability and Cell Viability in Extrusion-Based Bioprinting from Experimental, Computational, and Machine Learning Views. *Journal of Functional Biomaterials*, *13*(2), 40. https://doi.org/10.3390/jfb13020040

Mamchaoui, K., Trollet, C., Bigot, A., Negroni, E., Chaouch, S., Wolff, A., Kandalla, P. K., Marie, S., Di Santo, J., St Guily, J. L., Muntoni, F., Kim, J., Philippi, S., Spuler, S., Levy, N., Blumen, S. C., Voit, T., Wright, W. E., Aamiri, A., … Mouly, V. (2011). Immortalized pathological human myoblasts : Towards a universal tool for the study of neuromuscular disorders. *Skeletal Muscle*, *1*(1), 34. https://doi.org/10.1186/2044-5040-1-34

Manita, P. G., Garcia-Orue, I., Santos-Vizcaino, E., Hernandez, R. M., & Igartua, M. (2021). 3D Bioprinting of Functional Skin Substitutes : From Current Achievements to Future Goals. *Pharmaceuticals*, *14*(4), 362. https://doi.org/10.3390/ph14040362

Mann, C. J., Perdiguero, E., Kharraz, Y., Aguilar, S., Pessina, P., Serrano, A. L., & Muñoz-Cánoves, P. (2011). Aberrant repair and fibrosis development in skeletal muscle. *Skeletal Muscle*, *1*(1), 21. https://doi.org/10.1186/2044-5040-1-21

Mézel, C., Souquet, A., Hallo, L., & Guillemot, F. (2010). Bioprinting by laser-induced forward transfer for tissue engineering applications : Jet formation modeling. *Biofabrication*, *2*(1), Article 1. https://doi.org/10.1088/1758-5082/2/1/014103

Michael, S., Sorg, H., Peck, C.-T., Koch, L., Deiwick, A., Chichkov, B., Vogt, P. M., & Reimers, K. (2013). Tissue Engineered Skin Substitutes Created by Laser-Assisted Bioprinting Form Skin-Like Structures in the Dorsal Skin Fold Chamber in Mice. *PLOS ONE*, *8*(3), e57741. https://doi.org/10.1371/journal.pone.0057741

Morales, M., Munoz-Martin, D., Marquez, A., Lauzurica, S., & Molpeceres, C. (2018). Laser-Induced Forward Transfer Techniques and Applications. In *Advances in Laser Materials Processing* (p. 339-379). Elsevier. https://doi.org/10.1016/B978-0-08-101252-9.00013-3

Motohashi, N., Shimizu-Motohashi, Y., Roberts, T. C., & Aoki, Y. (2019). Potential Therapies Using Myogenic Stem Cells Combined with Bio-Engineering Approaches for Treatment of Muscular Dystrophies. *Cells*, *8*(9), 1066. https://doi.org/10.3390/cells8091066

Munoz-Martin, D., Brasz, C. F., Chen, Y., Morales, M., Arnold, C. B., & Molpeceres, C. (2016). Laser-induced forward transfer of high-viscosity silver pastes. *Applied Surface Science*, *366*, 389-396. https://doi.org/10.1016/j.apsusc.2016.01.029

Murru, C., Duvert, L., Magdinier, F., Casanova, A., Alloncle, A.-P., Testa, S., & Al-Kattan, A. (2024). Assessment of laser-synthesized Si nanoparticle effects on myoblast motility, proliferation and differentiation : Towards potential tissue engineering applications. *Nanoscale Advances*, *6*(8), 2104-2112. https://doi.org/10.1039/D3NA01020A

Nagashima, T., Hadiwidjaja, S., Ohsumi, S., Murata, A., Hisada, T., Kato, R., Okada, Y., Honda, H., & Shimizu, K. (2020). In Vitro Model of Human Skeletal Muscle Tissues with Contractility Fabricated by Immortalized Human Myogenic Cells. *Advanced Biosystems*, *4*(11), 2000121. https://doi.org/10.1002/adbi.202000121

Nagel, M., & Lippert, T. (s. d.). Nanomaterials : Processing and Characterization with Lasers. *2012*.

Narrog, F., Lensing, R., Piotrowski, T., Nottrodt, N., Wehner, M., Nießing, B., König, N., Gillner, A., & Schmitt, R. H. (2023). LIFTOSCOPE : Development of an automated AI-based module for time-effective and contactless analysis and isolation of cells in microtiter plates. *Journal of Biological Engineering*, *17*(1), 10. https://doi.org/10.1186/s13036-023-00329-9

Naso, M. F., Tomkowicz, B., Perry, W. L., & Strohl, W. R. (2017). Adeno-Associated Virus (AAV) as a Vector for Gene Therapy. *Biodrugs*, *31*(4), 317-334. https://doi.org/10.1007/s40259-017-0234-5

National Research Council, C. on the B. and B. A. of S. C. R. (avec Commission on Life Sciences, National Research Council, Board on Life Sciences, Board on Neuroscience and Behavioral Health, Division on Earth and Life Studies, & Institute of Medicine). (2002). *Stem Cells and the Future of Regenerative Medicine*. National Academies Press.

Nayak, N. C., Lam, Y. C., Yue, C. Y., & Sinha, A. T. (2008). CO2-laser micromachining of PMMA : The effect of polymer molecular weight. *Journal of Micromechanics and Microengineering*, *18*(9), 095020. https://doi.org/10.1088/0960-1317/18/9/095020

Nicholson, M. W., Ting, C.-Y., Chan, D. Z. H., Cheng, Y.-C., Lee, Y.-C., Hsu, C.-C., Huang, C.-Y., & Hsieh, P. C. H. (2022). Utility of iPSC-Derived Cells for Disease Modeling, Drug Development, and Cell Therapy. *Cells*, *11*(11), Article 11. https://doi.org/10.3390/cells11111853

Obed, D., Dastagir, N., Liebsch, C., Bingoel, A. S., Strauss, S., Vogt, P. M., & Dastagir, K. (2022). In Vitro Differentiation of Myoblast Cell Lines on Spider Silk Scaffolds in a Rotating Bioreactor for Vascular Tissue Engineering. *Journal of Personalized Medicine*, *12*(12), Article 12. https://doi.org/10.3390/jpm12121986

Of, B., Gw, P., C, W., & Rr, F. (1994). Facioscapulohumeral muscular dystrophy in early childhood. *Archives of Neurology*, *51*(4). https://doi.org/10.1001/archneur.1994.00540160085011

Of, B., Gw, P., Cj, R., R, B., Ja, de L., & Jj, G. (1991). Hearing loss in facioscapulohumeral muscular dystrophy. *Neurology*, *41*(12). https://doi.org/10.1212/wnl.41.12.1878

Ohara, P. T., & Buck, R. C. (1979). Contact guidance in vitro. A light, transmission, and scanning electron microscopic study. *Experimental Cell Research*, *121*(2), 235-249. https://doi.org/10.1016/0014-4827(79)90002-8

Okano, T., Satoh, S., Oka, T., & Matsuda, T. (1997). Tissue engineering of skeletal muscle. Highly dense, highly oriented hybrid muscular tissues biomimicking native tissues. *ASAIO Journal (American Society for Artificial Internal Organs: 1992)*, *43*(5), M749-753.

Olson, J. L., Atala, A., & Yoo, J. J. (2011). Tissue Engineering : Current Strategies and Future Directions. *Chonnam Medical Journal*, *47*(1), 1-13. https://doi.org/10.4068/cmj.2011.47.1.1

Ostrovidov, S., Hosseini, V., Ahadian, S., Fujie, T., Parthiban, S. P., Ramalingam, M., Bae, H., Kaji, H., & Khademhosseini, A. (2014). Skeletal Muscle Tissue Engineering : Methods to Form Skeletal Myotubes and Their Applications. *Tissue Engineering. Part B, Reviews*, *20*(5), 403-436. https://doi.org/10.1089/ten.teb.2013.0534

Ovsianikov, A., Gruene, M., Pflaum, M., Koch, L., Maiorana, F., Wilhelmi, M., Haverich, A., & Chichkov, B. (2010). Laser printing of cells into 3D scaffolds. *Biofabrication*, *2*(1), 014104. https://doi.org/10.1088/1758-5082/2/1/014104

Pagès, E., Rémy, M., Kériquel, V., Correa, M. M., Guillotin, B., & Guillemot, F. (2015). Creation of Highly Defined Mesenchymal Stem Cell Patterns in Three Dimensions by Laser-Assisted Bioprinting. *Journal of Nanotechnology in Engineering and Medicine*, *6*(021006). https://doi.org/10.1115/1.4031217

Papazoglou, S., & Zergioti, I. (2017). Laser Induced Forward Transfer (LIFT) of nano-micro patterns for sensor applications. *Microelectronic Engineering*, *182*, 25-34. https://doi.org/10.1016/j.mee.2017.08.003

Park, J., Choi, J. H., Kim, S., Jang, I., Jeong, S., & Lee, J. Y. (2019). Micropatterned conductive hydrogels as multifunctional muscle-mimicking biomaterials : Graphene-incorporated hydrogels directly patterned with femtosecond laser ablation. *Acta Biomaterialia*, *97*, 141-153. https://doi.org/10.1016/j.actbio.2019.07.044

Patrascioiu, A., Fernández-Pradas, J. M., Palla-Papavlu, A., Morenza, J. L., & Serra, P. (2014). Laser-generated liquid microjets : Correlation between bubble dynamics and liquid ejection. *Microfluidics and Nanofluidics*, *16*(1-2), 55-63. https://doi.org/10.1007/s10404-013-1218-5

Philippou, A., & Barton, E. R. (2014). Optimizing IGF-I for skeletal muscle therapeutics. *Growth Hormone & IGF Research: Official Journal of the Growth Hormone Research Society and the International IGF Research Society*, *24*(5), 157-163. https://doi.org/10.1016/j.ghir.2014.06.003

Piqué, A. (2014). Laser-Induced Forward Transfer of Functional Materials : Advances and Future Directions. *Journal of Laser Micro/Nanoengineering*, *9*(3), 192-197. https://doi.org/10.2961/jlmn.2014.03.0002

Piqué, A., & Charipar, K. M. (2021). Laser-Induced Forward Transfer Applications in Micro-engineering. In K. Sugioka (Éd.), *Handbook of Laser Micro- and Nano-Engineering* (p. 1325-1359). Springer International Publishing. https://doi.org/10.1007/978-3-030-63647-0_26

Piqué, A., Chrisey, D. B., Auyeung, R. C. Y., Fitz-Gerald, J., Wu, H. D., McGill, R. A., Lakeou, S., Wu, P. K., Nguyen, V., & Duignan, M. (1999). A novel laser transfer process for direct writing of electronic and sensor materials. *Applied Physics A*, *69*(1), S279-S284. https://doi.org/10.1007/s003390051400

Pirlo, R. K., Wu, P., Liu, J., & Ringeisen, B. (2012). PLGA/hydrogel biopapers as a stackable substrate for printing HUVEC networks via BioLP™. *Biotechnology and Bioengineering*, *109*(1), 262-273. https://doi.org/10.1002/bit.23295

Powell, C. A., Smiley, B. L., Mills, J., & Vandenburgh, H. H. (2002). Mechanical stimulation improves tissue-engineered human skeletal muscle. *American Journal of Physiology-Cell Physiology*, *283*(5), C1557-C1565. https://doi.org/10.1152/ajpcell.00595.2001

Rangarajan, S., Madden, L., & Bursac, N. (2014). Use of flow, electrical, and mechanical stimulation to promote engineering of striated muscles. *Annals of biomedical engineering*, *42*(7), 1391-1405. https://doi.org/10.1007/s10439-013-0966-4

Rao, L., Qian, Y., Khodabukus, A., Ribar, T., & Bursac, N. (2018). Engineering human pluripotent stem cells into a functional skeletal muscle tissue. *Nature Communications*, *9*(1), 126. https://doi.org/10.1038/s41467-017-02636-4

Ravi-Kumar, S., Lies, B., Lyu, H., & Qin, H. (2019). Laser Ablation of Polymers : A Review. *Procedia Manufacturing*, *34*, 316-327. https://doi.org/10.1016/j.promfg.2019.06.155

Ray, A., Lee, O., Win, Z., Edwards, R. M., Alford, P. W., Kim, D.-H., & Provenzano, P. P. (2017). Anisotropic forces from spatially constrained focal adhesions mediate contact guidance directed cell migration. *Nature Communications*, *8*(1), 14923. https://doi.org/10.1038/ncomms14923

Refaaq, F. M., Chen, X., & Pang, S. W. (2020). Effects of topographical guidance cues on osteoblast cell migration. *Scientific Reports*, *10*(1), 20003. https://doi.org/10.1038/s41598-020-77103-0

Ricotti, V., Mandy, W. P. L., Scoto, M., Pane, M., Deconinck, N., Messina, S., Mercuri, E., Skuse, D. H., & Muntoni, F. (2016). Neurodevelopmental, emotional, and behavioural problems in Duchenne muscular dystrophy in relation to underlying dystrophin gene mutations. *Developmental Medicine and Child Neurology*, *58*(1), 77-84. https://doi.org/10.1111/dmcn.12922

Rodino-Klapac, L. R., Janssen, P. M. L., Shontz, K. M., Canan, B., Montgomery, C. L., Griffin, D., Heller, K., Schmelzer, L., Handy, C., Clark, K. R., Sahenk, Z., Mendell, J. R., & Kaspar, B. K. (2013). Micro-dystrophin and follistatin co-delivery restores muscle function in aged DMD model. *Human Molecular Genetics*, *22*(24), 4929-4937. https://doi.org/10.1093/hmg/ddt342

Rougerie, P., Silva dos Santos, R., Farina, M., & Anselme, K. (2021). Molecular Mechanisms of Topography Sensing by Osteoblasts : An Update. *Applied Sciences*, *11*(4), Article 4. https://doi.org/10.3390/app11041791

Rowe, R. G., & Daley, G. Q. (2019). Induced pluripotent stem cells in disease modelling and drug discovery. *Nature Reviews Genetics*, *20*(7), 377-388. https://doi.org/10.1038/s41576-019-0100-z

Santoso, J. W., & McCain, M. L. (2020). Neuromuscular disease modeling on a chip. *Disease Models & Mechanisms*, *13*(7), dmm044867. https://doi.org/10.1242/dmm.044867

Sanz-Horta, R., Matesanz, A., Gallardo, A., Reinecke, H., Jorcano, J. L., Acedo, P., Velasco, D., & Elvira, C. (2023). Technological advances in fibrin for tissue engineering. *Journal of Tissue Engineering*, *14*, 20417314231190288. https://doi.org/10.1177/20417314231190288

Schiele, N. R., Chrisey, D. B., & Corr, D. T. (2011). Gelatin-Based Laser Direct-Write Technique for the Precise Spatial Patterning of Cells. *Tissue Engineering Part C: Methods*, *17*(3), 289-298. https://doi.org/10.1089/ten.tec.2010.0442

Segeritz, C.-P., & Vallier, L. (2017). Chapter 9 - Cell Culture : Growing Cells as Model Systems In Vitro. In M. Jalali, F. Y. L. Saldanha, & M. Jalali (Éds.), *Basic Science Methods for Clinical Researchers* (p. 151-172). Academic Press. https://doi.org/10.1016/B978-0-12-803077-6.00009-6

Serra, P., Colina, M., Fernández-Pradas, J. M., Sevilla, L., & Morenza, J. L. (2004). Preparation of functional DNA microarrays through laser-induced forward transfer. *Applied Physics Letters*, *85*(9), Article 9. https://doi.org/10.1063/1.1787614

Serra, P., & Piqué, A. (2019). Laser-Induced Forward Transfer : Fundamentals and Applications. *Advanced Materials Technologies*, *4*(1), 1800099. https://doi.org/10.1002/admt.201800099

Shefer, G., & Yablonka-Reuveni, Z. (2005). Isolation and Culture of Skeletal Muscle Myofibers as a Means to Analyze Satellite Cells. In C. D. Helgason & C. L. Miller (Éds.), *Basic Cell Culture Protocols* (p. 281-304). Humana Press. https://doi.org/10.1385/1-59259-838-2:281

Shiomi, K., Kiyono, T., Okamura, K., Uezumi, M., Goto, Y., Yasumoto, S., Shimizu, S., & Hashimoto, N. (2011). CDK4 and cyclin D1 allow human myogenic cells to recapture growth property without compromising differentiation potential. *Gene Therapy*, *18*(9), 857-866. https://doi.org/10.1038/gt.2011.44

Slater, C. R., & Schiaffino, S. (2008). Innervation of Regenerating Muscle. In S. Schiaffino & T. Partridge (Éds.), *Skeletal Muscle Repair and Regeneration* (p. 303-334). Springer Netherlands. https://doi.org/10.1007/978-1-4020-6768-6_14

Smoak, M. M., & Mikos, A. G. (2020). Advances in biomaterials for skeletal muscle engineering and obstacles still to overcome. *Materials Today Bio*, *7*, 100069. https://doi.org/10.1016/j.mtbio.2020.100069

Sopeña i Martínez, P. (2020). Laser-induced forward transfer for printed electronics applications. *Tesis Doctorals - Facultat - Física*. https://diposit.ub.edu/dspace/handle/2445/174225

Sopeña, P., Fernández-Pradas, J. M., & Serra, P. (2020). Laser-induced forward transfer of conductive screen-printing inks. *Applied Surface Science*, *507*, 145047. https://doi.org/10.1016/j.apsusc.2019.145047

Sorkio, A., Koch, L., Koivusalo, L., Deiwick, A., Miettinen, S., Chichkov, B., & Skottman, H. (2018). Human stem cell based corneal tissue mimicking structures using laser-assisted 3D bioprinting and functional bioinks. *Biomaterials*, *171*, 57-71. https://doi.org/10.1016/j.biomaterials.2018.04.034

Sun, Q., Zhang, Z., & Sun, Z. (2014). The potential and challenges of using stem cells for cardiovascular repair and regeneration. *Genes & Diseases*, *1*(1), 113-119. https://doi.org/10.1016/j.gendis.2014.07.003

Takahashi, K., Tanabe, K., Ohnuki, M., Narita, M., Ichisaka, T., Tomoda, K., & Yamanaka, S. (2007). Induction of pluripotent stem cells from adult human fibroblasts by defined factors. *Cell*, *131*(5), 861-872. https://doi.org/10.1016/j.cell.2007.11.019

Takahashi, K., & Yamanaka, S. (2006). Induction of pluripotent stem cells from mouse embryonic and adult fibroblast cultures by defined factors. *Cell*, *126*(4), 663-676. https://doi.org/10.1016/j.cell.2006.07.024

Tao Xu, Xu, T., Joyce Jin, Jin, J., Cassie Gregory, Gregory, C., James J. Hickman, Hickman, J. J., Thomas Boland, & Boland, T. (2005). Inkjet printing of viable mammalian cells. *Biomaterials*, *26*(1), 93-99. https://doi.org/10.1016/j.biomaterials.2004.04.011

Tchao, J., Kim, J. J., Lin, B., Salama, G., Lo, C. W., Yang, L., & Tobita, K. (2013). Engineered Human Muscle Tissue from Skeletal Muscle Derived Stem Cells and Induced Pluripotent Stem Cell Derived Cardiac Cells. *International Journal of Tissue Engineering*, *2013*(1), 198762. https://doi.org/10.1155/2013/198762

Testa, S., Fornetti, E., Fuoco, C., Sanchez-Riera, C., Rizzo, F., Ciccotti, M., Cannata, S., Sciarra, T., & Gargioli, C. (2021). The War after War : Volumetric Muscle Loss Incidence, Implication, Current Therapies and Emerging Reconstructive Strategies, a Comprehensive Review. *Biomedicines*, *9*(5), Article 5. https://doi.org/10.3390/biomedicines9050564

Thakur, S. S., Swiderski, K., Chhen, V. L., James, J. L., Cranna, N. J., Islam, A. M. T., Ryall, J. G., & Lynch, G. S. (2020). HSP70 drives myoblast fusion during C2C12 myogenic differentiation. *Biology Open*, *9*(7), bio053918. https://doi.org/10.1242/bio.053918

Thomas Boland, Boland, T., Tao Xu, Xu, T., Brook Damon, Damon, B., Xiaofeng Cui, & Cui, X. (2006). Application of inkjet printing to tissue engineering. *Biotechnology Journal*, *1*(9), 910-917. https://doi.org/10.1002/biot.200600081

Thomson, J. A., Itskovitz-Eldor, J., Shapiro, S. S., Waknitz, M. A., Swiergiel, J. J., Marshall, V. S., & Jones, J. M. (1998). Embryonic stem cell lines derived from human blastocysts. *Science (New York, N.Y.)*, *282*(5391), 1145-1147. https://doi.org/10.1126/science.282.5391.1145

Turkoz, E., Fardel, R., Arnold, C., Piqué, A., & Serra, P. (2018). *Advances in Blister-Actuated Laser-Induced Forward Transfer (BA-LIFT)* (p. 91-121). https://doi.org/10.1002/9783527805105.ch5

Turner, N. J., & Badylak, S. F. (2012). Regeneration of skeletal muscle. *Cell and Tissue Research*, *347*(3), 759-774. https://doi.org/10.1007/s00441-011-1185-7

Uhrig, M., Ezquer, F., & Ezquer, M. (2022). Improving Cell Recovery : Freezing and Thawing Optimization of Induced Pluripotent Stem Cells. *Cells*, *11*(5), 799. https://doi.org/10.3390/cells11050799

Uquillas, J. A., Moroni, L., & de Boer, J. (2023). Chapter 1—An introduction to tissue engineering; the topic and the book. In J. De Boer, C. A. V. Blitterswijk, J. A. Uquillas, & N. Malik (Éds.), *Tissue Engineering (Third Edition)* (p. 1-12). Academic Press. https://doi.org/10.1016/B978-0-12-824459-3.00001-9

Valentine, B. A. (2017). Skeletal Muscle. *Pathologic Basis of Veterinary Disease*, 908-953.e1. https://doi.org/10.1016/B978-0-323-35775-3.00015-1

Van Norman, G. A. (2019). Limitations of Animal Studies for Predicting Toxicity in Clinical Trials. *JACC: Basic to Translational Science*, *4*(7), 845-854. https://doi.org/10.1016/j.jacbts.2019.10.008

van der Maarel, S. M., & Frants, R. R. (2005). The D4Z4 Repeat–Mediated Pathogenesis of Facioscapulohumeral Muscular Dystrophy. *American Journal of Human Genetics*, *76*(3), 375-386.

Volpi, M., Paradiso, A., Costantini, M., & Święszkowski, W. (2022). Hydrogel-Based Fiber Biofabrication Techniques for Skeletal Muscle Tissue Engineering. *ACS Biomaterials Science & Engineering*, *8*(2), 379-405. https://doi.org/10.1021/acsbiomaterials.1c01145

von der Linde, D., & Sokolowski-Tinten, K. (2000). The physical mechanisms of short-pulse laser ablation. *Applied Surface Science*, *154-155*, 1-10. https://doi.org/10.1016/S0169-4332(99)00440-7

Wang, L. H., & Tawil, R. (2016). Facioscapulohumeral Dystrophy. *Current Neurology and Neuroscience Reports*, *16*(7), 66. https://doi.org/10.1007/s11910-016-0667-0

Xiong, R., Zhang, Z., Chai, W., Chrisey, D. B., & Huang, Y. (2017). Study of gelatin as an effective energy absorbing layer for laser bioprinting. *Biofabrication*, *9*(2), 024103. https://doi.org/10.1088/1758-5090/aa74f2

Yaffe, D. (1968). Retention of differentiation potentialities during prolonged cultivation of myogenic cells. *Proceedings of the National Academy of Sciences*, *61*(2), 477-483. https://doi.org/10.1073/pnas.61.2.477

Yaffe, D., & Saxel, O. (1977). Serial passaging and differentiation of myogenic cells isolated from dystrophic mouse muscle. *Nature*, *270*(5639), 725-727. https://doi.org/10.1038/270725a0

Yao, Y., Molotnikov, A., Parkington, H. C., Meagher, L., & Forsythe, J. S. (2022). Extrusion 3D bioprinting of functional self-supporting neural constructs using a photoclickable gelatin bioink. *Biofabrication*, *14*(3). https://doi.org/10.1088/1758-5090/ac6e87

Yusuf, F., & Brand-Saberi, B. (2012). Myogenesis and muscle regeneration. *Histochemistry and Cell Biology*, *138*(2), 187-199. https://doi.org/10.1007/s00418-012-0972-x

Zacharatos, F., Makrygianni, M., & Zergioti, I. (2021). Laser-Induced Forward Transfer (LIFT) Technique as an Alternative for Assembly and Packaging of Electronic Components. *IEEE Journal of Selected Topics in Quantum Electronics*, *27*(6), 1-8. IEEE Journal of Selected Topics in Quantum Electronics. https://doi.org/10.1109/JSTQE.2021.3084443

Žemaitis, A., Gečys, P., Račiukaitis, G., & Gedvilas, M. (2020). Efficient ablation by ultra-short pulse lasers. *Procedia CIRP*, *94*, 962-965. https://doi.org/10.1016/j.procir.2020.09.083

Zeng, B., Cai, Z., Lalevée, J., Yang, Q., Lai, H., Xiao, P., Liu, J., & Xing, F. (2021). Cytotoxic and cytocompatible comparison among seven photoinitiators-triggered polymers in different tissue cells. *Toxicology in Vitro: An International Journal Published in Association with BIBRA*, *72*, 105103. https://doi.org/10.1016/j.tiv.2021.105103

Zeng, F., & Zhou, Q. (2011). Induced Pluripotent Stem Cells : On the Road Toward Clinical Applications. In K. Appasani & R. K. Appasani (Éds.), *Stem Cells & Regenerative Medicine : From Molecular Embryology to Tissue Engineering* (p. 427-438). Humana Press. https://doi.org/10.1007/978-1-60761-860-7_26

Zennifer, A., Subramanian, A., & Sethuraman, S. (2022). Design considerations of bioinks for laser bioprinting technique towards tissue regenerative applications. *Bioprinting*, *27*, e00205. https://doi.org/10.1016/j.bprint.2022.e00205

Zhang, J., Byers, P., Erben, A., Frank, C., Schulte-Spechtel, L., Heymann, M., Docheva, D., Huber, H. P., Sudhop, S., & Clausen-Schaumann, H. (2021). Single Cell Bioprinting with Ultrashort Laser Pulses. *Advanced Functional Materials*, *31*(19), 2100066. https://doi.org/10.1002/adfm.202100066

Zhang, Y., & Habibovic, P. (2022). Delivering Mechanical Stimulation to Cells : State of the Art in Materials and Devices Design. *Advanced Materials*, *34*(32), 2110267. https://doi.org/10.1002/adma.202110267

Zhang, Z., Xiong, R., Corr, D. T., & Huang, Y. (2016). Study of Impingement Types and Printing Quality during Laser Printing of Viscoelastic Alginate Solutions. *Langmuir*, *32*(12), 3004-3014. https://doi.org/10.1021/acs.langmuir.6b00220

Zhang, Z., Xiong, R., Mei, R., Huang, Y., & Chrisey, D. B. (2015). Time-Resolved Imaging Study of Jetting Dynamics during Laser Printing of Viscoelastic Alginate Solutions. *Langmuir*, *31*(23), 6447-6456. https://doi.org/10.1021/acs.langmuir.5b00919

Zhang, Z., Xu, C., Xiong, R., Chrisey, D. B., & Huang, Y. (2017). Effects of living cells on the bioink printability during laser printing. *Biomicrofluidics*, *11*(3), 034120. https://doi.org/10.1063/1.4985652

Zhao, S., Chen, J., Wu, L., Tao, X., Yaqub, N., & Chang, J. (2023). Induced Pluripotent Stem Cells for Tissue-Engineered Skeletal Muscles. *International Journal of Molecular Sciences*, *24*(14), Article 14. https://doi.org/10.3390/ijms241411520

Zschüntzsch, J., Meyer, S., Shahriyari, M., Kummer, K., Schmidt, M., Kummer, S., & Tiburcy, M. (2022). The Evolution of Complex Muscle Cell In Vitro Models to Study Pathomechanisms and Drug Development of Neuromuscular Disease. *Cells*, *11*(7). https://doi.org/10.3390/cells11071233